Theoretical investigation of surfaces and interfaces at the atomic scale : ultrathin films supported on metals and intermetallics

Thiago Trevizam Dorini

To cite this version:

Thiago Trevizam Dorini. Theoretical investigation of surfaces and interfaces at the atomic scale : ultrathin films supported on metals and intermetallics. Materials Science [cond-mat.mtrl-sci]. Université de Lorraine, 2022. English. NNT : 2022LORR0191 . tel-04127287

HAL Id: tel-04127287
https://hal.univ-lorraine.fr/tel-04127287

Submitted on 13 Jun 2023

Université de Lorraine (UL), Institut Jean Lamour (IJL)
Lorraine Université d'Excellence (LUE)
École Doctorale C2MP

THÈSE

Pour l'obtention du titre de :

DOCTEUR DE L'UNIVERSITÉ DE LORRAINE

Spécialité : Science des matériaux

Présentée par :

TREVIZAM DORINI Thiago

THEORETICAL INVESTIGATION OF SURFACES AND INTERFACES AT THE ATOMIC SCALE: ULTRATHIN FILMS SUPPORTED ON METALS AND INTERMETALLICS

Thèse soutenue publiquement le 15/12/2022 à Nancy devant le jury composé de :

Président :	M. Sébastien Lebègue	Directeur de recherche, LPCT, CNRS, Université de Lorraine
Rapporteurs :	Mme. Anne Hemeryck	Chargée de recherche, LAAS-CNRS
	M. Jacek Goniakowski	Directeur de recherche, INSP, CNRS, Sorbonne Université
Examinateurs :	M. Stefan Förster	Chercheur, Institute of physics, MLU Halle-Wittenberg
	Mme. Céline Dupont	Chargée de recherche, ICB, CNRS, Université de Franche Comté
Directrice :	Mme. Émilie Gaudry	Professeure, IJL, CNRS, Université de Lorraine
Invité :	M. Anton Kokalj	Directeur de recherche, Jožef Stefan Institute

Institut Jean Lamour - UMR 7198 - Département P2M - Équipe 102

Acknowledgements

It has been a long journey until the end of this work, full of moments that will stay in my memories forever. I would like to spend a few words to the people whom I've met and that contributed, directly or indirectly, be it scientifically or emotionally, to this final state of my work.

First of all, I would like to thank my supervisor Prof. Dr. Émilie Gaudry for your unconditional support throughout these three years of thesis. Thanks for all discussions, insights, patience, and for always being available when I needed help, you have truly been a great supervisor and I feel very lucky to have worked with you. I would also like to thank our collaborator Dr. Anton Kokalj for all your valuable contributions to this work's quality during my stays in Ljubljana (accompanied by skiing sections) or by videoconference. I thank the members of the 203 team: Julian Ledieu, Vincent Fournée, Muriel Sicot, and Marie-Cécile for the help during our group meetings and corridor discussions. I appreciate not only all help when I needed it but also the great friendly ambiance of our team. In addition, I thank all members of team 102 for the fruitful discussions and friendliness. I've learned many things about how to be a great researcher from all of you and want to keep following your steps.

I thank the members of the jury: Dr. Anne Hemeryck and Dr. Jacek Goniakowski for the time they devoted to the careful reading of my manuscript and for their pertinent and constructive feedback, and to Dr. Stefan Förster, Dr. Sébastien Lebègue, and Dr. Céline Dupont for being part of my work's evaluation.

Moving to a more emotional part, I would like to thank everyone in the blessed family that I have. They are the solid ground that made me who I am and I'll always be grateful for their support and encouragement for the decisions I made in my life. I thank my mother Andrea and my father Marcio for being such loving parents, and my sisters Andressa and Vanessa for their companionship during all moments in my life. I also thank my grandmother Darci, my grandfather Irineu, my aunt Alessandra, my uncle Marcos, and my cousin Guilherme for the love they've given me.

In addition, the greatest gift that life gave me during this period is my wife Catalina. What started as a beautiful friendship evolved into a great love. It is extremely hard to put into words how important you are to me and how happy I'm with you, which is something that I try to express every single day. I've learned with you that the simplest things in life are the most important, so I'll also be simple here: I thank you for your love. With that being said, I would like to thank the new members of my family, my mother-in-law Martha and father-in-law Germán, Martha Lucia, Plínio, Ana, Pedro, and everyone else that I had the pleasure to meet. I thank you all for your support and the loving time we've spent in Colombia.

I thank my childhood friends, Paulo, Gabriel Lacerda, Beatriz, Arthur, and Gabriel Rossi for your unconditional support in all moments in my life, and my friends from Lorena: Pedro, Luiz, Carlos, Gilberto, Eduardo, Tiago, Thomas, Daniel, Glina, Danilo, Mizéria, Leonardo, Nabil, Dennis, Julio, Marcos.

To the new friends that I made: Sébastien, Dominique, Mihai, Yiming, Rafa, Alexis, Mauricio, Lorena, Wilfried, Adrian, Aurelia, Vishal, Corentin, Kathleen, Miguel, Kanika, Nathan, Zil, Sofía, Killian, Safouane, Soufiane, Thomas, Luigi, Alejandro, Clovis, Florian, Marco, Giselle, Leandro, Chaves, Dzevad, Monika, Ana Kras, Matjas, Lea, Eric, Ivan, and Matic. It has been an extremely rich experience to have met people from so many nationalities, I thank you all for your friendship and I wish we continue to keep in touch.

Muito obrigado.

For Catalina, Andréa, Marcio, Andressa, Vanessa, Darci, Irineu, Alessandra, Marcos, Guilherme,
and
in memory of my cousin Renan.

Abstract

The growth of two dimensional (2D) oxide materials on metals or intermetallics can lead to complex atomic arrangements, whose structural description at the atomic scale is not straightforward. Considerable progress has been made in crystal structure prediction in recent years through the development of efficient computer codes and the availability of powerful computational resources. In this work, several approaches are used that are based on tiling configurations, evolutionary algorithms, and ab initio molecular dynamics, combined with Density Functional Theory. We focus on two distinct ultrathin films systems : oxide quasicrystalline approximants (OQA) and complex oxide films grown on PdIn(001). In the former system, we start from the structural models derived from the works of Förster et al. and Cockayne et al., and systematically investigate the intrinsic properties of these 2D OQA supported on metallic substrates. We reveal structure-property relationships and compare with recently discovered phases. On the latter system, we apply a combination of DFT and evolutionary computations to propose several possible atomic structures of ultrathin indium oxide films on PdIn(001). For both systems, the stability is investigated with formation enthalpies and surface free energies, using thermodynamic models to account for the growth conditions. The scanning tunneling microscopy (STM) images, which are correlated with the tiling configurations for each structure, are simulated as well. Electronic-structure calculations also provide insights about the oxide–substrate interactions. This computational work can be used as a basis for future experiments and is valuable for the theoretical understanding of the structure-properties relationship for these ultrathin films.

Résumé

La croissance de matériaux oxydes bidimensionnels (2D) sur des métaux ou des intermétalliques peut conduire à des arrangements atomiques complexes, dont la description structurale à l'échelle atomique n'est pas simple. Des progrès considérables ont été réalisés dans la prédiction de structures cristallines ces dernières années, grâce au développement de codes de calcul efficaces et à la disponibilité de ressources de calcul importantes. Dans ce travail, plusieurs approches sont utilisées, basées sur des configurations de pavage, un algorithmes évolutif, ou des calculs de dynamique moléculaire ab initio, combinés à la Théorie de la Fonctionnelle de la Densité. Nous nous concentrons sur deux systèmes de films ultra-minces distincts : les approximants quasi-cristallins d'oxyde (OQA) et les films d'oxyde complexes supportés sur PdIn(001). Dans le premier système, on part des modèles structuraux issus des travaux de Förster et al. et Cockayne et al. et nous étudions systématiquement les propriétés intrinsèques de ces OQA 2D lorsqu'ils sont déposés sur des substrats métalliques. Cela nous permet de révéler les relations structure-propriété et les comparer aux phases récemment découvertes. Sur le deuxième système, nous appliquons une combinaison de DFT et de calculs évolutifs pour proposer plusieurs structures atomiques possibles de films d'oxyde d'indium ultrafins sur PdIn(001). Pour les deux systèmes, la stabilité est évaluée par le calcul des enthalpies de formation et des énergies de surface, en utilisant des modèles thermodynamiques pour rendre compte des conditions de croissance. Les images de microscopie à effet tunnel (STM), qui sont corrélées avec le pavage (arrangements des des tuiles) pour chaque structure, sont simulées. Les calculs de structure électronique fournissent également des informations sur l'interaction oxyde-substrat. Ce travail théorique peut être utilisé comme base solide pour de futures expériences et est précieux pour la compréhension théorique de la relation structure-propriétés de ces films ultra-minces.

Synthèse

Introduction

Une nouvelle famille de nanomatériaux, communément appelés matériaux bidimensionnels (2D) ou matériaux ultraminces, présente des structures en forme de feuillets dont l'épaisseur se situe entre celle d'un seul et de quelques atomes (généralement moins de 5 nm) [1]. Il y a trois raisons principales qui font que les films 2D ultraminces diffèrent d'autres classes de matériaux comme les nanoparticules de dimension zéro (0D), les nanofils unidimensionnels (1D) ou les réseaux tridimensionnels (3D). Tout d'abord, les matériaux bidimensionnels présentent une surface spécifique très élevée en raison de leur grande dimension latérale et de leur épaisseur extrêmement fine. Cette propriété est très avantageuse pour une variété d'applications, notamment en catalyse ou pour fabriquer des supercondensateurs [1]. Deuxièmement, par rapport aux nanomatériaux conventionnels, les nanomatériaux 2D ultrafins autosupportés peuvent présenter des caractéristiques électriques intéressantes en raison du confinement des électrons en deux dimensions. Cela en fait des candidats pour la recherche fondamentale sur la matière condensée. Enfin, ils sont prometteurs pour la fabrication de dispositifs électroniques et optoélectroniques flexibles et transparents [2].

Oxydes 2D ultraminces sur matériaux métalliques

Les matériaux ultrafins présentent uune grande variété d'applications. Dans ce travail, nous nous concentrons sur un groupe spécifique de ces matériaux : les systèmes interfaciaux ultraminces oxyde-sur-métal (UTOx). Une grande partie de ce travail concerne les système de type perovskite (ABO_3) sur la surface dense de métaux FCC. La réduction de l'épaisseur jusqu'à la limite de la monocouche altère leurs structures et modifie leurs propriétés physiques et chimiques, comme cela a déjà été démontré dans le cas d'autres types de films d'oxydes 2D ultraminces [3], [4] - TiOx /Pt(111), [5] MnO_x /Pd(100) [6] et VO_x/Pd(111) [7], [8], pour n'en citer que quelques-uns. Cela a récemment conduit à l'émergence de nouvelles structures avec un ordre apériodique, c'est-à-dire des interfaces quasicristallines d'oxyde dodécagonaux dans les systèmes $BaTiO_3$/Pt(111) et $SrTiO_3$/Pt(111), dont les premiers spécimens ont été découverts par le groupe du professeur docteur Widdra [9]–[12]. La force motrice de ces modifications structurelles uniques, résultant de la réduction de l'épaisseur, est loin d'être entièrement dévoilée. Les coordinations de liaison réduites, une forte polarisation de surface possible, les effets de support et les conditions expérimentales sont supposés jouer un rôle, mais aucune image claire n'a encore été dressée [3], [4].

Films ultraminces sur le système In_xO_y/PdIn

Un domaine de recherche très actif est l'étude des catalyseurs et des réactions pour la formation du méthanol, qui est une molécule extrêmement importante pour l'avenir de l'énergie, servant de source de carbone pour l'industrie chimique et de vecteur d'hydrogène [13], [14]. Aujourd'hui, le méthanol est principalement produit par la conversion de gaz de synthèse, un mélange gazeux de CO, CO_2 et H_2 obtenu à partir de charbon ou de gaz naturel, en utilisant un procédé à des températures et des pressions élevées, et un catalyseur principal à base de cuivre (Cu/ZnO/Al_2O_3) [15]. Cependant, cette conversion est encore confrontée à de nombreux problèmes de sélectivité du CO_2 car elle est également active pour la réaction du gaz à l'eau inverse (RWGSR, reverse water gas shift reaction), produisant du CO comme sous-produit. Par conséquent, de nombreux travaux sont actuellement consacrés à la recherche d'un catalyseur présentant de meilleures propriétés que celles de Cu/ZnO/Al_2O_3. Les alliages à base de Pd et les systèmes contenant des oxydes d'indium ultrafins constituent des systèmes candidats prometteurs. Les principes régissant les bonnes propriétés catalytiques des alliages à base de Pd commencent à être élucidés, mais de nombreuses recherches sont encore nécessaires. Les intermétalliques à base de Pd peuvent présenter d'excellentes propriétés catalytiques selon le concept d'isolation de site [16], [17], en particulier lorsque les atomes de Pd sont entourés d'éléments tels que In, Zn ou Ga.

Il est intéressant de noter que des études ont également rapporté les propriétés catalytiques supérieures de l'oxyde d'indium (In_xO_y). Sur de tels systèmes, le méthanol semble être le résultat le plus favorisé de l'hydrogénation du CO_2 sur des surfaces d'In_2O_3(110) non défectueuses et défectueuses, et la réaction semble suivre un mécanisme impliquant la formation et l'annihilation cycliques de lacunes d'oxygène [18]. Une augmentation de l'activité catalytique de cette phase d'oxyde peut être obtenue par la présence de Pd comme promoteur [19], ce qui réduit la réaction du gaz à l'eau inverse. Ces études sugèrent qu'un système composé d'un substrat PdIn (terminé par du Pd) qui supporte un oxyde d'indium peut avoir une activation et une sélection de réaction très élevées. Jusqu'à présent, de nombreuses recherches ont montré l'existence d'un tel oxyde d'indium ultrafin supporté par un substrat de Pd ou de PdIn [20]–[22], mais ces études sont basées sur les structures de In_2O_3 massif et non sur les caractéristiques d'un film ultrafin, dont nous avons vu qu'il peut varier considérablement en structure, composition et propriétés. La première étape ici est l'élaboration d'un modèle structural pour les films d'oxyde d'indium ultraminces avec différentes compositions supportées sur le PdIn(001), en déterminant aussi bien ses stabilités, ses propriétés électroniques, et une base de données d'images STM théoriques qui serviront de base aux futurs travaux expérimentaux et théoriques.

Films ultraminces d'oxydes quasipériodiques : les phases sigma

La phase Förster-σ

Nous aborderons nos résultats sur la phase approximant σ, construite en utilisant le modèle de Förster. L'un des objectifs de notre étude est d'évaluer la stabilité thermodynamique relative des approximants d'oxydes quasicristallins (OQA, oxide quasicrystalline approximants), d'étudier quels paramètres contrôlent leur formation et de prédire quelques propriétés physiques. La série des OQA 2D est étudiée en utilisant des modèles structurels dérivés de celui conçu pour $BaTiO_3/Pt(111)$ [10]. Une grande variété de compositions chimiques est considérée ici, par le biais de substitutions atomiques basées sur le motif chimique $A_5B_4O_{12}$, avec A = Ba, Ca, Sr et B = Ti, V, Cr, Mn, Fe, Co, Ni. Des calculs pour évaluer les DOS (densités d'états) et les COHP (Crystal Orbital Hamiltonian Populattion) ont été effectués pour l'ensemble complet des OQAs, autosuppportées ou sur substrat métallique. Ils suggèrent des hybridations au sein de la couche d'oxyde (principalement entre les atomes B et O). Les DOS des monocouches d'oxyde autosupportées sont considérablement modifiées dans les OQAs supportés. L'effet le plus évident est probablement l'élargissement des bandes. Par exemple, alors que l'hybridation entre les états Ti et O se produit dans la plage $[-4.4, -2.0]$ eV dans la monocouche d'oxyde autoportée, elle s'étend de -5.5 eV à l'énergie de Fermi pour l'OQA $BaTiO_3$ supporté sur Pt. Cette observation est moins claire pour les métaux comme le fer ou le cobalt, car la contribution des états de l'élément B de la couche autosupportée sont situés dans une plage d'énergie plus large, jusqu'à environ 1 eV. Nos calculs suggèrent également que le transfert de charge est un paramètre important qui contrôle la structure de l'OQA. Une corrélation est mise en évidence entre la corrugation du film ($R = z^+ - z^-$, avec z étant la hauteur moyenne des (+) cations et des (-) anions) et la charge de Bader portée par les atomes B. Le transfert de charge influence également la thermodynamique du système à travers l'énergie d'adhésion.

Dans l'ensemble, une plus forte adhésion du film correspond en effet à une plus grande charge de Bader sur B (Q_B), alors que ni la corrugation ni l'inadéquation des paramètres de maille de surface ne montrent de corrélations claires avec l'énergie d'adhésion. La corrugation du film d'oxyde, le transfert interfacial d'électrons et les énergies d'adhésion présentent des tendances générales dans la série. Les propriétés magnétiques sont influencées par la nature du substrat et du métal B, tandis que le type de métal alcalino terreux A a un impact sur ΔW, c'est-à-dire le changement du travail de sortie du substrat métallique induit par le dépôt du film d'oxyde. Notamment, aucune corrélation claire n'a été trouvée entre l'inadéquation des paramètres des mailles de surface et les énergies d'adhésion, bien que ce critère soit généralement considéré comme la principale force motrice vers la formation de couches d'oxyde ultra-minces sur les métaux, y compris les OQA. En revanche, les effets électroniques ont été identifiés comme des paramètres importants qui influencent la formation des OQAs. En particulier, les énergies d'adhésion et la corrugation semblent corrélées au transfert de charge, déterminé par la charge sur le métal de type B.

La phase Cockayne-σ

Un modèle structural diférent pour décrire la phase approximante sigma a été proposé par Cockayne et al. [23]. Il permet d'avoir un meilleur accord entre les images STM simulées et expérimentales [9]. Cette phase Cockayne-σ (avec composition $Sr_2Ti_6O_9$) est plus stable que la phase Förster-σ (avec composition $Sr_5Ti_4O_{12}$), compte tenu de l'enthalpie de formation, des énergies d'adhésion. Néanmoins, il y a quelques similitudes à noter entre ces deux modèles, comme la distribution globale de la charge dans le substrat et l'oxyde, montrée par les isosurfaces des différences de densité de charge et la charge atomique moyenne de Bader portée par les atomes à l'interface. Pour la phase Cockayne-σ, l'énergie d'adhésion est de -0.23 eV/Å^2 , ce qui est beaucoup plus fort que celle calculée pour l'approximant Förster-σ (-0.07 eV/Å^2), mais plus faible que pour la structure en nid d'abeille (-0.40 eV/Å^2). Afin d'analyser les liaisons chimiques responsables de l'adhésion oxyde/substrat, nous avons utilisé la méthode COHP [24] telle qu'implémentée dans le programme LOBSTER [25].

En ce qui concerne l'interaction oxyde-substrat, les calculs COHP montrent que les liaisons Ti-Pt sont fortes, ce qui n'est pas le cas des liaisons Sr-Pt. Considérant que les liaisons jusqu'à 4 Å, ce résultat suggère que l'adhésion est induite pour une large part par les liaisons Ti-Pt (ICOHP = -1.63 eV en moyenne, avec 17 liaisons considérées). Les liaisons Sr-Pt sont plus faibles (ICOHP = -0.50 eV en moyenne pour 4 liaisons). En regardant les liaisons chimiques dans l'oxyde, nous pouvons identifier une forte hybridation Ti-O (en moyenne pour 30 liaisons, ICOHP = -4.17 eV) alors que les liaisons Sr-O sont plus faibles (ICOHP = -0.26 eV en moyenne pour 12 liaisons considérées). Les atomes de Ti assurent la cohésion dans la couche d'oxyde, et l'adhesion avec le substrat. Une analyse similaire réalisée dans le système autosupporté (sans le substrat Pt(111)) montre que lorsque l'interaction de la couche d'oxyde avec le substrat est supprimée, les liaisons Ti-O dans le plan d'oxyde deviennent beaucoup moins fortes, avec un peuplement des interactions antiliantes. Le cas des liaisons Sr-O est encore plus extrême, puisque les interactions anti-liantes dominent sur toute la gamme d'énergie des états occupés. Cette preuve montre que l'interaction avec le substrat est un facteur clé pour la formation des oxydes à deux dimensions supportés. Le transfert de charge à l'interface implique une perte d'électrons de l'oxyde 2D au profit de la première couche du substrat Pt.

Films ultraminces d'oxydes quasipériodiques : modélisation DFT à partir du pavage NGT et de décorations atomiques de tuiles

Nous allons présenter ici les résultats sur d'autres phases approximants que l'on peut trouver dans la littérature, dans le système Sr-Ti-O/Pt(111). A partir des différents modèles traduits de la phase Cockayne-σ, nous avons vu que l'énergie ne varie pas de manière significative lorsque les atomes de Ti, qui sont ceux responsables de l'adhésivité de l'oxyde comme vu dans les calculs COHP, sont positionnés de plusieurs manières différentes par rapport au substrat Pt(111). Le principal facteur qui modifie, notamment l'énergie d'adhésion de chaque oxyde, est la quantité totale de Ti dans la cellule unitaire. L'UTOx hexagonal et géant présentent des enthalpies de formation similaires : -1.08 eV/Å^2 et -1.03 eV/Å^2. Leur stabilité à 0 K semble être supérieure à celle du Cockayne-σ, du petit hexagone, de la phase fictive 1 et des phases monocliniques, avec des enthalpies de formation de -0.62, -0.44, -0.72, -0.60 et -0.60 eV/Å^2, respectivement (structures dans Figure 1).

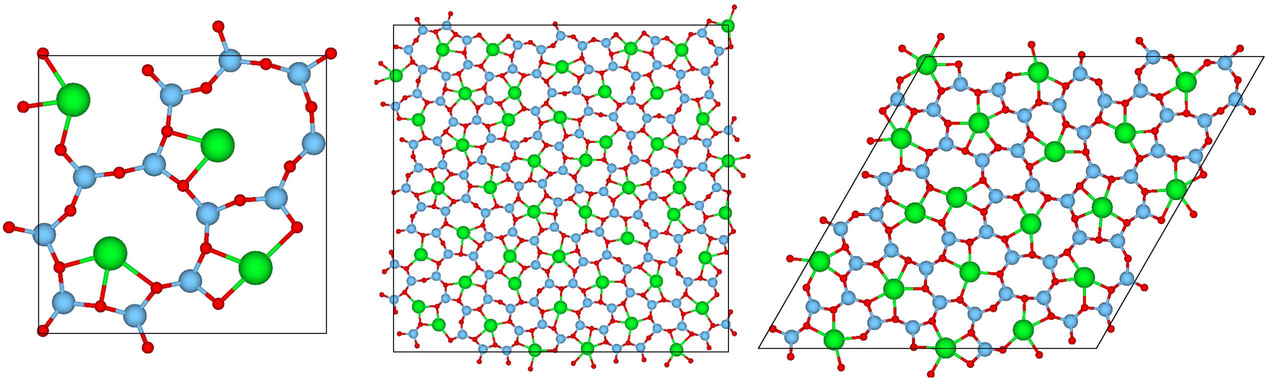
(a) Cockayne-σ

(b) Approx. géant

(c) Approx. hexagonale

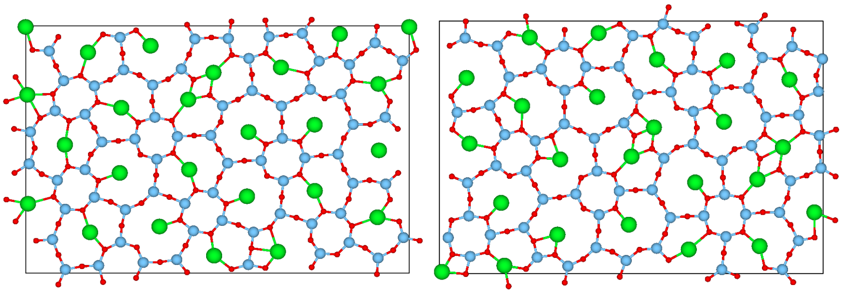
(d) Monoclinique

(e) Monoclinique mod.

(f) Petit hexagonal

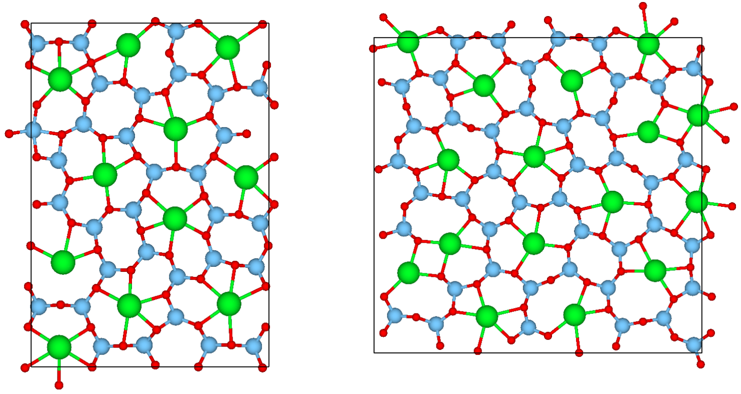
(g) Approx 1

(h) Approx 2

(i) Approx 3

Figure 1: Vue de dessus du (a) Cockayne-σ, (b) approximant géant, (c) l'hexagone approximant, (d) monoclinique, (e) monoclinique modifié, (f) petit hexagonal, et (g-i) sont les structures des approximants créés manuellement à partir du pavage NGT idéal. Sr, Ti et O sont représentés respectivement en vert, gris, et rouge.

Il est intéressant de noter que les phases ayant la valeur absolue la plus élevée de ΔH_{f} sont les phases fictives 2 et 3 (-1.19 eV/Å^2 et -1.18 eV/Å^2, respectivement) créées manuellement à partir du pavage idéal dodécagonal NGT. Ce résultat peut suggérer que ces approximants, et peut-être beaucoup d'autres, peuvent également être stables, mais il est nécessaire de faire des calculs phonons précis et des calculs à température variable pour le confirmer. L'approximant hexagonal et l'approximant géant présentent également des énergies d'adhésion similaires (-0.30 eV/Å^2 et -0.28 eV/Å^2, respectivement). L'énergie d'adhésion de la phase hexagonale est la plus élevée parmi toutes les phases, tandis que les Cockayne-σ présentent la plus faible. Lorsqu'ils sont supportés sur Pt(111), les UTO présentent des relaxations structurelles significatives dans la direction z, c'est-à-dire la direction normale à la surface. Une telle ondulation peut atténuer la déformation élastique due à la différence de taille entre les films supportés et non supportés [26], [27].

Les images STM des différentes phases ont été calculées. Les images STM expérimentales et théoriques sont en très bon accord pour les phases géantes et hexagonales. Les protubérances brillantes sont dus à la présence des atomes de Sr. Malgré que la contribution forte des atomes de Ti à la densité électronique pour les états non occupés, nous n'avons pas observé une modification du contraste des images avec l'application d'une polarisation positive, sans doute à cause de la position des atomes de titane en contact avec le substrat (hauteur plus fable que celle des atomes de Sr). En conclusion, le modèle de Cockayne et al. présente un excellent accord avec les images STM expérimentales et est cohérent avec plusieurs autres quantités calculées (telles que les énergies d'adhésion). Cela implique que cette approche est pertinente pour simuler ces phases et d'autres qui restent à découvrir.

Oxyde ultramince In_xO_y/PdIn(001) : algorithme génétique couplé aux calculs DFT

Dans ce chapitre, nous illustrons la prédiction de structure grâce à une approche couplant un algorithme génétique et des calculs DFT. Le système considéré est un film d'oxyde d'indium ultra-mince sur un substrat PdIn(001). Pour cela, nous utiliserons le code USPEX. Au total, 148 484 configurations ont été calculées, couvrant une large diversité de compositions. Après avoir sélectionné une centaine de structures prometteuses, sur la base de calculs énergétiques, nous avons calculé, à l'aide d'un code à haut débit développé par l'auteur (Vulcan), plusieurs quantités, telles que l'énergie d'adhésion, de surface, les densités électroniques, les images STM, etc. Nous avons mis en place des modèles thermodynamiques, pour prendre en compte les conditions expérimentales (pression, température) et identifier les modèles les plus stables. Au final, nous avons dégagé une vue complète à l'échelle atomique de ces films d'oxyde In_xO_y ultraminces. Les images STM ont été systématiquement calculées, afin que les expériences futures puissent être comparées à nos résultats. Selon nos calculs, l'oxyde d'indium InO adopte une configuration hexagonale déformée pour In et O. En augmentant la composition en oxygène à $x_O = 0.57$ et $x_O = 0.62$, nous pouvons obtenir soit un pavage rectangulaire, soit une combinaison couplant un pavage hexagonal et rectangulaire déformé, les atomes d'indium étant liés à trois ou quatre atomes d'oxygène. Les tuiles identifiées ici permettent de décrire l'ensemble des configurations.

Dans une deuxième étape, nous avons essayé de corréler la stabilité de ces structures atomiques avec quelques paramètres électroniques. Il existe une relation entre la distribution de charges dans le plan du substrat (Pd) en contact avec l'oxyde et la corrugation dans l'oxyde. Pour stimuler le travail des expérimentateurs, nous avons simulé les images STM de la centaine de structures sélectionnées avec 4 tensions de polarisation différentes (-1.0 V, -0.5 V, $+0.5$ V, et $+1.0$ V). Le contraste brillant dans toutes les images STM simulées est attribué aux atomes d'oxygène qui protrudent à la surface. Il implique deux grands types de tuiles : rectangulaire et hexagonale distordue. Le contraste associé à la présence d'indium à la surface est moins visible. Nous espérons que ces résultats pourront servir de feuille de route pour les expérimentateurs travaillant sur ces systèmes.

List of Figures

List of Tables

Glossary

ABINIT ABINIT is a software that allows one to find the total energy, charge density, and electronic structure of systems made of electrons and nuclei within DFT, using pseudopotentials and a plane-wave basis (https://www.abinit.org).

ASE The Atomic Simulation Environment (ASE) is a set of tools and Python modules for setting up, manipulating, running, visualizing and analyzing atomistic simulations (https://wiki.fysik.dtu.dk/ase/).

CEA The CEA (Commissariat à l'Énergie Atomique) is a French public government-funded research organisation in the areas of energy, defense and security, information technologies, and health technologies.

CINES The C.I.N.E.S. (Centre Informatique National de l'Enseignement Supérieur) is a Public Institution of national administrative character (EPA), based in Montpellier, and placed under the supervision of the Ministry of Higher Education, Research and Innovation (MESRI).

HCP High-performance computing (HPC) uses supercomputers and computer clusters to solve advanced computational problems.

LOBSTER The *Local Orbital Basis Suite Toward Electronic-Structure Reconstruction* (LOBSTER) is based on an analytic projection from projector-augmented wave (PAW) density-functional theory (DFT) computations, reconstructing chemical information and opening the output of PAW-based DFT codes to chemical interpretation (http://schmeling.ac.rwth-aachen.de/cohp/index.php?menuID=1).

Pymatgen Pymatgen (Python Materials Genomics) is a robust, open-source Python library for materials analysis (https://pymatgen.org).

TGCC The TGCC (Très Grand Centre de Calcul) is an infrastructure for very high performance scientific computing and Bigdata, capable of hosting petaflop-scale supercomputers.

USPEX USPEX code was developed to solve the problem of crystal structure prediction and allows the determination of crystal structure with arbitrary P, T conditions by knowing only chemical composition of the material (https://uspex-team.org).

VASP The Vienna Ab initio Simulation Package (VASP) is a computer program for atomic scale materials modelling, e.g. electronic structure calculations and quantum-mechanical molecular dynamics, from first principles (https://www.vasp.at).

VESTA VESTA (Visualization for Electronic and STructural Analysis) is a 3D visualization program for structural models, volumetric data such as electron/nuclear densities, and crystal morphologies (https://jp-minerals.org/vesta/en/).

XCrySDen XCrySDen is a crystalline and molecular structure visualisation program aiming at display of isosurfaces and contours, which can be superimposed on crystalline structures and interactively rotated and manipulated (http://www.xcrysden.org).

Acronyms

AIMD *Ab Initio* Molecular Dynamics

BP Black Phosphorus

COF Covalent Organic Framework

COHP Crystal Orbital Hamilton Populations

COOP Crystal Orbital Overlap Populations

CP Car-Parrinello

CSP Crystal Structure Prediction

DFT Density Functional Theory

DOS Density of States

FFT Fast Fourier Transform

FK Frank-Kasper

FT Fourier Transform

GGA Generalized gradient approximation

h-BN Hexagonal Boron Nitride

KS Kohn-Sham

LCAO Linear Combination of Atomic Orbital

LDA Local Density Approximation

LDH Layered Double Hydroxides

LDOS Local Density of States

LEED Low-Energy Electron Diffraction

LIB Lithium-Ion Battery

LRO Long-Range-Ordered

LSDA Local Spin Density Approximation

MC Monte Carlo

MD Molecular Dynamics

MLCC Multilayer Ceramic Capacitors

MOF Metal Organic Framework

NEB Nudge Elastic Band

NGT Niizeki-Gaähler tiling

OQA Oxide Quasicrystal Approximant

PAW Projector-Augmented Wave

PES Potential Energy Surface

PP Pseudo-potentials

PTCR Positive Temperature Coefficient of Resistance

RWGSR Reversed-Water-Gas-Shift Reaction

SHS Single-layer Hexagonal Structured

STM Scanning Tunneling Microscope

STO $SrTiO_3$

SXRD Surface X-Ray Diffraction

TCP Tetrahedral Close Packing

TMD Transition Metal Dichalcogenides

TPF Thick Perovskite Film

UHV Ultra-High Vacuum

UTO Ultra Thin Oxide

XC Exchange and Correlation

XPS X-Ray Photoemission Spectroscopy

ZPE Zero Point Energy

Symbols

E Total energy

E_{xc} Exchange and correlation energy

G Gibbs free energy

T Kinetic energy

Z Partition function

ΔH_{f} Enthalpy of formation

Φ Work function

Ψ Many-body wavefunction

ϵ Permittivity of vacuum

γ Surface free energy

$\hat{\mathbf{p}}$ Quantum mechanical momentum operator

$\hbar$ Reduced Planck constant

μ Chemical potential

∇ Nabla operator

ϕ Single electron wave function

ρ Electronic charge density

$\vec{G}$ Reciprocal space vectors

$\vec{k}$ Bloch wave vector

e Electron charge

k_B	Boltzmann constant
H	Hamiltonian operator
V	Potential energy
ψ	Wave function
m_e	Electron mass

Contents

Chapter I

General introduction

I. Introduction to ultrathin films

Ultrathin two-dimensional (2D) materials have sheet-like structures that are only a few or one atom thick (typically less than 5 nm) [1]. Even though these materials have been studied for a long time, the year 2004 saw a rebirth of ultrathin 2D nanomaterials when Novoselov et al. [28] successfully separated graphene from graphite using Scotch tape, reveling that the 2D characteristics are special and essential for accessing previously unattainable electrical, physical, and chemical properties due to electron confinement in two dimensions. These surprising properties of graphene have motivated many researchers to investigate other ultrathin 2D nanomaterials, including hexagonal boron nitride (h-BN) [29], transition metal dichalcogenides (TMDs; for example, $MoSe_2$, TiS_2, and TaS_2) [30]–[33], perovskites [34], and layered metal oxides [35].

In this introduction, we start by discussing what discern these ultrathin films from its bulk counterparts, correlating also their composition with crystal structure, followed by an analysis of various applications of these materials, and finishing by introducing the 2D ultrathin films that are the subject of this thesis.

I.1. What makes ultrathin films special?

There are mainly three important points that make these 2D ultrathin films different from other classes of materials such as zero-dimensional (0D) nanoparticles, one-dimensional (1D) nanowires, or three-dimensional (3D) networks. First, they present a very high specific surface area due to their wide lateral dimension and extremely thin thickness, which is very advantageous for a variety of surface-active applications, including photocatalysis, electrocatalysis, organic catalysis, and supercapacitors [1]. Second, when compared to con-

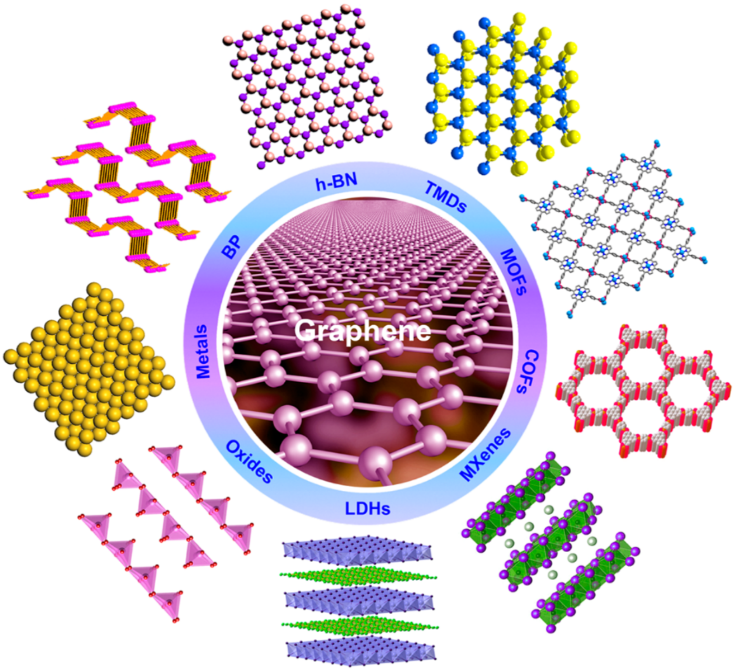

Figure I.1: Schematic illustration of different kinds of typical ultrathin 2D nanomaterials, such as graphene, h-BN, TMDs, Metal Organic Frameworks (MOF's), Covalent Organic Frameworks (COF's), MXenes, Layered double hydroxides (LDH's), oxides, metals, and Black Phosphorus (BP). Image used with permission by the American Chemical Society (ACS) from the work of Zhang [1].

ventional nanomaterials, ultrathin 2D nanomaterials have far more compelling electrical characteristics due to the electron confinement in two dimensions. This makes them desirable candidates for basic condensed matter research and electronic device applications. Finally, they are promising for the manufacture of very flexible and transparent electronic and optoelectronic devices since their atomic thickness affords them a great mechanical flexibility and optical transparency [2].

One other appealing aspect of ultrathin 2D nanomaterials is that they have very sensitive electronic structures to external stimuli, including chemical modification, mechanical deformation, external electric fields, and the adsorption of other molecules or materials [2], which makes it possible to tailor their electronic characteristics in a desirable manner at a highly controlled level.

The most classical example that demonstrate the striking properties of such materials is graphene. This material consists of a monolayer of carbon atoms packed closely together forming a two-dimensional (2D) honeycomb lattice. Graphene serves as the fundamental building block for all other graphitic materials. It can be rolled into 1D nanotubes, stacked into 3D graphite, or wrapped in 0D fullerenes. With ongoing researched for more than sixty years [36], [37], graphene is frequently used to describe the characteristics of many carbon-based materials. It was discovered that graphene also offers a condensed matter analog of (2+1)-dimensional quantum electrodynamics [38], [39], which helped graphene become a booming theoretical toy model.

Ultrathin 2D nanomaterials have extraordinary physical, electrical, chemical, and optical capabilities that result from their distinctive structural features, which opens up a wide range of possible applications. We can choose materials that are unique to the required application thanks to the large number of ultrathin 2D nanomaterials with a pletora of features. These materials have been used mainly in areas like catalysis, electronics, optoelectronics, sensors, energy storage and conversion. We outline some of the most promissing uses for ultrathin 2D nanomaterials in this section.

Ultrathin 2D films have demonstrated outstanding performance in catalysis due to their extremely large specific surface area. In general, attaining outstanding activities in catalytic processes depends on electrical conductivity and effective active sites. One of the most efficient approaches to increase the number of active sites and, hence, achieve better catalytic performance is by engineering strains, defects, and crystal boundaries in ultrathin 2D nanomaterials, as well as by doping with heteroatoms. As an example, bulk indium oxide (In_2O_3, with thickness of ≈ 18 Å) specially when supported by Pd or PdIn substrate, have recently been shown to be a powerful catalyst with high activity and selectivity for the conversion of CO_2 to methanol, and it is widely acknowledged that the oxygen vacancies on the surface of In_2O_3 are a key factor in defining its activity toward CH_3OH [40]. This process has been shown to be even more efficient by enhancing the conductivity of ultrathin In_2O_3 films when supported on a Pd or PdIn substrate [21].

Another example is that adding N, S, P, and/or B atoms to graphene greatly enhances its ability to operate as an electrocatalyst for the oxygen reduction process [41]. The heteroatom-doped graphene demonstrates high activity toward the electrocatalytic oxygen evolution process, despite the fact that graphene itself is almost inert for electrocatalysis.

II. Ultrathin 2D oxides on metallic materials

As described above, there is a vast class of ultrathin materials with a plethora of different applications. Now, we focus on a specific group of these materials: ultrathion oxides (UTOx) supported on metals.

Even though oxides are frequently insulators or semi-conductors, when they become ultrathin, charging effects are prevented, allowing charge transfer with the underlying metal [3]. Although UTOx systems display structural and electrical phenomena that are similar to bulk oxides, they are manifested in distinct ways as a result of the 2D confinement and the interaction between UTOx and the support, leading to unexpected emerging phenomena. As an example, such phenomena were verified by the analysis of the electronic density of states (DOS) on silica supported on a Mo(112) substrate, where the peak structure of the DOS differs significantly for ultrathin films [42].

UTOx systems offer advantages and disadvantages in terms of cutting-edge scientific and technological applications. When simple charge transfer is required, the existence of a metal substrate that can serve as an electron reservoir is advantageous. On the other hand, the ultrathin oxide coating has the disadvantage that its close interaction with the substrate muffles its unique properties. For instance, electrostatic interactions are decreased through the metallization of the oxide due to screening caused by the metal [43].

II.1. Structural motifs

The definition and clarification of structural motifs of 2D ultrathin materials are extremely helpful in categorizing a system and enabling one to characterize a specific UTOx structure and catalog it in a database. Turning these data into a structure prediction tool (and possibly correlate directly to its properties) is a more ambitious aim of such a categorization. This type of catagorization have been done, for instance, in the TiO_x/Pt(111) system, where the same principles and tendencies found for this system were successfully applied to many other (111)/(111) epitaxial systems and to oxide systems with radical different natures [44]. In Figure I.2 we can see the tiling configurations determined for this TiO_x/Pt(111) system, where the ultrathin film can be categorized in terms of three distinct building blocks, i.e., a triangle, rectangle, and square with compositions MO_3, MO_4, and MO_3, respectively, that are replicated to fill the 2D plane. It is possible to organize structural motifs into a generic database or catalogue, which can then be verified against 2D materials databases to ensure that the method is comprehensive.

The knowledge of such structural motives can be used in structure prediction. Structure databases can be used as an initial source of structures in a global optimization procedure, and can consequently be used in a genetic algorithm. The fundamental step is to divide a system into a collection of well-known recognizable components or structural motifs, each of which is then extended and translated to fill the plane [3]. The global energy of the system may then be used to predict the structures of novel UTOx phases, the optimal dimension of the metal/oxide unit cell, and the shape and stoichiometry of the oxide layer under certain

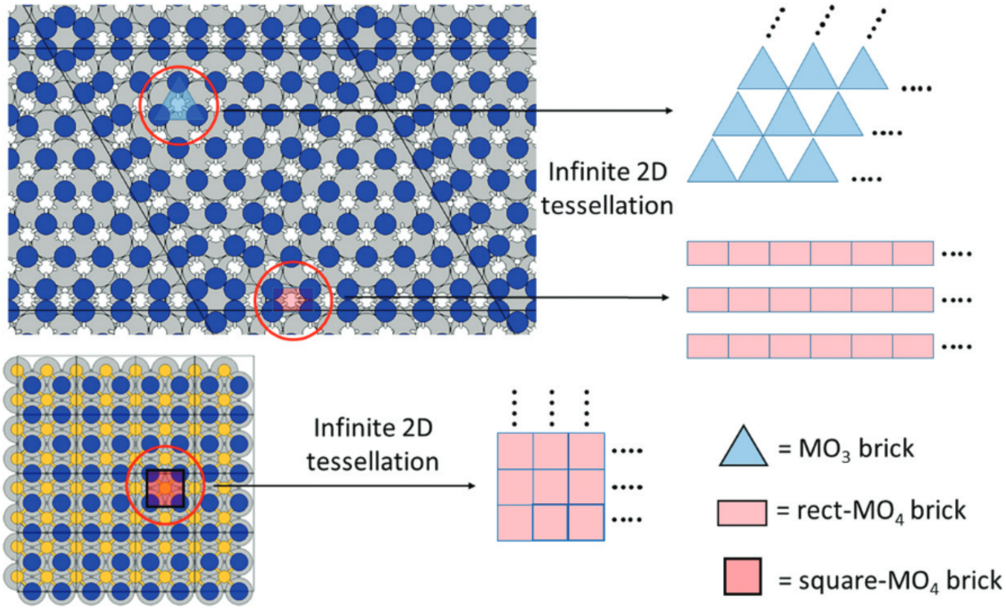

Figure I.2: Two infinite-plane tessellations with MO$_4$ and MO$_3$ compositions. Reproduced from [3] with permission from the PCCP Owner Societies.

conditions.

In the next section, we devote our attention to a specific class of materials of 2D ultrathin oxides supported on metals. In particular, we describe a system where the first 2D oxide quasicrystal was found, BaTiO$_3$/Pt(111), initially discovered by the Förster et al. [9]. The description that follows consists of three parts: (1) the initial surface studies on epitaxialy grown ultrathin oxide films (BaTiO$_3$) on a Pt(111) substrate, (2) the discovery and definition of quasicrystalline phases, and (3) the oxide quasicrystal phases discovered in these systems as well as their approximant structures.

III. The BaTiO$_3$/Pt(111) system

The BaTiO$_3$ is one of the most important and widely used materials in electro-ceramics such as positive temperature coefficient of resistance (PTCR) thermistors [45], electro-optic devices [46], and multilayer ceramic capacitors (MLCC) [47]. The phase diagram of the BaO–TiO$_2$ system, presented in Figure I.3, shows that there are many possible polimorphs for the BaTiO$_3$ structure, which include, but not shown, a cubic to tetragonal phase transition around the Curie point at 130 °C. This tetragonal phase is the thermodynamically stable phase at room temperature and is one of the most interesting due to the presence of ferroelectricity [48].

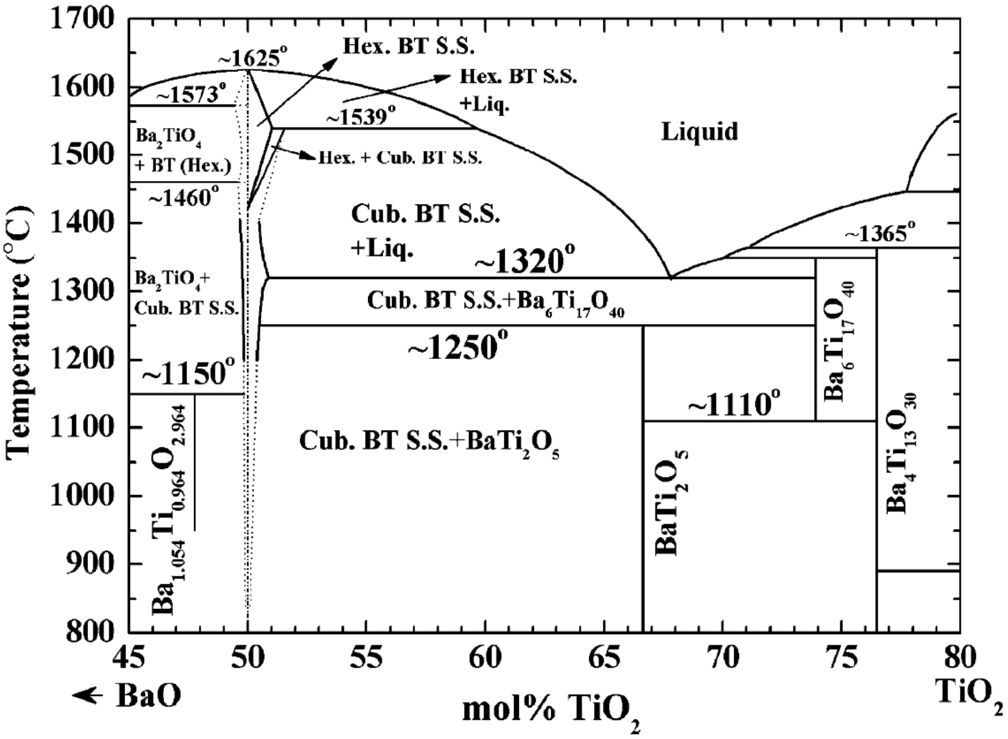

Figure I.3: Pseudo-binary phase diagram of the BaO–TiO$_2$ system. Reproduced from [49] with permission from Elsevier.

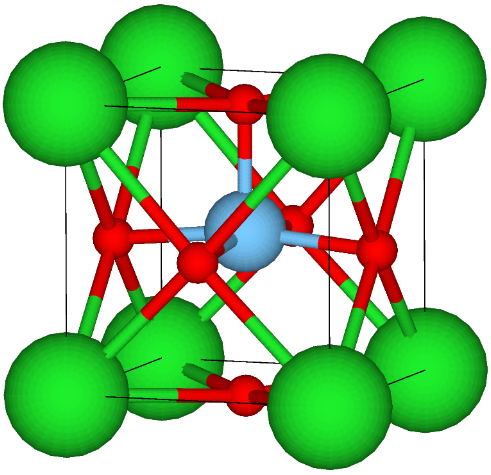

Space group:	$P4mm$ (#99)
Pearson's symbol:	$tP5$
Prototype:	BaTiO$_3$
Lattice parameters:	$a = b = 4.00$ Å; $c = 4.20$ Å

	Site	Wyckoff	x	y	z
🟢	Ba	1b	0.50	0.50	0.00
🔵	Ti	1a	0.00	0.00	0.52
🔴	O1	1a	0.00	0.00	0.96
🔴	O2	2c	0.00	0.50	0.48

Figure I.4: Schematic representation and crystalographic data of the BaTiO$_3$ $P4mm$ structure [50].

In bulk BaTiO$_3$ (space group $P4mm$) with a tetragonal symmetry, the Ba and Ti sublattices are slightly displaced in relation to the negatively charged O ions, and result in a persistent electrical polarization. Its structure is shown in Figure I.4. In its bulk form, numerous computational and experimental studies have demonstrated the persistence of ferroelectricity at nanoscales, where $BaTiO_3$ down to only 3 unit-cell layers as a component of the oxide superlattices were discovered to preserve its ferroelectricity [51], [52]. As it was pointed out in the work by Cohen [53], the ferroelectricity in these perovksite phases arise from a very delicate balance between short-range repulsion and long-range Coulomb forces, which favors the nonpolar cubic structure and the ferroelectric state, respectively, and the hybridization between Ti 3*d* and oxygen 2*p* states seems to be essential for its appearance.

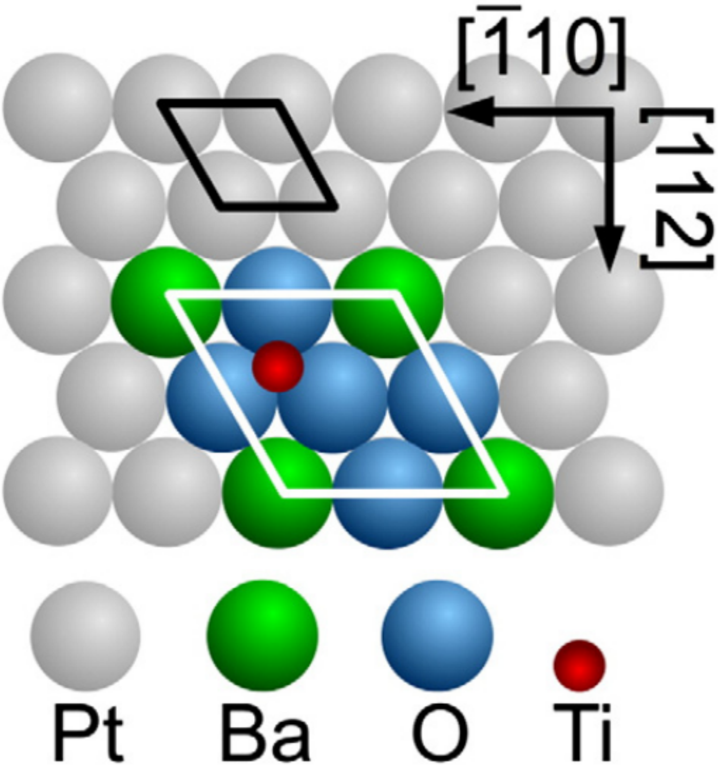

Figure I.5: The $BaTiO_3$(111) structure superposed with Pt(111). The black and white lines indicate the unit cells of Pt(111) and $BaTiO_3$(111), respectively. Reproduced from [54] with permission from Elsevier.

When we approach an ultrathin limit in these perovskite films, extensive structural and electronic variability opens up that is linked to a vast number of conceivable unique chemical compositions — more than $\simeq 10^7$, according to Li *et al.* [55]. The combination of the low dimension with the structural flexibility of this class of crystals opened the door to a rich spectrum of applications in many fields, such as energy transition and catalysis [56], correlated materials [57], and electronic devices [58], [59].

By depositing an ultrathin $BaTiO_3$ film on a Pt(111), with a 2×2 unit cell, one can anticipate an epitaxial growth due to the small lattice mismatch of only 2%. This system is shown in Figure I.5

Decreasing the thickness of two-dimensional (2D) perovskites down to the monolayer limit when deposited over metalic substrates is expected to deeply alter their structures and modify the physical and chemical properties, as already demonstrated in the case of other types of ultra-thin 2D oxides films [3], [4] — TiO_x/Pt(111) [5], MnO_x/Pd(100) [6] and VO_x/Pd(111) [7], [8], to name a few. This has recently led to the emergence of novel structures with aperiodic ordering, i.e., dodecagonal oxide quasicrystal interfaces in the $BaTiO_3$/Pt(111) and $SrTiO_3$/Pt(111) systems [9]–[12]. The driving force for these unique structural modifications, resulting from thickness reduction, are far from being fully unveiled. Reduced bonding coordinations, possible strong surface polarizations, support effects and experimental conditions are supposed to play a role, but no clear picture has yet been drawn [3], [4].

III.1. Quasicrystals (QC)

The discovery of quasicrystals on these ultrathin oxide films is another huge step forward on the history of quasiperiodicity in materials, with its origins in 1984 with the first observed quasicrystal by Dr. Dan Shechtman in an intermetallic Al-Mn phase [60] (Electron diffraction pattern of this phase is shown in Figure I.6). This type of structure is very paradoxical: on the one hand, it displays a long-range order similar to that found in crystals due to the sharpness of the diffraction spots, but on the other hand, it could not be crystalline due to its general pentagonal symmetry [61].

Surprisingly, quasicrystals were accidentally created even before Shechtman's discovery during studies of intermetallic phase diagrams. The fivefold diffraction symmetry typical of icosahedral QC's did not immediately grab the eye, in contrast to Shechtman's electron diffraction patterns, because at that time only X-ray powder diffraction techniques were often utilized for sample evaluation. Interestingly, it appears that QC's were generated by nature far earlier, where findings in meteorites suggest that QC's may have developed billions of years ago [62]. Additionally, quasicrystalline materials have been found in the aftermath of the Trinity atomic bomb test of 1945 [63].

Intermetallic binary or ternary compounds of QC's are frequently accompanied by low-order approximant phases (which are periodic) that have slightly shifted chemical composition. These approximant structures that are made from the same constituents as the related quasicrystals are found existing alongside the QC, and frequently have unit cells with smaller or bigger portions of the parent aperiodic pattern [64]. Figure I.7 shows an example of an approximant of an icosahedral quasicrystal phase in the Al-Mn system.

Even if the main goal is to study the structure and properties of QC's, from a practical

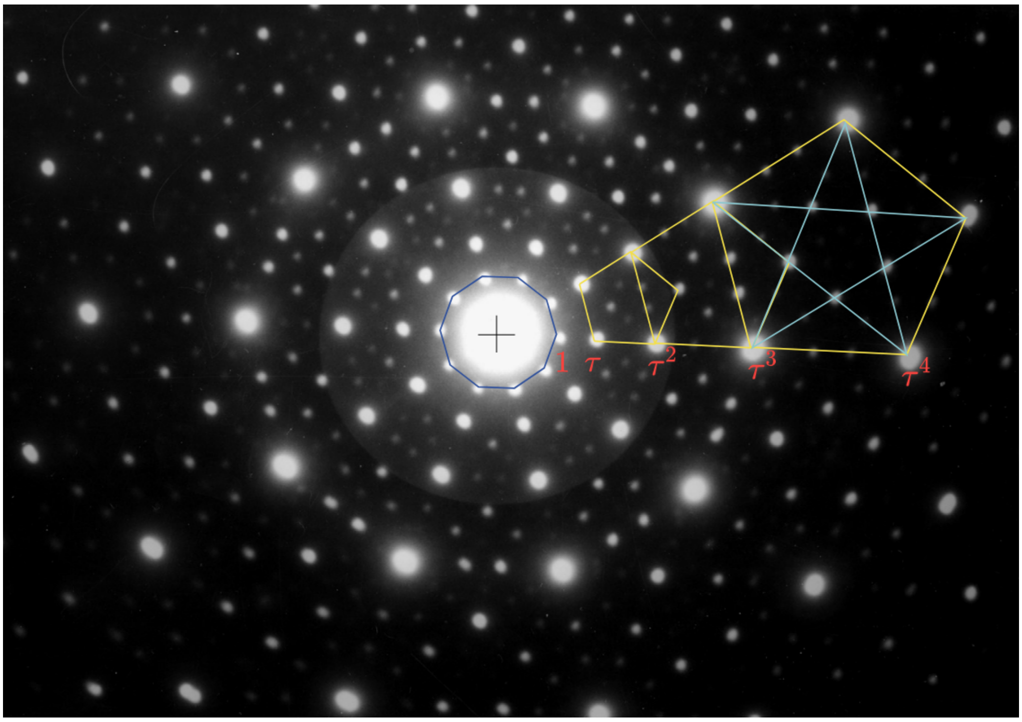

Figure I.6: Dan Shechtman's renowned electron diffraction pattern of the icosahedral phase of the Al_6Mn intermetallic, where the bright diffraction spots are comparable to those in high-quality crystals but are dispersed along a pentagonal symmetry, which prevents this material from having a periodic distribution of atoms. Figure taken from the open-access article by Gratias and Quiquandon [61].

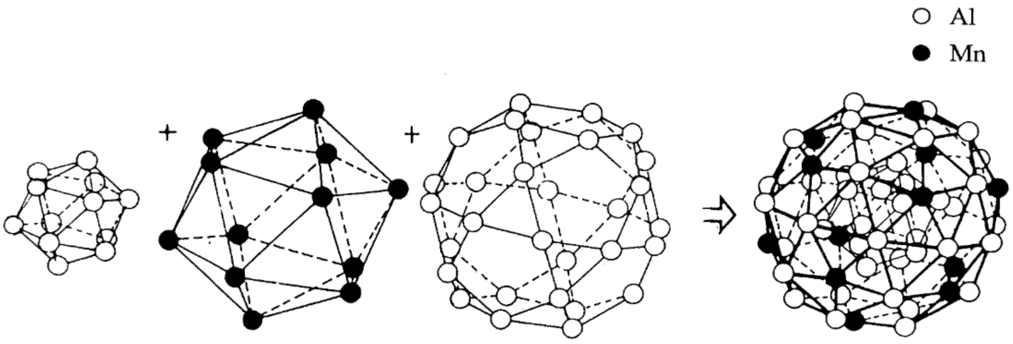

Figure I.7: Approximant crystalline structure of an Al-Mn icosahedral alloy constituing of three atomic shells, also known as the "Mackey" icosahedron [65]. Reproduced from [66] with permission from the American Physical Society.

point of view, there are many reasons to study its approximant phases first. (1) The approximant phase posses a well-defined starting point for modeling local atomic structure of quasicrystals. Namely, approximants can be modeled with modern quantum mechanical theories such as Density Functional Theory (that rely on periodic boundary conditions), to study its properties. (2) The composition of a QC is usually really close to that of its approximants. (3) Both phases present similar physical properties.

III.2. Oxide quasicrystal approximants (OQA)

An extremely interesting class of materials was discovered by the group of Prof. Dr. Widdra [9], where they have reported the formation of a 2D oxide quasicrystal phase grown on a metallic substrate with 3-fold symmetry. The system used in this first discovery was a perovskite $BaTiO_3$ grown on Pt(111) single-crystal. A high resolution STM image of this dodecagonal OQC phase is shown in Figure I.8.

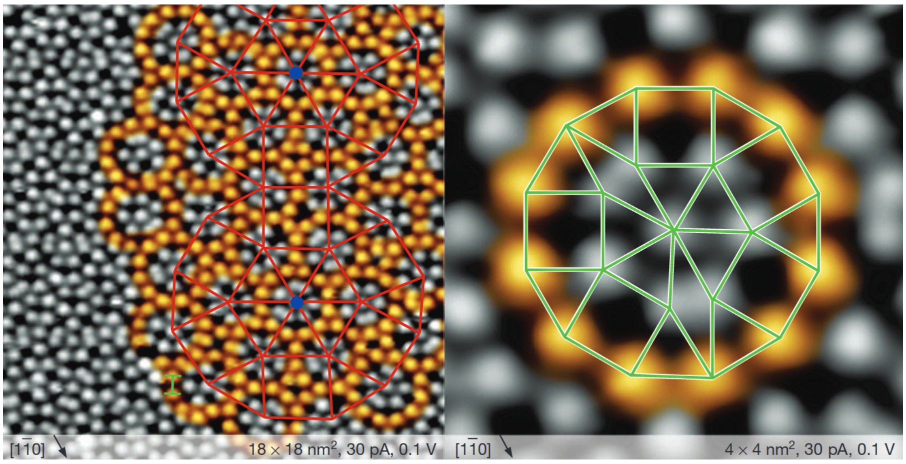

Figure I.8: STM images of the first reported dodecagonal OQC phase on the Ba–Ti–O system. Reproduced from [9] with permission from the Springer Nature.

The modeling of such aperiodic systems had great advances with the work by Penrose, who discovered that one could combine only two types of tilings (called "kites" and "darts" [67]) to fill a plane non-periodically, in this case in a five-fold symmetry [68]. This type of lattice was later observed in the STM images of Al–Mn alloy with three-dimentional icosahedral symmetry [69]. For the case of a dodecagonal system, the tiling consists of a combination of three elements: squares, equilateral triangles, and 30°-rhombuses. This type of lattice is called Niizeki-Gähler tiling (NGT), and were described mathematically by Gähler [70] and Niizeki et al. [71]. One type of NGT tiling (C_a) is shown in Figure I.9.

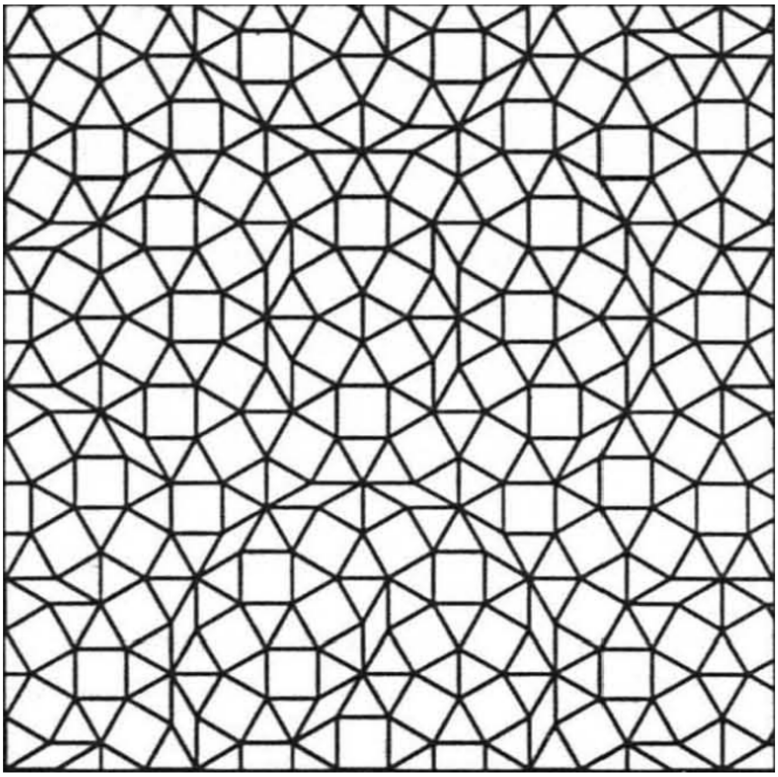

Figure I.9: NGT tiling "C_a". Reproduced from [70] with permission from Springer Nature.

Despite this outstanding discovery of the first OQC, the actual atomic structure was unknown, leading to several attempts to model these new class of structures. Earlier attempts to model the OQA came from the work by Cockayne et al. [23] following initial decoration models given by Gähler [70] on a dodecagonal tiling, with the three tiling configurations represented in Figure I.10. In this model, the Ba atoms occupy the vertices of the tiles, while the Ti atoms are coordinated by three oxygen atoms (except from those inside the 30° rhombs). By combining these three tilings, one can construct and model the OQC by connecting the bright spots in the experimental STM images [9], which present the patterns of the "C_a" tiling pattern found by Gähler [70].

By using DFT to model some OQA phases built from the tilings proposed by Gähler, who found a remarkable resemblence between the simulated and experimental STM images and initally propose various approximant phases that might form based on these three tilings.

The second attempt to model these OQA phases was made by the same group that discovered OQ a few years before [10], alongside with the analysis of the first reported approximant phase on the $BaTiO_3/Pt(111)$ system, the σ-phase. This approximant phase follows a $3^2.4.3.4$ Archimedean tiling [72], [73], and SXRD experiments, supported by DFT, have been used to propose its structure. By combining STM, LEED, SXRD, and DFT, they have suggested that the Ti atoms are forming the snub-square tiling, and the OQA is built based on TiO_3 units with two different oxygen species, one bound uniquely with the substrate and another connecting the TiO_3 with a Ba atom. A countour plot showing atomic positions within the unit cell is shown in Figure I.11.

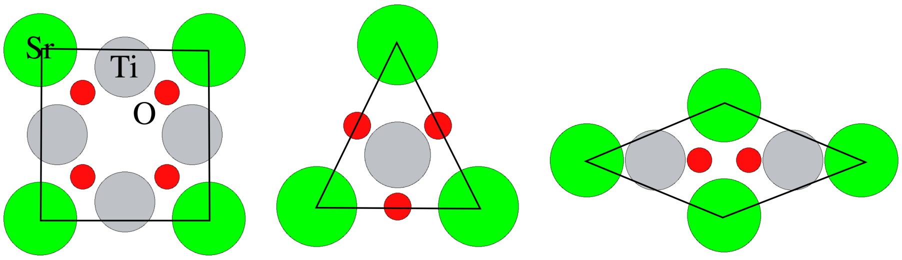

Figure I.10: (a) Square, (b) triangle and (c) rombus tilling configurations proposed by [23].

In addition to the models discussed so far, the work by Marques et al. [74] attempted to make a high-throughput search in the configurational space of binary Ba–O and Ti–O unsupported ultrathin films by using a combination of Density-Functional Tight-Bindind (DFTB) calculations and standard DFT. Their aim was to shed a light with respect to the controvertial atomic structure of these OQs and even propose new tiling configurations that may appear in real phases. They argue that the main reason why these square-triangle tilings occurs has to do with the competition between the square and hexagonal phases in the modified phase diagram. Given that edge sharing between squares and triangles does not cause instabilities, there is a strong possibility that stable square-triangle-based constructions are likewise low-energy being either near or on the convex hull of thermodynamical stability.

The competition between OQC and OQA at high temperatures and UVH seems not to be the only happening. If one allows a shift in composition with a lower content of Ba/Sr, a periodic honeycomb-like structure may form when supported on a metallic substrate. In fact, there are several studies demonstrating the stability of such honeycomb structure in a variety of oxide and substrate's compositions [27], [75]–[77]. The Ba/Sr atoms fill the hollow sites in the middle of the Ti_2O_3 honeycomb with several different compositions. The work by Noguera et al. [77] clearly shows in the STM images a hexagonal configuration of Ba atoms in the hollow sites, leading up, at higher Ba contents, to a disordered labyrinth phase, as can be seen in Figure I.12.

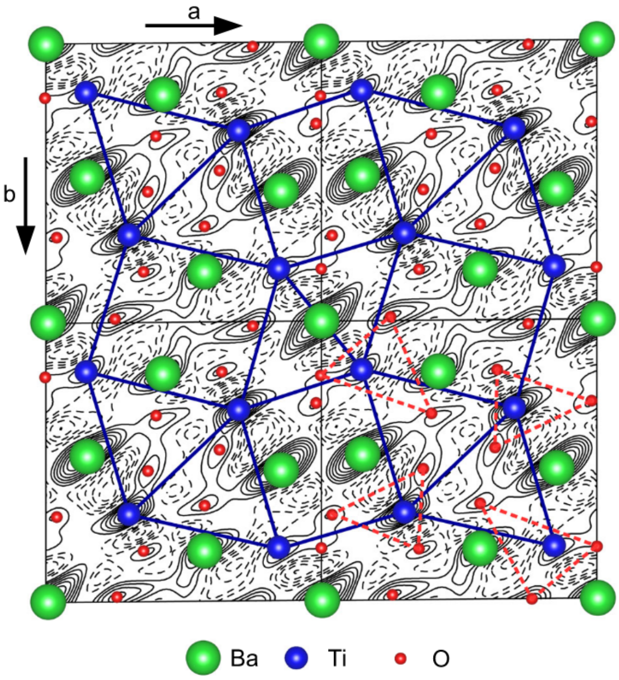

Figure I.11: Contour plot of four 2D unit cells of the σ-approximant phase with SRXD-derived charge density $\rho(x, y)$. Reproduced from [10] with permission from the American Physical Society.

It is no mystery that the composition play an extremely important role to the formation of all phases presented so far. And, in the same line, the work by Li et al. [78] presents an interesting alternative route to obtain the OQC or OQA. By a initial deposition and growth of an ultrathin Ba-O film on Pt(111) and followed by Ti incorporation, they've also found the OQC and the OQA at a similar temperature and pressure range.

We can find a plethora of new approximant phases discovered on systems with different compositions, including Sr–Ti–O/Pt(111), Sr–Ti–O/Pd(111), and Ba–Ti–O/Ru(0001). These new phases include, for instance, a giant and hexagonal approximants [79]–[83], and monoclinic one [12], giving rise to a rich and exciting field to explore and understand such phases.

As a conclusion, these periodic approximant structures to quasicrystals represent a very useful class of materials to deepen our understanding of quasicrystalline phases. When modelled with large crystal supercells, approximants exhibit atomic arrangements similar to those encountered in quasicrystals, hence they bridge the gap between periodic and aperiodic positional order, and can be studied by methods based on density functional theory (DFT). The main objective of this work is to shed a light on the overall relashionship between structure and properties for several compositions and tiling models, as well as compare these models with recent experimental evidence on new approximant phases, so that, in the end, we could have a better understanding of this rich new field that recently emerged.

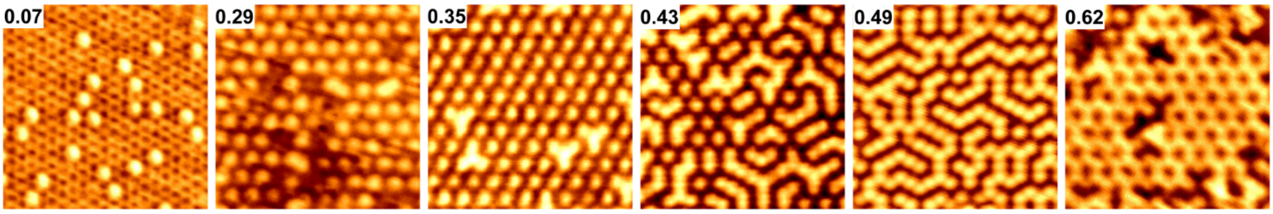

Figure I.12: STM images for different Ba coverages in the $Ba_xTi_2O_3/Au(111)$ system. Reproduced from [77] with permission from the American Physical Society.

IV. Ultrathin films on the In_xO_y/PdIn system

As discussed above, nanoscale materials often manifest new interesting and unexpected properties when compared to the bulk counterpart, and more specifically ultrathin oxide films are of particular technological interest, since they can be used in applications such as fuel cells, corrosion and abrasive protection, heterogeneous catalyst, to name a few [42].

Within these applications, a very active field of research is the study of catalysts and reactions for methanol formation, which is an extremely important molecule for the future of energy, serving as a carbon source for the chemical industry and as a hydrogen carrier [13], [14]. Nowadays, methanol is mainly produced by the conversion of syngas, a gas mixture of CO, CO_2 and H_2 obtained from coal or natural gas, using a Cu-based alloy ($Cu/ZnO/Al_2O_3$) as the main catalyst under elevated temperatures and pressures [15]. However, this conversion still faces many problems in its CO_2 selectivity since it is also active for the reverse-water-gas-shift reaction (RWGSR), producing CO as a byproduct. Consequently, a vast amount of research is now being dedicated to find a catalyst with better properties than those of the Cu-based alloy, and promising candidate systems are Pd-based alloys and some ultrathin oxide films such as the In_2O_3.

The principles governing the good catalytic properties of Pd-based alloys is beginning to be unraveled, but still a lot of research is needed. The Pd-based intermetallics may present great catalytic properties following the site-isolation concept, [16], [17] specially when the Pd atoms are surrounded by elements such as In, Zn, or Ga. The idea is that when we have an alloy whose crystal structure possesses neighboring Pd sites, the formation of multisite complex molecules could be favored over linear molecules, decreasing the reaction's selectivity. In addition, Kovnir et al. [16] suggests that the absence of neighboring Pd sites can also increase the catalyst's stability due to the suppression of carbon deposition.

Following this idea, an interesting system to study is based on Pd-In intermetallics. The catalytic properties of such materials have been studied for CO_2 hydrogenation to methanol using DFT and a microkinetic method [84]. This study suggested that the PdIn intermetallic nanoparticles showed an improvement of 70% in activity over the conventional Cu/ZnO/Al_2O_3 catalyst and a over 90% of methanol selectivity. Even with the excellent performance of the PdIn intermetallic, this study also argues that the formation of oxides over Pd-based alloys, such as Pd/Ga_2O_3, Pd/ZnO, and Pd/In_2O_3, could improve its catalytic properties [21], [85], [86]. In addition, in a more realistic approach, the "perfect" PdIn surface would only be stable at very specific conditions (e.g., UHV), while the formation of an oxide film is expected under ambient conditions. Thus, it could be more interesting, computationally and experimentally, to study the properties of these intermetallics with a supported oxide film.

As recent studies suggest, the interplay between intermetallic PdIn compounds and the oxide support material is thought to be the source of the system's great versatility and properties, albeit the exact mechanism has not yet been fully elucidated [13]. They also claim that the aforementioned paradigm would be demonstrated by the potential incorporation of chemically bound oxygen at the interface region of InPd, which would show that the interface region and not the sole intermetallic is responsible for a high CO_2 selectivity. A schematic representation of these systems with respect to the activity and selectivity of CO_2 for methanol formation is shown in Figure I.13.

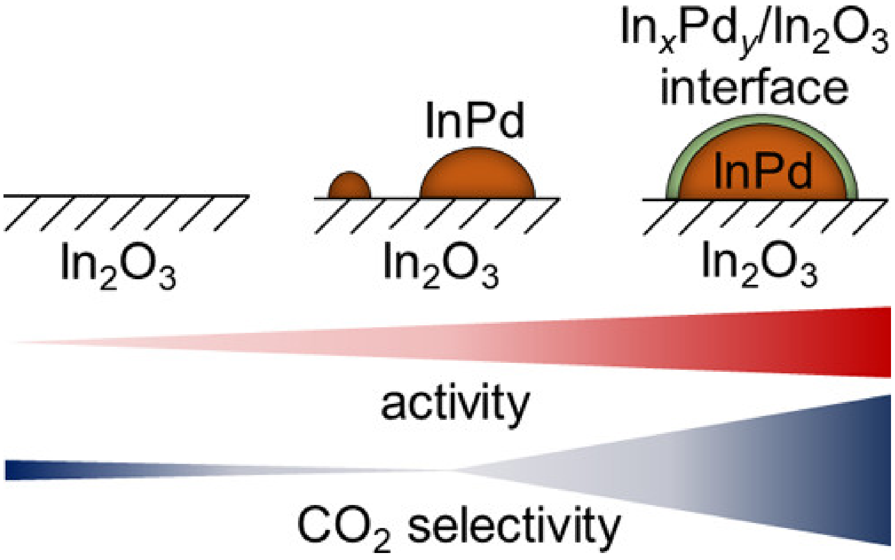

Figure I.13: Schematic representation of activity and CO_2 selectivity for methanol formation in different systems. Reprinted (adapted) with permission from [13] Copyright 2020 American Chemical Society.

These findings imply that the intermetallic compound is not the active site, but rather that the remarkable CO_2 selectivity of these catalytic materials is due to active redox chemistry at the phase border between oxide and intermetallic compound. The authors also observed a partially crystalline shell formed due to the rapidly adapting the size and composition of the PdIn intermetallic to the reaction conditions at the particle surface. The partially crystalline oxidic shell, which causes deactivation at lower temperatures, appears to be the main factor for the unprecedented high CO_2 selectivity. The temperature for the formation of this shell under reaction conditions may account for the better selectivity in comparison to other investigations on PdIn materials [13].

Interestingly, there are also studies reporting the superior individual catalytic properties of indium oxide films (specially In_2O_3) without the substrate. On such systems, methanol seems to be the most favored product of CO_2 hydrogenation over non-defective and defective In_2O_3(110) surfaces, and the reaction appears to follow a mechanism involving the cyclic formation and annihilation of oxygen vacancies [18]. Boost of the catalytic activity of such oxide phases can be achieved by metal promotion with Pd [19], which reduces the reverse water-gas shift reaction. These studies demonstrate that a system composed of both components, i.e., a PdIn substrate (Pd terminated) supporting an indium oxide, seems to be a promising system to be studied. A schematic representation of this PdIn/In_xO_y system, compared to the conventional Cu/ZnO/Al_2O_3 system, forming methanol as a product, is shown in Figure I.14.

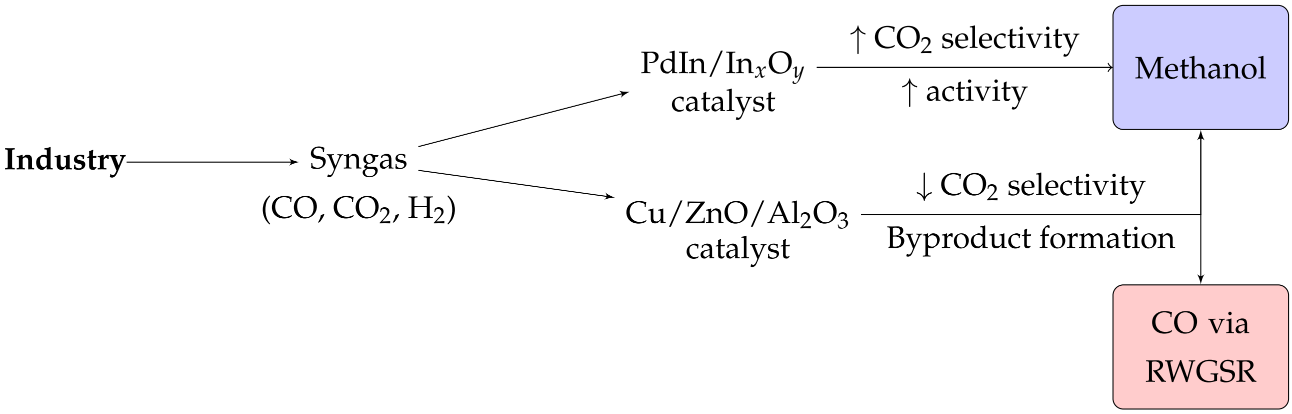

Figure I.14: Schematic representation of two possible ways to convert syngas to methanol, either through the conventional Cu/ZnO/Al_2O_3 catalyst, or a more active and selective PdIn/In_xO_y catalyst.

From the experimental point of view, it is also advantageous to investigate an ultrathin oxide supported on a metallic substrate, rather than the isolated bulk oxide, because there is a coupling of the film to the metal's Fermi level and possibly a charge transfer at the interface, allowing modern surface techniques such as scanning tunneling microscopy (STM) or low-energy electron diffraction (LEED), which cannot be applied to semiconductors and insulators, to be used.

Up to this point, there are many studies that show the existence of such ultrathin indium oxide supported on either a Pd or PdIn substrate [20]–[22], but these studies are based on the bulk In_2O_3 structures and not on the characteristics of an ultrathin film, which we have seen can vary considerably in structure, composition, and properties. Moreover, we are committed in the present work to study systematically the structures of ultrathin indium oxide films with different compositions supported on the intermetallic PdIn(001), determining their stabilities, electronic properties, and creating a database of simulated STM images that will serve as a basis for future experimental and computational work.

V. Thesis architecture and objectives

Following the introduction of the present thesis, we continue in Chapter II with the description of all methods applied in this work. The chapter begins with a detailed description of the principles of Density Functional Theory followed by the main techniques used (all based on DFT) to determine and analyze useful quantities in ultra-thin films. In addition, we also describe other methods for structure investigation, such as *ab initio* molecular dynamics and genetic algorithms adopted to crystal structure prediction. We also present a code developed by the author (Vulcan) to automate electronic structure calculations and post-processing of the In_xO_y/PdIn(001) systems (Chapter V).

In Chapter III and Chapter IV, we present our results regarding the approximant phases, specially in the (Ba/Sr)–Ti–O/Pt(111) system and extending to some other compositions for comparing properties, such as adhesion energies, enthalpies of formation, charge distribution, etc. The chapter begins with the determination of general properties and the stability of the approximant phase suggested by Förster's et al. [10] with the Ti atoms at the protrusions of the STM images, identifying also at what experimental conditions this type of approximant could form when compared to the perovskite structure. This analysis will be supported by using thermodynamic models to study the stability of supported oxides while changing the composition considering other transition metals (Ti, V, Cr, Mn, Fe, Co, Ni) and alkaline-earth elements (Ba, Sr, Ca).

We follow with the study of the σ-phase using the Cockayne's tiling configuration [23] with the Ba/Sr atoms at the protrusions in the STM images. The interface between oxide and substrate using this model will be analyzed in depth by means of Crystal Orbital Hamilton Population (COHP) calculations and charge distribution analysis. The results using both structures will allow us to select the best model to represent the structure of the approximant phases, concluding if the visible bright protrusion on the experimental STM images comes from the Ti or the Sr/Ba atoms.

Based on the best model selected, we will calculate the electronic structure of many experimentally found approximant phases in the literature and study the bonding characteristics at the interface between the approximant phase and the substrate. These calculations include phases that were found by different research groups, such as a giant [79] and a monoclinic [12] approximant, as well as fictitious approximants (or at least that have not yet been discovered experimentally) created manually from an ideal NGT tiling configuration, in the Sr–Ti–O/Pt(111) system. We begin by describing how to model these structures on a Pt(111) substrate, following by a discussion on the interaction between the oxide and substrate to justify the models created, finishing with a discussion of the general properties (enthalpies of formation, charge distribution, adhesion energies, etc.) of these approximant phases.

In Chapter V we focus on the structure determination of ultra-thin indium oxide films formed when supported on a PdIn(001) substrate. For this matter, we will use the USPEX code to search for films in several compositions and sizes. After the selection of the most promising structures, we calculated, using a high-throughput code developed by the author (Vulcan), several electronic properties, such as the total energy, DOS, STM, adhesion energy, COHP, etc., so that we could identify the main intrinsic aspects of such ultrathin films. In addition, we use thermodynamic models, based on the *ab initio* atomistic thermodynamics framework, to interpret and suggest what are the most stable surface structures. In the end, we have a complete view at the atomic scale of these ultrathin oxide In_xO_y films, where we could identify the most probable surface phases to form and generate a database with all STM images so that future experiments could compare with our results.

Chapter II

Methodology

This chapter is intended to discuss and explain the core concepts of DFT, as well as some of its limitations and approximations. This methodology have been implemented in many different codes, such as Quantum ESPRESSO [87], Abinit [88], Vienna Ab initio Simulation Package (VASP) code [89]–[91], and many others. For the present work, we have used the last code. This chapter was largely inspired from [92], [93], focusing specially on topics used for this work.

I. Principles of Density Functional Theory (DFT)

I.1. Schrödinger equation

There are many theories and approaches regarding material's modeling nowadays, but the one that is the most widely used is Density Functional Theory. But before explaining what DFT is about, we need to consider the Schrödinger equation. Since we are mostly interested in stationary states in the present work, we can consider the *time independent* Schrödinger equation with the form:

$$H\psi = E\psi \tag{II.1}$$

This is a classical linear algebra problem, in which we need to obtain the eigenvalue (E) and eigenvectors ψ for a specific Hamiltonian operator (H). As an example, for the case of one electron under the potential energy $V(\mathbf{r})$, eq. II.1 can be written as:

$$\left[\overbrace{\frac{\hat{\mathbf{p}}^2}{2m_\mathrm{e}}}^{T}+\overbrace{V\left(\mathbf{r}\right)}^{V}\right]\psi\left(\mathbf{r}\right)=E\psi\left(\mathbf{r}\right) \tag{II.2}$$

where m_e is the electron mass, and the quantum mechanical momentum operator is:

$$\hat{\mathbf{p}}=-i\hbar\nabla \tag{II.3}$$

with $\hbar$ the reduced Planck constant. The first two terms T and V of the Hamiltonian H in Equation (II.2) represent the kinetic and potential energy of the electron, respectively.

Instead of focusing on one electron, we are interested in systems that are made of many electrons and many nuclei, so the eigenvector of interest is called the *many-body* wavefunction Ψ, which is a function of the position and spin (but for simplicity, we neglect spin) of all electrons (N) and nucleus (M) in the system:

$$\Psi=\Psi\left(\mathbf{r}_1,\mathbf{r}_2,\cdots,\mathbf{r}_\mathrm{N};\mathbf{R}_1,\mathbf{R}_2,\cdots,\mathbf{R}_\mathrm{M}\right) \tag{II.4}$$

The eigenvalue for such *many-body* wavefunction now is represented as the *total energy* of the system (E_tot). From Born's statistical interpretation of the wave function, in the same way that $|\psi(\mathbf{r})|^2$ is the probability of finding an electron at $\boldsymbol{r}$, $|\Psi(\mathbf{r}_1,\cdots,\mathbf{r}_\mathrm{N};\mathbf{R}_1,\ldots,\mathbf{R}_\mathrm{M})|^2$ is the probability of finding concurrently electron 1 at $\mathbf{r}_1$, electron 2 at $\mathbf{r}_2$, etc.

Considering that electrons are *indistinguishable* particles[1] and that the electron density is the sum of probabilities of finding each electron at the position $\mathbf{r}$, the electronic charge density (ρ) of a many-body system is given by:

$$\rho\left(\mathbf{r}\right)=N\int|\Psi\left(\mathbf{r},\mathbf{r}_2,\cdots,\mathbf{r}_\mathrm{N};\mathbf{R}_1,\mathbf{R}_2,\cdots,\mathbf{R}_\mathrm{M}\right)|^2 d\mathbf{r}_2\cdots d\mathbf{r}_N d\mathbf{R}_1\cdots d\mathbf{r}_M \tag{II.5}$$

Going back to the Hamiltonian operator of Equation (II.1), like in classical mechanics, the Hamiltonian of the many-body system is the sum of the kinetic and potential energy (T and V, respectively) for each electron and nuclei involved. To understand how to construct the Hamiltonian, it is important to understand that a material is stable due to a fine balance between repulsive and attractive Coulomb interactions of the electrons and nuclei involved. The kinetic contribution (T) in such systems is described as an expansion of the first term of Equation (II.2) for N electrons and M nuclei:

---

[1] ψ must be anti-symmetric.

$$T = -\sum_{i=1}^{N} \frac{\hbar^2}{2m_{\mathrm{e}}} \nabla_i^2 - \sum_{I=1}^{M} \frac{\hbar^2}{2M_I} \nabla_I^2 \tag{II.6}$$

where $M_1, M_2, \ldots$ are the masses of the nuclei and ∇^2 is the Laplacian operator.

For the potential energy (V), we must consider three types of Coulomb interactions: repulsion between electrons, repulsion between nuclei, and attraction between electrons and nuclei, all of which can be written, respectively, as:

$$V_{\mathrm{ee}} = \frac{1}{2} \sum_{i \neq j} \frac{e^2}{4\pi\epsilon_0} \frac{1}{|\mathbf{r}_i - \mathbf{r}_j|} \tag{II.7}$$

$$V_{\mathrm{nn}} = \frac{1}{2} \sum_{I \neq J} \frac{e^2}{4\pi\epsilon_0} \frac{Z_I Z_J}{|\mathbf{R}_I - \mathbf{R}_J|} \tag{II.8}$$

$$V_{\mathrm{en}} = -\sum_{i,I} \frac{e^2}{4\pi\epsilon_0} \frac{Z_I}{|\mathbf{r}_i - \mathbf{R}_i|} \tag{II.9}$$

ϵ_0 being the permittivity of vacuum, e is the electron charge, and Z_I represent the atomic numbers. The indices i and j goes from 1 to N and indices I and J from 1 to M, where N is the number of electrons and M is the number of nuclei. We exclude the self-interaction terms $i = j$ and $I = J$.

Therefore, combining Equations (II.6) to (II.9) into Equation (II.1) we can write the full many-body Schrödinger equation:

$$\Bigg[\overbrace{-\sum_{i=1}^{N} \frac{\hbar^2}{2m_{\mathrm{e}}} \nabla_i^2}^{T_{\mathrm{e}}} \overbrace{- \sum_{I=1}^{M} \frac{\hbar^2}{2M_I} \nabla_I^2}^{T_{\mathrm{n}}} + \overbrace{\frac{1}{2} \sum_{i \neq j} \frac{e^2}{4\pi\epsilon_0} \frac{1}{|\mathbf{r}_i - \mathbf{r}_j|}}^{V_{\mathrm{ee}}} + \overbrace{\frac{1}{2} \sum_{I \neq J} \frac{e^2}{4\pi\epsilon_0} \frac{Z_I Z_J}{|\mathbf{R}_I - \mathbf{R}_J|}}^{V_{\mathrm{nn}}} - \overbrace{\sum_{i,I} \frac{e^2}{4\pi\epsilon_0} \frac{Z_I}{|\mathbf{r}_i - \mathbf{R}_i|}}^{V_{\mathrm{ne}}} \Bigg] \Psi = E_{\mathrm{tot}} \Psi \tag{II.10}$$

If we were able to solve this equation and find the eingenstate with the lowest energy, it would be possible to know the equilibrium properties of the system, such as enthalpies of formation, elastic constants, thermal properties, and phase diagrams. Unfortunately, this is an extremely complex equation to solve (if not impossible), in which we only know how to solve for the simplest systems.

I.2. Born-Oppenheimer approximation

In order to solve Equation (II.10), we need to simplify it. In our case, we will concentrate in solids and molecules, for which we can consider the nuclei as fixed. This is called the Born-Oppenheimer approximation, and it is based on the fact that even the mass of the lightest nucleus is much higher than that of the electron (mass ratio $\approx 1:2000$, which implies that –> $m_\mathrm{n} \gg m_\mathrm{e}$; $T_\mathrm{n} \ll T_\mathrm{e}$). This approximation implies that the kinetic energy of the nuclei in Equation (II.10) is set to zero. Consequently, the V_nn term becomes a constant for a given configuration of nuclei and can be incorporated into the E_tot term:

$$E = E_\mathrm{tot} - \frac{1}{2}\sum_{I \neq J} \frac{e^2}{4\pi\epsilon_0} \frac{Z_I Z_J}{|\mathbf{R}_I - \mathbf{R}_J|} \tag{II.11}$$

We can now consider the wavefunction as a function of only the position of electrons: $\Psi = \Psi(\mathbf{r}_1, \cdots, \mathbf{r}_N)$. As a result, we can rewrite Equation (II.10), in atomic units, as:

$$\left[-\sum_i \frac{\nabla_i^2}{2} - \sum_{i,I} \frac{Z_I}{|\mathbf{r}_i - \mathbf{R}_I|} + \frac{1}{2}\sum_{i \neq j} \frac{1}{|\mathbf{r}_i - \mathbf{r}_j|} \right] \Psi = E\Psi \tag{II.12}$$

It can be noted that this equation is similar to the single–particle Schrödinger equation Equation (II.2), but now we are dealing with several electrons and their respective Coulomb repulsion.

I.3. Independent electron approximation

The main problem from Equation (II.12) comes from the Coulomb repulsion between the electrons, and, as a first approximation to solve this complex equation, we can make use of a (drastic) simplification called *independent electron approximation* and ignore completely the electron–electron interactions.

In this approximation, the probability of finding electron 1 at $\mathbf{r}_1$ and electron 2 at $\mathbf{r}_2 \ldots$ and electron number N at $\mathbf{r}_N$ is given as the product of the individual probabilities $|\phi_i(\mathbf{r}_i)|^2$ finding the electron at the position $\mathbf{r}_i$. Thus, we can write the solution of Equation (II.12) as:

$$\Psi(\mathbf{r}_1, \cdots, \mathbf{r}_N) = \phi(\mathbf{r}_1) \cdots \phi(\mathbf{r}_N) \tag{II.13}$$

Supposing that ϕ_i could be obtained as the solutions of the single electron Schrödinger equation:

$$\hat{H}_0(\mathbf{r})\phi_i(\mathbf{r}) = \epsilon_i \phi_i(\mathbf{r}) \tag{II.14}$$

where $\hat{H}_0$ is the *single-electron Hamiltonian* $[\hat{H}_0(\mathbf{r}) = -\frac{1}{2}\nabla^2 + V_\mathrm{n}(\mathbf{r})]$, with:

$$V_\mathrm{n}(\mathbf{r}) = -\sum_I \frac{Z_I}{|\mathbf{r} - \mathbf{R}_I|} \tag{II.15}$$

Due to the intuition given by this approximation, it is a good idea to work on how to describe the electron–electron interaction within this simplification. However, there are two drawbacks that appear, which are: (1) the wavefunction must obey Pauli's exclusion principle, which implies that wave-function must be anti-symmetric with respect to the exchange of two electrons, and (2) the magnitude of the eliminated Coulomb term is, in fact, non negligible.

In order to overcome problem (1), which comes from the fact that two electrons cannot occupy the same electronic state, we can write the many-body wave function Ψ as a Slater determinant [94].

$$\Psi(\mathbf{r}_1, \cdots, \mathbf{r}_n) = \frac{1}{\sqrt{n!}} \begin{vmatrix} \phi_1(\mathbf{r}_1) & \dots & \phi_n(\mathbf{r}_1) \\ \vdots & \ddots & \vdots \\ \phi_1(\mathbf{r}_n) & \dots & \phi_n(\mathbf{r}_n) \end{vmatrix} \tag{II.16}$$

where $\frac{1}{\sqrt{n!}}$ is a normalization factor.

As for problem (2), we need to be able to re-implement the electron–electron Coulomb interaction in the Hamiltonian while maintaining the independent electron approximation. To this end, we introduce the Hartree potential, which is a classical derivation of Poisson's equation and describes an average charge felt by each electron:

$$V_H(\mathbf{r}) = \int \frac{\rho(\mathbf{r'})}{|\mathbf{r} - \mathbf{r}'|} \mathrm{d}\mathbf{r}' \tag{II.17}$$

where ρ is the distribution of electronic charge.

I.4. Hohenberg-Kohn theorems

The Hohenberg-Kohn theorems were introduced in the famous article [95] and are the cornerstones of Density Functional Theory. They are based on two key ideas.

I.4.1. Density as a basic variable

The proof for the first concept was conceived by *reductio ad absurdum*, coming from the assumption that two different potentials, $V(\mathbf{r})$ and $V'(\mathbf{r})$ with ground states Ψ and Ψ' result in the same density $\rho(\mathbf{r})$. By comparing the Hamiltonian and the energies associated with these two wavefunctions and potentials, we have, by the minimal property of the ground state:

$$E' = \langle \Psi' | H' | \Psi' \rangle < \langle \Psi | H' | \Psi \rangle = \langle \Psi | \left(H + V'(\mathbf{r}) - V(\mathbf{r}) \right) | \Psi \rangle \tag{II.18}$$

with a Hamiltonian in the form:

$$H = T + V \tag{II.19}$$

with T and V being the kinetic and potential energies, respectively.

Equation (II.18) leads to the following inconsistency:

$$E + E' < E + E' \tag{II.20}$$

Therefore, the potential $V(\mathbf{r})$ is a unique functional[2] of $\rho(\mathbf{r})$. Since, in turn, the Hamiltonian is determined by $V(\mathbf{r})$, the many-body wavefunction is a unique functional of the density: $E \equiv E[\rho]$.

I.4.2. Variational principle

The second theorem is derived from the variational principle of quantum mechanics. It states that the functional that gives the density of the ground-state of the system delivers the lowest energy if and only if the input density is the true ground-state density ρ_0. In other words, if the charge density is the ground-state density, the corresponding energy is stationary, i.e.:

$$\left. \frac{\delta E[\rho]}{\delta \rho} \right|_{\rho_0} = 0 \tag{II.21}$$

I.5. Kohn-Sham equations

The problem of finding the ground-state energy would be rather simple if $E[\rho]$ were a known functional of ρ, because it involves a functional's minimization of the three dimensional density function. However, the main problem lies exactly on finding the exact form of this universal functional, which would be valid for any number of particles and any external potential. This is what will be addressed in this section.

By using the relation between the wavefunction and the electron density, one can rewrite the ground-state energy as:

---

[2] A functional is a linear form that takes as input a function and gives (output) a scalar.

$$E[\rho] = \overbrace{\underbrace{\int \rho(\mathbf{r}) V_n(\mathbf{r}) d\mathbf{r}}_{\text{External potential}} - \underbrace{\sum_i \int \phi_i^*(\mathbf{r}) \frac{\nabla^2}{2} \phi_i(\mathbf{r}) d\mathbf{r}}_{\text{Kinetic energy}} + \underbrace{\frac{1}{2} \int \int \frac{\rho(\mathbf{r})\rho(\mathbf{r}')}{|\mathbf{r}-\mathbf{r}'|} d\mathbf{r} d\mathbf{r}'}_{\text{Hartree energy}}}^{\text{Total energy in the independent electron approximation}} + \underbrace{E_{\text{xc}}[\rho]}_{\text{XC energy}} \qquad \text{(II.22)}$$

The XC energy $E_{\text{xc}}[\rho]$ is called the exchange and correlation energy, and it contains all the not included effects. If we were able to find the exact form of this functional, we would be able to calculate the total energy of the system in its ground state using the electron density.

By using the Hohenberg–Kohn variational principle from Equation (II.21) and considering the single-particle wavefunctions to be orthonormal, we can write the Kohn-Sham equations:

$$\left[-\frac{1}{2}\nabla^2 + V_{\text{n}}(\mathbf{r}) + V_{\text{H}}(\mathbf{r}) + V_{\text{xc}}(\mathbf{r}) \right] \phi_i(\mathbf{r}) = \epsilon_i \phi_i(\mathbf{r}) \qquad \text{(II.23)}$$

with the *exchange and correlation potential*, V_{xc} given by:

$$V_{\text{xc}}(\mathbf{r}) = \left. \frac{\delta E_{\text{xc}}[\rho]}{\delta \rho} \right|_{\rho_0} \qquad \text{(II.24)}$$

I.6. Exchange and correlation energy

As it was pointed out in the last section, we must find the form of the $E_{\text{xc}}[\rho]$ to solve the Kohn-Sham equations and determine the ground-state energy[3]. A great effort was put into this task, and several approximate functionals are available today. Here, we will briefly discuss three families of functionals that are relevant for the present work.

I.6.1. Local Density Approximantion (LDA)

The first introduced XC functional is the *local density approximation* (LDA) [95], shown here for its simplicity, utility, and historical reason. The exchange part of this functional was calculated approximately by studying a *homogeneous electron gas*, which closely resembles a "free electron gas" model, while the correlation part is calculated using numerical methods.

In this model, the density is considered to be locally homogeneous and slowly varying, and it is defined as:

---

[3] Unfortunately the exact form of this $E_{\text{xc}}[\rho]$ functional is still unknown.

$$E_{\mathrm{xc}}^{\mathrm{LDA}}[\rho] = \int_V \rho(\mathbf{r})\epsilon_{\mathrm{xc}}(\rho(\mathbf{r}))d\mathbf{r} \tag{II.25}$$

where ϵ_{xc} is the XC energy per particle of a homogeneous electron gas of density ρ.

Despite the simplicity of this functional, it received an impressive practical success, [96], [97]. Its main drawback is that it underbinds the core electrons in an atom and overbinds the atoms in solids and molecules.

I.6.2. Generalized gradient approximation (GGA)

This functional improves on the LDA approximation by taking into account also the dependency of the gradient of the electronic density in the ϵ_{xc} energy [98], [99]. It is given by:

$$E_{\mathrm{xc}}^{\mathrm{GGA}} = \int_V \rho(\mathbf{r})\epsilon_{\mathrm{xc}}(\rho(\mathbf{r}), \nabla\rho(\mathbf{r}))d\mathbf{r} \tag{II.26}$$

The GGA exchange energy density is given by:

$$E_{\mathrm{x}}(\rho, s) = E_{\mathrm{x}}^{\mathrm{LDA}}(\rho)F_{\mathrm{x}}(s) \tag{II.27}$$

where $F_{\mathrm{x}}(s)$ is the enhancement fact (which depends on the reduced density gradient $s = |\nabla n|/2(3\pi^2)^{1/3}n^{4/3}$) and $E_{\mathrm{x}}^{\mathrm{LDA}}(\rho)$ is the LDA exchange energy density. This enhancement factor of revPBE and PBE has the form:

$$F_{\mathrm{x}}^{\mathrm{PBE}}(s) = 1 + \kappa - \frac{\kappa}{1 + \frac{\mu s^2}{\kappa}} \tag{II.28}$$

κ and μ are empirical coefficients originally proposed by Becke [100].

I.6.3. OptPBE-vdW

The LDA and GGA functionals are unable to describe London dispersion interactions. There has been many attempts to account for these interactions approximately [101]–[107]. One rigorous and promising approach is the non-local van der Waals density functional (vdW-DF) [101], where the exchange-correlation functional takes the following form:

$$E_{\mathrm{xc}} = E_{\mathrm{x}}^{\mathrm{GGA}} + E_{\mathrm{c}}^{\mathrm{LDA}} + E_{\mathrm{c}}^{\mathrm{nl}} \tag{II.29}$$

where $E_{\mathrm{x}}^{\mathrm{GGA}}$, $E_{\mathrm{c}}^{\mathrm{LDA}}$, and $E_{\mathrm{c}}^{\mathrm{nl}}$ are the GGA exchange energy, the LDA correlation energy, and the non-local correlation. The non-local correlation $E_{\mathrm{c}}^{\mathrm{nl}}$ is obtained along with the revised version of the PBE functional [108] from Zhang and Yang (revPBE) [109].

By optimizing the values of κ and μ by comparing the atomic total energies and molecular atomization energies, it was found that a value of $\kappa = 1.04804$ and $\mu = 0.175519$, within vdW-DF, leads to a better description of the experimental results in the treatment of weak interactions [110]. This functional is called "optPBE-vdW".

I.6.4. Hubbard model (DFT+U)

Even thought DFT is a remarkable theory, considered to be a reliable tool to describe the ground state of the electronic structure of a solids, it does have its drawbacks. One of the most common problems is that it poorly describes systems that contain atoms/ions with partially filled valence d or f shells. For example, many of the transition metal oxides are predicted to have metallic ground states instead of experimentally observed insulating ones [111]. This failure is associated with an erroneous description of the strong Coulomb repulsion between $3d$ electrons localized on metal ions [112], as the electron transfer between d electrons of two metal ions give rise to large fluctuations of the system's total energy and to the formation of band gaps [113].

In order to overcome this problem, the most common approach was described by Dudarev et al. [114], in which a correction is added to the LSDA (*local spin density approximation*) total energy expression:

$$E_{\mathrm{LSDA+U}} = E_{\mathrm{LSDA}} + \frac{(\overline{U} - \overline{J})}{2} \sum_{\sigma} \left(n_{\mathrm{m},\sigma} - n^2_{\mathrm{m},\sigma} \right) \tag{II.30}$$

where n_σ is the expectation value of the operator for the number of electrons occupying a particular site. The sum is performed over the orbital momentum's projection ($m = -2, -1, \cdots, 2$), and the total number of electrons N_σ is $N_\sigma = \sum_m n_{m,\sigma}$.

I.7. Numerical implementation

As it was seen in the previous chapters, only the electron-density is needed to calculate Kohn-Sham total energy. Figure II.1 shows a flow-chart with the steps necessary to calculate the density and total ground state energy, and we can notice that it uses a self-consistent approach. An initial "guess" electron density is used to estimate the XC and Hartree potentials, proceeding to the total potential V_{tot}.

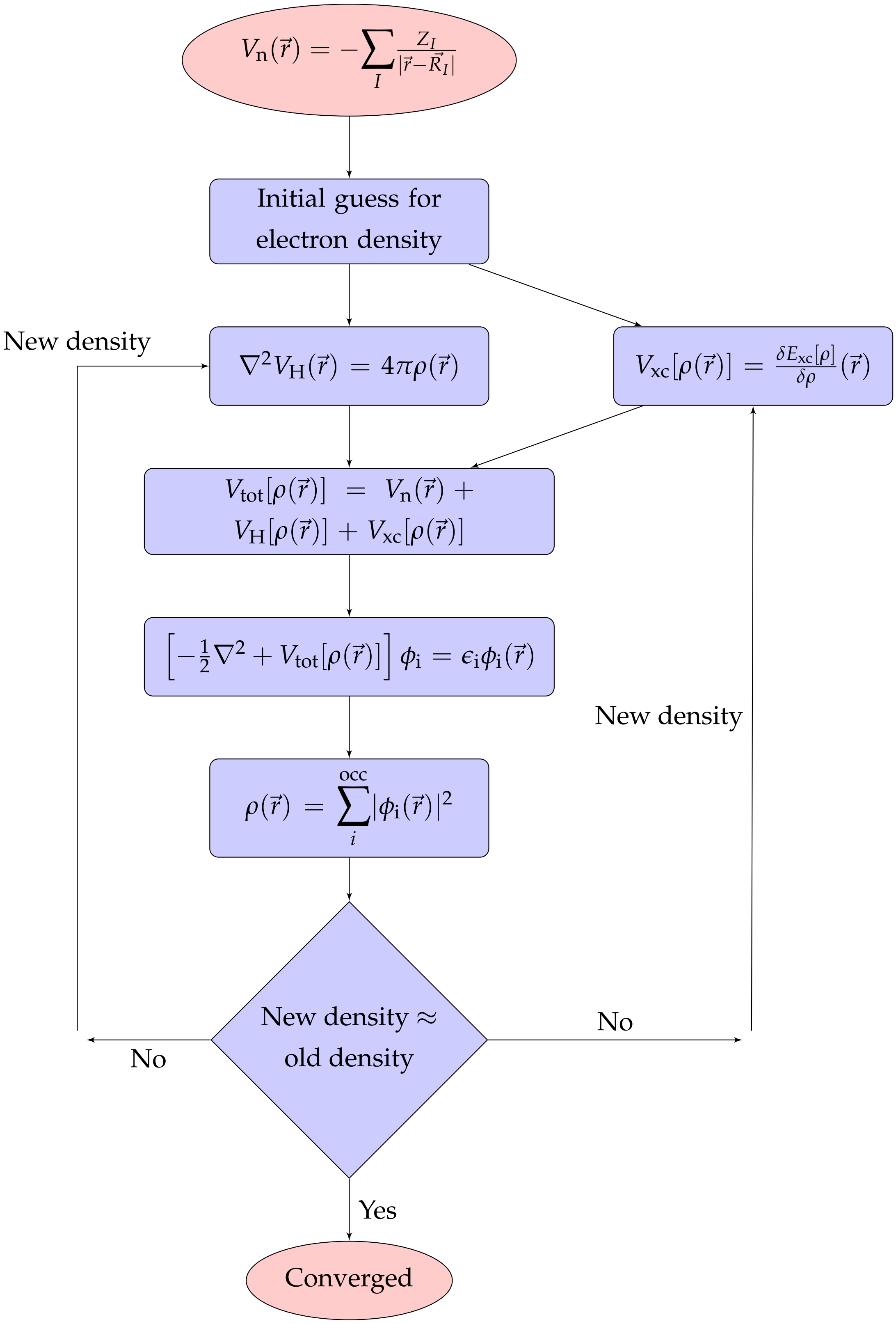

Figure II.1: Flow-chart for determining self-consistently the solutions of the Kohn-Sham equations. The final ≈ symbol checks if the new density differs by less than a desired tolerance, input by the user.

By solving the Kohn-Sham equations, new wavefunctions are obtained (ϕ_{i}), which are used to estimate a better density ρ and a new V_{tot}. This process is repeated until achieving self-consistency at a desired tolerance.

This self-consistent loop is implemented in several codes and there are many different ways how to (technically) solve the Kohn-Sham equations. In our specific case, we will be using plane-waves with periodic boundary conditions implemented in VASP [89]–[91] throughout the whole work. In order to obtain the desired electronic properties at a sufficient precision, it is imperative to make use of High Performance Computing (HPC) resources. There are four supercomputers that were used in the present work:

- *Explor* at Université de Lorraine, Institut Jean Lamour, Nancy, France;
- *Jeanzay* at IDRIS (Institut du Développement et des Ressources en Informatique Scientifique);
- *Occigen* at CINES[4] (Centre Informatique National de l'Enseignement Supérieur);
- *Topaze* at the CEA (The French Alternative Energies and Atomic Energy Commission) and the TGCC (Très Grand Centre de Calcul), Bruyères-le-Châtel, Essonne, France.
- *Irene* at the CEA and the TGCC, Bruyères-le-Châtel, Essonne, France.

I.7.1. Reciprocal space discretization and plane waves

A possible way to solve the Kohn-Sham equations consists of describing the wavefunctions using a Fourier series, which is very effective when using periodic boundary conditions that avoid dealing with an incalculable number of electrons. The one-particle wavefunctions in the Kohn-Sham equations can be described by means of the Bloch theorem and the translational invariant principle [115]:

$$\phi_{n\vec{k}}(\vec{r}) = u_{n\vec{k}}(\vec{r})e^{i\vec{k}\cdot\vec{r}} \quad \text{with} \quad u_{n\vec{k}}(\vec{r}+\vec{R}) = u_{n\vec{k}}(\vec{r}) \tag{II.31}$$

therefore,

$$\phi_{n\vec{k}}(\vec{r}+\vec{R}) = e^{i\vec{k}\vec{R}}\phi_{n\vec{k}}(\vec{r}) \tag{II.32}$$

where $\vec{k}$ is the Bloch wavevector in the first Brillouin zone of the reciprocal lattice, $\vec{R}$ is a translation vector, n is the band index, and $u_{n\vec{k}}(\vec{r})$ is the cell function that has the periodicity of the lattice.

---

[4] This supercomputer is no longer operational and was substituted by a new machine called *Adastra*.

By expressing the cell function $u_{n\vec{k}}(\vec{r})$ as a Fourier series, the wavefunctions are represented as the sums of plane waves:

$$u_{n\vec{k}}(\vec{r}) = \sum_{\vec{G}} C_{\vec{G}n\vec{k}} e^{i\vec{G}\cdot\vec{r}}; \;\; \phi_{n\vec{k}}(\vec{r}) = \sum_{\vec{G}} C_{\vec{G}n\vec{k}} e^{i(\vec{G}+\vec{k})\cdot\vec{r}} \tag{II.33}$$

where $C_{\vec{G}n\vec{k}}$ are the plane waves coefficient, and $\vec{G}$ are the reciprocal space vectors. In practice, we need to restrict this expansion such that it is still accurate enough to describe wave functions properly. Thus, the E_{cutoff} represents the maximum considered plane wave kinetic energy, given by:

$$\frac{1}{2}|\vec{G}+\vec{k}|^2 \leq E_{\text{cutoff}} \tag{II.34}$$

Although plane waves are convenient and efficient, they are very smooth functions. Hence, incredibly high cutoff energy would be required to describe core states with rapid oscillations around nuclei. The problem can be circumvented with pseudopotentials that treat core electrons implicitly. With the pseudopotential method, only valence electrons are therefore described explicitly. The Projector-Augmented Wave (PAW) method is a very accurate and also efficient implementation of the pseudopotential method [116], [117].

II. DFT applications to ultra-thin films

In this section we will introduce the techniques used (all based on DFT) to determine and analyze some useful quantities when studying ultra-thin films.

II.1. *Ab initio* atomistic thermodynamics

Density functional theory has nowadays become a standard tool to model the behavior of electrons and their resulting chemical bonds that dictate processes among atoms and molecules, being applicable to realistic environmental conditions with varying temperature and pressure [118]. This statement may seem an illogical argument since DFT in known as a zero-temperature/pressure technique, providing 'only' the electronic structure and total ground state energy of the system. However, one should realize that the energy can be obtained as a function of the atomic configuration $\{\mathbf{R}_I\}$, which leads to a potential energy surface (PES) $E\{\mathbf{R}_I\}$ that contains important information to describe a system's behavior as a function of the temperature.

Thus, the idea is to use the information on the PES to calculate important thermodynamic functions, like the Gibbs free energy [119], [120], and then it is possible to describe the system's macroscopic properties using the general concepts of thermodynamics.

II.1.1. Surfaces in realistic environments

In *ab initio* atomistic thermodynamics, we can obtain the temperature's contribution by explicitly taking into account the gas phase [121]. For the sake of simplicity, we will first discuss the equations considering an elemental metal and oxygen atmosphere. In Sections II.1.2. and II.1.4. we will apply the same principles for intermetallics and oxides, respectively.

Figure II.2 is a schematic representation of a solid substrate in contact with a surrounding gas phase at a temperature T and pressure P.

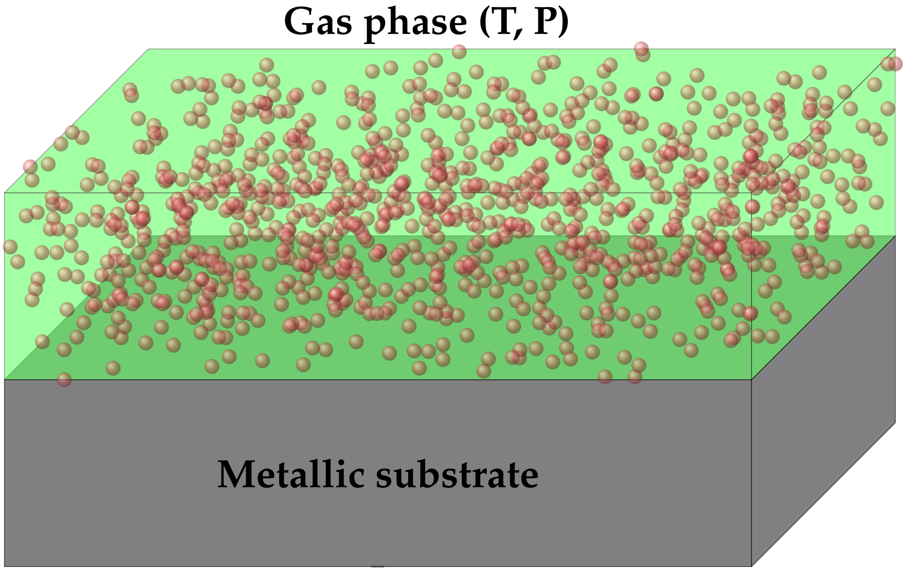

Figure II.2: A metallic substrate in contact with a surrounding O_2 gas at temperature T and pressure P.

The total Gibbs free energy of this system can be divided into the contributions of the solid phase G_{bulk}, the homogeneous gas phase G_{gas}, and a term related to the surface ΔG_{surf}:

$$G = G_{\text{bulk}} + G_{\text{gas}} + \Delta G_{\text{surf}} \tag{II.35}$$

Considering a homogeneous surface, ΔG_{surf} will have a linear dependence on the area A, and it is possible to introduce the surface free energy per area (γ):

$$\gamma = \frac{1}{A}\left(G - G_{\text{bulk}} - G_{\text{gas}}\right) \tag{II.36}$$

By concentrating on the supercell part of the infinite system that is affected by the surface energy, Equation (II.36) can be rewritten, considering N_{M} metal atoms and N_{O} oxygen atoms per supercell area, as:

$$\gamma(T,P) = \frac{1}{A}\left(G(T,P) - N_{\mathrm{M}}g_{\mathrm{M}}(T,P) - N_{\mathrm{O}}\mu_{\mathrm{O}}(T,P)\right) \tag{II.37}$$

where g_{M} is the Gibbs free energy per metal atom and μ_{O} is the chemical potential of oxygen atom. For an infinite homogeneous system, the term g_{M} is equivalent to the chemical potential μ_{M}. In a more general case of a multi–component homogeneous system, Equation (II.37) can be re-written as:

$$\gamma(T,P) = \frac{1}{A}\left(G(T,P) - \sum_{i} N_{\mathrm{i}}\mu_{\mathrm{i}}(T,P_{\mathrm{i}})\right) \tag{II.38}$$

The representation of $G(T,P)$ and μ depends on each system and one must be careful on how to treat each term. We will discuss how to expand each of these terms according to the studied systems in this work, beginning with the description of the chemical potential of the O_2 molecule, and then of the Gibbs free energies of the solid phases.

II.1.1.1. Oxygen chemical potential

The chemical potential of the O_2 molecule can be determined by considering that the solid phase is in thermodynamic equilibrium with the gas phase, which is seen as a *reservoir* and described by ideal gas laws. Chemical potential can be written as a function of the partition function $Z^{\mathrm{tot}}_{\mathrm{O_2(g)}}$, the temperature T, and pressure P as:

$$\mu_{\mathrm{O}}(T,P) = \frac{1}{2}\mu_{\mathrm{O_2(g)}}(T,P) = \frac{1}{2}\left(-k_{\mathrm{B}}T\ln Z^{\mathrm{tot}}_{\mathrm{O_2(g)}} + PV\right)/N \tag{II.39}$$

As a result, we need to calculate the partition function of an ideal gas composed of N indistinguishable O_2 molecules:

$$Z^{\mathrm{tot}}_{\mathrm{O_2(g)}} = \frac{1}{N!}\left(z^{\mathrm{trans}}z^{\mathrm{rot}}z^{\mathrm{vib}}z^{\mathrm{electr}}z^{\mathrm{nucl}}\right)^{N} \tag{II.40}$$

where z^{trans}, z^{rot}, z^{vib}, z^{electr}, z^{nucl} are the translational, rotational, vibrational, electronic, and nuclear partition functions of an O_2 molecule. By assuming that the vibrational and rotational motions are represented on different time scales and that the vibrational/rotational degrees of freedom are decoupled, we can write:

$$\mu_{\mathrm{O}}(T,P) = -\frac{1}{2N}\left[k_{\mathrm{B}}T\ln\left(\frac{{z_{\mathrm{trans}}}^{N}}{N!}\right) - PV\right] + \frac{1}{2}\mu^{\mathrm{rot}} + \frac{1}{2}\mu^{\mathrm{vib}} + \frac{1}{2}\mu^{\mathrm{electr}} + \frac{1}{2}\mu^{\mathrm{nucl}} \tag{II.41}$$

All terms for this particular case are well-known. For a detailed description of how to obtain them please refer to [122], [123]. The final formula for the chemical potential, considering the vibrational modes, total energy of the gas phase, rotational constant, and spin degeneracy can be the written as:

$$\mu_{\mathrm{O}}(T,P) = \frac{1}{2}E^{\mathrm{total}}_{\mathrm{O}_2} + \frac{1}{2}E^{\mathrm{ZPE}}_{\mathrm{O}_2} + \Delta\mu_{\mathrm{O}}(T,P) \tag{II.42}$$

where $E^{\mathrm{ZPE}}_{\mathrm{O}_2}$ is the zero point energy. The $\Delta\mu_{\mathrm{O}}(T,P)$ is expanded by its temperature and pressure free energy contributions:

$$\Delta\mu_{\mathrm{O}}(T,P) = -\frac{1}{2}k_{\mathrm{B}}T\left\{\overbrace{\ln\left[\left(\frac{2\pi m}{h^2}\right)^{3/2}\frac{(k_{\mathrm{B}}T)^{5/2}}{P}\right]}^{\text{Translational}} + \overbrace{\ln\left(\frac{k_{\mathrm{B}}T}{\sigma^{\mathrm{sym}}B_0}\right)}^{\text{Rotational}} - \overbrace{\ln\left[1-\exp\left(\frac{\hbar\omega_0}{k_{\mathrm{B}}T}\right)\right]}^{\text{Vibrational}} + \overbrace{\ln\left(I^{\mathrm{spin}}\right)}^{\text{Electronic}}\right\} \tag{II.43}$$

where $\hbar$ is the reduced Planck constant[5], σ^{sym} is the symmetry number for the O_2 molecule, B_0 is the rotational constant[6], ω_0 is the vibrational mode of the O_2 molecule considering an harmonic oscillator, and I^{spin} is the electronic spin degeneracy of the ground state. Most of these values are available at themochemical tables [124].

The contribution of each partition function term is plotted in Figure II.3, where one can clearly see that the terms that contribute the most are the translation and rotation partition functions.

II.1.1.2. Gibbs free energy

For solids, the translational and rotational degrees of freedom are not considered. Hence, the Gibbs free energy of solids can be decomposed into the following contributions:

$$G = E^{\mathrm{tot}} + F^{\mathrm{vib}} + F^{\mathrm{conf}} + PV \tag{II.44}$$

where E^{tot} is the total energy, F^{vib} is the vibrational free energy, and F^{conf} is the configurational free energy.

---

[5] $\hbar = \frac{h}{2\pi}$

[6] $B_0 = \frac{\hbar}{2I}$, with I being the moment of inertia.

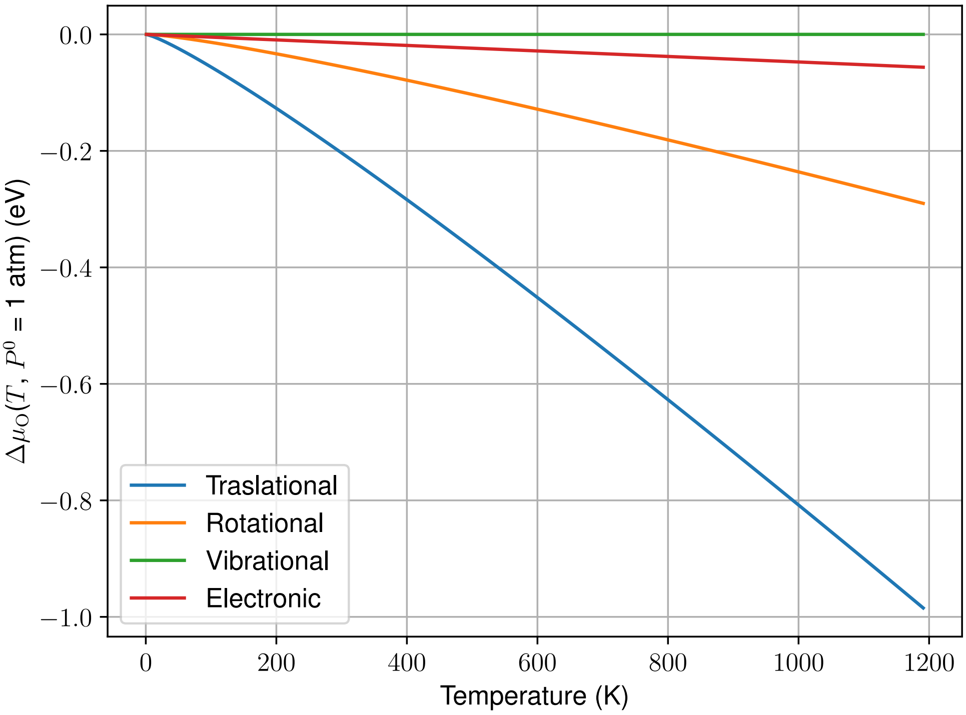

Figure II.3: The dependence of various components of oxygen chemical potential on the temperature (relative to $T = 0$ K) at $P = 1$ atm. The parameters used for Equation (II.43) were taken from [124]: $\sigma^{\text{sym}} = 2$, $I^{\text{spin}} = 3$, $B_0 = 0.18$ meV and $\omega_0 = 196$ meV.

The principal term in Equation (II.44) is the total energy calculated directly through DFT calculations. Due to the size of the systems being calculated in the present study, the three final terms are neglected. This approximation is reasonable for our case due to four main factors:

- The Gibbs free energy relevant for the present work deals with *differences*, and not with absolute values of the Gibbs free energies, which allow for a good degree of error canceling.
- The PV-contribution to the surface free energy per surface area is very small for solids, being in the order of ≈ 0.1 meV/Å^2 (even for $P \approx 100$ atm). [123]
- For metallic surfaces in contact with oxygen environment, it was noted that the resulting variation in the vibrational free energy stays within the range $\approx \pm 5$ meV/Å^2. There are known applications in which this term cannot be neglected, e.g. in hydrogen containing environments [125].

- Typically for transition metal surfaces, the contribution for the configurational entropy terms is ≤ 3 meV/Å^2 for $T < 1000$ K [126].

Therefore, the Gibbs free energy of solids is approximated by total internal energy calculated with DFT:

$$G = E_{\text{tot}} \tag{II.45}$$

II.1.2. PdIn/In$_x$O$_y$ surfaces in oxygen atmosphere

In this section we will describe the *ab initio* thermodynamic framework to calculate the surface free energy for the PdIn(100)/In$_x$O$_y$ system with an oxygen surrounding environment. For a general description of a multicomponent alloy surrounded by several gas phases, please refer to the work by Kitchin et al. [127]. As it was already seen in Section II.1., the surface structure which minimizes Equation (II.38) is the most stable one at particular conditions. For simplicity, we rewrite it here:

$$\gamma(T, P) = \frac{1}{A}\left(G(T, P) - \sum_{i} N_{\text{i}}\mu_{\text{i}}(T, P_{\text{i}})\right) \tag{II.46}$$

In our specific case, we have an asymmetric slab with two different surfaces. The bottom surface is the Pd-termination of the PdIn(100) intermetallic and the other side is the In$_x$O$_y$ surface, as it is shown in Figure II.4. The In$_x$O$_y$ surface is the one for which we want to calculate the surface free energy.

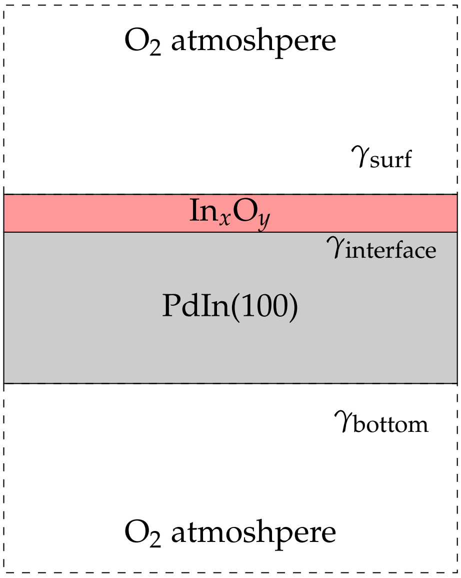

Figure II.4: Side view of the PdIn(100)/In$_x$O$_y$ system.

Therefore, Equation (II.38) takes the form:

$$\gamma_{\text{surf}}\left(T, P_{\text{O}_2}\right) + \gamma_{\text{bottom}} + \gamma_{\text{interface}} = \frac{1}{A}\left[G_{\text{slab}}\left(T, P_{\text{O}_2}\right) - N_{\text{Pd}}\mu_{\text{Pd}} - N_{\text{In}}\mu_{\text{In}} - N_{\text{O}}\mu_{\text{O}}\left(T, P_{\text{O}_2}\right)\right] \quad \text{(II.47)}$$

For our case, we will approximate the $\gamma_{\text{interface}}$ parameter as the adhesion energy per unit area (E_{adh}/A), where E_{adh} is calculated by the difference in total energy between the complete (E_{tot}) and separated systems ($E_{\text{substrate}}$ and E_{oxide}):

$$E_{\text{adh}} = E_{\text{tot}} - E_{\text{substrate}} - E_{\text{oxide}} \quad \text{(II.48)}$$

By considering that there is enough bulk material to serve as a reservoir, the chemical potentials in the bulk are no longer independent and are related to the Gibbs free energy on the bulk intermetallic:

$$g_{\text{PdIn}}^{\text{bulk}} = \mu_{\text{Pd}} + \mu_{\text{In}} \quad \text{(II.49)}$$

where g denotes the Gibbs free energy by unit formula.

By inserting Equation (II.49) into Equation (II.47) we have:

$$\gamma_{\text{surf}}\left(T, P_{\text{O}_2}\right) + \gamma_{\text{bottom}} + \gamma_{\text{interface}} = \frac{1}{A}\left[G_{\text{slab}}\left(T, P_{\text{O}_2}\right) - N_{\text{Pd}}\left(g_{\text{PdIn}}^{\text{bulk}} - \mu_{\text{In}}\right) - N_{\text{In}}\mu_{\text{In}} - N_{\text{O}}\mu_{\text{O}}\left(T, P_{\text{O}_2}\right)\right] \quad \text{(II.50)}$$

By expanding the chemical potential of oxygen using Equation (II.43), we now show that γ_{surf} only depends on the indium chemical potentials and on the temperature/pressure conditions of the oxygen reservoir through the oxygen chemical potential. In addition, as discussed in Section II.1.1., we will neglect the vibrational and configurational terms in the Gibbs free energies and input directly the total energy obtained in DFT calculations as the predominant term. Thus, Equation (II.50) becomes:

$$\gamma_{\text{surf}}\left(T, P_{\text{O}_2}\right) + \gamma_{\text{bottom}} + \gamma_{\text{interface}} = \frac{1}{A}\left[E_{\text{slab}}\left(T, P_{\text{O}_2}\right) - N_{\text{Pd}}\left(E_{\text{PdIn}}^{\text{bulk}} - \mu_{\text{In}}\right) - N_{\text{In}}\mu_{\text{In}} - N_{\text{O}}\mu_{\text{O}}\right] \quad \text{(II.51)}$$

II.1.2.1. Range of allowed chemical potentials of In

Instead of focusing on a system with a well determined 'perfect' structure and calculate precisely the chemical potential for In (e.g. by cluster expansion techniques [128]–[131]), we will discuss the general effects of dilute bulk antisites, i.e. In on Pd sites for In-rich samples and Pd on In sites for Pd-rich samples, and roughly estimate the range that μ_{In} can span. Therefore, we will use as the upper limit when the bulk reservoir is rich in In, and the lower limit when it is rich in Pd:

$$\begin{cases} \mu_{\text{In}} \leq \mu_{\text{In}}^{\text{bulk}} \\ \mu_{\text{Pd}} \leq \mu_{\text{Pd}}^{\text{bulk}} \end{cases} \tag{II.52}$$

For the upper limit we can therefore consider the chemical potential of bulk In to be the cohesive energy of the most stable In structure at 0K ($\mu_{\text{In}}^{\text{bulk}} = E_{\text{coh}}^{\text{In}-\text{bulk}}$), while for the lower limit we can use the relation with the formation enthalpy:

$$\begin{aligned} \mu_{\text{Pd}} &= \mu_{\text{Pd}}^{\text{bulk}} \\ \Delta H_f &= E_{\text{PdIn}}^{\text{bulk}} - E_{\text{Pd}} - E_{\text{In}} \\ \Delta H_f &= \overbrace{\cancel{\mu_{\text{Pd}}}}^{\mu_{\text{Pd}}^{\text{bulk}}} + \mu_{\text{In}} - \cancel{\mu_{\text{Pd}}^{\text{bulk}}} - \mu_{\text{In}}^{\text{bulk}} \\ \mu_{\text{In}} &= \Delta H_f + \underbrace{\mu_{\text{In}}^{\text{bulk}}}_{E_{\text{coh}}^{\text{In}-\text{bulk}}} \end{aligned} \tag{II.53}$$

In the end, we have the following limits:

$$\Delta H_f + E_{\text{coh}}^{\text{In}-\text{bulk}} \leq \mu_{\text{In}} \leq E_{\text{coh}}^{\text{In}-\text{bulk}} \tag{II.54}$$

All terms in Equation (II.51) (except γ_{bottom}) and the limits in Equation (II.54) can be determined by total energy DFT calculations and we are able to estimate the surface free energy of our systems according to the temperature and pressure imposed by the chemical potential of oxygen.

II.1.2.2. Surface energy of PdIn(100)

The last parameter left to calculate in Equation (II.51) is γ_{bottom}, which is the surface free energy of PdIn(100). For this structure, there are only two terminations to be considered: In-rich and Pd-rich. The methodology to describe the surface free energy of this intermetallic is analogous of the one described in the last sections (for further details, see the work of

McGuirk et al. [132]), but without an oxygen environment and considering a symmetric slab. Therefore, Equation (II.38) becomes:

$$\gamma_{\text{bottom}} = \frac{1}{2A}\left[E_{\text{slab}}(N_{\text{In}}, N_{\text{Pd}}) - N_{\text{In}}\mu_{\text{In}} - N_{\text{Pd}}\left(E^{\text{bulk}}_{\text{PdIn}} - \mu_{\text{In}}\right)\right] \tag{II.55}$$

here we divide by $2A$ to account for two symmetric surfaces. The two limits are the same as in Equation (II.54).

II.1.3. PdIn/In$_x$O$_y$ surface formation energy – Grand potential (Ω)

Another way to determine the surface stability is by calculating the free energy of the surface phase with respect to a bulk reservoir of In_2O_3 in equilibrium with an oxygen atmosphere, given by its chemical potential [133]:

$$\Omega = \frac{E_{\text{In}_x\text{O}_y/\text{PdIn}(001)} - E_{\text{PdIn}(001)} - \frac{x}{2}E_{\text{In}_2\text{O}_3} - \left(y - \frac{3}{2}x\right)\mu_{\text{O}}}{(x+y)\,A} \tag{II.56}$$

where $E_{\text{In}_x\text{O}_y/\text{PdIn}(001)}$, $E_{\text{PdIn}(001)}$, and $E_{\text{In}_2\text{O}_3}$ are the total energies of the complete system, the bare PdIn(001) substrate, and the bulk In_2O_3 (space group $Ia\overline{3}$). This formalism does not consider a solid solution substitution of In atoms by Pd in the oxide since previous studies indicate that Pd is substantially more stable at the surface [19]. In addition, we should highlight that this equation is more suitable when compared with experiments where the thin film was transformed from the bulk oxide, in which a supply of In atoms are available [13], while it should be used with more care when the thin film is grown natively on the PdIn(001) surface.

II.1.4. Thermodynamic model for the $BaTiO_3$/Pt(111) system

II.1.4.1. Structures

One of the aims of our study is to assess the relative thermodynamic stability of supported oxide quasicrystal approximants (OQA) against the periodic systems with similar compositions. Hence, three types of structures are considered.

The 2D OQA series is studied using structural models derived from the one designed for $BaTiO_3$/Pt(111) [10]. According to a combination of scanning tunneling microscopy, low-energy electron diffraction, surface X-ray diffraction and ab initio calculations, it consists in a 3^2.4.3.4 Archimedean tiling, with Ti atoms at the corners of each tiling element and three-fold coordinated to oxygen atoms (Figure II.5). A wide variety of chemical compositions is considered herein, through atomic substitutions based on the $A_5B_4O_{12}$ chemical motif, with A = Ba, Sr and B = Ti, Fe, Co, Ni.

To evaluate the relative stability of the previous aperiodic-like single oxide layers against possible periodic arrangements, we considered a second model, which is an archetypal structure for 2D periodic ultra-thin oxide films. It consists of a single-layer hexagonal structured (SHS) B_2O_3, doped with alkali earth elements (A). Such a honeycomb structure, deposited on Me(111), has been experimentally observed for Ti_2O_3/Au(111) [77] (Figure II.5b). In contrast to the OQA model, the SHS model contains the A-element as a dopant. Thus, its content is much lower than the one of the B-element (AB_4O_6 is the surface cell motif).

The experimentally observed OQA structure of $BaTiO_3$/Pt(111) is prepared from Thick $BaTiO_3$ Perovskite Films (TPFs) grown by RF magnetron sputter deposition. [54] The TPFs are modelled here by 7 Å-thick films. TPFs films are built with the [*abc*] direction of the bulk crystal perpendicular to the Me(111) termination planes, with [*abc*]=[111] for cubic perovskites and [*abc*]=[100] for hexagonal perovskites (Figure II.5c–Figure II.5d). The simulation box contains two interfaces: Me/TPF and TPF/void. Since bulk perovskite crystals are described by a stacking of two types of planes along the [*abc*] direction — low-density pure B-element planes and AO_3 planes — several configurations are possible. We chose AO_3/Me and AO_3/void interfaces, because the atomic density of the AO_3 planes are much higher than the pure B-element ones.

II.1.4.2. Formation enthalpies

The formation energies of the freestanding and supported 2D oxides (ΔH_f^{free} and ΔH_f^{sup}, respectively), in both OQA and SHS configurations, are calculated for different compositions using the O_2 molecule and the elemental solids as references ($X \in \{\text{OQA, SHS}\}$), i.e.:

$$\Delta H_f^{\text{free}}(X) = E(A_xB_yO_z) - xE(A) - yE(B) - \frac{z}{2}E_{O_2} \tag{II.57}$$

and

$$\Delta H_f^{\text{sup}}(X) = \Delta H_f^{\text{free}}(X) + E(\text{Me}_w\text{Ba}_xB_yO_z) - E(\text{Ba}_xB_yO_z) - wE(\text{Me}) \tag{II.58}$$

where E is the total energy. The effect of the substrate–oxide interaction can be quantified through the adhesion energy ($E_{\text{adh}}(X)$), which can be calculated either from energy differences between the constituted oxide/metal system ($E(X/\text{Me})$) and its separated components — bare metal substrate ($E(\text{Me})$) and freestanding oxide single-layer at its equilibrium lattice parameter ($E(X)$) or it can be evaluated from a Born-Haber cycle:

$$E_{\text{adh}}(X/\text{Me}) = E(X/\text{Me}) - E(X) - E(\text{Me}) = \Delta H_f^{\text{sup}}(X/\text{Me}) - \Delta H_f^{\text{free}}(X) \tag{II.59}$$

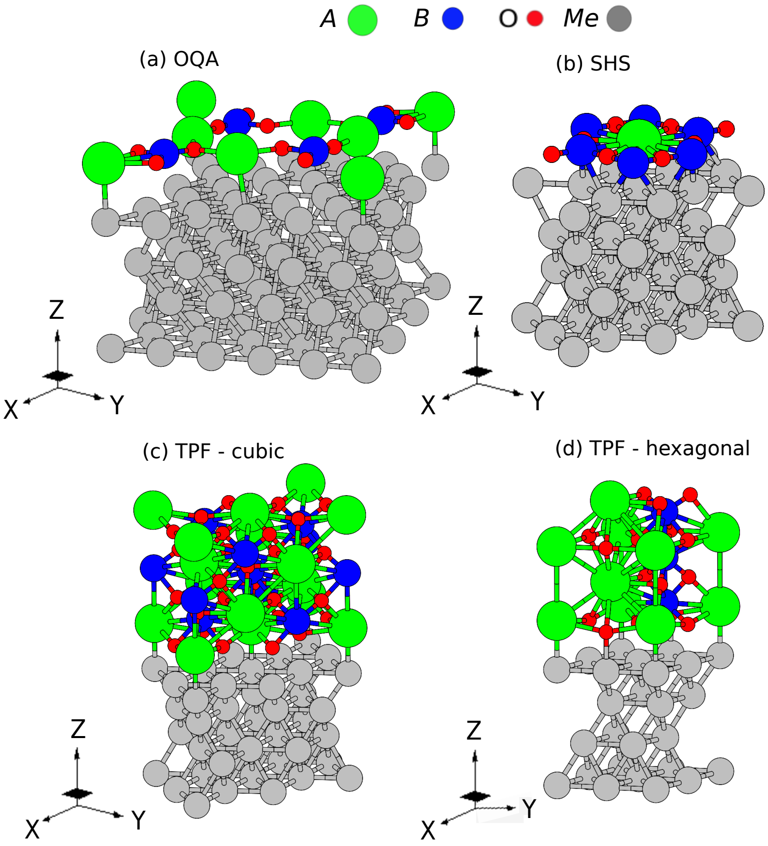

Figure II.5: Structural models for the oxide films grown on Pt(111), plotted using XCrySDen: [134] OQA (a), SHS (b), TPF built from the cubic perovskite structure (c) and TPF built from the hexagonal perovskite structure (d).

II.1.4.3. Gibbs free energies

The evaluation of the formation energy of OQAs is a necessary but not sufficient condition to assess the stability of the system. Thus, we calculate the OQAs formation enthalpies with respect to the competing periodic phases (SHSs, TPFs), taking into account the experimental conditions (pressure, temperature). Experimentally, $BaTiO_3$ TPF is first grown by RF magnetron sputter deposition [10], [54] and then the OQA is formed by annealing in ultrahigh vacuum (UHV). [11] By exposing the 2D OQA at elevated temperatures to O_2, a rapid transition back into 3D $BaTiO_3$ islands occurs. [11]

According to experiments, key parameters for the OQA and SHS formation includes the oxygen pressure, the temperature, and the number of annealing cycles. We evaluate the formation Gibbs free energies of the ABO_3 OQAs and SHSs for several compositions ($BaTiO_3$, $SrTiO_3$, $BaFeO_3$, $BaCoO_3$, $BaNiO_3$) by considering the following reactions:

$$n_{\mathrm{TPF}}\,\mathrm{TPF/Me} \longrightarrow n_{X/\mathrm{Me}}\,X/\mathrm{Me} + n_{\mathrm{Ba}B\mathrm{O}_3}\mathrm{Ba}B\mathrm{O}_3 + n_{\mathrm{O}_2}\mathrm{O}_2 + n_{\mathrm{Ba}}\mathrm{Ba} \tag{II.60}$$

$$\Delta G_{\mathrm{f}}^{X/\mathrm{Me}} = n_{X/\mathrm{Me}}\, E(X/\mathrm{Me}) + n_{\mathrm{Ba}B\mathrm{O}_3} E(\mathrm{Ba}B\mathrm{O}_3) + n_{\mathrm{O}_2}\mu_{\mathrm{O}_2} + n_{\mathrm{Ba}} E(\mathrm{Ba}) - n_{\mathrm{TPF}}\, E(\mathrm{TPF}) \quad \text{(II.61)}$$

This description was chosen, since it corresponds to the experimental setup in which the bulk perovskite and the oxygen partial pressure are controlled. The pressure is included in the model through the chemical potential of oxygen gas, accounting for only its rotational and translational contributions to the partition function.

III. Electronic structure analysis

III.1. Density of States (DOS)

The Density of States of a system if defined as $\rho(\epsilon)d\epsilon =$ number of states between ϵ and dϵ, and the integrated DOS $N(\epsilon_{\mathrm{i}})$ is given, at the energy range that the electrons are allowed to occupy, as:

$$N(\epsilon_{\mathrm{i}}) = \int_{-\infty}^{\epsilon_{\mathrm{i}}} \rho(\epsilon) d\epsilon \quad \text{(II.62)}$$

The DOS may be discrete (e.g. atoms and molecules) or continuous (e.g. metals), and a high DOS below the Fermi energy means that there are many states that are occupied.

III.2. Work function (Φ)

The *Work function* is defined as the minimum energy required to withdraw an electron from a metal to a point just outside it, which is directly related to how tightly the electrons are confined in the surface. It is a very important quantity for many different applications, such as photoelectronic devices and cathode-ray tubes.

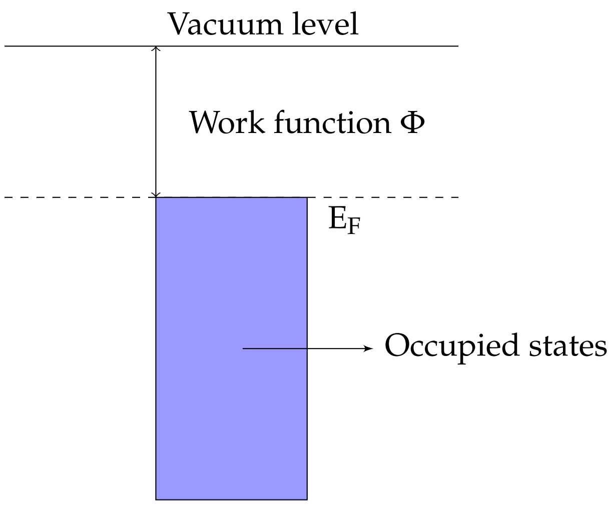

Figure II.6: Schematic energy diagram of a metal.

Figure II.6 shows a schematic representation on the energy diagram of a metal, in which the valence bands are filled with electrons up to the Fermi energy (E_F) and the work function corresponds to the energy difference between the vacuum level and E_F:

$$\Phi = V_\mathrm{el} - E_\mathrm{F} \tag{II.63}$$

where V_el is the electrostatic potential in the vacuum region.

III.3. Bader analysis

The task of assigning an oxidation state to an ion using computational chemistry codes is a challenging one, given that the charge is not an observable since the wave functions of electrons in a crystal are delocalized and multicentered. In other words, charges cannot be assigned for cases in which the electron density overlap, and it relies heavily on the choice of the model to partition the electron density between atomic centers [135]. The scheme proposed by Bader [136] uses the concept of zero flux surfaces[7] to divide atoms into Bader volumes, which are a good approximation of the total electronic charge of an atom. The zero flux property is expressed as:

$$\nabla\rho(\vec{r}) \cdot s(\vec{r}) = 0 \tag{II.64}$$

where $\nabla\rho(\vec{r})$ is the gradient of the charge density and $s(\vec{r})$ is the normal to the zero-flux surface.

---

[7] A zero flux surface is a 2-D surface on which the flux of the charge density perpendicular to the surface is zero.

The absolute values of calculated atomic charges based on any partition method should be always used carefully, because the calculated charge depends on the type of analysis and is never definitive. However, the relative charges in similar chemical environments are a good tool to discern trends.

The Henkelman group created an open source grid-based algorithm for the partition of the charge density based on the Bader method, which is the one used in the present work [137]–[140].

III.4. Modeling Scanning Tunneling Microscopy (STM) images

Describing the surface structure is one of the most fundamental problems in surface physics, and nowadays there are very precise techniques that can be used. Experimentally, the most common one is the *Scanning Tunneling Microscopy* (STM), and it is used to determine metallic surface structures in *real-space*. In this technique, a small tip is brought very close to the material's surface so that the electrons could tunnel from the surface to the tip (or vice-versa depending on the potential applied). By scanning the surface in two dimensions, one can obtain a contour map of the surface electronic structure containing valuable information about its structure.

To be able to quantitatively compare experimental results with DFT calculations, one of the most used method to calculate the STM images is called the Tersoff-Hamann approximation [141], [142], in which the tunneling current is proportional to the position of the tip and the surface local density of states (LDOS) around the Fermi level (E_F) at that position. It relies on the assumptions that the tip is punctual, modeled as a locally spherical potential with s-type wave functions, which has little interaction with the surface. Thus, it only considers the LDOS at states that fall between E_F and the applied bias potential. The equation that describes the tunneling current according to these assumptions is given by [141]:

$$I_\mathrm{t}(\mathbf{r}_0) \approx \frac{4\pi^2 e}{h}\rho_\mathrm{tip}(\epsilon_\mathrm{F}) \int_{\epsilon_\mathrm{F}}^{\epsilon_\mathrm{F}+V_\mathrm{b}} \rho_\mathrm{surf}(\mathbf{r}_0, \epsilon) d\epsilon \tag{II.65}$$

where ρ_tip are the tip electronic density, $\mathbf{r}_0$ its position, ρ_surf is the LDOS, ϵ_F is the Fermi level, and V_b is the bias applied between the surface and the tip.

III.5. Crystal Orbital Hamilton Populations (COHP)

It is a surprising challenge that computational chemistry faces when it comes to extracting chemical information from complex calculations. So far, one still needs to use *interpretational schemes* for molecular wave functions, since bonding descriptors cannot be unambiguously defined by quantum mechanics [24].

In molecules, the work by Mulliken showed how we can assign electrons to atomic centers and to bonds [143]. The bonding interactions between two atomic orbitals φ_μ and φ_ν (from a molecular orbital ϕ) is carried through the *overlap integral* $S_{\mu\nu}$. In addition, it was experimentally verified that shared electrons can be seen as a measure of the bond strength (or *bond energies*) for small molecules [144], [145].

But how to translate the theory for molecules to crystals? For historical reasons, solid-state theory has been concerned with metals in Drude's model, in which bonding is assumed to be metallic, i.e. highly delocalized. However, it has been shown that local bonding characteristics are extremely important, leading to the idea that compounds can be treated as large molecules [146].

In order to deal with bonds in crystals, a tool was developed by Hughbanks and Hoffmann [147], [148] in which the Mulliken's overlap population technique is applied to the crystal once its electronic band structures has been calculated, investigating the bonds within a certain energy interval. In this way, they defined the overlap population-weighted DOS, in which all pairwise orbital interactions between two atoms are evaluated by the product of the DOS matrix elements and the overlap matrix. This method is called *Crystal Orbital Overlap Population* (COOP). Another analogous method to study orbital interactions is called *Crystal Orbital Hamilton Population* (COHP), and was introduced by Dronskowski and Blöchl [24]. The concept is similar to the COOP, still based on the extended Hükel theory [148], but the COHP partition the band-structure energy in terms of orbital-pair contributions. The interaction between two atomic orbitals μ and ν, centered at neighboring atoms, is given by their Hamiltonian matrix $H_{\mu\nu} = \langle \psi_\mu | \hat{H} | \psi_\nu \rangle$, and by its multiplication with the corresponding DOS matrix results in a measure of bonding strength [149].

In our DFT calculations, all the wavefunction information is stored in the form of plane waves, which is not useful for COHP analysis because this method requires a local description of the electronic structure in terms of atom-centered orbitals [150]. Nonetheless, we can reconstruct the electronic wavefunction and regain its locality by projecting it onto a suitable local auxiliary basis [151]–[156].

In this work, electronic structures were calculated using a plane-wave basis set and a fine-meshed **k**-points in reciprocal space within Bloch's theorem. In the end, we have the band functions $\psi_j(\vec{k},\vec{r})$ (j is the band number). Any band function is expressed as:

$$\psi_j(\vec{k},\vec{r}) = \sum_{\vec{G}} C_{j\vec{G}}(\vec{k}) \exp\left\{ i(\vec{k}+\vec{G})\cdot\vec{r} \right\} \tag{II.66}$$

where $\vec{G}$ are the reciprocal lattice vectors and $C_{j\vec{G}}(\vec{k})$ are the expansion coefficients. The idea is to transform these plane waves into a linear combination of atomic orbitals (LCAO), which, in the end, have the same information. Such a $\vec{k}$-dependent LCAO function $\Phi_j(\vec{k},\vec{r})$ for the jth band can be written as a combination of normalized atom-centered one-electron functions $\psi_\mu(\vec{r})$ with coefficients $c_{j\mu}(\vec{k})$:

$$\Phi_j(\vec{k},\vec{r}) = c_{j\mu}(\vec{k})\psi_\mu(\vec{r}) + c_{j\nu}(\vec{k})\psi_\nu(\vec{r}) + \cdots \approx \psi_j(\vec{k},\vec{r}) \tag{II.67}$$

The overlap matrix between the local orbitals $\langle\phi_\mu|$ and the band functions can be calculated as:

$$T_{j\mu}(\vec{k}) = \langle\psi_j(\vec{k})|\phi_\mu\rangle \tag{II.68}$$

$T(\vec{k})$ is called the *transfer matrix*.

The chemical information, when using plane waves, is stored in the transfer matrix, while in the LCAO it is directly extracted from the atomic orbital coefficients c, and by multiplying c_μ and c_ν we get the density-matrix element $P_{\mu\nu}$. Thus, we can calculate the projected density matrix P^{proj} for every $\vec{k}$ point and band j as:

$$P^{\text{proj}}_{\mu\nu j}(\vec{k}) = T^*_{j\mu}(\vec{k})T_{j\nu}(\vec{k}) \tag{II.69}$$

Finally, we need to be able to express the Hamiltonian matrix elements $H_{\mu\nu}(\vec{k})$ in the local functions' basis, which is written as [157]:

$$H^{\text{proj}}_{\mu nu}(\vec{k}) = \sum_j \epsilon_j P^{\text{proj}}_{\mu\nu j}(\vec{k}) \tag{II.70}$$

Therefore, the projected crystal orbital Hamilton population (pCOHP) is [149]:

$$\text{pCOHP}_{\mu\nu}(E,\vec{k}) = \sum_j \text{Re}\left[P^{\text{proj}}_{\mu\nu j}(\vec{k}) H^{\text{proj}}_{\mu nu}(\vec{k}) \right] \times \delta(\epsilon_j(\vec{k}) - E) \tag{II.71}$$

where δ is the delta function.

The method described above is implemented in the LOBSTER code [25], which can work directly from the electronic-structure output from several *ab initio* softwares, such as VASP, Quantum ESPRESSO, and ABINIT. In addition to the COHP and COOP discussed above, LOBSTER can also output the Mulliken and Löwdin population analysis.

To proceed with the Mulliken population analysis, the gross orbital population GP_μ can be written, in terms of the density-matrix formalism, as:

$$\mathrm{GP}_\mu = \sum_k \sum_\nu P_{\mu\nu}(\mathbf{k}) S_{\mu\nu}(\mathbf{k}) w(\mathbf{k}) \tag{II.72}$$

where $w_\mathbf{k}$ is the $\mathbf{k}$-point weight and $S_{\mu\nu}(\mathbf{k})$ is the overlab matrix element between two different orbitals.

In Löwdin's approach, the symmetric orthogonalization,

$$\chi'_k = \mathbf{S_k}^{-1/2} \chi_k, \tag{II.73}$$

$$\mathbf{C'_k} = \mathbf{S_k}^{-1/2} \mathbf{C_k} \tag{II.74}$$

where $S_\mathbf{k}$ is applied to the j-band Slater-type orbitals, $\chi_{j\mathbf{k}}$, and to their linear combination coefficients, $C_{j\mu\mathbf{k}}$, using the following relation:

$$\left|\Psi'_{j\mathbf{k}}\right\rangle = \sum_\mu C'_{j\mu\mathbf{k}} \left|\chi'_{j\mathbf{k}}\right\rangle \tag{II.75}$$

In this manner, one have calculated the Löwdin charge q_A for all atoms from the difference of the number N_A of the atom's valence electrons and the gross atomic population (GP) of orbitals μ belonging to a given atom A:

$$q_A = N_A - \sum_{\mu \in A} \mathrm{GP}_\mu, \tag{II.76}$$

with the Löwdin gross orbital population as

$$\mathrm{GP}_\mu = \sum_\mathbf{k} P_{\mu\mu}(\mathbf{k}) w(\mathbf{k}) \tag{II.77}$$

where $P_{\mu\mu}(\mathbf{k})$ is the $\mathbf{k}$-dependent density matrix element obtained from the new basis set $\chi'_\mathbf{k}$.

By using these analyses in complement with the COHP, one can have a more complete understanding of the charge distribution in the system under consideration when used in combination with the Bader charge analysis.

IV. Other methods for structure investigations

IV.1. Molecular Dynamics (MD)

From the moment that computers reached enough availability and speed in the early 90's, researchers have developed several techniques, translated into computer code, that would help simulate the behavior of atoms and molecules as a function of time in many different systems and environments. In this context, Molecular Dynamics was developed following the success of other techniques such as Monte Carlo (MC) simulations [158], which nowadays can be seen as two very powerful complementary tools. The main difference between these two methods is that the latter involves determining micro and macroscopic properties from the average of different representative configurations of the system under consideration, while the former uses time-based integration to determine these properties [159].

MD simulations, at their core, can be used to determine the time-averaged microscopic properties (forces, atomic positions, velocities, etc.) of a classical system, and can be translated into useful macroscopic properties (temperature, pressure, etc.) by using the statistical mechanics. Therefore, by determining the atoms' positions and momenta (i.e. phase space), it is possible to determine an observable property (O) as a function of the phase space (Γ) as the time average of many instantaneous values of O:

$$O = \langle O \rangle_{\text{time}} = \langle O\left(\Gamma\left(t\right)\right)\rangle_{\text{time}} = \lim_{t_{\text{obs}}\to\infty} \frac{1}{t_{\text{obs}}} \int_0^{t_{\text{obs}}} O(\Gamma(t))dt \tag{II.78}$$

It is known in thermodynamics that we can determine the state of a specific system by a small set of parameters, such as the temperature T, pressure P, and number of particles N. All the other thermodynamic properties of the system, once completely defined, can be derived through the fundamental equations of thermodynamics. As a result, the complete thermodynamic state is defined by a small number of variables (e.g. NPT), which in turn can be determined once a sufficient region of the phase space is sampled. Here lies one key parameter of any MD simulation. The fact that we cannot run the simulation for an infinite time leads us to choose a reasonable amount of finite time τ_{obs} to average the observable on. Consequently, we solve the equations of motion for the atoms in a step-by-step manner with a large finite number τ_{obs} of time steps of length $\delta t = t_{\text{obs}}/\tau_{\text{obs}}$:

$$O_{\text{obs}} = \frac{1}{\tau_{\text{obs}}} \sum_{\tau=1}^{\tau_{\text{obs}}} O(\Gamma(\tau)) \tag{II.79}$$

In practice, we always need to question if a sufficient region of the phase space can be sampled in a specific chosen time τ_{obs} to yield suitable time averages in a reasonable computer time and if we get thermodynamic consistency when comparing the macroscopic parameters obtained in the same system but with different initial conditions.

The most current tool to solve Newton's equations of motion for our purposes is through finite-difference approach. By determining the microscopic dynamic properties (velocities, positions, etc.) at a specific time t, we want to calculate these properties for a later time $t + \delta t$, within a reasonable accuracy. There are many ways to perform such task, but by far the most used method is the Verlet algorithm, due to its simplicity, accuracy and speed [160]. The Verlet algorithm is written in three steps:

$$\mathbf{v}\left(t + \tfrac{1}{2}\delta t\right) = \mathbf{v}\left(t\right) + \tfrac{1}{2}\delta t \mathbf{a}\left(t\right) \tag{II.80}$$

$$\mathbf{r}\left(t + \delta t\right) = \mathbf{r}\left(t\right) + \delta t \mathbf{v}\left(t + \tfrac{1}{2}\delta t\right) \tag{II.81}$$

$$\mathbf{v}\left(t + \delta t\right) = \mathbf{v}\left(t + \tfrac{1}{2}\delta t\right) + \tfrac{1}{2}\delta t \mathbf{a}\left(t + \delta t\right) \tag{II.82}$$

At the end of each step, it is possible to calculate many quantities such as the total momentum vector or the kinetic energy.

When performing a MD simulation in molecular systems there is another important parameter that needs to be addressed, which is the atomic intra- and inter-molecular forces. When treating the system empirically (i.e. without quantum mechanics), one needs to be sure to select a potential that describes correctly these interactions with reasonable accuracy, so that the final phase space is properly sampled. The complexity of the potential vary according to the complexity of the system itself, and there is very limited transferability of potentials between different systems, since the interactions may vary greatly from system to system.

IV.1.1. *Ab Initio* Molecular Dynamics (AIMD)

Despite the outstanding success of traditional MD methods [161], [162], the fact that it is based on a fixed potential has always caused serious problems for chemically complex systems for two main reasons:

- The types of bondings for these systems have big qualitative changes during the simulation.
- With many different types of atoms and molecules, there are a big amount of interatomic interactions that need to be taken into account and parameterized;

In this work, we used the Born–Oppenheimer *ab initio* molecular dynamics [163], where the forces are calculated by minimizing the KS energy functional at each time step. This minimization must be carried out at a high level of accuracy.

IV.2. Genetic Algorithms

In materials science there are four components that are essential in the development of new materials or improvement of existing ones, which are *processing*, *structure*, *properties*, *performance* (Figure II.7). The way in which a material is processed has a direct relationship with the structure that will be obtained. For a given processed material, its properties (e.g. mechanical, electrical, thermal, magnetic, and optical) are due to its structure, and will finally affect the material's performance [164].

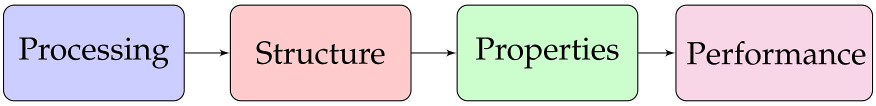

Figure II.7: The four components of materials science and engineering.

Here we will focus on the *structure* of a material and its direct relationship with its properties. With this perspective, one very interesting concept is that if we were able to predict the crystal structure of a given material before it is synthesized, it would be possible to discover very quickly new materials with specific desired properties. This would be extremely useful specially for the study of materials at extreme conditions, where experimental information is difficult to obtain.

Finding the most stable atomic configuration for a given composition has been one of the most challenging unsolved scientific problems. In his famous paper, Maddox said: "One of the continuing scandals in the physical sciences is that it remains in general impossible to predict the structure of even the simplest crystalline solids from a knowledge of their chemical composition". The sheer number of possible structures, even for a small number of atoms, makes it an impossible problem to be overcome by trial and error, becoming essential to develop techniques that are able to search and rank the best structures. There were many methods that have been developed to tackle this problem, like simulated annealing, metadynamics, random sampling, basin hopping, minima hopping, and data mining [165]. Recently, one of the most popular method for Crystal Structure Prediction (CSP) is called the hybrid evolutionary algorithm USPEX (Universal Structure Predictor: Evolutionary Xtallography).

To put the problem in perspective, the number of possible distinct structures for a given number of atoms N and a unit cell with volume V is given by:

$$C = \binom{V/\delta^3}{N} \prod_i \binom{N}{n_{\mathrm{i}}} \tag{II.83}$$

where δ is the discretization parameter and n_{i} is the number of atoms of ith type in the unit cell.

Even for small systems ($N \approx 20$), the value of C is astronomical, in the order of 10^{N} for $\delta = 1$ Å and $V = 10$ Å^3. Another interesting parameter to consider is the dimensionality of the energy landscape, which is given by:

$$d = 3N + 3 \tag{II.84}$$

where six dimensions are attributed to the lattice parameters and $3N - 3$ for the atomic positions. For the same example described above, the number of dimensions is 63. With such high-dimensional problem, one can clearly see that exhaustive search methods are impossible to conduct.

There are a number of software packages available for crystal structure prediction, such as CALYPSO [166], USPEX [167], minima hopping method for Lennard-Jones [168], and more recently a Python implementation in the Atomic Simulation Environment (ASE) [169]. In this work, we have chosen to work with USPEX due to the large success rate and extense documentation.

IV.2.1. The USPEX method

In the USPEX method [165], [167], [168], [170]–[173], the population of a structure with a given composition evolves by trying to reach the most promising regions (local minima) of the energy landscape. The success of this algorithm comes from three aspects:

1. The global optimization problem is combined with structure relaxations, correcting the atomic position and avoiding unfavorable interactions. Modern *first principles* codes such as VASP or Quantum ESPRESSO can be used to perform these atomic relaxations and calculate the total energy of the system, which is the property used to determine the best structures.

2. The structures of a given generation bear resemblance from the more successful structures of the previous generation by selecting those that have the lowest energy or by

using variation operators (algorithms that modify the best parent structures to create child ones).

There are four variation operators used in USPEX:

- *Heredity:* Two structures are used to create a new candidate, and it is achieved by creating child structures from cuts on planar slabs of two parent structures [167];
- *Mutation:* Random deformation to the shape of the unit cell;
- *Permutation:* Two atoms of different types are exchanged a specific number of times (this can be done only for systems with more than one type of atom);
- *Special coordinate mutations:* Specific atomic displacement according to the chemical environment.

3. The search in the energy landscape should be the as diverse as possible, allowing a good sampling of all the local minimum.

More specifically, the USPEX method is described by the following procedure: (1) The first generation structures are produced randomly, only satisfying the user input constraints. User-provided structures (called *seeds*) can also be used. (2) The structures are ranked by comparing their total energies. The worst ones are rejected and the best ones are used in the variation operators to create child structures for the next generation. (3) The simulation ends when the halting criterion is met.

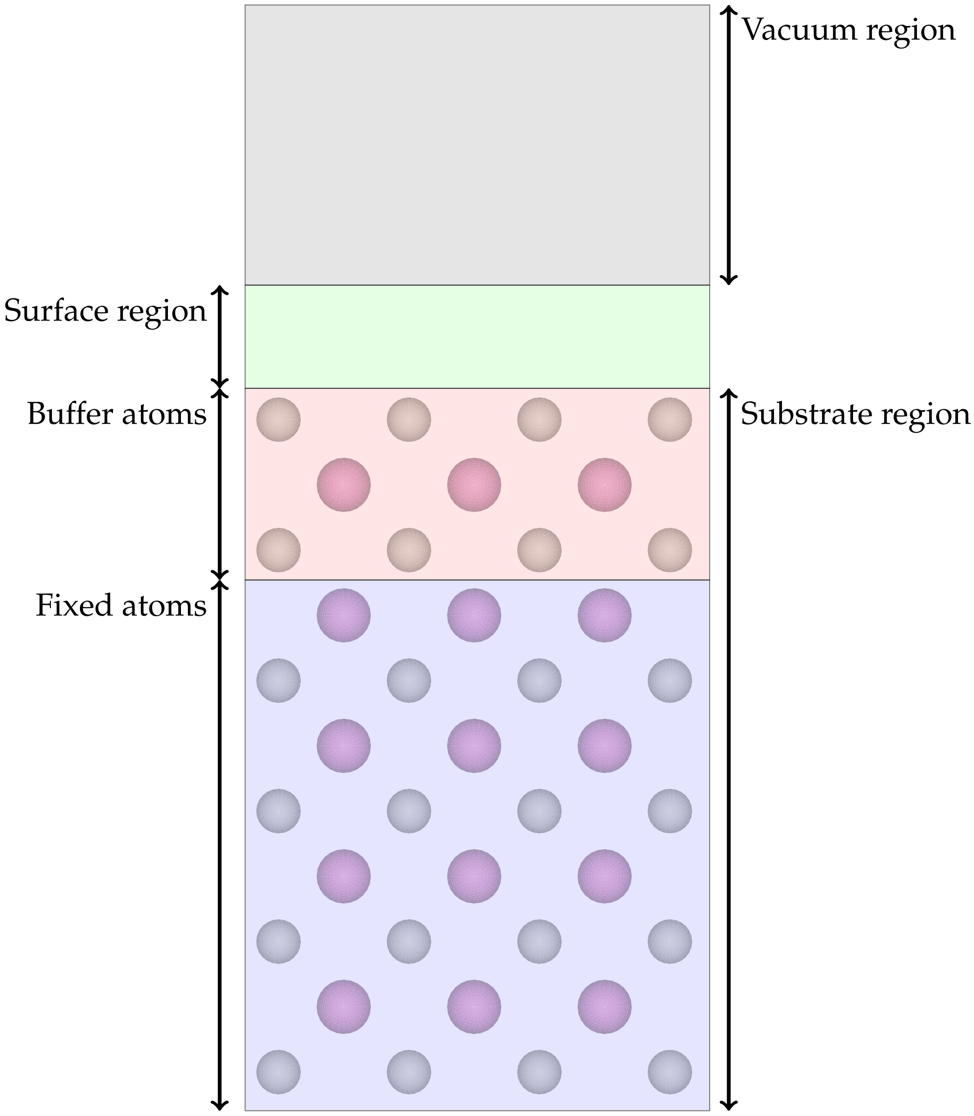

Figure II.8: Surface model used as input for the USPEX code. The four distinct regions are represented on a 1x3 supercell of PdIn bulk intermetallic (space group $Pm\overline{3}m$).

For a surface calculation in USPEX, there are certain regions that we need to define. Figure II.8 show a schematic representation of each region using as a substrate the PdIn bulk structure (space group $Pm\overline{3}m$, 1x3 supercell, 11 layers). The "Substrate" region is composed of the "Buffer" and "Fixed" regions, in which the atoms are allowed to relax and are fixed, respectively. The "Surface" region is where USPEX will input the In and O atoms according to the variation operators used. This region is constrained within 3 Å, and the "Vacuum" region is set to 20 Å to avoid a surface interaction with the fixed atoms due to periodic boundary conditions.

V. Vulcan launching program

For Chapter V, after the selection of the best In_xO_y oxide structures by USPEX, we have developed a Python code to optimize and automate all subsequent calculations (finer relaxation, adhesion energies, charge analysis, simulated STM images, density of states, etc.). An initial version of the code is available at https://github.com/DoriniTT/Vulcan.git and a simple manual at https://vulcan-a-vasp-launcher-code.readthedocs.io/en/latest/. It was developed to work exclusively on VASP (for now) and in a remote supercomputer cluster with a queue system, and makes heavy use of the Atomic Simulation Environment (ASE) [174].

Even though this script can launch any type of calculation performed by VASP, it was created, in this early stage of development, to solve the problems found by the authors. Therefore, the focus of this code are 2D structures consisting of two slabs of diffent materials. Its usage heavily on the user programming experience to adapt the code to their own problems.

The flowchart in Figure II.9 shows a schematic representation of how the code works. Three initial steps need to be defined as follows: (1) The code takes as initial input a list containing the ASE-Atoms objects that one intends to study. The user can use any available method to construct structures, but at the end the structures must be converted to the Atoms objects. (2) Configure the VASP calculator according to the input structures and the type of calculation that it is intended to be performed. Keywords that are dependent on the type of calculation, such as number of ionic steps, construction of the charge density, projection of atomic orbitals, etc., are automatically adopted depending on what calculation the user wants to perform, and only those parameters that are system dependent, such as how to determine the partial occupancies, size of the plane-wave basis set, dipol correction, etc., are kept fixed. The *k*-point grid is determined automatically depending on the size of the system, but one can also set it manually. (3) Configure the job script to work with the queue system of a cluster where calculations will be performed. All these three steps are detailed in the manual.

After defining the inputs, the user can define all the calculations intended, which will run in parallel for each structure whereas the calculations performed on each structure run sequentially one after the other. If all calculations finish correctly, the code makes a backup of some selected important files in the $HOME folder for postprocessing. If one has identified that some of the calculations have not finished well, simply running the vulcan script again will restart those calculations.

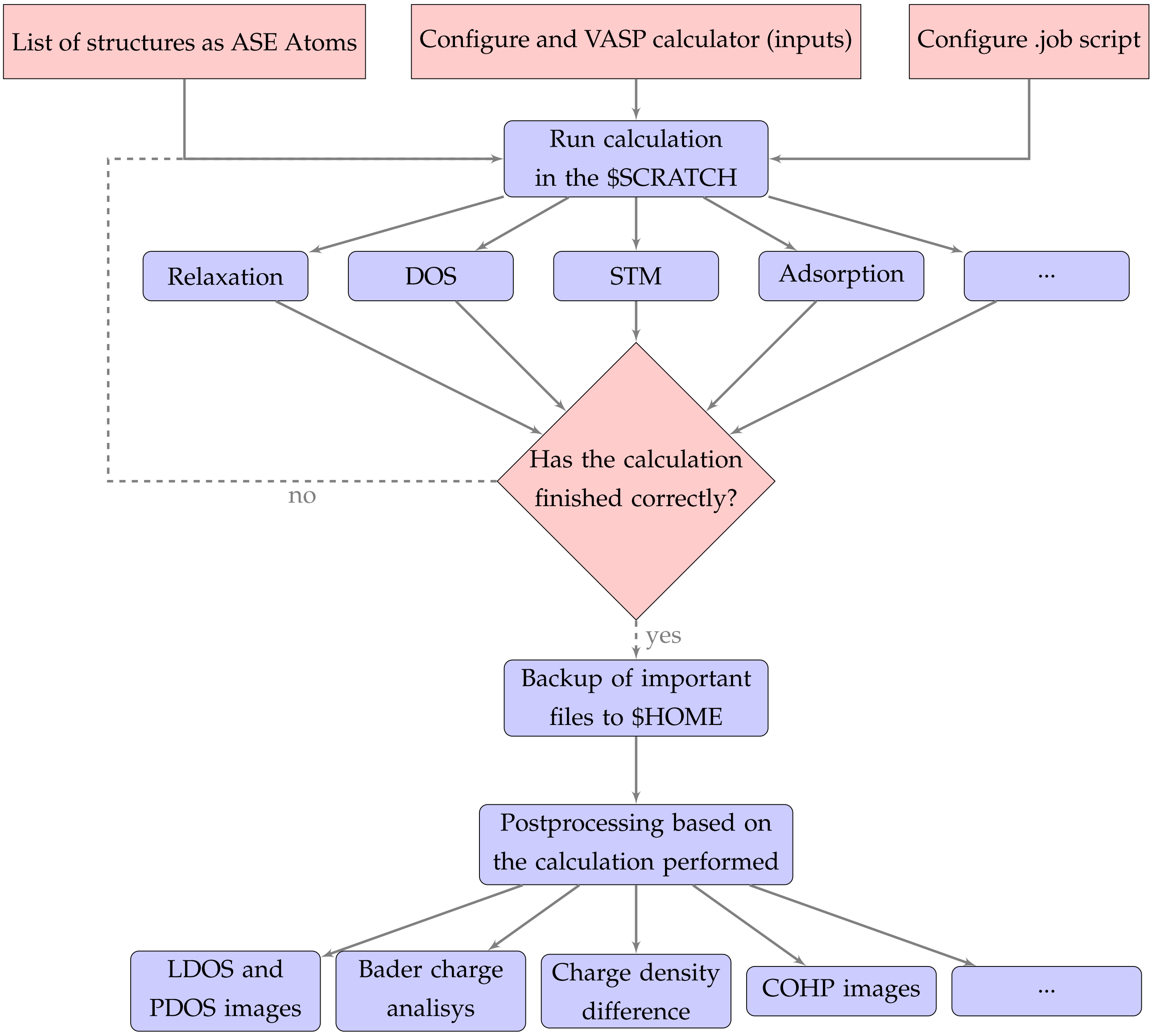

Figure II.9: Flowchart with the steps performed by the Vulcan code.

At the end, with all important files gathered, there are several implemented functions to analyze the outputs, such as the Bader charge analysis, charge density difference, DOS, COHP, etc., and can be easily adapted depending on user's preference.

VI. Conclusion

This chapter introduced Density Functional Theory and several theoretical methods (all within DFT) that are used throughout this work. We started from a basic description on how to obtain the Kohn-Sham equations and on their implementation in *ab initio* codes such as VASP. The second major part of this chapter was dedicated to different methods that can be used to extract relevant information regarding thin-films and the analysis of their electronic structure.

56

Chapter III

Ultra-thin films of quasi-periodic oxides: σ phases

I. Introduction

In this chapter, we will present our results regarding the σ phases in the (Ba/Sr)–Ti–O/Pt(111) system and extend them to some other compositions for comparing properties such as adhesion energies, enthalpies of formation, charge distribution, etc. This chapter is divided into two main parts. The first is the determination of general properties and the stability of the approximant phase suggested by Förster et al. [10] with the Ti atoms at the protrusions in the STM images, identifying also at what experimental conditions this type of approximant could form when compared to the perovskite structure. The second part is the study of the σ-phase now using the Cockayne's tiling configuration with the Ba/Sr atoms at the protrusions of the STM.

II. σ-approximant (Förster's model)

II.1. Structures

One of the aims of our study is to assess the relative thermodynamic stability of supported Oxide Quasicrystal Approximants (OQA) against the periodic systems with similar compositions. Hence, three types of structures are considered.

The 2D OQA series is studied using structural models derived from the one designed for $BaTiO_3$/Pt(111) [10]. According to a combination of scanning tunneling microscopy, low-energy electron diffraction, surface X-ray diffraction and *ab initio* calculations, it consists in a

$3^2.4.3.4$ Archimedean tiling, with Ti atoms at the corners of each tiling element and threefold coordinated to oxygen atoms (Figure II.5a). A wide variety of chemical compositions is considered herein, through atomic substitutions based on the $A_5B_4O_{12}$ chemical motif, with A = Ba, Ca, Sr and B = Ti, V, Cr, Mn, Fe, Co, Ni.

To evaluate the relative stability of the previous aperiodic-like single oxide layers against possible periodic arrangements, we considered a second model, which is an archetypal structure for 2D periodic ultra-thin oxide films. It consists of a single-layer hexagonal structured (SHS) B_2O_3, doped with alkali earth elements (A). Such a honeycomb structure, deposited on Me(111), has been experimentally observed for Ti_2O_3/Au(111) [77] (Figures II.5b). In contrast to the OQA model, the SHS model contains the A-element as a dopant. Thus, its content is much lower than the one of the B-element (AB_4O_6 is the surface cell motif).

The experimentally observed OQA structure of $BaTiO_3$/Pt(111) is prepared from Thick $BaTiO_3$ Perovskite Films (TPFs) grown by RF magnetron sputter deposition [54]. The TPFs are modeled here by 7 Å-thick films. TPF films are built with the [abc] direction of the bulk crystal perpendicular to the Me(111) termination planes, with [abc]=[111] for cubic perovskites and [abc]=[100] for hexagonal perovskites (Figures II.5c–II.5d). The simulation box contains two interfaces: Me/TPF and TPF/void. Since bulk perovskite crystals are described by a stacking of two types of planes along the [abc] direction — low-density pure B-element planes and AO_3 planes — several configurations are possible. We chose AO_3/Me and AO_3/void interfaces, because the atomic density of the AO_3 planes are much higher than the pure B-element ones.

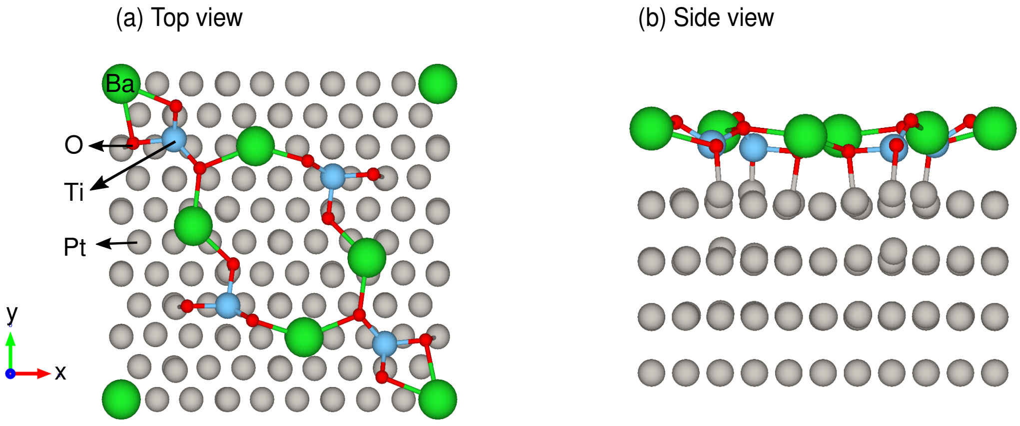

Figure III.1: Top and side views of the relaxed $BaTiO_3$/Pt(111) structure. These images were produced using the VESTA software [175].

II.2. Specific Computational Methods

All calculations were performed with Density Functional Theory (DFT) using the Vienna *ab initio* simulation package (VASP) [89]–[91] combined with the Atomic Simulation Environment (ASE) [174]. Spin-polarised calculations were performed with plane-wave basis set and projector-augmented wave (PAW) method, [115]–[117]. using the optPBE functional [110], [176]. The following electrons were treated explicitly: $5s^2 5p^6 6s^2$ (Ba), $4s^2 4p^6 5s^2$ (Sr), $3s^2 3p^6 4s^2$ (Ca), $2s^2 2p^4$ (O), $3s^2 3p^6 4s^2 3d^4$ (Ti), $3p^6 3d^4 4s^1$ (V), $3p^6 3d^5 4s^1$ (Cr), $3p^6 4s^2 3d^7$ (Mn), $3d^7 4s^1$ (Fe), $3d^8 4s^1$ (Co), $3d^9 4s^1$ (Ni), $5d^9 6s^1$ (Pt), $4s^1 3d^9$ (Pd), $4s^1 3d^{10}$ (Au). The strong on-site Coulomb interaction of localized electrons was treated through the GGA+U approach [114], using the values for U from the literature [27], [177]: 1.0 eV (Ti), 1.7 eV (V), 3.0 eV (Cr, Fe), 4.3 eV (Mn, Co, Ni). These values differ from that of the bulk oxide [178], but give very convergent descriptions of the electronic structure of both freestanding and supported honeycomb layer, according to a comparison with the results obtained using the hybrid HSE03 exchange-correlation functional [27], [75]. The one-electron Kohn-Sham orbitals were expanded in a plane-wave basis set with a kinetic energy cutoff of 500 eV. Total energies were minimised until the energy differences were less than 10^{-5} eV between two electronic cycles. The reciprocal space integration was approximated with a Monkhorst-Pack k-point grid of 3×3×1 and 6×6×1 (surface cell 14.11 Å × 14.66 Å, built from the calculated bulk Pt with lattice constant of 3.99 Å) for the structural relaxations and the density of state calculations for the approximant structures, respectively. For the cubic perovskites and honeycomb slabs we used a 8×4×1 (surface cell 5.64 Å × 9.76 Å) respectively, and 8×8×1 (surface cell 5.64 Å × 5.64 Å) for the hexagonal perovskite slabs.

The $AB\mathrm{O}_3$/Me(111) systems have been built using 5-layer thick asymmetric slabs consisting of four Me(111) layers and one oxide-layer with the approximant structure shown in Figure III.1 and detailed in [10]. Adjacent slabs (along the surface normal direction) were separated by 20 Å of vacuum and a dipole correction was applied to cancel an artificial electric field that develops due to imposed periodic boundary conditions in surface normal direction. All atomic positions, with the exception of the bottom layer of Me, were relaxed using the Conjugate Gradient Algorithm until all forces were less than 0.05 eV/Å^2 (Pt and Pd substrates) and 0.1 eV/Å^2 (Au substrate). The previous set-up gives cohesive energies and lattice parameters of bulk systems in good agreement with the experimental data (Tables III.1 and III.2).

Metal	Structure	a (Å)	c (Å)	Cohesive energy (eV/at.)	Ref.
Ba	bcc ($Im\bar{3}m$)	4.99		−1.91	this work
		5.03		−1.88	PBE [179]
		5.01		−1.91	exp. [180], [181]
Sr	fcc ($Fm\bar{3}m$)	6.02		−1.57	this work
		6.02		−1.62	PBE [179]
		6.08		−1.73	exp. [181], [182]
Ti	hcp ($P6_3mmc$)	2.93	4.64	−5.17	this work
		2.95	4.68	−5.47	PBE [179], [183]
		2.93	4.67	−5.45	PBE [184]
		2.95	4.68	−4.85	exp. [181], [182]
V	bcc ($Im\bar{3}m$)	2.98		−5.45	this work
		3.00		−5.92	PBE [179]
		2.98		−6.03	PBE [184]
		3.03		−5.31	exp. [181], [182]
Fe	bcc ($Im\bar{3}m$)	2.83		−4.97	this work
		2.83		−4.32	PBE [184]
		2.83		−4.85	PBE [179]
		2.86		−4.28	exp. [181], [182]
Co	hcp ($P6_3mmc$)	2.50	4.02	−4.89	this work
		2.49	4.01	−4.44	PBE [184]
		2.50	4.09	−5.14	PBE [179]
		2.51	4.07	−4.39	exp. [181]
Ni	fcc ($Fm\bar{3}m$)	3.53		−4.75	this work
		3.52		−4.48	PBE [184]
		3.52		−4.83	PBE [179]
		3.92		−4.44	exp. [181], [182]
Pt	fcc ($Fm\bar{3}m$)	3.99		−5.63	this work
		3.95		−5.87	PBE [184]
		3.98		−5.32	PBE [179]
		3.92		−5.84	exp. [181], [182]
Au	fcc ($Fm\bar{3}m$)	4.18		−3.18	this work
		4.17		−3.83	PBE [184]
		4.16		−3.11	PBE [179]
		4.07		−3.81	exp. [181], [182]

Table III.1: Lattice parameters, space groups, cohesive energies of the metals taken as references to calculate the formation enthalpies of OQAs and SHSs.

Perovskite	Structure	a (Å)	b (Å)	c (Å)	Formation enthalpy (eV/at.)	Ref.
$BaTiO_3$	$Pm\bar{3}m$	4.05			-3.35	this work
	$R3m$	4.08 (α=89.67°)			-3.50	PBE [50]
$SrTiO_3$	$Pm\bar{3}m$	3.96			-3.38	this work
	$Pm\bar{3}m$	3.94			-3.56	PBE [50]
$BaFeO_3$	$Pm\bar{3}m$	4.01			-2.07	this work
	$Pm\bar{3}m$	4.03			-2.25	PBE [50]
$BaCoO_3$	$Cmcm$	5.70	9.99	4.81	-1.83	this work
	$P6_3mmc$	5.74		5.77	-2.11	PBE [50]
$BaNiO_3$	$P6_3mmc$	5.71		4.80	-1.48	this work
	$P6_3mmc$	5.72		4.83	-1.48	PBE [50]

Table III.2: Lattice parameters, space groups, and formation enthalpies of perovskites considered in the thermodynamic model.

II.3. Adhesion energies

Adhesion is favoured in all cases ($E_{\mathrm{adh}} < 0$), although it is much weaker for OQA arrangements than for SHSs (Table III.3). It ranges from -0.082 eV/Å^2 ($BaTiO_3$/Pt OQA) to -0.033 eV/Å^2 ($BaNiO_3$/Au OQA) and from -0.435 eV/Å^2 ($BaTiO_3$/Pt SHS) to -0.128 eV/Å^2 ($BaCoO_3$/Au SHS). This trend is consistent with the fact that B metals in SHSs are all located in favourable threefold adsorption sites on Me, because the dense surface of close-packed Me and the SHSs are both periodic and commensurate. In contrast, the approximant structure makes it unmanageable to locate all B metals of OQAs in the favourable hollow sites of the substrate, thus weakening adhesion.

Irrespectively of the substrate and alkaline earth element (A = Ba, Sr, Ca), adhesion is systematically stronger for oxide films from the beginning of the transition metal series (Ti, V). In addition, adhesion does not seem to vary significantly in the OQA with different substrates or alkali earth elements (A). Nonetheless, the change of the substrate in the SHS from Pt to Au results in a clearly stronger interaction with Pt, as also shown in the work by Goniakowski and Noguera [75]. Adhesion is impacted by both the strength of the direct metal–oxide interaction at the interface and the elastic strain of the freestanding single-layer, necessary to match its in-plane lattice parameter with the metal substrate. The contribution from elastic strain, non favourable for adhesion, is calculated from the energy difference between the strained and freestanding single-layer. Elastic strain is alleviated by the film rumpling. This has been checked using the freestanding layer of the $BaTiO_3$ OQA, for which the contributions of the elastic strain (30 meV/at.) is much lower than that of the rumpling (152 meV/at.).

II.4. Gibbs free energies

Within the standard DFT approach, and considering the stable perovskite bulk structures, the formation Gibbs free energies ($\Delta G_\mathrm{f}^{\mathrm{OQA/Me}}$) are all positive, in the range from 0.15 eV/at. to 0.19 eV/at, and 0.07 eV/at. to 0.11 eV/at. for Pt and Au as substrates, respectively, at $T = 300$ K and $P = 10^{-10}$ mbar. Note that we are dividing by the total number of atoms in the slab, thus our results are comparable when the oxide is supported on four layers of substrate. These results mean that the formation of single-layer oxide films is not likely under these conditions. Instead, the growth of thick $BaBO_3$ perovskite layers is predicted. This is in agreement with the experimental results, which report a $BaTiO_3$(111)–(1×1) structure on Pt(111)–(2×2), observed by Low Energy Electron Diffraction [54].

	OQA					SHS				
A	Ba	Sr	Ba	Ba	Ba	Ba	Sr	Ba	Ba	Ba
B	Ti	Ti	Fe	Co	Ni	Ti	Ti	Fe	Co	Ni
	Freestanding layer					Freestanding layer				
$\Delta H_\mathrm{f}^{\mathrm{free}}$	−2.02	−2.04	−1.14	−1.12	−0.84	−1.05	−1.20	0.00	−0.39	0.38
	Pt substrate					Pt substrate				
E_{adh}	−0.082	−0.075	−0.051	−0.068	−0.051	−0.435	−0.403	−0.209	−0.157	−0.152
$\Delta H_\mathrm{f}^{\mathrm{sup}}$	−0.42	−0.41	−0.24	−0.26	−0.20	−0.84	−0.84	−0.28	−0.31	−0.11
ΔG_f	+0.12	+0.13	+0.15	+0.15	+0.13	+0.46	+0.48	+0.43	+0.43	+0.41
	Au substrate					Au substrate				
E_{adh}	−0.077	−0.076	−0.045	−0.049	−0.033	−0.322	−0.299	−0.174	−0.128	−0.134
$\Delta H_\mathrm{f}^{\mathrm{sup}}$	−0.42	−0.42	−0.24	−0.25	−0.18	−0.72	−0.73	−0.24	−0.28	−0.08
ΔG_f	+0.08	+0.07	+0.11	+0.10	+0.08	+0.47	+0.48	+0.40	+0.38	+0.37

Table III.3: Formation enthalpies ΔH_f (eV/at.), Gibbs free energies ΔG_f (eV/at., at T = 300 K and $P = 10^{-10}$ bar), and adhesion energies E_{adh} (eV/Å^2) for the $BaBO_3$ quasicrystalline approximant and honeycomb freestanding and supported layers.

Increasing the temperature under UHV conditions makes the $\Delta G_\mathrm{f}^{\mathrm{OQA/Me}}$ exergonic (Figure III.2, Tables III.4 to III.6) thus favouring the growth of the OQAs. The theoretical formation temperature (T_{form}) at which the OQAs are formed, that is, the temperature at which

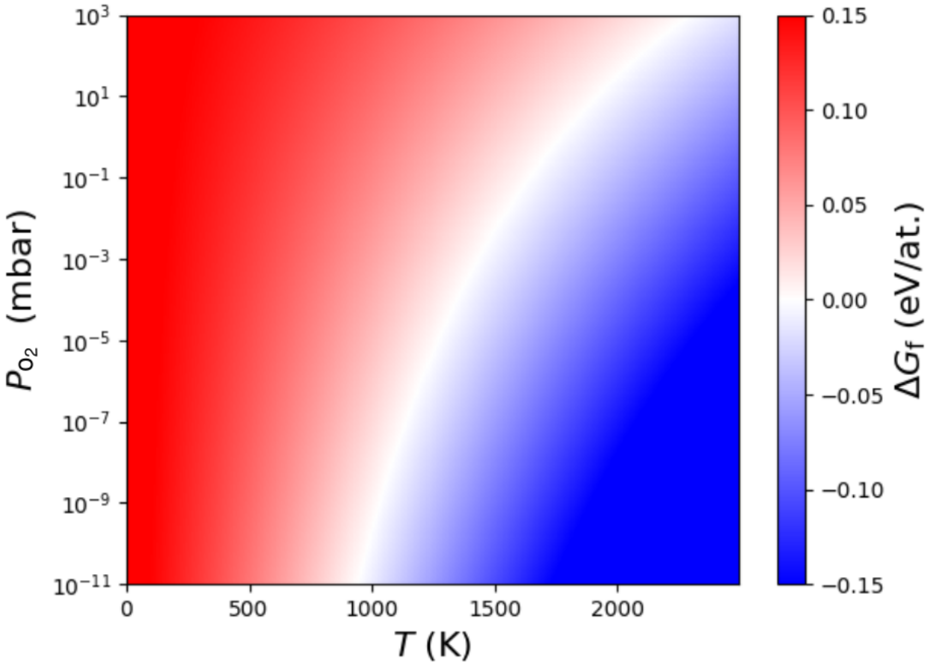

Figure III.2: Gibbs free energy ($\Delta G_{\mathrm{f}}^{\mathrm{OQA/Pt}}$), as a function of the temperature and pressure, for the formation of the $BaTiO_3$ oxide quasicrystal approximant on Pt(111).

$\Delta G_{\mathrm{f}}^{\mathrm{OQA/Me}} < 0$, is calculated to be 986 K for $BaTiO_3$/Pt at $P = 10^{-10}$ mbar, as shown in Figure III.2. This temperature is in reasonable agreement with the experimental one ($T_{\mathrm{form}}^{\mathrm{exp}}$ = 1250 K) [10]. The formation temperature does not vary much within the series, i.e., it ranges from 737 K ($SrTiO_3$/Au) to 1164 K ($BaFeO_3$/Pt), as shown in Figure III.4. A similar analysis performed for SHSs (Figure III.3) shows that the temperatures at which they grow ($\Delta G_{\mathrm{f}}^{\mathrm{SHS/Me}} < 0$) are systematically higher than the ones for OQAs. It suggests that OQAs can be formed preferentially to SHSs.

	$BaTiO_3$/Me	$SrTiO_3$/Me	$BaFeO_3$/Me	$BaCoO_3$/Me	$BaNiO_3$/Me
			Pt substrate		
ΔH_{f} (eV/at.)	−0.42	−0.41	−0.24	−0.26	0.20
			Au substrate		
ΔH_{f} (eV/at.)	−0.42	−0.42	−0.24	−0.24	−0.17

Table III.4: Formation enthalpy of the supported OQA (T = 0 K) according to $5\mathrm{Ba} + 4\mathrm{TM} + 6\mathrm{O}_2 + \mathrm{Pt}_{120} \rightarrow \mathrm{Pt}_{120}\mathrm{Ba}_5\mathrm{TM}_4\mathrm{O}_{12}$

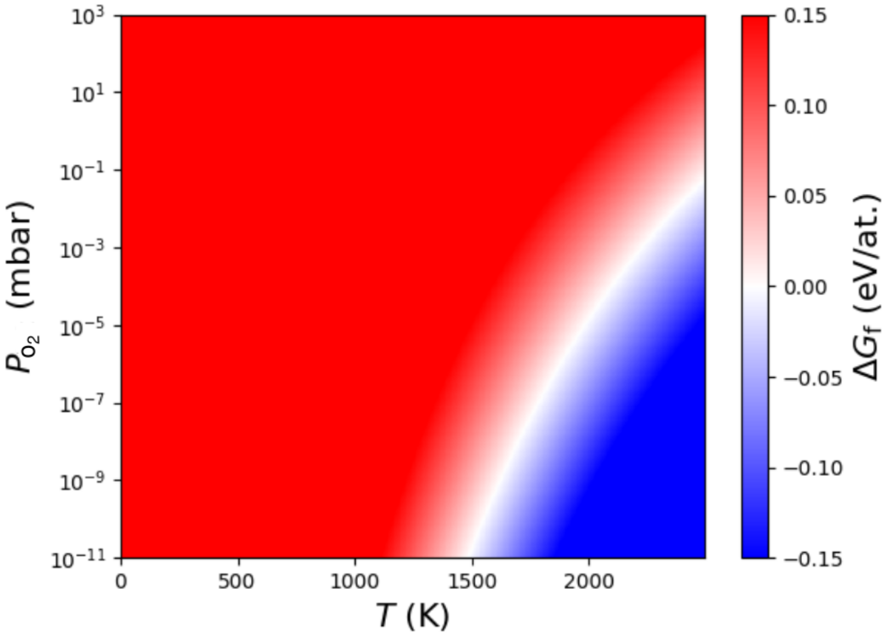

Figure III.3: Gibbs free energy of the reaction $Pt_{32}Ba_8Ti_6O_{24} \rightarrow Pt_{32}BaTi_4O_6$ + 2 $BaTiO_3$ + 6 O_2 + 5/2 Ba. The thick $BaTiO_3$ film is more stable than the SHS in the red region. The SHS is more stable than the thick $BaTiO_3$ film in the blue region.

	$BaTiO_3$/Me	$SrTiO_3$/Me	$BaFeO_3$/Me	$BaCoO_3$/Me	$BaNiO_3$/Me
			Pt substrate		
ΔH_f (eV/f.u.)	−1.52	−1.56	−0.94	−0.99	−0.79
			Au substrate		
ΔH_f (eV/f.u.)	−1.48	−1.50	−0.91	−0.92	−0.73

Table III.5: Formation enthalpy of the supported TPF (T = 0 K) according to 8Ba + 6TM + $6O_2$ + $Pt_{32} \rightarrow Pt_{32}Ba_8TM_6O_{24}$

At a given temperature, the increase of the O_2 pressure leads to an increase of $\Delta G_f^{OQA/Me}$, up to positive values. This increase reveals a nearly isothermal reversibility between a 2D quasicrystal and a periodic 3D island structure, controlled by an external parameter — here the oxygen chemical potential — as observed experimentally [11].

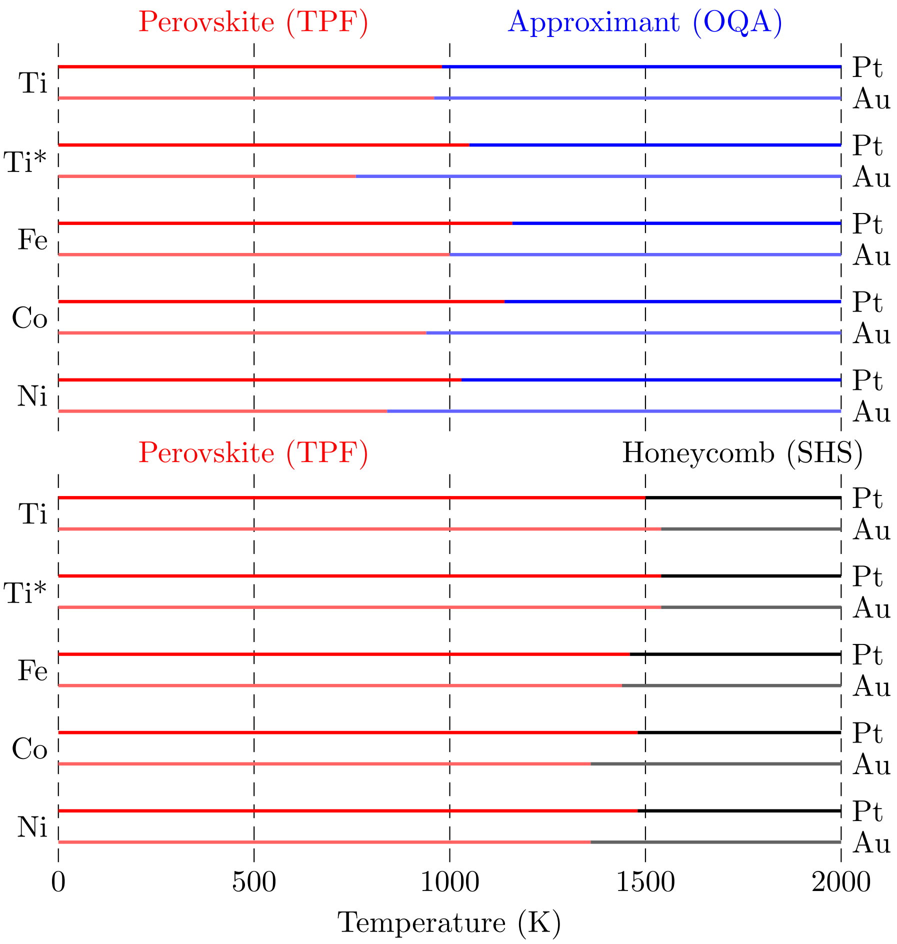

Figure III.4: Relative stabilities of the OQA/TPF (upper panel) and SHS/TPF (lower panel) systems. TPFs are stable at lower temperatures, whereas OQAs and SHSs are stable at higher temperatures. *B*-elements (Ti, Fe, Co, or Ni) are stated on the left and the metal substrates (Pt or Au) are stated on the right. The alkali earth is A = Ba, except when Ti is labelled as Ti* for which A = Sr. The pressure is $P = 10^{-10}$ mbar.

	$BaTiO_3$/Me	$SrTiO_3$/Me	$BaFeO_3$/Me	$BaCoO_3$/Me	$BaNiO_3$/Me
			Pt substrate		
ΔH_f (eV/at.)	−0.84	−0.83	−0.28	−0.31	−0.11
			Au substrate		
ΔH_f (eV/at.)	−0.72	−0.72	−0.24	−0.28	−0.09

Table III.6: Formation enthalpy of the supported SHS (T = 0 K) according to $Ba + 4TM + 3O_2 + Pt_{32} \rightarrow Pt_{32}BaTi_4O_6$

II.5. Driving forces for the formation of OQAs

Up to now, experimentalists have mainly considered the $BaTiO_3$ and $SrTiO_3$ perovskites to grow OQAs on Pt, because of the small oxide–metal lattice mismatch [10]. However, the thermodynamic approach presented above, predicted that a wide range of OQA compositions are stable on Pt and Au.

As a general principle, the formation of new 2D oxide structures is attributed to size-mismatch. A severe lattice mismatch between the oxide and the metal surface tends to avoid the formation of ordered oxide films over metals. A typical example is CaO deposited on Mo(001) [185]. Amorphous CaO films are formed at low growth temperature, but a rocksalt-type Ca_3MoO_4 structure, with a small oxide–metal lattice mismatch, is obtained after annealing at high temperature. Here, a detailed analysis of the structural properties of OQA freestanding and supported systems has been performed to address the question of how the size-mismatch impacts the OQAs formation. In this section, we also address the influence of electronic effects on the OQAs formation, through charge transfer and density of states analyses.

II.6. Size-mismatch and rumpling

Atomic relaxations of the freestanding OQA layers lead to flat planes, distorted from the initial orthorhombic lattice, with parameters larger than the ones of the substrate. This result is in agreement with the literature, at least for the $BaFeO_3$/Pt OQA [186]. The B–O first neighbor distances are almost identical in all systems, due to the similarity of the transition metal (B) ionic radii, with only a weak systematic decrease along the transition metal series. In contrast, the distances between the alkaline earth metals (A) and their oxygen neighbors (A–O distances) increase consistently with the A ionic radii ($r_{\mathrm{Ca}} < r_{\mathrm{Sr}} < r_{\mathrm{Ba}}$).

The surface cell mismatch (Δ) is defined as:

$$\Delta = \frac{||\vec{a} \wedge \vec{b}||_{\mathrm{sub}} - ||\vec{a} \wedge \vec{b}||_{\mathrm{free}}}{||\vec{a} \wedge \vec{b}||_{\mathrm{sub}}} \tag{III.1}$$

where $\vec{a}$ and $\vec{b}$ are the in-plane lattice vectors of the relaxed freestanding layer (labeled by subscript free) and of the substrate (sub). Cell mismatch can reach quite high values (up to 50 %). It remains around 20 to 35% for a number of systems, being higher when the OQA layer is supported on Au than on Pt or Pd.

With respect to the perfectly planar geometry of the freestanding films, supported OQAs display significant structural relaxations, quantified by the vertical separation (rumpling,

$R = z^+ - z^-$) between the average z-position of the anions (z^-) and cation (z^+), where z-coordinate represents the surface normal direction. Overall, in most systems, on average, the cations are closer to the substrate than the oxygen atoms, thus resulting in negative values for R. A more detailed analysis shows that the oxygen atoms are positioned either in one plane or in two planes separated by about 1.4 Å ($BaTiO_3$ OQA). The B–O and Ba–O distances in the supported films are similar to the ones in the freestanding layer (but slightly longer by 0.05 Å and 0.11 Å, respectively). This is consistent with a contraction of interatomic distances when the atomic coordination decreases [187]. It also highlights that lattice mismatches can be rather easily accommodated by the rumpling of the film, the bending distortions being of much lower energies than bond-length modifications [27]. However, no clear correlation has been found between the surface cell mismatch and the rumpling (Figure III.5(a)), suggesting that electronic effects also influence the atomic structure of the OQAs.

II.6.1. Charge transfer

The structural distortions described in the previous section can be understood as a response to the electrostatic dipole produced by the interface charge transfer [188]. A negatively charged substrate ($Q_{\mathrm{Me}} < 0$) attracts the cations and thus tends to produce a negative rumpling ($R < 0$) whereas a positive rumpling is expected for a positive charging of the substrate. The negative rumpling calculated for all investigated OQAs and SHSs series is then attributed to a charge transfer from the oxide film to the substrate. This picture is in agreement with the planar integrated charge density differences, which indicates that the net electron charge is being concentrated in the oxide/metal bonding region with the predominant electron donation coming from the oxide layer (Figures III.6 and III.7).

The aforementioned hypothesis of the oxide–to–substrate charge transfer is also consistent with the Bader charge analysis (Tables III.7 to III.9). While in the freestanding layer, the positive charge of A- and B-type atoms originates from an "in plane" electron transfer toward the more electronegative oxygen atoms, the picture is slightly altered in the supported films, in which the charge transfer also occurs towards the substrate. In comparison to the freestanding film, the B-metal of supported OQAs and SHSs carry a higher positive charge, and the oxygen atoms have a less negative charge, thus leading to interfacial Me atoms carrying an excess of electrons. The charge transfer decreases along the transition metal series, but is similar for all considered substrates (Au, Pt, Pd). In contrast, the charges on the alkaline earth atoms (Ba, Sr, Ca) are quite constant (1.5–1.6 e), suggesting that they only weakly participate to the oxide/metal interaction.

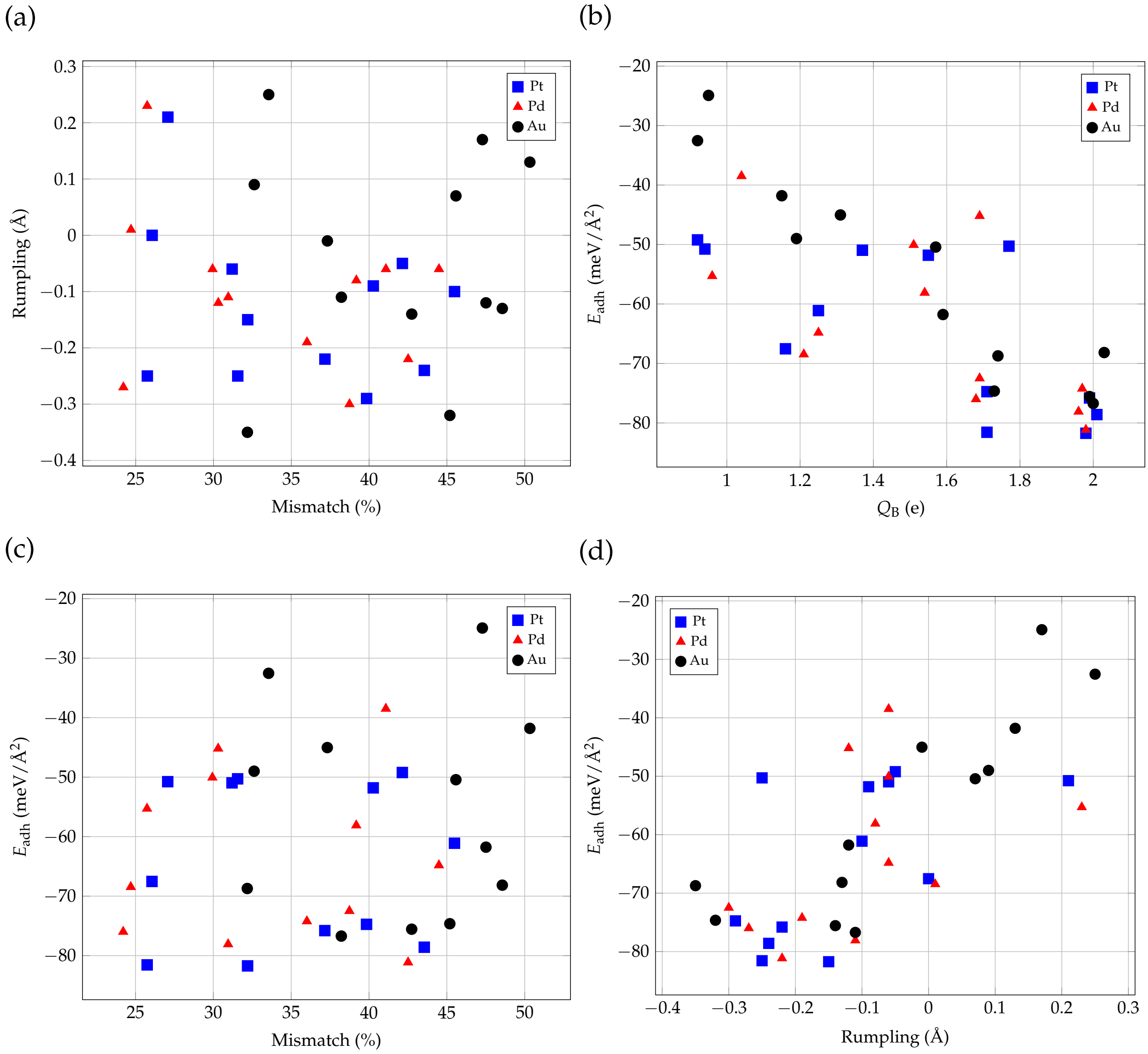

Figure III.5: Relations between (a) Rumpling and the size mismatch, (b) adhesion energy (E_{adh}) and the Bader charge of the B atom (Q_{B}), (c) E_{adh} and the size mismatch, and (d) E_{adh} and the rumpling for selected structures.

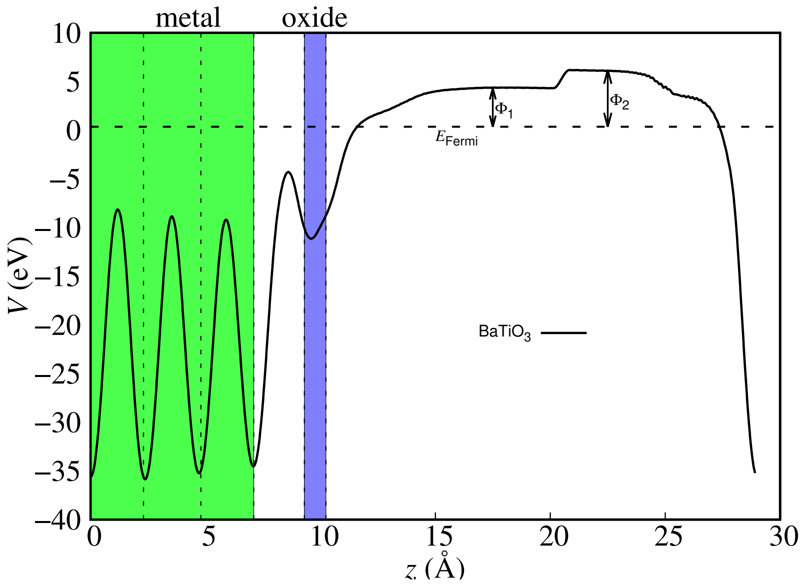

Figure III.6: Planar averaged electrostatic potential ($\overline{V}(z) = \frac{1}{A}\int_A V(x,y,z)\mathrm{d}x\mathrm{d}y$, where A is the surface area) for $BaTiO_3$ on Pt. Green band represents the Pt(111) slab and blue stripe indicates the position of the OQA layer. Φ_1 and Φ_2 are the values in the plateaus of the average electrostatic potential in the vacuum level (with the Fermi energy as a zero reference) for the metal-oxide and metal systems, respectively.

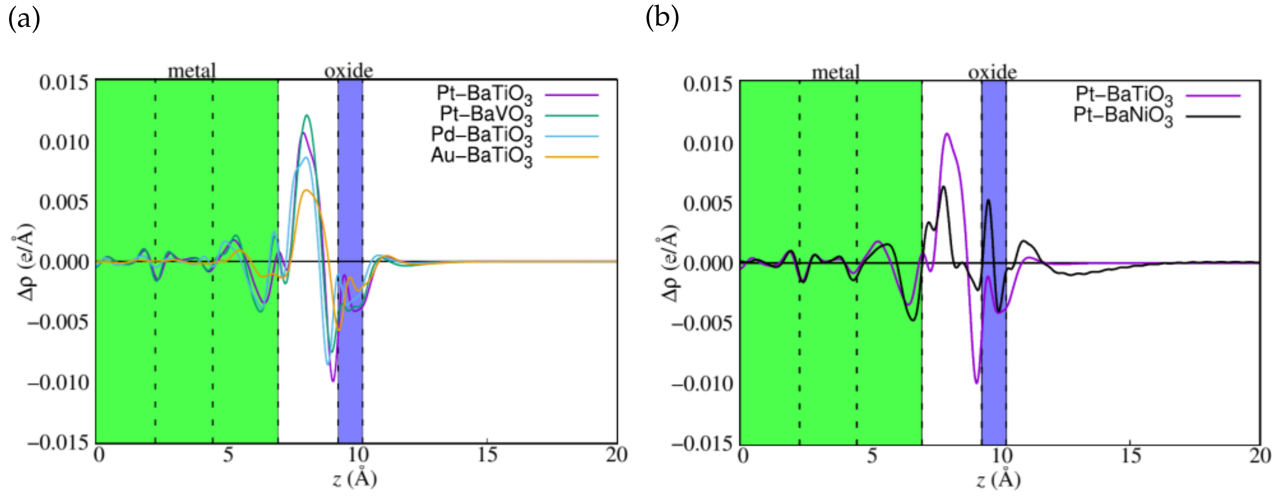

Figure III.7: Planar averaged electron charge density differences $\Delta\rho(z) = \int_A \Delta\rho(x,y,z)\,\mathrm{d}x\mathrm{d}y$, where integration was performed over the area (A) spanned by the surface supercell for several OQA structures studied in this work. Green represents the Pt(111) slab and blue stripe indicates the position of the OQA layer.

	$BaTiO_3$	$BaVO_3$	$BaCrO_3$	$BaMnO_3$	$BaFeO_3$	$BaCoO_3$	$BaNiO_3$
Freestanding layer							
Q_{Ba} (e)	1.58	1.60	—	—	1.63	1.63	1.63
Q_B (e)	1.96	1.39	—	—	1.18	1.13	1.05
Q_{O} (e)	−1.31	−1.13	—	—	−1.07	−1.06	−1.03
m_B (μ_{B})	0.2	0.5	—	—	2.5	1.4	0.11
Pt substrate							
R (Å)	−0.17	−0.27	−0.19	—	−0.06	0.11	0.21
Q_{Ba} (e)	1.54	1.53	1.50	—	1.52	1.54	1.51
Q_B (e)	1.98	1.71	1.76	—	1.37	1.16	0.94
Q_{O} (e)	−1.09	−0.94	−0.97	—	−0.97	−0.98	−0.95
Q_{Pt} (e)	−0.10	−0.12	−0.11	—	−0.07	−0.03	0.00
H_{for} (0K)	−0.42	−0.36	−0.15	—	−0.24	−0.26	−0.21
E_{adh} (meV/Å^2)	−81.73	−81.56	—	—	−50.96	−67.53	−50.76
mismatch (%)	32.20	25.75	—	—	31.20	26.06	27.07
$\Delta\Phi$ (eV)	2.01	2.15	2.20	—	2.18	2.25	2.25
D_z (eÅ)	-2.12	-2.37	-2.85	—	-2.44	-2.62	-2.76
m_B (μ_{B})	0.0	0.0	1.09	—	−3.33	−0.42	0.53
MS	NM	NM	FM	—	FM	AFM	AFM
Pd substrate							
R (Å)	−0.11	−0.23	−0.18	0.03	0.07	0.25	0.31
Q_{Ba} (e)	1.51	1.50	1.48	1.51	1.50	1.51	1.49
Q_B (e)	1.96	1.68	1.73	1.57	1.51	1.21	0.96
Q_{O} (e)	−1.12	−0.95	−0.97	−1.04	−0.94	−0.98	−0.91
Q_{Pd} (e)	−0.07	−0.09	−0.08	−0.04	−0.05	−0.02	0.01
H_{for} (0K)	−0.41	−0.35	−0.14	−0.23	−0.24	−0.26	−0.20
E_{adh} (meV/Å^2)	−78.08	−75.99	—	—	−50.06	−68.46	−55.29
mismatch (%)	30.95	24.21	—	—	29.94	24.70	25.74
$\Delta\Phi$ (eV)	2.16	2.19	2.21	2.21	2.20	2.22	2.20
D_z (eÅ)	−1.85	−2.07	−2.30	−2.30	−2.21	−2.56	−2.29
m_B (μ_{B})	0.0	0.0	0.57	0.88	3.59	2.56	1.53
MS	NM	NM	AFM	AFM	FM	FM	FM
Au substrate							
R (Å)	−0.16	−0.36	—	−0.03	0.03	0.17	0.21
Q_{Ba} (e)	1.58	1.57	—	1.57	1.56	1.55	1.54
Q_B (e)	2.00	1.74	—	1.57	1.31	1.19	0.92
Q_{O} (e)	−1.14	−0.97	—	−1.09	−1.03	−1.00	−0.99
Q_{Au} (e)	−0.08	−0.11	—	−0.07	−0.06	−0.04	0.00
H_{for} (0K)	−0.42	−0.35	—	−0.24	−0.24	−0.24	−0.18
E_{adh} (meV/Å^2)	−76.72	−68.72	—	—	−45.03	−49.00	−32.54
mismatch (%)	38.22	32.18	—	—	37.32	32.62	33.55
$\Delta\Phi$ (eV)	2.12	2.15	—	2.15	2.17	2.17	2.20
D_z (eÅ)	−1.58	−1.94	—	−1.95	−2.25	−2.13	−2.46
m_B (μ_{B})	0.0	0.0	—	2.39	−0.23	−2.78	−1.93
MS	NM	NM	—	AFM	AFM	FM	AFM

Table III.7: BaBO$_3$/Me(111) systems (B = Ti, V, Cr, Mn, Fe, Co, Ni and Me = Pt, Pd, Au): film rumplings (R), Bader charges (Q), enthalpies of formation at 0K (H_{for}), adhesion energies (E_{adh}), lattice mismatch, work function differences ($\Delta\Phi$), dipole moments in the z direction (D_z), and atomic magnetic moments (m). Bader charges are expressed in units of elementary charge (e), positive charges indicate cations. Q_{Me} corresponds to the average charge of Me atoms in the topmost metal layer of Me(111). Q_B and m_B stand for Bader charge and magnetic moment of atom B of ABO_3. MS stands for the ground-state spin order.

	$SrTiO_3$	$SrVO_3$	$SrCrO_3$	$SrMnO_3$	$SrFeO_3$	$SrCoO_3$	$SrNiO_3$
Freestanding layer							
Q_{Sr} (e)	1.60	1.61	1.63	1.62	—	—	1.61
Q_B (e)	1.90	1.44	1.61	1.60	—	—	1.12
Q_{O} (e)	−1.30	−1.15	−1.14	−1.21	—	—	−1.04
m_B (μ_{B})	0.1	0.4	1.39	0.0	—	—	0.9
Pt substrate							
R (Å)	−0.22	−0.29	−0.25	−0.05	−0.12	−0.05	0.20
Q_{Sr} (e)	1.56	1.56	1.54	1.56	1.57	1.57	1.57
Q_B (e)	1.99	1.71	1.77	1.55	1.36	1.25	0.92
Q_{O} (e)	−1.10	−0.95	−0.98	−1.05	−0.98	−0.99	−0.94
Q_{Pt} (e)	−0.10	−0.12	−0.11	−0.06	−0.07	−0.05	−0.04
H_{for} (0K)	−0.40	−0.35	−0.14	−0.24	−0.23	−0.25	0.87
E_{adh} (meV/Å^2)	−75.8	−74.74	−50.28	−51.8	—	—	−49.22
mismatch (%)	37.16	39.84	31.56	40.27	—	—	42.14
$\Delta\Phi$ (eV)	2.15	2.20	2.19	2.16	2.19	2.21	2.19
D_z (eÅ)	-1.65	-2.20	-2.43	-1.65	-1.93	-1.72	-2.11
m_B (μ_{B})	0.00	0.00	1.18	3.41	−0.60	−0.04	0.20
MS	NM	NM	FM	FM	AFM	AFM	AFM
Pd substrate							
R (Å)	−0.14	−0.27	−0.23	0.1	0.05	0.23	0.23
Q_{Sr} (e)	1.56	1.53	1.56	1.55	1.53	1.54	1.54
Q_B (e)	1.97	1.69	1.69	1.54	1.35	1.20	1.04
Q_{O} (e)	−1.13	−0.97	−1.04	−1.06	−0.99	−1.00	−0.95
Q_{Pd} (e)	−0.02	−0.10	−0.07	−0.05	−0.05	−0.03	−0.03
H_{for} (0K)	−0.41	−0.34	−0.13	−0.24	−0.23	−0.26	−0.19
E_{adh} (meV/Å^2)	−74.22	−72.49	−45.19	−58.1	—	—	−38.49
mismatch (%)	36.01	38.74	30.31	39.18	—	—	41.08
$\Delta\Phi$ (eV)	2.14	2.14	2.15	2.20	2.16	2.19	2.20
D_z (eÅ)	−1.45	−1.61	−1.89	−1.30	−2.09	−2.16	−2.13
m_B (μ_{B})	0.00	0.00	1.21	0.00	3.43	2.59	−0.31
MS	NM	NM	FM	FM	FM	FM	FM
Au substrate							
R (Å)	−0.19	−0.39	—	0.07	−0.07	0.11	0.20
Q_{Sr} (e)	1.58	1.57	—	1.57	1.57	1.57	1.56
Q_B (e)	1.99	1.73	—	1.57	1.34	1.12	0.95
Q_{O} (e)	−1.16	−0.97	—	−1.11	−1.01	−1.03	−1.02
Q_{Au} (e)	−0.08	−0.11	—	−0.03	−0.05	−0.02	0.00
H_{for} (0K)	−0.42	−0.36	—	−0.24	−0.22	−0.23	−0.18
E_{adh} (meV/Å^2)	−75.56	−74.64	—	−50.43	—	—	−24.93
mismatch (%)	42.74	45.19	—	45.58	—	—	47.28
$\Delta\Phi$ (eV)	2.10	2.13	—	2.14	2.12	2.14	2.15
D_z (eÅ)	−1.28	−1.60	—	−1.58	−1.58	−1.67	−1.92
m_B (μ_{B})	0.00	0.00	—	−0.00	1.55	−2.35	0.30
MS	NM	NM	—	AFM	AFM	FM	FM

Table III.8: SrBO$_3$/Me(111) systems (B = Ti, V, Cr, Mn, Fe, Co, Ni and Me = Pt, Pd, Au): film rumplings (R), Bader charges (Q), enthalpies of formation at 0K (H_{for}), adhesion energies (E_{adh}), lattice mismatch, work function differences ($\Delta\Phi$), dipole moments in the z direction (D_z), and atomic magnetic moments (m). Bader charges are expressed in units of elementary charge (e), positive charges indicate cations. Q_{Me} corresponds to the average charge of Me atoms in the topmost metal layer of Me(111). Q_B and m_B stand for Bader charge and magnetic moment of atom B of ABO$_3$. MS stands for the ground-state spin order

	$CaTiO_3$	$CaVO_3$	$CaCrO_3$	$CaMnO_3$	$CaFeO_3$	$CaCoO_3$	$CaNiO_3$
Freestanding layer							
Q_{Ca} (e)	1.55	—	—	1.57	—	1.58	—
Q_B (e)	1.94	—	—	1.64	—	1.32	—
Q_{O} (e)	−1.29	—	—	−1.20	—	−1.10	—
m_B (μ_{B})	0.3	—	—	0.0	—	2.3	—
Pt substrate							
R (Å)	−0.24	−0.35	−0.31	—	−0.04	0.07	0.14
Q_{Ca} (e)	1.53	1.53	1.51	—	1.54	1.54	1.54
Q_B (e)	2.01	1.73	1.78	—	1.40	1.25	1.05
Q_{O} (e)	−1.10	−0.94	−0.97	—	−0.98	−0.98	−0.93
Q_{Pt} (e)	−0.09	−0.12	0.11	—	−0.06	−0.05	−0.04
H_{for} (0K)	−0.40	−0.34	−0.13	—	−0.23	−0.25	−0.19
E_{adh} (meV/Å^2)	−78.59	—	—	—	—	−61.11	—
mismatch (%)	43.55	—	—	—	—	45.49	—
$\Delta\Phi$ (eV)	2.11	2.11	2.15	—	2.16	2.15	2.14
D_z (eÅ)	−1.25	−1.62	−1.82	—	−1.90	−1.83	−1.68
m_B (μ_{B})	0.0	0.0	1.55	—	−0.77	0.65	−0.45
MS	NM	NM	FM	—	AFM	AFM	AFM
Pd substrate							
R (Å)	−0.17	−0.30	−0.32	0.07	−0.02	0.07	0.29
Q_{Ca} (e)	1.53	1.49	1.49	1.53	1.50	1.51	1.51
Q_B (e)	1.98	1.70	1.72	1.54	1.36	1.25	1.01
Q_{O} (e)	−1.13	−0.97	−0.99	−1.06	−1.00	−1.02	−0.95
Q_{Pd} (e)	−0.07	−0.09	−0.08	−0.02	−0.04	−0.03	−0.02
H_{for} (0K)	−0.40	−0.34	−0.14	−0.24	−0.23	−0.24	−0.20
E_{adh} (meV/Å^2)	−81.14	—	—	—	—	−64.81	—
mismatch (%)	42.51	—	—	—	—	44.49	—
$\Delta\Phi$ (eV)	2.10	2.11	2.12	2.16	2.12	2.13	2.12
D_z (eÅ)	−1.00	−1.13	−1.06	−0.89	−1.26	−1.37	−1.35
m_B (μ_{B})	0.00	0.00	1.16	0.00	3.46	1.05	0.56
MS	NM	NM	FM	FM	FM	AFM	AFM
Au substrate							
R (Å)	−0.16	−0.40	−0.36	0.06	0.04	0.14	0.23
Q_{Ca} (e)	1.55	1.54	1.53	1.55	1.54	1.54	1.53
Q_B (e)	2.03	1.75	1.80	1.59	1.38	1.15	1.02
Q_{O} (e)	−1.16	−0.96	−1.02	−1.07	−1.05	−1.06	−1.00
Q_{Au} (e)	−0.08	−0.11	−0.09	−0.04	−0.03	0.00	0.00
H_{for} (0K)	−0.40	−0.34	−0.12	−0.25	−0.23	−0.23	−0.18
E_{adh} (meV/Å^2)	−68.16	—	—	−61.77	—	−41.80	—
mismatch (%)	48.56	—	—	47.51	—	50.33	—
$\Delta\Phi$ (eV)	2.07	2.07	2.07	2.11	2.08	2.11	2.14
D_z (eÅ)	−0.93	−1.03	−0.92	−0.73	−1.11	−1.39	−1.68
m_B (μ_{B})	0.00	0.00	0.53	0.00	−3.66	−1.17	1.21
MS	NM	NM	AFM	AFM	FM	AFM	FM

Table III.9: CaBO$_3$/Me(111) systems (B = Ti, V, Cr, Mn, Fe, Co, Ni and Me = Pt, Pd, Au): film rumplings (R), Bader charges (Q), enthalpies of formation at 0K (H_{for}), adhesion energies (E_{adh}), lattice mismatch, work function differences ($\Delta\Phi$), dipole moments in the z direction (D_z), and atomic magnetic moments (m). Bader charges are expressed in units of elementary charge (e), positive charges indicate cations. Q_{Me} corresponds to the average charge of Me atoms in the topmost metal layer of Me(111). Q_B and m_B stand for Bader charge and magnetic moment of atom B of ABO$_3$. MS stands for the ground-state spin order

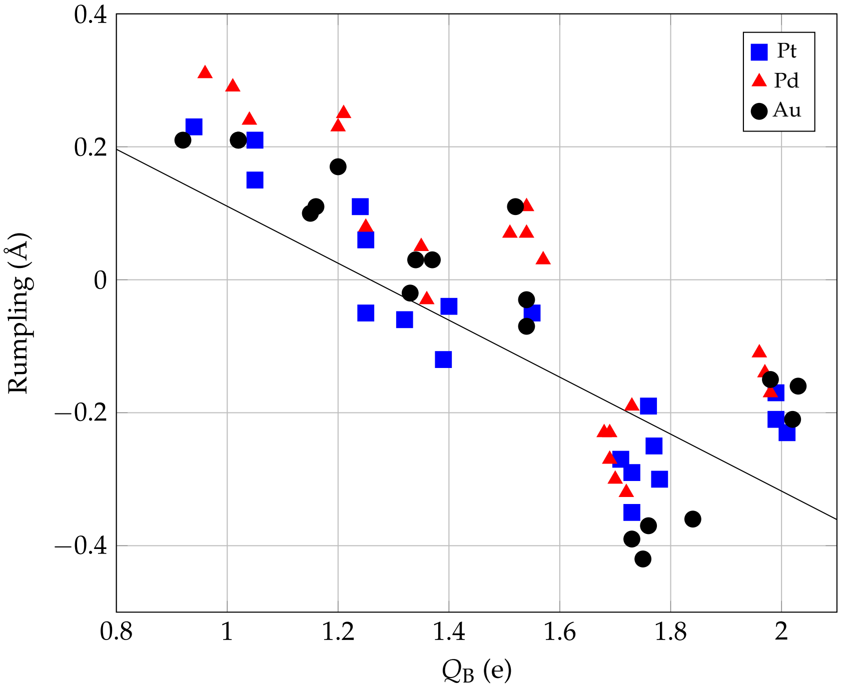

Figure III.8: Film rumpling (R) as a function of the Bader charge of B-type atoms (Q_B; note that positive Q_B values correspond to cations). The data located around $Q_B = 1.8$ and $Q_B = 2.0$ correspond to B=V and B=Ti, respectively.

The charge transfer is an important parameter that controls the structure of the OQA. It is shown in Figure III.8, where a correlation is evidenced between the film rumpling (R) and the Bader charge of B atoms. The charge transfer also influences the thermodynamics through the adhesion energy. Overall, a stronger adhesion of the film indeed corresponds to a larger Q_B, while neither the rumpling nor the size mismatch show clear correlations with the adhesion energy (Tables III.7 to III.9).

II.6.2. Electronic structure and oxide/metal bonding scheme

Density of states (DOS) calculations have been performed for the complete set of OQAs freestanding and supported layers. They show hybridizations within the oxide layer (mainly between B and O atoms). Associated with the interfacial electron transfer, the local density of states of the freestanding oxide single-layers (Figure III.10 and Figure A.18) are substantially modified in supported OQAs (Figure III.9 and Figures A.15 to A.17). The most obvious effect is probably the widening of the bands. For example, while hybridization between Ti and O states occurs in the $[-4.4, -2.0]$ eV range in the freestanding oxide single-layer, it extends from -5.5 eV to the Fermi energy for the $BaTiO_3$ OQA supported on Pt. This observation is less clear for late transition metals (*B* = Fe, Co), because the *B*-states of the freestanding layer are displayed in a wider energy range, up to about 1 eV.

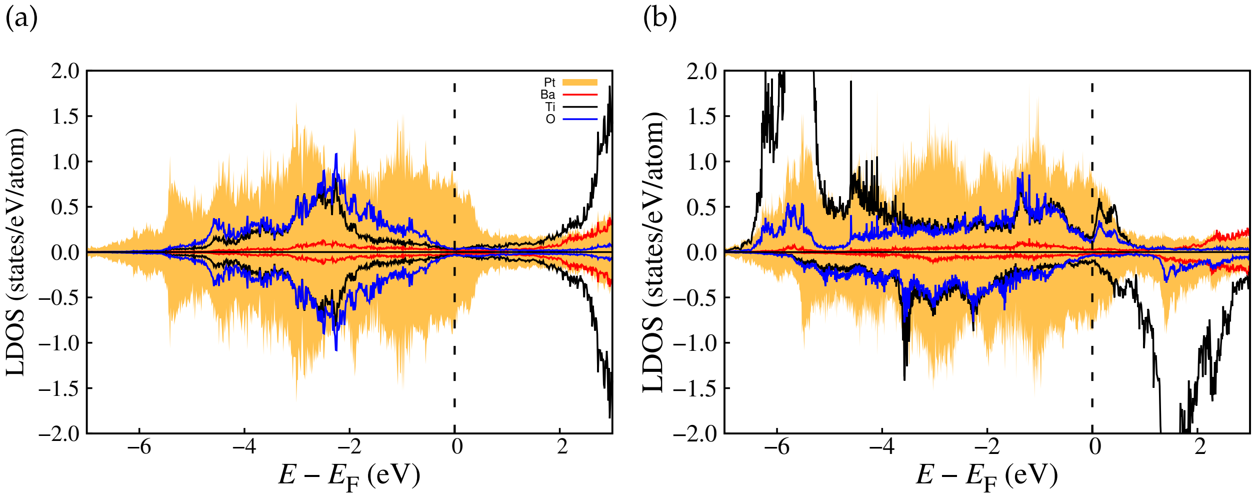

Figure III.9: Local density of states (LDOS) for the (a) σ-$BaTiO_3$/Pt(111) and (b) σ-$BaFeO_3$/Pt(111) systems.

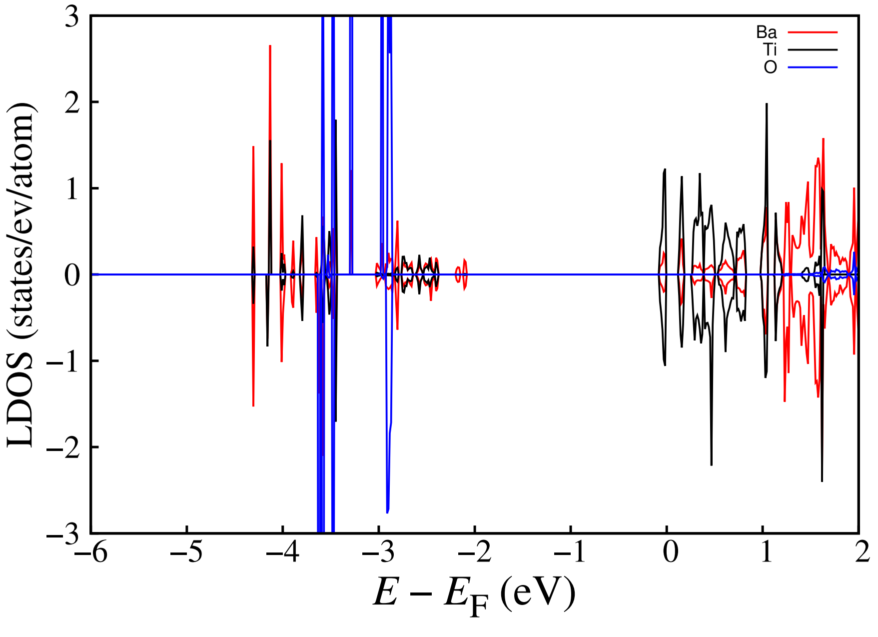

Figure III.10: Local density of states (LDOS) for the σ-$BaTiO_3$ freestanding layer. Ba, Ti, and O are represented as red, black, and blue, respectively.

The DOS of the *B* element contributions extend from the bottom of the oxide band to above the Fermi energy (E_F), most states being positioned 2 eV above E_F and beyond. Overall, the interaction with the substrate leads to OQAs with a metallic character, with a strong overlap between O- and B-states, indicating a strong interaction. For $BaTiO_3$/Pt, this is in agreement with the hybridization of O-2p and Ti-3d states and with the occupied Ti-3d states at E_F that have been experimentally observed [189].

Within the transition metal series, the spin-up contribution from the B-type atoms of the OQAs is progressively shifted away from the Fermi energy, from Ti to Ni, in agreement with the filling of d-states and the magnetic properties of the oxide layer. By combining the previous trends with the variations induced by the different substrates, we can obtain insight into the Me–OQA interactions. The decreasing work function from Pt to Pd ($\Phi_{Pt(111)} = 5.64$ eV and $\Phi_{Pd(111)} = 5.21$ eV) [190] shifts the metal Fermi energy slightly upwards. This comes in addition to the bandwidth increase from 3d to 4d metals. As a consequence, the overlap between the states of the oxide layer and the substrate, which is effective for $BaTiO_3$ and $BaVO_3$, start to be weaker from B = Cr, in agreement with the predicted lower adhesion. This effect is stronger for Me = Pd than for Me = Pt, in relation to the wider bandwidth of Pt compared to Pd. The situation is slightly different in the case of gold, since its d-band center is significantly down shifted and is located considerably below the Fermi energy. Here, the weaker Me–OQA interaction is attributed to the small overlap in the region just below E_F ($-2\text{ eV} \leq E \leq E_F$).

The interactions between the ultra-thin films and the metallic substrates has also been analysed in terms of COHP (Crystal Orbital Hamilton Population, Figure III.11(b) and Figures A.9 to A.14 and their energy-integrated counterparts (ICOHP, Figure III.11 (a)). COHP is a partitioning of the band-structure energy in terms of orbital-pair contributions. The energy-resolved COHP(E) plots facilitate the identification of bonding, non bonding and anti-bonding contributions, while the energy-integrated ICOHP is a useful measure of the interaction strength, i.e., the more negative is the ICOHP value, the stronger is the interaction. Figure III.11(a) therefore reveals that, overall, the interaction is stronger for Me–O bonds than for Me–B ones. In addition, the trends in the 3d series differs for the two bond types. When the atomic number of the B-species increases, the Me–B bonds gradually weakens, in agreement with a smaller orbital overlap consistent with the smaller radii of the B-type elements. In contrast, the Me–O bonds get stronger in the series, in agreement with the shorter Me–O bond, on average, over the series. Overall, substrate–oxide interactions are weaker on Au than on Pt, in agreement with the lower adhesion energy calculated on Au than on Pt. The ICOHPs calculated on Pd are smaller than on Pt. This is attributed to the smaller atomic radii of Pd compared to Pt.

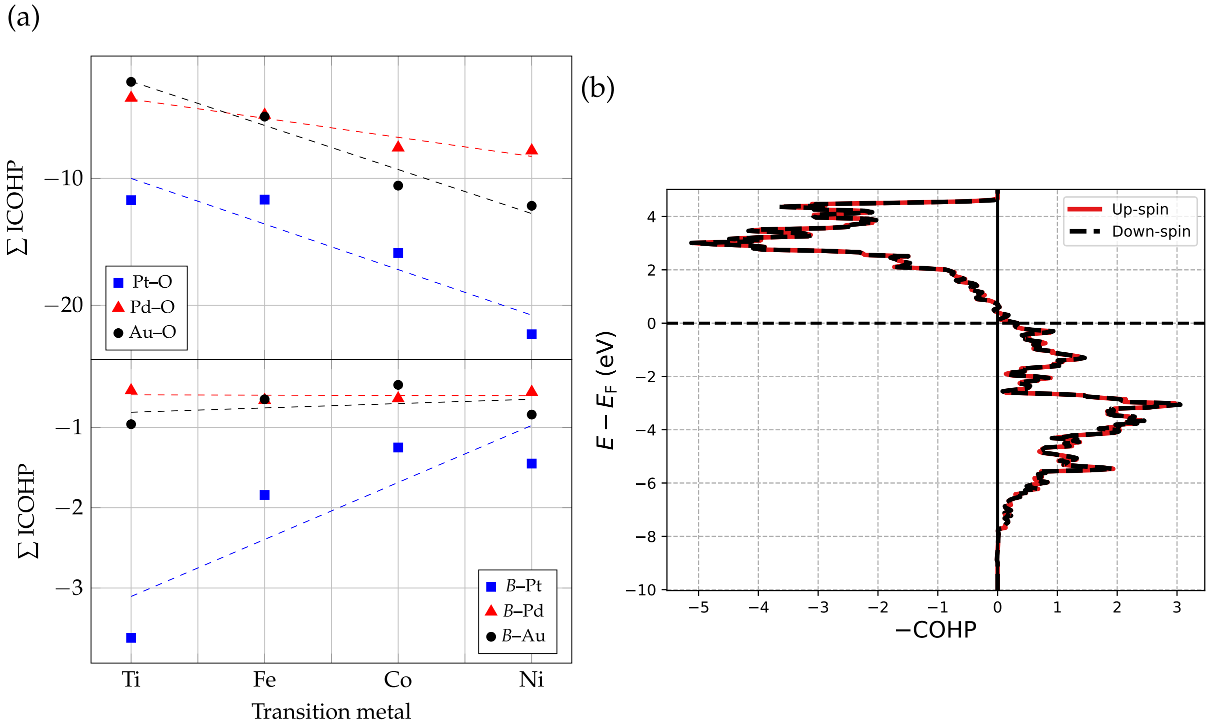

Figure III.11: (a) Interaction between the OQA layer and the metallic substrate analysed with the ICOHP. The sum of ICOHPs ($\sum$ ICOHP) for Me–B and Me–O bonds is plotted for several BaBO$_3$/Me systems with $B \in$ {Ti, Fe, Co, Ni} and Me $\in$ {Pt, Pd, Au}. The sum of ICOHPs covers all bonds of a given type, with a bond length (R_{ij}) smaller than 4 Å: $\sum \text{ICOHP} = \sum_{R_{ij}<4} \text{ICOHP}(R_{ij})$. (b) Averaged COHP of the Ti–Pt bond.

II.7. Work functions and magnetic properties

The knowledge of material's work functions provides an absolute electron energy-level reference relative to the vacuum energy, which is important for device applications. Due to their low work functions, perovskites — especially SrVO$_3$ — have already been identified as promising materials for new electron emission cathodes [191]. DFT calculations show a decrease of the ABO$_3$/Me work function in comparison to the bare metallic surface. The change of the work function ($\Delta\Phi = \Phi_{\text{OQA/Me}} - \Phi_{\text{Me}}$, Figure III.12 and Tables III.7 to III.9) is about 2 eV. It is impacted by the nature of the A element, in agreement with what has been reported for the adsorption of alkali metal atoms deposited on ultra-thin oxide films [192]. The work functions are strongly correlated to the electronic surface dipoles. The latter are non negligible in all investigated systems and both the rumpling and the charge transfer contribute to their values [75].

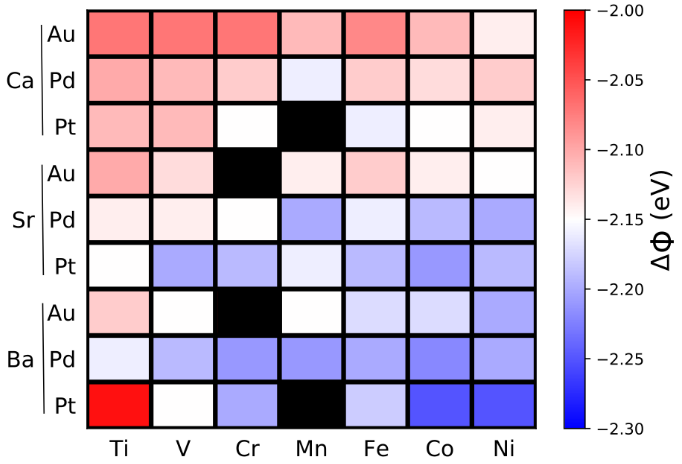

Figure III.12: Work function change ($\Delta\Phi = \Phi(\text{OQA/Me}) - \Phi(\text{Me})$) of the OQAs supported on Pt, Pd, and Au. Black rectangles are missing data.

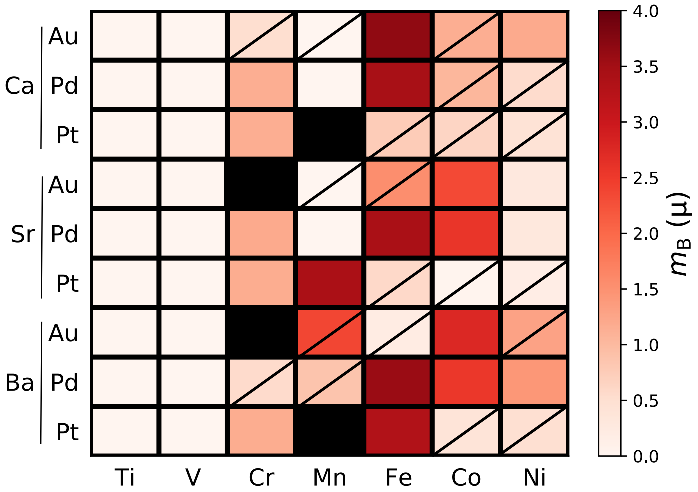

Figure III.13: B-element average magnetic moment calculated for several OQA/Me systems. The crossed squares indicate an anti-ferromagnetic ordering. Black rectangles are missing data.

Perovskites are also well-known for the remarkable variety of magnetic properties. Magnetism persists down to the single-layer limit (Figure III.13). Magnetic properties of the films are induced by the shift between the majority and minority spin states that occurs for all OQA except those with $B \in \{\text{Ti, V}\}$. This is further confirmed by the magnetic moments calculated on B-type atoms ($B \notin \{\text{Ti, V}\}$), which show a great diversity of magnetic coupling, attributed both to electronic effects (number of electrons) and geometric effects (rumpling and interatomic distance between the cations). Focusing on the $BaFeO_3$ OQA, a magnetic moment of 3.3 μ_B per Fe atom has been calculated, in good agreement with the literature (3.3 μ_B per Fe atom [189]). It is slightly smaller than for the SHS system (3.63 μ_B per Fe atom). A polarization of the O- and Pt-atoms in the vicinity is also noticeable, similarly to what has been pointed by [189].

III. σ-approximant (Cockayne's model)

A different model to create the oxide approximant structures on the (Ba, Sr)–Ti–O/Pt(111) system was proposed by Cockayne et al. [23] in order to have a better fit with the experimental STM images [9]. The decoration model proposed is shown in Figure I.10, which correspond to the compositions $SrTi_4O_4$, $SrTiO_3$, and $SrTi_2O_2$ for the square, triangle, and rhombus motifs, respectively.

It must be noted that we are focusing here on structures that are composed by these three tilings due to the large amount of approximants found experimentally, but recent experimental evidence shows that there are other possible motifs that can be formed [193], and the composition of such new tiling remains to be discovered. Some examples of the approximants found using these three tiling configurations are:

- A complex monoclinic oxide on $SrTiO_3$/Pt(111) [12];
- A rectangular σ phase at antiphase boundary domains with square-triangle tilings in the Ba-Ti-O/Pd(111) system [83];
- A large hexagonal approximant phase, formed by a combination of triangles, squares, and rhombuses found in two systems (Ba-Ti-O/Pt(111) and Sr-Ti-O/Pt(111)), found independently by different research groups [79], [82];
- A giant square approximant phase with the three tiling elements and with a ratio of squares, triangles, and rhombus very close to that of the dodecagonal quasicrystal following the Niizeki-Gaähler tiling (NGT) [79];

Regarding the approximant's structure, we can better understand the difference between the two types of tilling configurations (Förster and Cockayne's models) by looking at the experimental STM image on the σ phase in Figure III.14 (a). The bright protrusions on the image are assigned approximately to the electronic density of either the Ti atoms (Förster's model), or to the Ba/Sr atoms (Cockayne's model). Figure III.14 (b) shows the σ approximant unit cell, which was generated based on Surface X-Ray Diffraction (SXRD) experiments to determine the position of each specific atom. In this structure, only the square and triangle tilings are used and are created by a network of Ti atoms. This was the structure used in the first section of this chapter.

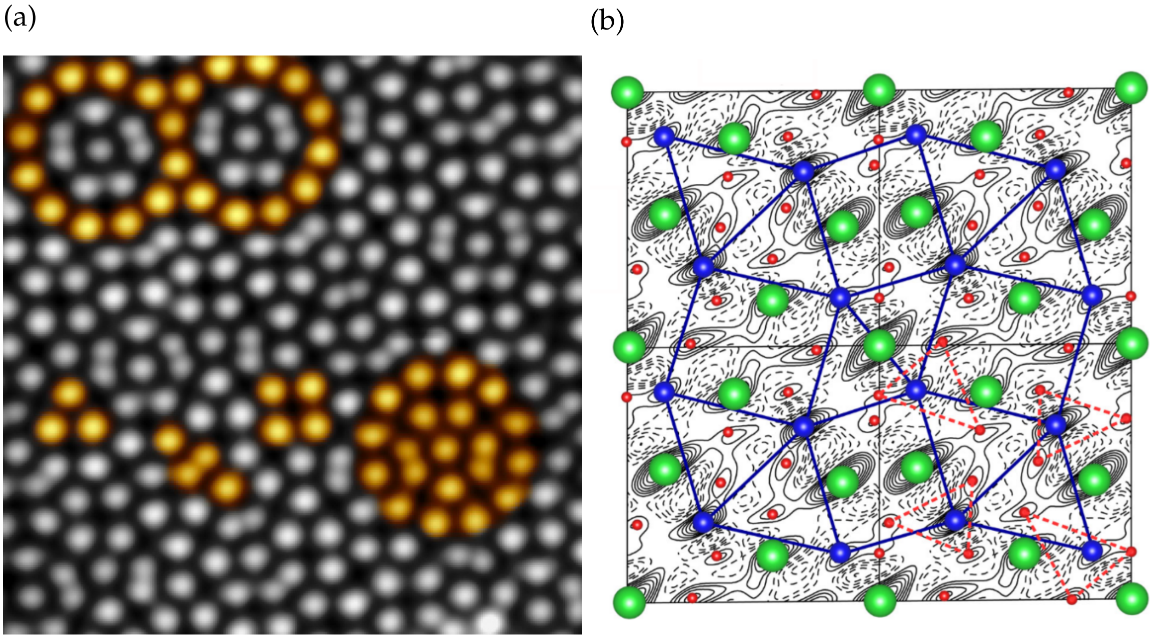

Figure III.14: (a) Atomically resolved STM image of the BaTiO$_3$-derived OQC on Pt(111) determined by Förster et al. [64]. The structure forms from three different tiling elements that build a characteristic dodecagon. The square, triangle, and rhombus building blocks are emphasized in orange. Bias used: -0.15 V. Reproduced from [64] with permission from John Wiley and Sons. (b) SXRD-derived charge density $\rho(x, y)$ contour plot of four 2D unit cells of the OQC approximant. The tiling configuration is indicated by the solid blue lines. Peaks in $\rho(x, y)$ are identified with Ba (green), Ti (blue), and O atoms (red). In the lower right part the threefold coordination of O atoms around Ti atoms is emphasized by dashed triangles [10]. Reproduced from [10] with permission from the American Physical Society.

On the other hand, by considering the Ba/Sr atoms as the protrusions on the STM image, using the tilings proposed by Cockayne et al., we can construct a new unit cell for the σ phase, shown in Figure III.15 (a) with a side comparison with the Förster's model in Figure III.15 (b). For simplicity, from now on, the approximant model of Försteret al. [10] will be named Förster-σ and the model of Cockayne et al. [23] will be named Cockayne-σ. The lattice parameters for this new model are fixed based on the DFT cell optimization of the Pt (FCC) (calculated lattice constant of 3.99 Å), also with the optPBE-vdW exchange and correlation functional, resulting in a final Pt(111) supercell with lattice parameters of 14.66 × 14.11 Å. This is in close agreement with the theoretical value of 14.40 × 13.90 Å by Förster et al. and with the experimental value of 13.10 × 12.90 [10] following a Fourier transform of the STM image.

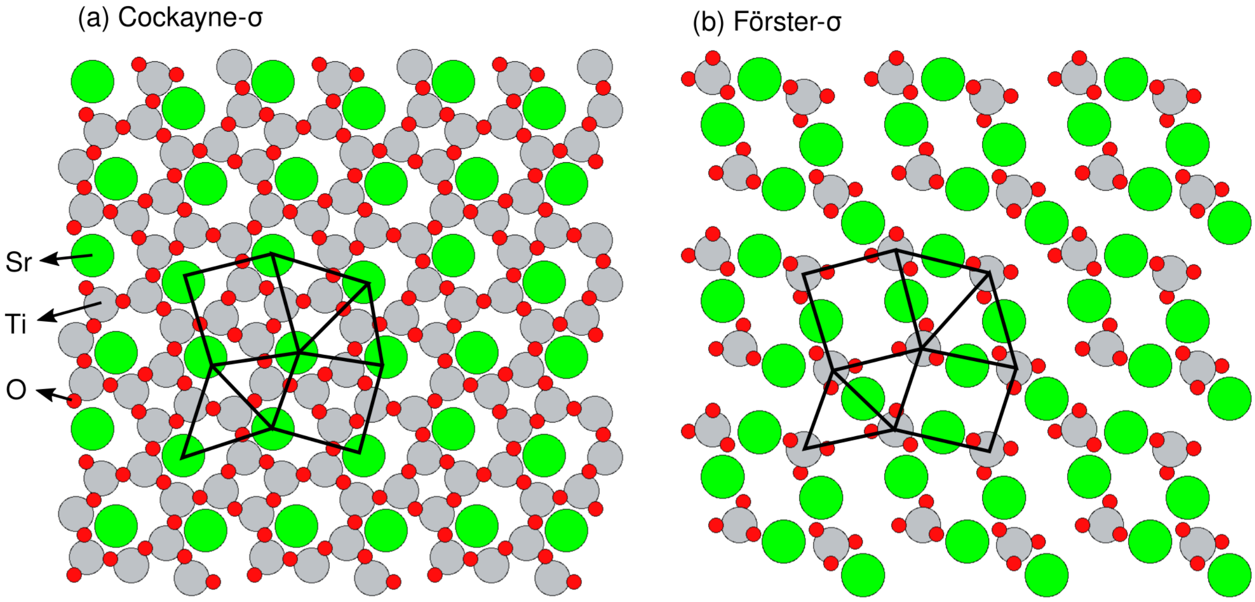

Figure III.15: Comparison between (a) our model based on the tillings by Cockayne et al. [23] and (b) Förster's model [10].

It can be noted in both models that all Ti atoms are surrounded by three O atoms (local 3-fold symmetry), while only in Cockayne-σ model each oxygen atom is located between two Ti atoms, possibly resulting in different oxidation states for Ti, when neglecting vacancies. In addition, a clear difference between both structures is that in Figure III.15 (a) we see a connected chain of Ti–O bonds, closely resembling a more simple and organized honeycomb structure also found on a similar thin oxide system (Ti_2O_3/Au(111)) [76]. We can visualize the formation of Ti_nO_n rings with $n = 4$ or $n = 7$ for the Cockayne-σ model, but the rings can also be found for $n = 5$ or $n = 6$ for other structures [23]. As a result, we have a much higher atomic density for the Cockayne-σ model (0.16 at./Å^2) than for the Förster-σ model (0.10 at./Å^2), both values considering a supercell area of 206.8 Å^2, possibly leading to a stronger adhesion energy with the metallic Pt(111) surface.

The same model used to create the Cockayne-σ model can be used for all approximants on this system consisting on the three tiling configurations. In this section, we will be focusing only on the general properties of this new approximant model on the Cockayne-σ model due to the relatively small unit cell compared to the other approximants, which could unveil the characteristics in the metallic-oxide interface for all approximants and quasicrystals found on these systems.

III.1. Specific computational details

All calculations were performed with density functional theory (DFT) using the Vienna ab initio simulation package (VASP) [89]–[91] combined with the atomic simulation environment (ASE) [174]. Spin-polarised calculations were performed with a plane-wave basis set and projector-augmented wave (PAW) method [115]–[117], using the optPBE functional [110], [176]. The following electrons were treated explicitly: $4s^2 5p^6 6s^2$ (Sr), $2s^2 2p^4$ (O), $3s^2 3p^6 4s^2 3d^4$ (Ti), and $5d^9 6s^1$ (Pt). The strong on-site Coulomb interaction of localized electrons was treated through the GGA+U approach [114], using U(Ti) = 1.0 eV [27], [177]. This value has been chosen because it provides a good agreement with theoretical quantities calculated using the hybrid HSE03 exchange correlation potential, as demonstrated recently in the case of an oxide layer with the honeycomb structure supported on a metal substrate [27], [75]. The one-electron Kohn–Sham orbitals were expanded in a planewave basis set with a kinetic energy cutoff of 500 eV. Total energies were minimized until the energy differences were less than 10^{-5} eV between two electronic cycles. The reciprocal space integration was sampled with a $3 \times 3 \times 1$ k-grid for the Cockayne-σ model and at the Γ k-point for the other approximants for total energy calculations. The partial occupancies have been considered within the Methfessel–Paxton scheme with a smearing set to 0.2 eV. A denser k-point grid of 6 x 6 x 1 was used for the DOS and COHP calculations for the Cockayne-σ structure, respectively. This set-up gives cohesive energies and lattice parameters of bulk systems in good agreement with the experimental data [26]. The ultrathin oxide (UTO) films supported on Pt(111) have been built using asymmetric slabs consisting of three Pt(111) layers and one oxide-layer. The bottom layer of the Pt substrate was kept fixed, while all other layers were allowed to fully relax in all directions, using the conjugate gradient algorithm, until all forces were less than 0.05 $\mathrm{eV\AA^{-1}}$. Adjacent slabs (along the surface normal direction) were separated by a 20 Å thick vacuum layer and dipole correction was applied to cancel the artificial electric field that develops due to imposed periodic boundary conditions in the surface normal direction. The average charges on each atom were calculated with the Bader approach [136], using the code distributed by the Henkelman group [137]–[140]. The STM images were calculated using the Tersoff-Hamman approximation [141], [142]. Charge differences were calculated by $\rho_{\mathrm{UTO/Pt}} - \rho_{\mathrm{Pt}} - \rho_{\mathrm{UTO}}$, where $\rho_{\mathrm{UTO/Pt}}$, ρ_{Pt} and ρ_{UTO} are the charge densities of the UTO/Pt(111) slab, Pt(111) slab and UTO free standing layer, respectively. Structures and STM images were plotted using VESTA [175] and p4vasp software, respectively.

The slab for the Cockayne-σ approximant phase shown in Figure III.15(a) is created by depositing the oxide on a Pt(111) supercell surface (with a final lattice parameter of 14.67 Å ×14.11 Å) 3 Å apart. A vacuum of 15 Å is applied to avoid interactions between the top and bottom terminations (due to periodic boundary conditions) and to simulate UHV conditions. At this stage, we are not considering any rotation of the oxide. We consider four layers of Pt(111) substrate, fixing the bottom layer to simulate the bulk structure and allowing the upper three layers to relax to account for the interactions with the oxide. After the model is built, we perform a structural relaxation with DFT using the parameters described in Section III.1. The final relaxed structure is shown in Figure III.16.

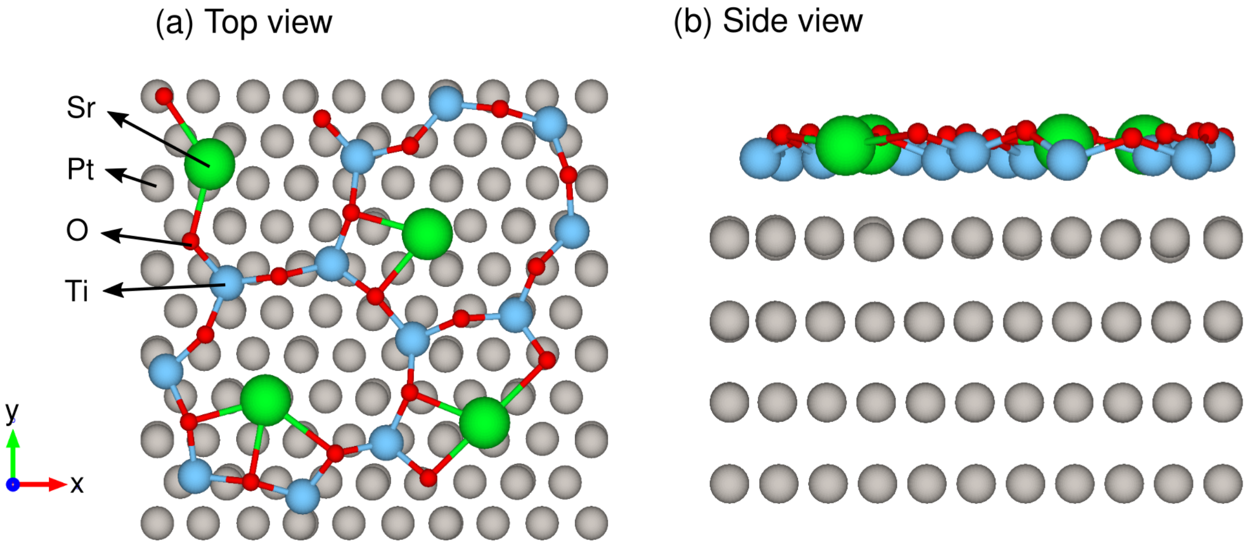

Figure III.16: (a) Top and (b) side view of the relaxed Cockayne-σ approximant phase.

In the relaxed Cockayne-σ structure, the tiling configuration are maintained, while the most visible distortion is the rotation of each three O atoms around the Ti atoms. Besides, we can identify that the closest atoms to the first layer of Pt are the Ti atoms, with the height of 2.33 Å, while Sr and O atoms are located at 2.71 Å and 2.96 Å, respectively. The average Ti–O bond is 1.9 Å. The O atoms may be very far from the substrate due to eletrostatic repulsion, since the average charge obtained by the Bader method [136]–[140] of both elements (O and the first layer of Pt) are negative (-1.2 e and -0.1 e, respectively), while Ti and Sr are positive (1.5 e and 2.0 e, respectively). All structural results are in excellent agreement with the values obtained by Cockayne et al. [23] for the Ba-Ti-O/Pt(111) system, where they reported and

Ti–O distances ranging from 1.80 to 1.95 Å and average heights of 3.10, 2.20, and 3.10 Å for Ba, Ti, and O, respectively.

III.2. Interfacial properties

One of the main goals of the present work is to fully characterize the interfacial properties of the 2D approximant phases and identify the aspects that govern the metal–oxide interaction.

In order to characterize the charge transfer and the chemical bonds between the oxide and metal, we calculated the *charge density difference*, which is, as a reminder, given by the difference in the charge of the complete and separated systems:

$$\Delta\rho(\mathbf{r}) = \rho_{\mathrm{slab}}(\mathbf{r}) - \rho_{\mathrm{oxide}}(\mathbf{r}) - \rho_{\mathrm{substrate}}(\mathbf{r}) \tag{III.2}$$

We used the planar averaged charge density difference $\Delta\overline{\rho}(z)$, defined as:

$$\Delta\overline{\rho}(z) = \frac{1}{A}\int_A \Delta\rho(x,y,z)\mathrm{d}x\mathrm{d}y \tag{III.3}$$

where the integration spans the slab's surface area and z is the direction perpendicular to the surface. This quantity was obtained with the help of the VASPKIT code [194].

Figure III.17 (a) shows the result of the planar averaged charge density difference for the Cockayne-σ phase. It should be noted that $\Delta\overline{\rho}(z)$ is very similar to the one obtained for the Förster-σ approximant (Figure III.7). The electron charge is being concentrated at the bonding region (gray area) and the oxide as a whole is losing its electrons to the interface region and to the first layer of Pt, which is consistent with the Bader analysis. A side view of the 3D charge density difference is shown in Figure III.17 (b) alongside the Cockayne-σ/Pt(111) structure.

The overall strength of the interaction between the approximant and the Pt substrate (E_{adh}) can be measured by DFT using a difference in the ground-state total energies given as:

$$E_{\mathrm{adh}} = E_{\mathrm{sys}} - E_{\mathrm{oxide}} - E_{\mathrm{substrate}} \tag{III.4}$$

where E_{sys}, E_{oxide}, and $E_{\mathrm{substrate}}$ are the total energies of the complete system, the isolated oxide, and the substrate, respectively.

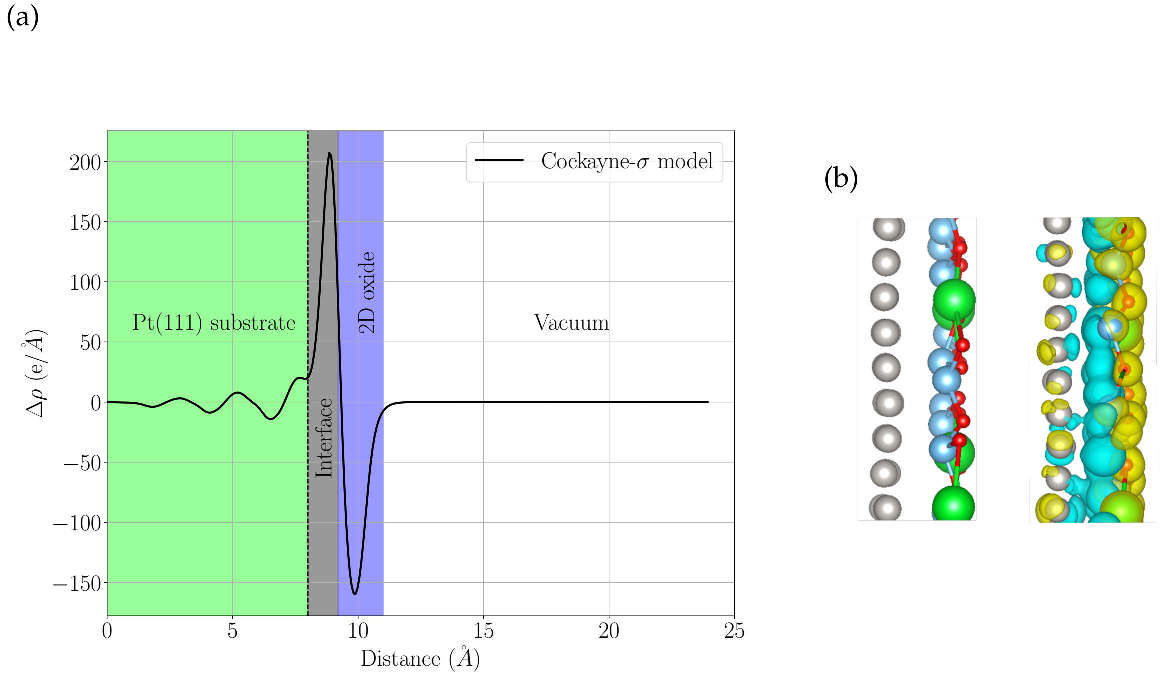

Figure III.17: (a) Planar averaged charge density difference 2D plot of the Cockayne-σ/Pt(111) system. (b) Side view of the Cockayne-σ/Pt(111) structure alongside its charge density difference. The blue region is given by a concentration of electrons, and the yellow region is losing its electrons. Plotted using the VESTA code [175]. Sr, Ti, O, and Pt are represented as green, blue, red, and gray, respectively.

For the Cockayne-σ/Pt(111) system, the adhesion energy is -0.23 eV/Å^2, which is much stronger than that calculated for the Förster-σ approximant (-0.07 eV/Å^2), but weaker than for the honeycomb structure (-0.40 eV/Å^2). In order to analyze the individual contribution of each bond to the oxide/substrate adhesion and obtain a more global view of the interface, we used the COHP method [24] as implemented in the LOBSTER program [25]. For this calculation, the number of non-occupied bands was increased by 10% and the k-points fixed to $6 \times 6 \times 1$. The final results were analyzed with a Python script using mainly the modules provided by Pymatgen [195].

Figure III.18 (a)–(d) show the average calculated COHP for the Ti–Pt, Ti–O, Pt–Sr, and O–Sr bonds up to a maximum distance of 4 Å respectively. Since there are no oxygen atoms within 4 Å of any Pt atoms, the interactions considered with the substrate were those with Ti and Sr. In this analysis, negative values of the COHP (blue region in Figure III.18 (a)) are given by bonding states, resulting in strong interactions and hybridization of the orbitals, while positive values (gray region in Figure III.18 (a)) represent the anti-bonding states.

(a) Ti–Pt bonds (b) Ti–O bonds

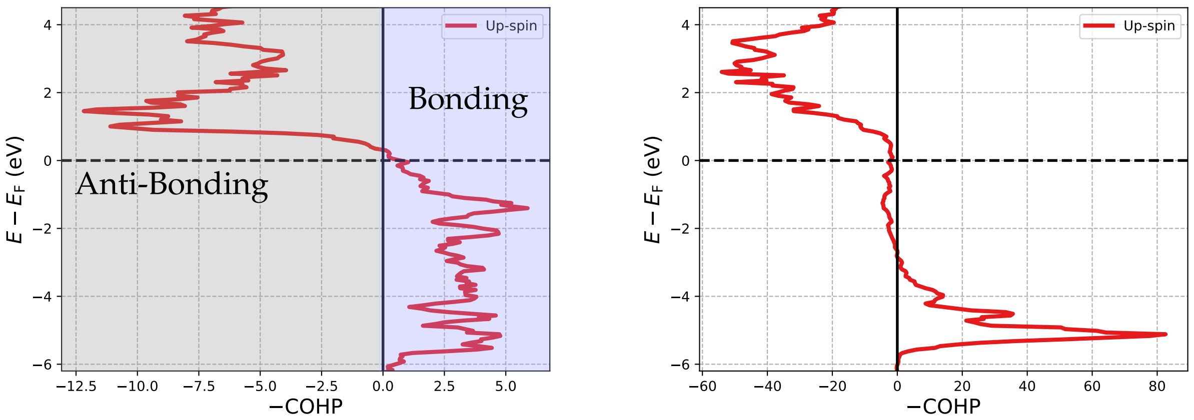

(c) Pt–Sr bonds (d) O–Sr bonds

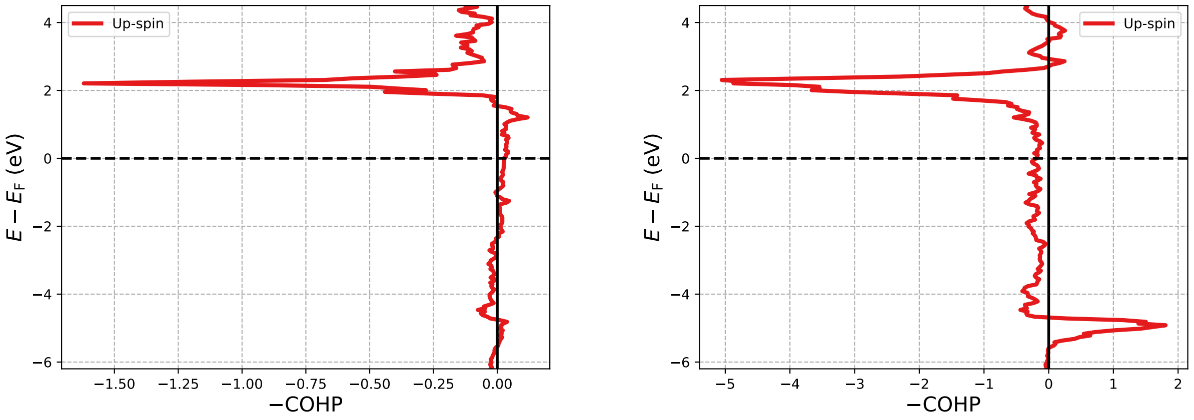

Figure III.18: Averaged COHP results for the (a) Ti–Pt, (b) Ti–O, (c) Pt–Sr, and (d) O–Sr bonds. Figure (a) shows a representation of the bonding (right, blue) and anti-bonding contributions (left, gray).

Regarding the oxide–substrate interaction, it can be seen in Figure III.18 (a) and (c) that there is a high amount of bonding states in the Ti–Pt bonds, resulting in a very stable interaction, while there is little (almost none) bonding states in the Sr–Pt bonds. This result may show that the main bonds responsible for the adhesion of the oxide to the substrate are the Ti–Pt bonds, with an ICOHP average of -1.63 eV with 17 considered bonds, in contrast to the Sr–Pt bonds with ICOHP of -0.50 eV for 4 bonds. Here, we considered all bonds up to a distance of 4 Å. Note that COHP measures only the covalent contribution to each bond, hence even though that our results point strictly to the fact that the Ti–Pt are the most important for the adhesion, we can not affirm for sure that the Sr–Pt interaction is negligible.

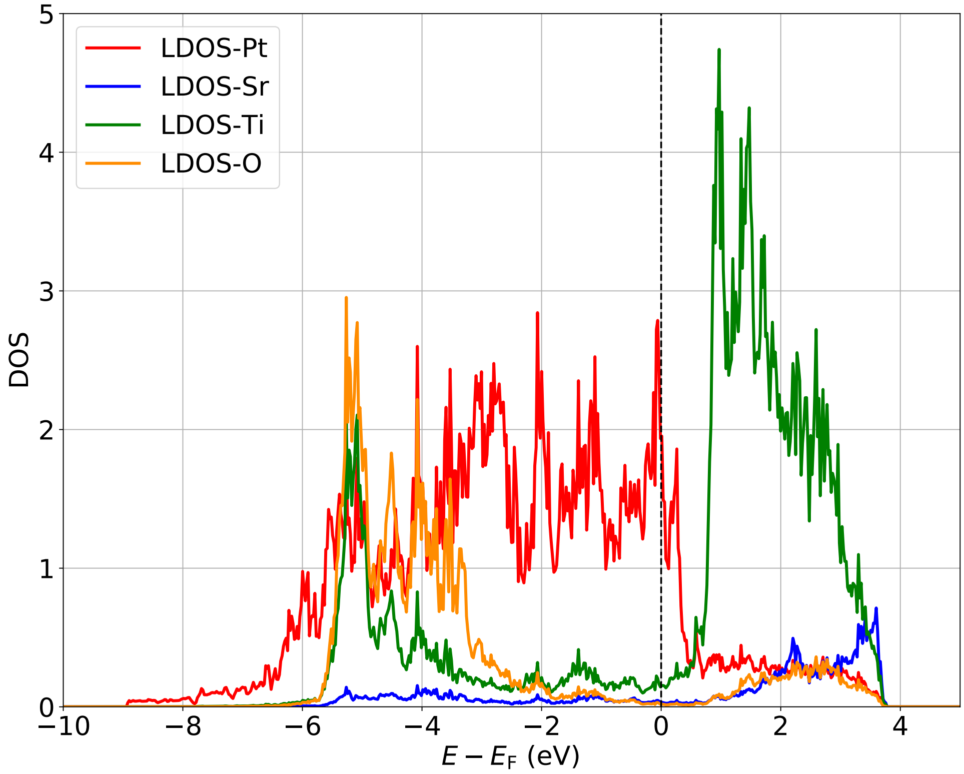

Figure III.19: Local density of states for the Cockayne-σ approximant.

Looking at the bonding in the oxide (Figure III.18 (b) and (d)), we can identify a strong Ti–O hybridization with an average ICOHP of −4.17 eV for 30 bonds considered, which is predominant in the energy region between −6 and −4 eV. This result is consistent and can also be visualized in the LDOS for this structure, as seen in Figure III.19. There is also a significant hybridization in the same energy range for the Sr–O bonds with an average ICOHP of −0.26 eV for 12 bonds considered. This result shows that the Ti atoms dominate the covalent bonding character in this system, having a higher ICOHP either in the oxide–substrate and intra-oxide bonding, while the Sr atoms present a much weaker interaction, leading to the conclusion that the latter interaction in the system is either weak or with a high amount of ionic bonding, as suggested in the Bader charge analysis.

A similar analysis was also performed for the unsupported system (without the Pt(111) substrate) in order to identify the bond strengths in the oxide. The results are shown in Figure III.20 (a) and (b). By comparing the COHP curves of Figure III.18 and Figure III.20, it is interesting to see that by removing the substrate interaction from the oxide, the in-plane bondings inside the oxide show a considerable increase in the amount of anti-bonding states. The case of the Sr–O bonds is even more extreme, since there the anti-bonding states dominate over the entire occupied states energy range. This evidence shows that the Pt interaction specially with the Ti atoms may be the key factor for the formation of the bonding states at the interface and in the two-dimentional oxide, leading to an overall stabilization of the supported system.

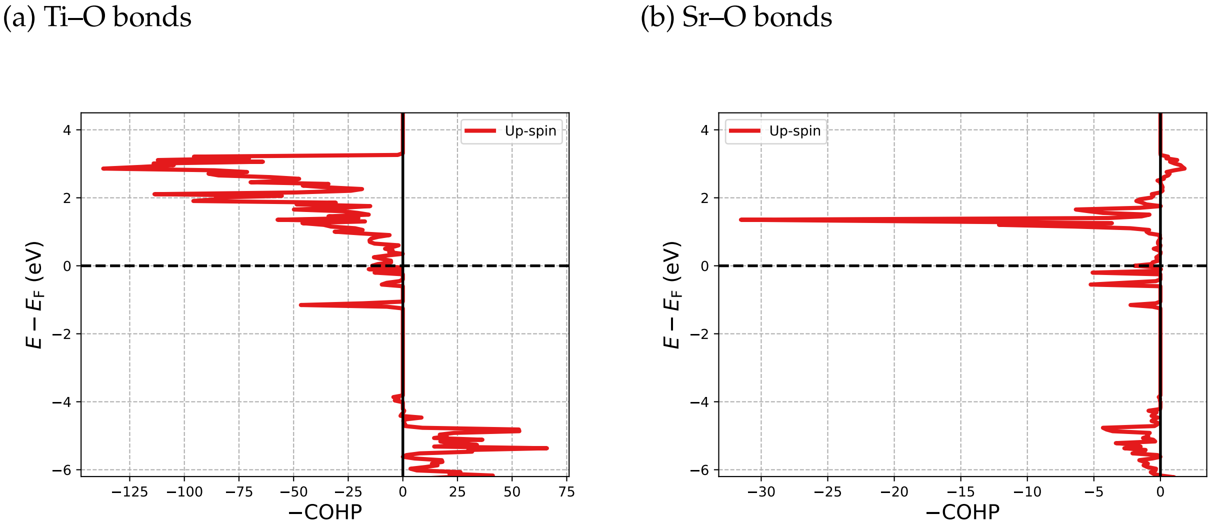
(a) Ti–O bonds

(b) Sr–O bonds

Figure III.20: Averaged COHP results for the (a) Ti–O and (b) Sr–O bonds.

III.3. Stability using *ab initio* Molecular Dynamics (AIMD)

In order to test the structural stability of the Cockayne-σ phase supported on Pt, we use the AIMD methodology to see different combinations of structures with its corresponding total energies. For this method, we used the canonical ensemble with the system in thermal equilibrium with a heat bath at a fixed temperature of 1000 K using the Nosé-Hoover thermostat. Hence, we simulated this phase in the temperature range where it was experimentally obtained. [10]. The number of particles (N) and the system's volume remains fixed, being part of what is called the NVT ensemble. We fixed the time steps to 2 fs while running the simulation for a total of 6000 steps, getting 12 ps of total simulation time. The number of k-points was reduced to only the Γ k-point due to the size of the simulation.

The evolution of total energy during the simulation is shown in Figure III.21, with the colorbar corresponding to the instantaneous temperature. From this result, we can select the most stable and unstable structure and identify qualitatively the cause of its stabilization/destabilization. First, we can identify two of the most stable structures (A and B).

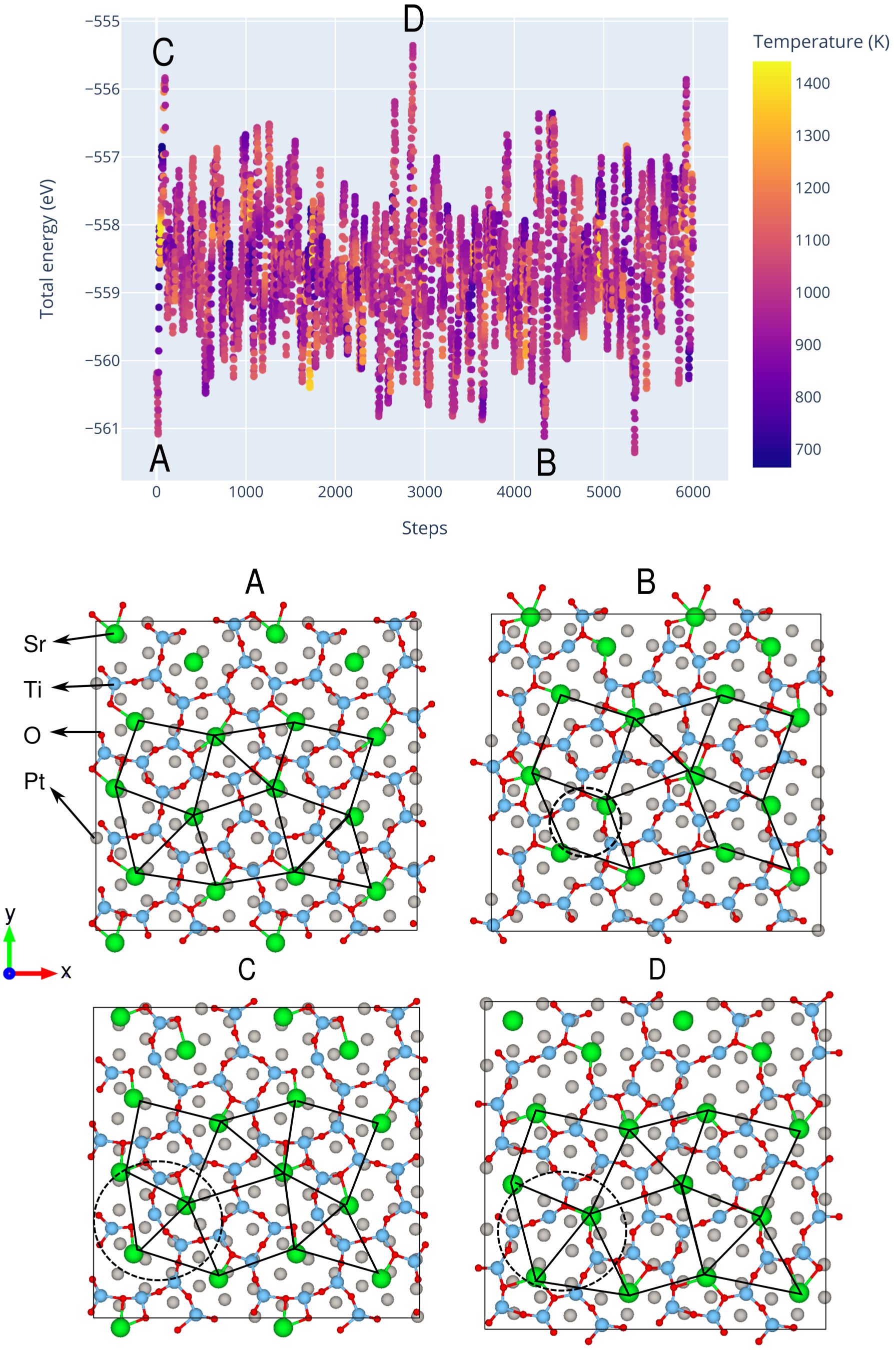

Figure III.21: *Ab initio* molecular dynamics performed for the σ-phase approximant. 6000 steps were performed with 2 fs between each step. The colorbar indicates the temperature at each structure.

The first (A) correspond to the starting configuration which was created directly from the experimental STM image. The second (B) shows that another possible stable configuration is a combination of the breaking of a Ti–O bond with the creation of a rhomboedrical tiling by the Sr atoms.

Finally, for the two least stable configurations (C and D), the first is very close to the initial state, but with a strong Ti–O bond broken in the oxide without forming any new Sr tiling (only a triangle tiling is slightly distorted). The second has the same Ti–O bond broken but without forming the rhomboedric configuration.

For a more complete view of other possible stable and unstable structures, we would need a much longer AIMD run, which is highly computationally demanding considering a structure of the size of the Cockayne-σ model. Nonetheless, this is a great starting point showing what are other configurations are probable during a heat treatment in the temperature range shown in Figure III.21, and that the structure analyzed in detal in the current section (structure on the bottom left of Figure III.21) is indeed one of the best structures so far identified.

IV. Conclusion

In the first part of this chapter, concerning the Förster-σ approximant model of Förster et al. [10], more than 80 ABO_3/Me systems ($A \equiv$ alkali earth metal, $B \equiv$ transition metal, Me $\equiv$ metal substrate) have been computationally explored. The relative stability of aperiodic oxide ultra-thin films, described with the approximant models, have been assessed against periodic atomic arrangements with similar compositions, and insights have been given to understand how OQA chemistry influences their atomic structures and properties.

The rumpling of the oxide film, the interfacial electron transfer and the adhesion energies display general trends within the series. Magnetic properties are influenced by the nature of the substrate and the B-metal, whereas the type of earth alkaline metal A impacts $\Delta\Phi$, i.e., the change in the metallic substrate work function induced by the deposition of the oxide film.

Notably, no clear correlation was found between the surface cell mismatch and the rumpling or the adhesion energies (Figure III.5 (a-d)) although size-mismatch is generally believed to be the main driving force towards the formation of ultra-thin oxide layers on metals, including OQAs. In contrast, electronic effects were identified as important parameters that influence the formation of OQAs. In particular, the rumpling and the adhesion energies roughly correlate with the charge transfer, determined through the charge on the B-type metal.

The second part of this chapter was also devoted to the σ phase but considered the model of Cockayne et al. [23] instead. The overall stability of this Cockayne-σ approximant phase was tested with AIMD. The AIMD simulation shows that indeed this oxide is relatively stable at the surface of Pt(111), being able to maintain its structural motifs throughout the whole simulation, but showing that there are specific Ti–O bonds that may break and form other types of tilings, such as a transition from a triangle to a rhombus, while other Ti–O bonds remain unbroken.

COHP calculations have demonstrated that the main bonds that account for the adhesion between the oxide and the Pt(111) substrate are the Pt–Ti bonds, which present high covalent bonding character, only with anti-bonding only appearing in the non-occupied states. Our assumption is that these Pt–Ti bonds may stabilize the structure of the oxide approximant as a whole, since the COHP calculation of the unsupported approximant revealed a considerable amount of anti-bonding interactions not only at the interface, but also within the oxide layer, such as the Sr–O and Ti–O bonds.

Chapter IV

Ultra-thin films of quasi-periodic oxides: DFT modeling from Niizeki-Gähler tiling and atomic decorations of tiles

I. Introduction

In this chapter we will present the results on other approximant phases that can be found in the literature (including phases that were described in our laboratory by the group of Dr. Vincent Fournée), as well as potential approximants (or at least that have not yet been discovered experimentally) created manually from an ideal Niizeki-Gähler tiling (NGT) configuration, in the Sr–Ti–O/Pt(111) system. First, we describe how to model these structures on a Pt(111) substrate, following by a discussion on the interaction between the oxide and substrate to justify the models created. This chapter ends with a discussion on the general properties (enthalpies of formation, charge distribution, adhesion energies, etc.) of these approximant phases.

II. Specific Computational Methods

All calculations were performed with Density Functional Theory (DFT) using the Vienna *ab initio* simulation package (VASP) [89]–[91] combined with the Atomic Simulation Environment (ASE) [174]. Spin-polarised calculations were performed with plane-wave basis set and projector-augmented wave (PAW) method [115]–[117] using the optPBE functional [110], [176]. The following electrons were treated explicitly: $4s^2 4p^6 5s^2$ (Sr) $2s^2 2p^4$ (O), $3s^2 3p^6 4s^2 3d^4$ (Ti), $5d^9 6s^1$ (Pt). The strong on-site Coulomb interaction of localized electrons was treated through the GGA+U approach [114], using the values for U from the literature [27], [177]: 1.0 eV (Ti). The one-electron Kohn-Sham orbitals were expanded in a plane-wave basis set with a kinetic energy cutoff of 500 eV. Total energies were minimised until the energy differences were less than 10^{-5} eV between two electronic cycles. Due to the size of the approximant phases and memory limitations, the reciprocal space integration was approximated with a Γ k-point and $2 \times 2 \times 1$ k-mesh for the structural relaxations and the density of state calculations for the hexagonal approximant, respectively.

The Sr–Ti–O_3/Pt(111) systems have been built using asymmetric slabs consisting of three Pt(111) layers and one oxide layer. Adjacent slabs (along the surface normal direction) were separated by 20 Å of vacuum and a dipole correction was applied to cancel an artificial electric field that develops due to imposed periodic boundary conditions in surface normal direction. All atomic positions, with the exception of the bottom layer of Pt, were relaxed using the Conjugate Gradient Algorithm until all forces were less than 0.1 eV/Å^2. Structures and STM images were plotted using VESTA [175] and p4vasp (`https://github.com/orest-d/p4vasp`) software, respectively.

III. Comparison between approximants

III.1. Choice of the supported model

There are two main decisions that one need to make when modeling complex 2D approximant phases, which are the lattice parameters of the supported system and how to orient the oxide related to the Pt(111) substrate. For the first question, we fixed the lattice parameter of the Pt(111) support according to the supercell generated from the relaxed bulk Pt ($a = 3.99$ Å) with the optPBE-vdw functional. The second question is harder to answer, since there are many ways in which one can orient the 2D complex approximant on top of the Pt(111) substrate. Here, we have chosen one orientation and several lateral positions for the oxide film, in order to test whether the total energy varies according to the relative position of the film and the substrate.

In order to determine how to orient the oxide related to the Pt(111) substrate, we created several translated models of the Cockayne-σ phase with different amounts of Ti located in the hollow sites of the Pt(111) surface (Figure IV.1), as represented in Figure IV.2.

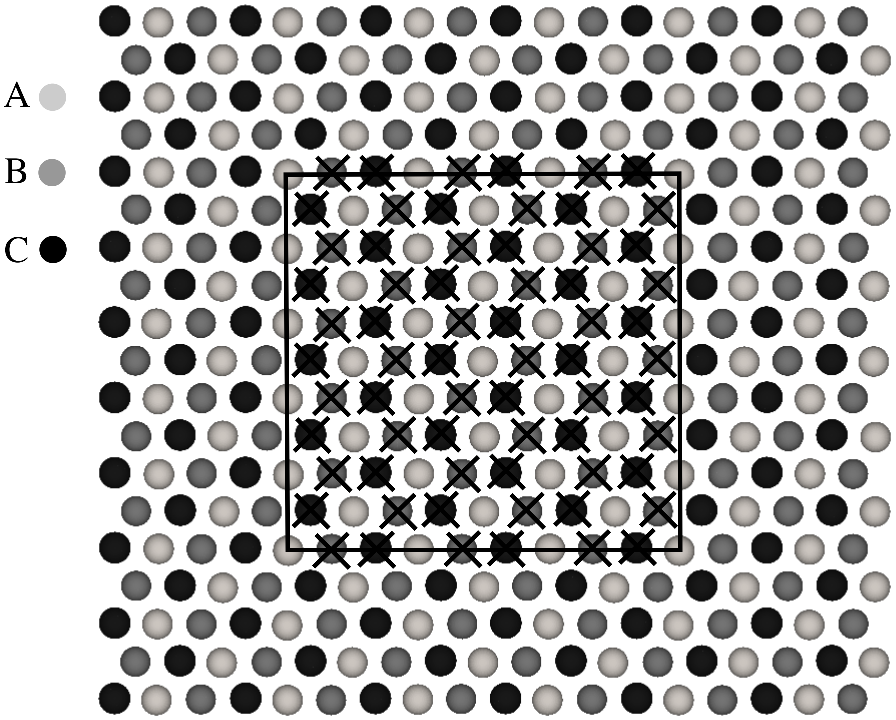

Figure IV.1: Hollow sites on the Pt(111) substrate used to support the Cockayne-σ model. The ABC staking is shown by different shades of gray, where A is the first Pt layer, B is the second, and C is the third layer. The supercell orientation is $\begin{pmatrix} 6 & 3 \\ 0 & 5 \end{pmatrix}$.

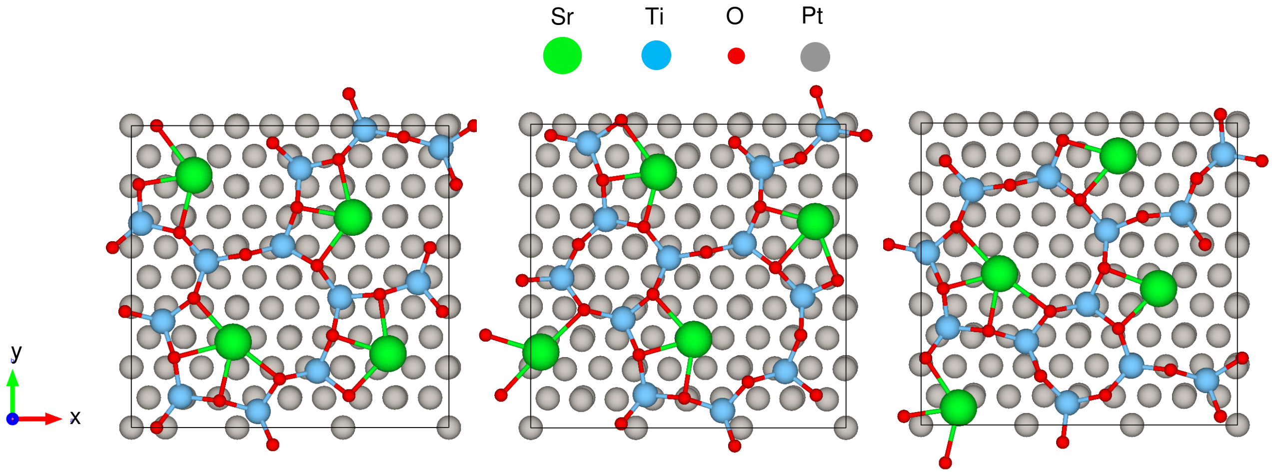

Figure IV.2: Three examples of the Cockayne-σ approximants with the oxide translated with respect to the Pt(111) substrate.

The algorithm used to determine whether each Ti atom is located in the hollow, bridge, or ontop position on the Pt(111) surface are described as follows:

- Create a list with the hollow, bridge, and ontop's positions;
- For each point, create a circle of radius $r = 0.5$ Å.
- Create a list with the position of the Ti atoms.
- Verify, using the following formula, how many Ti atoms are centered in hollow, top, or bridge sites.

$$(x - x_0)^2 + (y - y_0)^2 < r^2 \tag{IV.1}$$

  where x and y is the Ti atom's coordinate, x_0 and y_0 is the hollow site's coordinate, and r is the radius.

The comparison between the total energy and the amount of Ti in the hollow sites are shown in Figure IV.3. Despite the intuition that the structures with higher amount of Ti in the hollow sites would give a more stable structure (and stronger adhesion), the calculations did not confirm this expectation. Figure IV.3 reveals that the total energy is similar for all considered models and does not depend on the relative position of the film and the substrate.

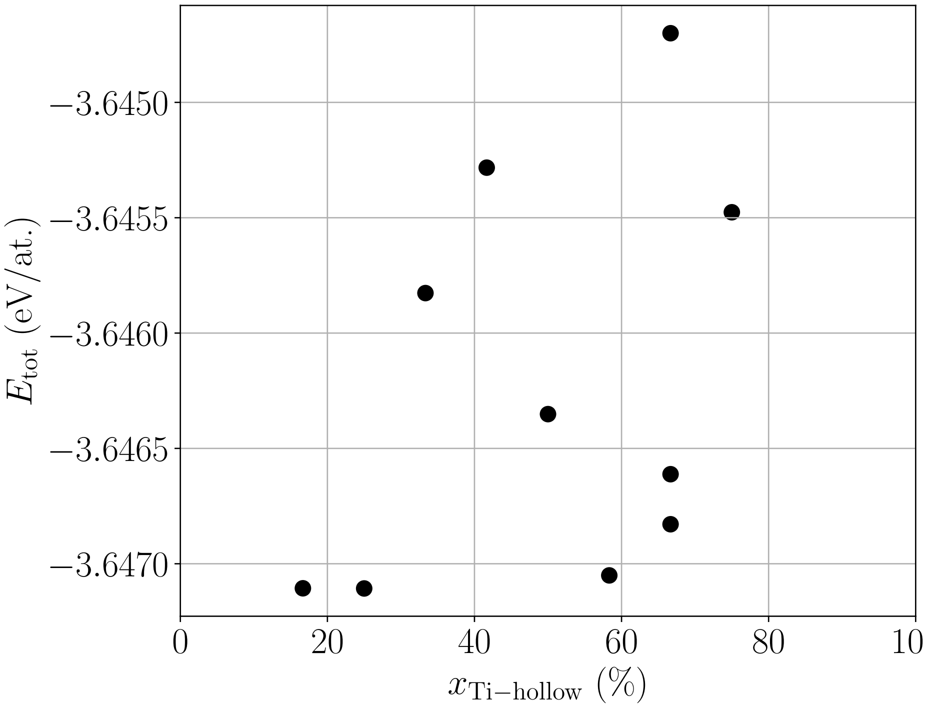

Figure IV.3: Total energy of the system vs the percentage of Ti atoms in the hollow sites.

These results lead us to assume that positioning of the Ti atoms with respect to the Pt substrate does not alter significantly the total energy. Another aspect of this conclusion will be addressed in the Section IV., with a comparison between all approximants calculated.

III.2. Hexagonal and giant square-like approximants

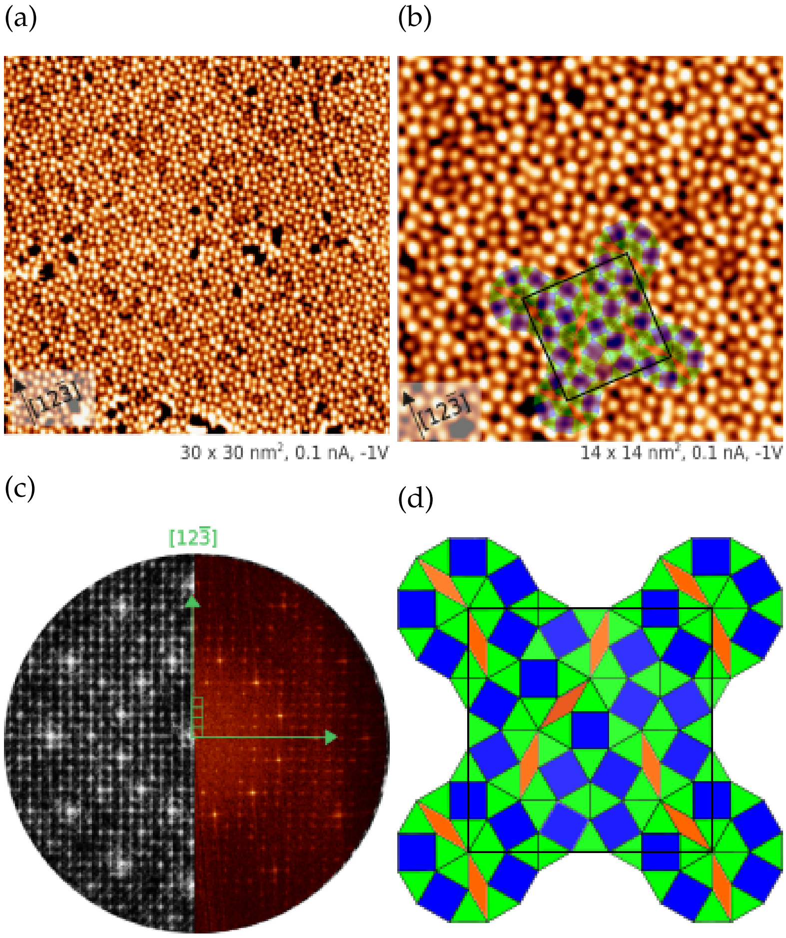

Figure IV.4: (a) Atomically resolved STM image of the STO derived approximant formed on Pt(111). (b) STM image of the square approximant with the square-like unit cell superimposed. (c) Left: Calculated FT of the idealized tiling. Right: FT of the STM image in (a). The square unit cell is colored in green (b). (d) Tiling decoration of the square unit cell. Reproduced from [79] with permission from the PCCP Owner Societies.

Recent experimental evidence on the Sr-Ti-O/Pt(111) system developed by the research group of Dr. Vincent Fournée at Institut Jean Lamour discovered two new approximant phases [79] derived from the same dodecagonal NGT configuration found for the oxide quasicrystal [9]. The experimentalists used a combination of STM, LEED, and XPS to characterize the surface structure.

For the giant square approximant phase, the real space structure and the local atomic arrangements were determined from atomically resolved STM images taken at room temperature (Figure IV.4 (a)). Although the LEED pattern shows an apparent dodecagonal pattern typical of an OQC, the Fourier transform (FT) of the real space image reveals an almost periodic square lattice, indicating that an approximant was formed instead of an OQC [79], [196]. The FT was used to determine the lattice parameters. Figure IV.4(b) gives a more detailed view of the identified approximant unit cell, with the in-plane measured lattice parameters of 42.2 ± 0.6 Å × 43.2 ± 0.6 Å, and angle between the edges of 89.7 ± 0.41 Å. The bright protrusions seen in the STM images are at the nodes of the same NGT tiling elements used to describe dodecagonal structures [70].

From the STM image on Figure IV.5 (a), an average distance of 6.4 ± 0.3 Å between the bright protrusions is deduced. The edge length of the tiling elements deduced from the ideal unit cell is 6.53 Å, for the vertical axis, and 6.68 Å, for the horizontal axis. The tiling decoration is shown in Figure IV.4 (d). The unit cell of the approximant can be expressed as a superstructure with respect to the Pt(111) lattice, resulting in the lattice parameters of 44.87 Å × 43.75 Å, with an angle between the edges of 89.7° and the Pt(111) primitive unit cell is fixed to 2.79 Å.

With increasing the number of oxidation–reduction cycles under the same experimental conditions as described earlier, another new UTO phase was observed having a large hexagonal unit cell. Figure IV.5 (a) and (b) show high resolution STM images of this structure, as well as the tiling decoration. The FT calculated image from this tiling decoration and the FT calculated image from the experimental STM image are shown in Figure IV.5 (c). The dimensions of the unit cell edges are $a = 27.8 \pm 0.6$ and $b = 28.1 \pm 0.6$ Å. This hexagonal unit cell can be decorated with the NGT tiling elements. A common edge length of 6.7 ± 0.2 Å is deduced from the average distance between the bright protrusions, and the lattice parameter of the hexagonal phase is 26.61 Å.

With the tile decoration model shown in Figure IV.4 (d) and Figure IV.5 (d) and using the composition and atomic positions by Cockayne et al. [23], the chemical composition of the square approximant is determined as $Sr_{0.36}TiO_{1.54}$ and that of the hexagonal phases as $Sr_{0.38}TiO_{1.56}$. The two structures are represented in Figure IV.6. They are very close to that of the ideal NGT tiling of the quasicrystalline phase with the same tile decoration model of $Sr_{0.37}TiO_{1.55}$ [23]. The surface atom densities of the square approximant and the hexagonal phase are 19.6 and 18.7 at./nm^2, respectively. The number of Sr atoms per surface unit cell deduced from these atom densities are in agreement with the number of vertices per unit cell deduced from the experimental STM images.

The top and side views of the relaxed giant and hexagonal approximants using the three tiling elements of Cockayne et al. [23] are shown in Figure IV.5 (a) and (b).

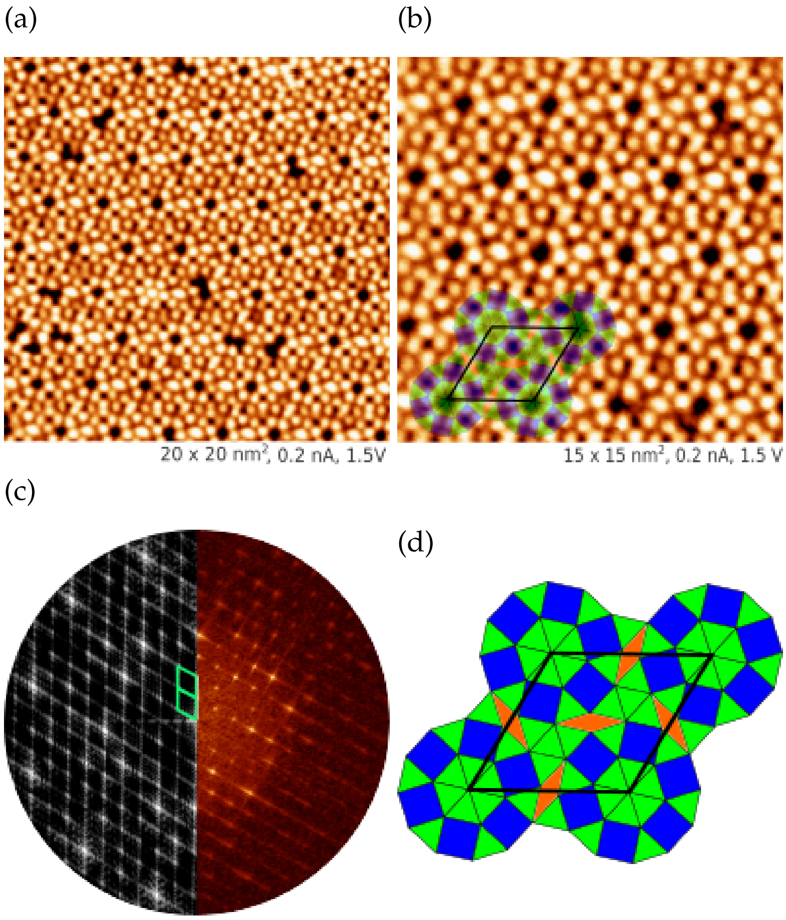

Figure IV.5: (a) Atomically resolved STM image of the STO derived large hexagonal phase formed on Pt(111). (b) Idealized unit cell of the large hexagonal phase decorated by the dodecagonal tiling elements: squares, triangles and rhombuses superimposed on the real STM image. (c) Left: Calculated Fourier Transform (FT) of the idealized tiling. Right: Fourier Transform (FT) of the STM image in (a). The hexagonal unit cell is colored green in (b). (d) Tiling decoration of the hexagonal unit cell. Reproduced from [79] with permission from the PCCP Owner Societies.

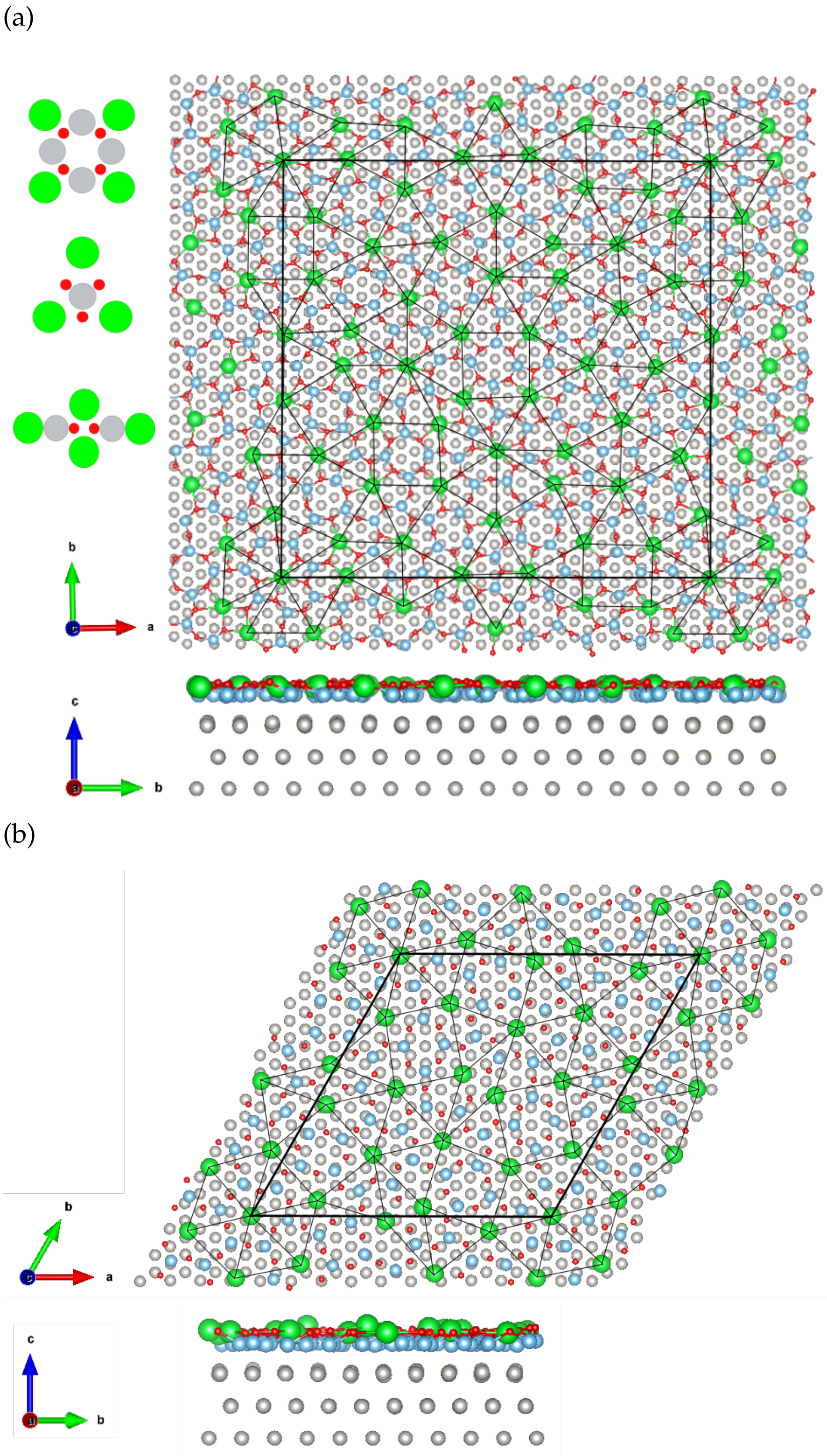

Figure IV.6: Top and side views of the relaxed (a) giant-square and (b) hexagonal approximant structures, along with the three types of tiles used to build it. Sr, Ti, O and Pt atoms are shown in green, blue, red and silver, respectively.

III.3. Monoclinic and small hexagonal approximants

We chose three more distinct phases from the literature to compare their general properties: two monoclinic approximants and one small hexagonal phase. The monoclinic approximant was first discovered by the work of Schenk et al. [12]. It has an angle of 95.1° and the lenghts of the short and long side axes of 25.1 Å and 37.7 Å, respectively. It contains all three tiling configurations discussed so far and is structured by 36 of such tilings (3 rhombs, 9 squares, and 24 triangles). In addition, as realized by Förster [193], the distribution of these tilings can be reorganized into a modified and stable monoclinic phase with a very similar local configuration. These structures are shown in Figure IV.7 (a) and (b). A supercell of Pt(111) with lattice parameters of 39.5 Å and 24.4 Å was used as a substrate for these approximants. We decided to orthogonalize the unit cell of these monoclinic structures to facilitate their deposition on Pt(111).

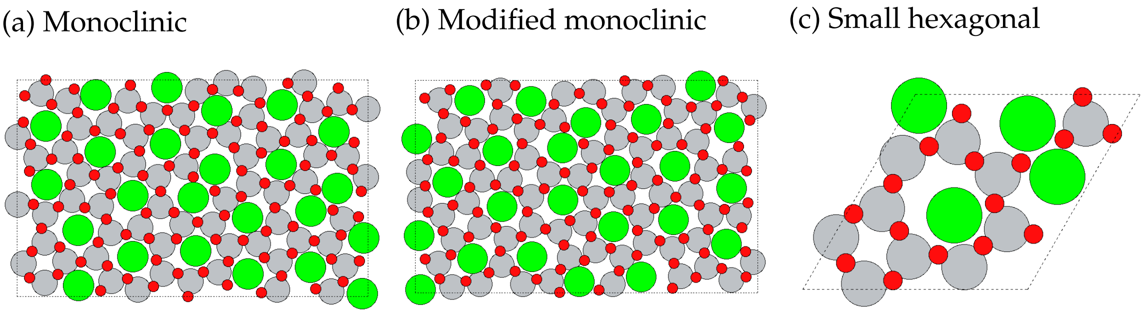
(a) Monoclinic
(b) Modified monoclinic
(c) Small hexagonal

Figure IV.7: Top view of the (a) monoclinic [12], (b) modified monoclinic [193], and (c) the small hexagonal phase [83]. Sr, Ti, and O are represented as green, gray, and red, respectively.

Another interesting phase that was recently found [83] is shown in Figure IV.7 (c). It is a hexagonal phase that appears as a result of 1D antiphase domain boundaries of neighboring Cockayne-σ phases. It possesses a unit cell with edges of 13.2 Å and 13.3 Å, and we used a supercell of Pt(111) with edges 13.9 Åand 13.9 Å.

III.4. Simulated approximants

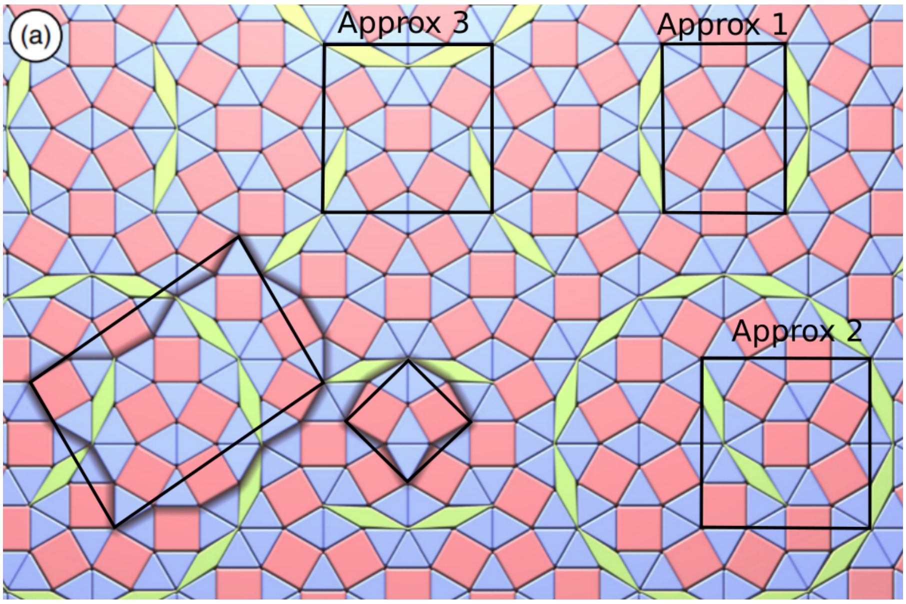

Figure IV.8: Illustration of the relationship of quasicrystals and their approximants on an ideal NGT tiling. Reproduced from [64] with permission from John Wiley and Sons.

Experimentally only a small number of approximants were found. In contrast, the number of potentially possible tiling configurations is unlimited. For this reason, we tried to understand which characteristics the approximants discovered so far possess that other possible tiling configurations do not. In order to answer this question, we manually selected three hypothetical approximant structures from the ideal dodecagonal NGT tiling and named them Approx 1, 2, and 3 Figure IV.8.

By using an edge length of 6.72 Å [12] for all tiling configurations, we can build several fictitious approximants as shown in Figure IV.9 (a), (b), and (c), where supercells of the Pt(111) substrate with lattice parameters of 16.9 Å × 24.4 Å, 25.4 Å × 24.4 Å, and 25.4 Å × 24.4 Å were used, respectively.

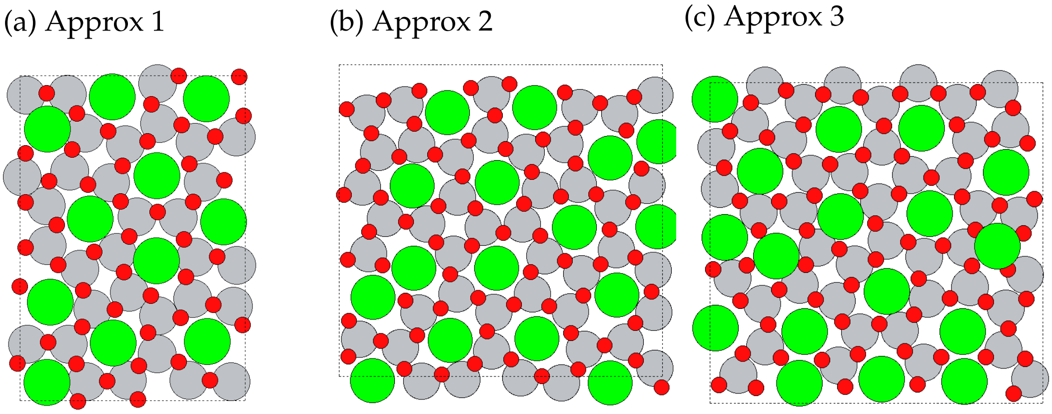
(a) Approx 1 (b) Approx 2 (c) Approx 3

Figure IV.9: Structures of the fictitious approximants created manually from the ideal NGT tiling. Sr, Ti, and O are represented in green, gray, and red, respectively.

IV. Electronic and interfacial properties

The hexagonal and giant complex UTOs present similar formation enthalpies: -1.08 eV/Å^2 and -1.03 eV/Å^2. Their stability at 0 K is higher than the Cockayne-σ, small hexagonal, the fictitious Approx 1, and the monoclinics phases, with enthalpy of formations of -0.62, -0.44, -0.72, -0.60, and -0.60 eV/Å^2, respectively. Interestingly, the phases with the highest absolute value of ΔH_f are the simulated Approx 2 and 3 phases created manually from the ideal dodecagonal NGT tiling (Figure IV.9). This result may suggest that these, and possibly many other approximants, may also be stable, but to answer this question more definitively requires a detailed phonon analysis and variable temperature calculations.

The hexagonal and giant approximants also present similar adhesion energies (-0.30 eV/Å^2 and -0.28 eV/Å^2, respectively). The adhesion energy of the hexagonal phase is the strongest between all phases, while the Cockayne-σ model present the least adherent one. The giant approximant, small hexagonal, all fictitious phases, and the monoclinic phases present similar adhesion energies. This is probably due to the amount of Ti per unit area in the oxide, as is discussed in Section IV.1. When supported on Pt(111), UTOs display significant structural relaxations in the z direction, i.e., the surface normal direction. Such corrugation can alleviate the elastic strain due to the size-mismatch between the unsupported and supported films [26], [27]. It is quantified by the vertical separation between the average z-position of the anions (z^-) and cations (z^+). The rumpling ($R = z^+ - z^-$) is negative for the two complex systems (Table IV.1).

Property	Giant	Hexagonal	Cockayne-σ	Small hex.	Monoclinic	Monoclinic mod.	Approx 1	Approx 2	Approx 3
Freestanding UTO									
$Q_{\mathrm{Ti}}(e)$	1.46	1.40	1.41	1.42	1.41	1.41	1.40	1.41	1.40
$Q_{\mathrm{Sr}}(e)$	1.51	1.51	1.52	1.51	1.50	1.50	1.51	1.52	1.51
$Q_{\mathrm{O}}(e)$	-1.29	-1.27	-1.25	-1.27	-1.26	-1.27	-1.26	-1.28	-1.27
Supported UTO									
R (Å)	-0.41	-0.47	-0.45	-0.42	-0.43	-0.42	-0.42	-0.43	-0.43
$Q_{\mathrm{Ti}}(e)$	2.04	2.07	2.00	2.01	2.01	2.02	2.01	2.01	2.02
$Q_{\mathrm{Sr}}(e)$	1.48	1.46	1.51	1.47	1.48	1.50	1.49	1.49	1.50
$Q_{\mathrm{Pt}}(e)$	-0.11	-0.11	-0.10	-0.08	-0.09	-0.08	-0.10	-0.09	-0.08
$Q_{\mathrm{O}}(e)$	-1.22	-1.17	-1.20	-1.15	-1.17	-1.19	-1.20	-1.18	-1.18
E_{adh} (eV/Å^2)	-0.28	-0.30	-0.23	/	/	/	/	/	/
ΔH_{f} (eV/at.)	-1.03	-1.08	-0.62	-0.44	-0.60	-0.60	-0.72	-1.19	-1.18

Table IV.1: Bader charges on ions, rumpling, adhesion energies, and enthalpies of formation for the approximant phases.

Indeed, the mean vertical distance between the topmost Pt atoms and the Ti atoms is much smaller (2.3 Å) than the one between the topmost Pt atoms and the O or Sr atoms (3.1 Å and 3.2 Å, respectively), in agreement with the values obtained by Cockayne et al. in the Ba-Ti-O system [23].

The rumpling is found to be larger for the complex UTOs ($R_{\mathrm{giant}} = 0.41$ Å and $R_{\mathrm{hex}} = 0.47$ Å for the giant and hexagonal structures, respectively) than for the UTOs with a smaller surface cell ($R_{\mathrm{Forster}-\sigma} = 0.22$ Å and $R_{\mathrm{honeycomb}} = 0.26$ Å for the Förster-σ and the honeycomb structures, respectively).

These structural results can be rationalized by the Bader charge analysis. Charge transfer is found to occur at the Pt/UTO interface, from most electropositive elements (Sr, Ti) to most electronegative elements (Pt and O). Thus, electrostatic interactions likely contribute to the location of Ti cations close to the negatively charged Pt substrate, while repelling the negative O atoms [23]. This is further confirmed by the charge density difference, which indicates non negligible values at the Pt/UTO interface. More generally, electronic effects are known to impact the rumpling and the adhesion energies. Using the Förster-σ, a correlation was evidenced (Figure III.8) between the Bader charge carried by the transition metal atoms (Q_{TM}) and both R and E_{adh}. Overall, a larger Q_{TM} leads to a stronger adhesion of the film and a larger R [26].

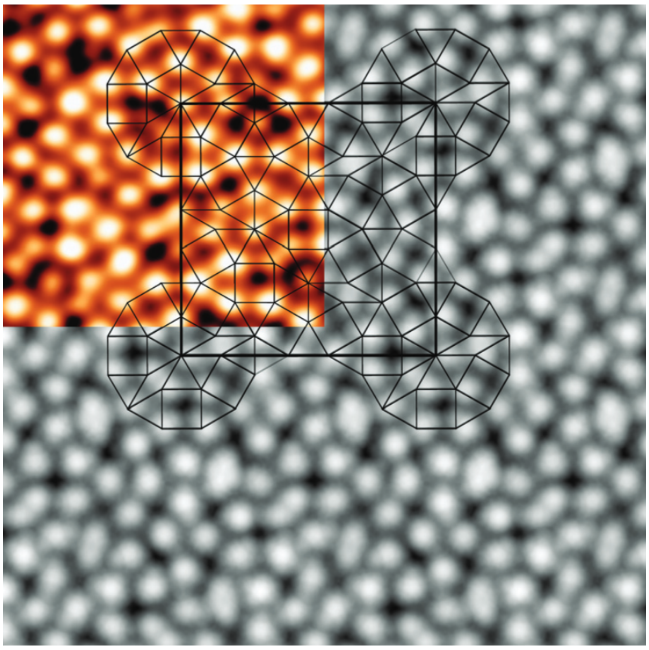

Figure IV.10: The simulated STM image is based on the charge density of 0.1 e/nm^3 and bias of $V_{\text{bias}} = 1$ V. An experimental STM image is superposed in the upper left corner.

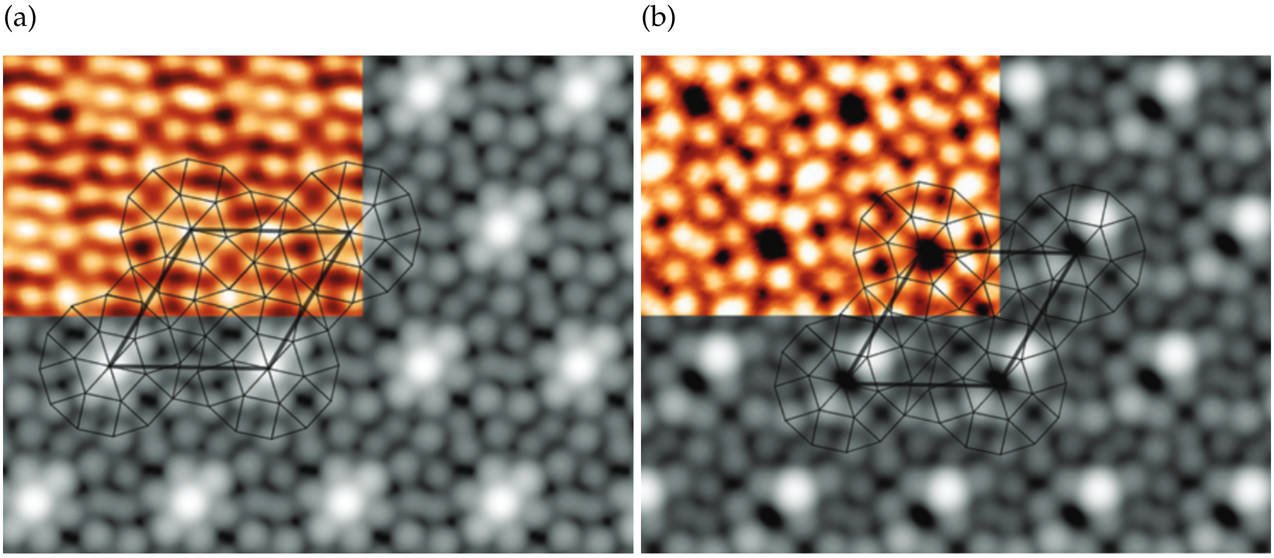

Figure IV.11: Simulated STM images of the complex hexagonal phase. The two variants were considered, either with (a) or without (b) the central protrusion at the center of the dodecagonal motifs. The STM images were calculated at the same bias as the experimental ones, shown in the upper left corner of each panel. ((a) $V_{\text{bias}} = 1$ V, isosurface with charge density equal to 0.2 e/nm^3, (b) $V_{\text{bias}} = 1.5$ V, isosurface with charge density equal to 0.1 e/nm^3).

We simulated the STM images for the hexagonal and the giant approximant phases for both positive and negative biases (Figures IV.10 and IV.11). The bright contrast is attributed to the protruding Sr atoms, while the Ti and O atoms are not visible, in agreement with the average z-positions of Sr, Ti, and O described previously. Overall, the good agreement between the simulated and experimental STM images suggest that the UTO structural models considered in this work are realistic for the new complex UTOs synthesized by Ruano et al. [79].

DOS calculations were performed using the two complex UTO structures (Figure IV.12). The main contribution to the DOS at the Fermi level originates from Ti atoms. A strong hybridization between Pt, O and Ti states is also visible, between -6 eV and -2 eV for the approximant UTO, and between -7 eV and -3 eV for the complex hexagonal UTO. Using the tetrahedron method with Blöchl corrections, a sharp pseudogap appears in the DOS of the hexagonal approximant (see the inset in Figure IV.12). Unfortunately, memory limitations did not allow a similar calculation to be performed with the square UTO.

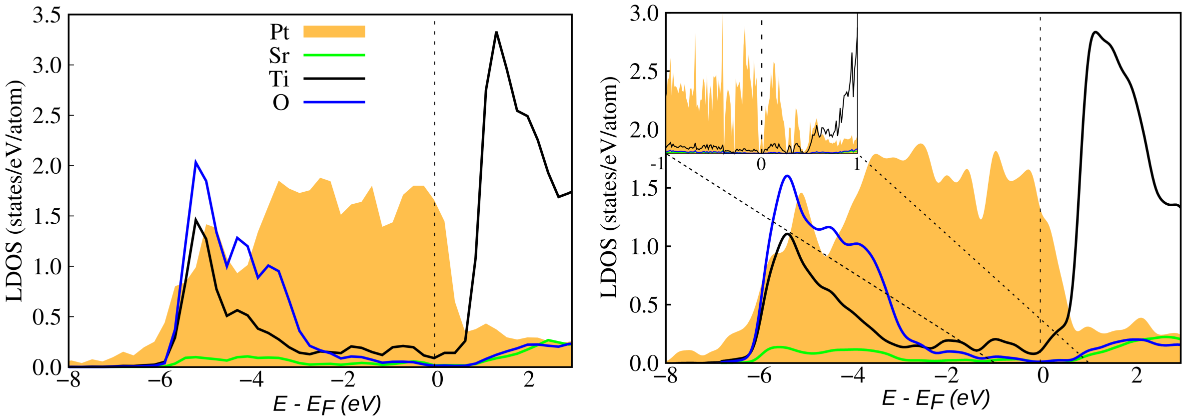

Figure IV.12: Density of states of the (a) square approximant and (b) of the complex hexagonal phase. The inset in (b) shows the DOS calculated using a tetrahedron method exhibiting a sharp pseudogap at the Fermi energy.

(a) Giant approximant: Bias = $+1$ V

(b) Giant approximant: Bias = -1 V

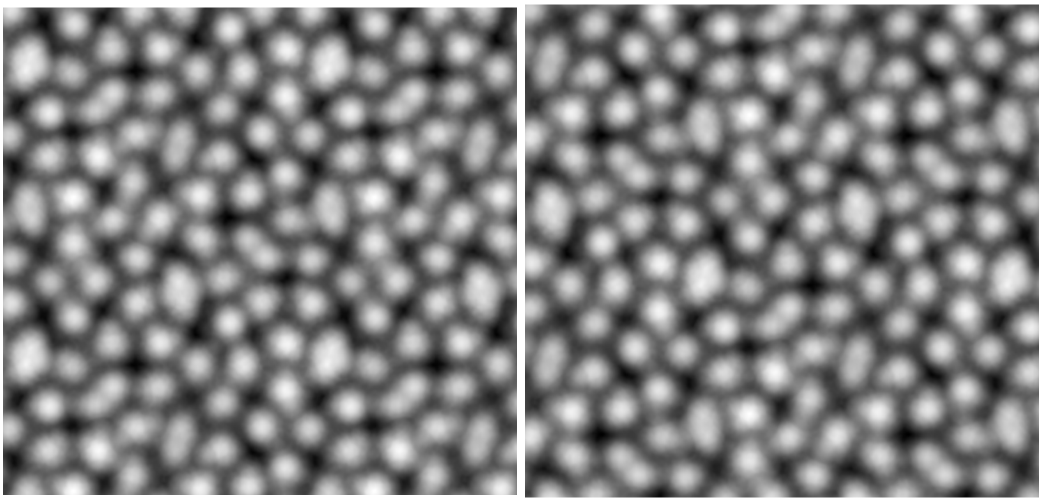

(c) Hexagonal approximant: Bias = $+1$ V

(d) Hexagonal approximant: Bias = -1 V

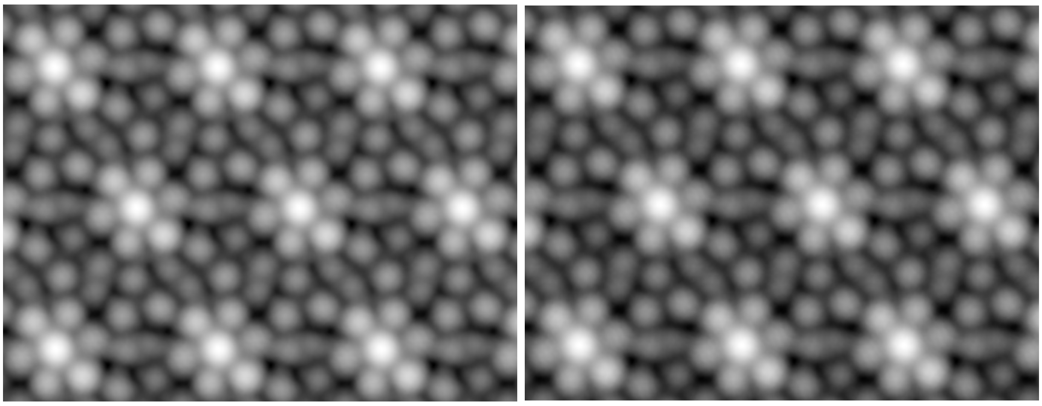

(e) Hexagonal approximant (with vacancy): Bias = $+1.5$ V

(f) Hexagonal approximant (with vacancy): Bias = -1.5 V

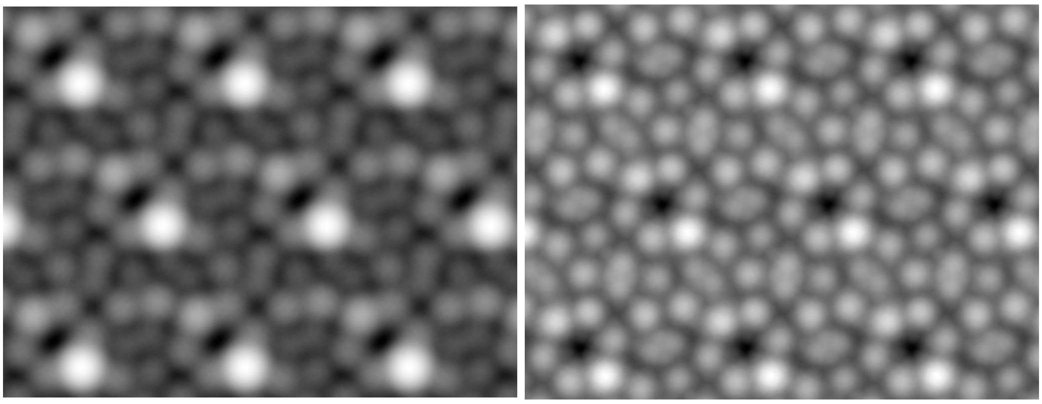

Figure IV.13: Simulated STM images using different biases for the (a), (b) giant square approximant (charge density of 0.1 e/nm^3), (c)-(f) hexagonal approximant with and without vacancy (charge density of 0.2 and 0.1 e/nm^3, respectively). Images were plotted using the *p4vasp* software.

Despite the difference in LDOS between Sr and Ti below and above the Fermi level (Figure IV.12), it is the height of the ions that revails, hence bright protrusions corresponds to Sr irrespective of the bias Figure IV.13.

IV.1. Adhesion energies

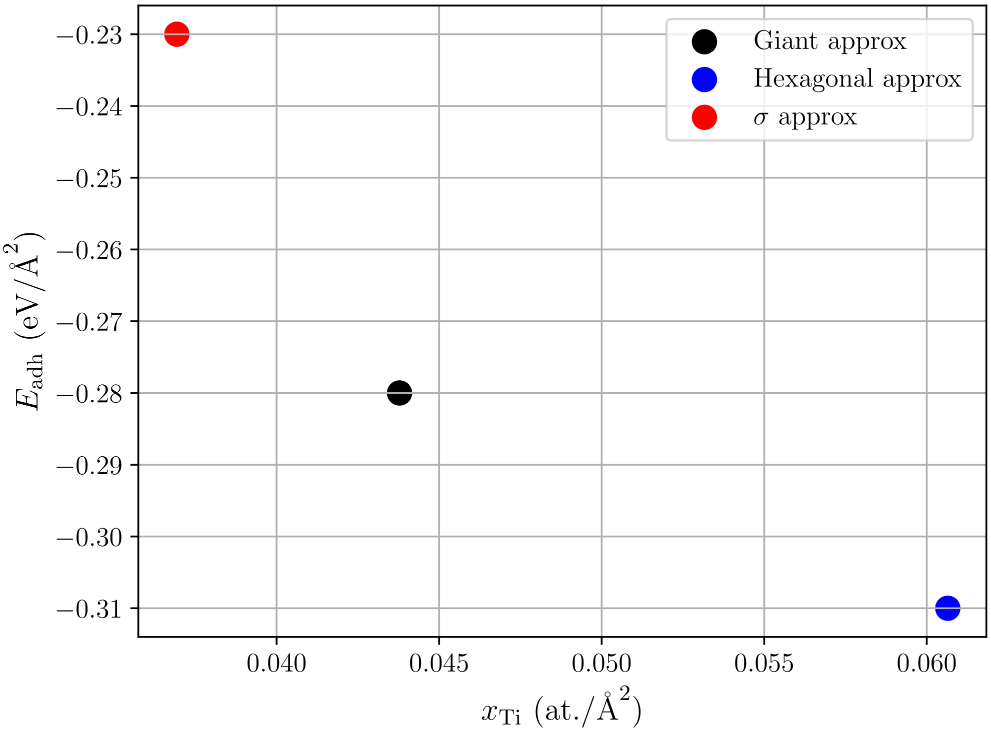

Figure IV.14: Adhesion energies of three approximant phases as a function of the amount of Ti per unit area.

The comparison between the amount of Ti per unit area with the E_{adh} is shown in Figure IV.14 for three approximant phases. The figure reveals that the adhesion energy becomes stronger as the amount of Ti increases. This trend agrees with the previously presented COHP analysis that revealed strong Pt–Ti interactions. Therefore, the amount of Ti appears more crucial than the details of how the interface model is built.

V. Conclusion

In this chapter, we focused on the structural and electronical properties of approximant phases that have been found experimentally (Cockayne-σ, giant, hexagonal, small hexagonal, and two monoclinic phases), as well as three fictitious phases that were obtained manually from the ideal dodecagonal NGT tiling.

For the considered models derived from the Cockayne-σ phase, the energy does not vary significantly when the Ti atoms, responsible for the adhesion of the oxide onto the metal support, are positioned in different sites on the Pt(111) substrate. Hence, the main factor determining the strength of the adhesion energy is the amount of Ti in the oxide (except for a slight deviation of the hexagonal structure).

As for stability of approximants, the two most stable phases at 0 K are the fictitious Approx 2 and 3 phases, indicating that there may be other approximant phases yet to be discovered.

By using the Cockayne's model to create the approximant's structures, we found a perfect match between the experimental and theoretical STM images for the giant and hexagonal approximant phases, where the Sr atoms are visible as the bright protrusions.

To conclude, the Cockayne-σ model fits the experimental STM images excellently. Furthermore, it also displays rather strong adhesion energy compared to other approximant structures. These lead us to conclude that the model is correct. Based on this model, new phases yet to be discovered can be simulated. Therefore, the calculations presented in this chapter may serve as a solid basis for future calculations and experiments.

Chapter V

Complex ultrathin oxide structures revealed by evolutionary computations on the In_xO_y/PdIn(001) system

I. Introduction

In this chapter we focus on the structure's determination of the ultra-thin oxide films formed when supported on a PdIn(001) substrate. For this matter, we used the USPEX code to search for films in several compositions and sizes. After selecting the most promising structures, we calculated, using a high-throughput code developed by the author (Vulcan), several electronic properties, such as the total energy, DOS, STM, adhesion energy, and COHP, so that we could identify the main intrinsic aspects of such ultrathin films. In addition, we used thermodynamic models, based on the *ab initio* atomistic thermodynamics framework, to interpret and suggest the most stable surface structures. In the end, we present an atomic scale analysis of the most stable identified surface phases, including the simulated STM images that future experiments can compare with.

II. Specific computational details

DFT calculations were performed using the Vienna *Ab initio* Simulation Package (VASP) [89]–[91]. The core and valence electrons' interaction have been described by the spin polarized projector augmented wave (PAW) method [117]. Exchange and correlation potential were described by the generalized gradient approximation (GGA) by Perdew, Burke, and Ernzerhof (PBE) [108]. Kohn-Sham orbitals were expanded in a plane-wave basis set up to a kinetic energy cutoff of 500 eV. The Methfessel-Paxton method [197] with a smearing of 0.2 eV was used. Atoms were allowed to relax until forces were below 0.02 eV/Å. The reciprocal space integration was performed with a Monkhorst–Pack k-point grid of 13×4×1 for the 1×3 substrates and 13×1×1 for the 1×5 and 1×7 substrates. In order to optimize the necessary time for the relaxation of each structure, the relaxation consisted of five steps with increasing accuracy until reaching the thresholds described above. The STM images were calculated using the Tersoff-Hamman approximation [141], [142]. Structures and STM images were plotted using VESTA [175] and p4vasp software, respectively. The average charges on each atom were calculated with the Bader approach [136], using the code distributed by the Henkelman group [137]–[140].

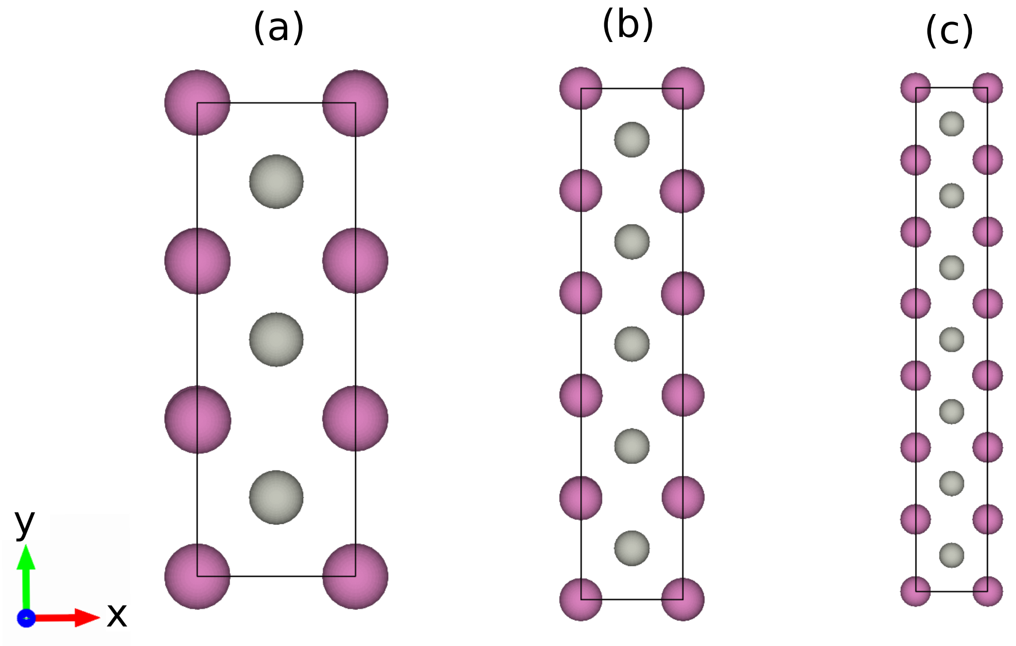

Figure V.1: Top view of the (a) 1×3, (b) 1×5, and (c) 1×7 supercell substrates used as initial structures for the genetic algorithm search. Pd and In atoms are represented in purple and gray, respectively.

For the structural model used for the substrate, we considered two cases: the PdIn(001) substrates (space group Pm$\overline{3}$m) have been built with at least 10-layer thick slabs with Pd top and bottom terminations (due to the fact that the oxide is rich in In), and the second was fixing the top termination of a PdIn(001) substrate as In-terminated, allowing the deposition of only oxygen atoms at the surface. The top 3 layers were free to relax alongside the oxide. In order to couple a sufficient size for the oxide structures with computationally demanding genetic algorithm codes, we selected three fixed sizes for the PdIn(001) substrates: 1×3, 1×5, and 1×7 supercells, as shown in Figure V.1. As for the oxide, the composition of the ultrathin In_xO_y films considered were in the range $0.42 \leq x \leq 0.60$ and $0.4 \leq y \leq 0.68$, encompassing a rich variety of stoichiometries, specially in between the compositions of InO and In_2O_3.

We used the *Universal Structure Predictor: Evolutionary Xtallography* (USPEX) method [165], [167], [168], [170]–[173], as described in Section IV.2.1.. This method was already used successfully to determine the crystal structure of 2D materials [198]–[200]. The initial In_xO_y oxide structures were obtained randomly, while the subsequent generations were obtained by using variation operators on the best structures of the previous generations. We fixed 30% of heredity, 10% of softmutations, 10% of transmutation, and 50% of random mutations to obtain a good sampling of the configurational space. The structures were relaxed by means of DFT with five consecutive relaxation steps with increasing accuracy, using total energies to rank the best structures. Figure V.2 shows an example for the 1 × 3 supercell with InO composition for the ultrathin film. We repeated these steps until the best structures' set remains unchanged for 15 generations.

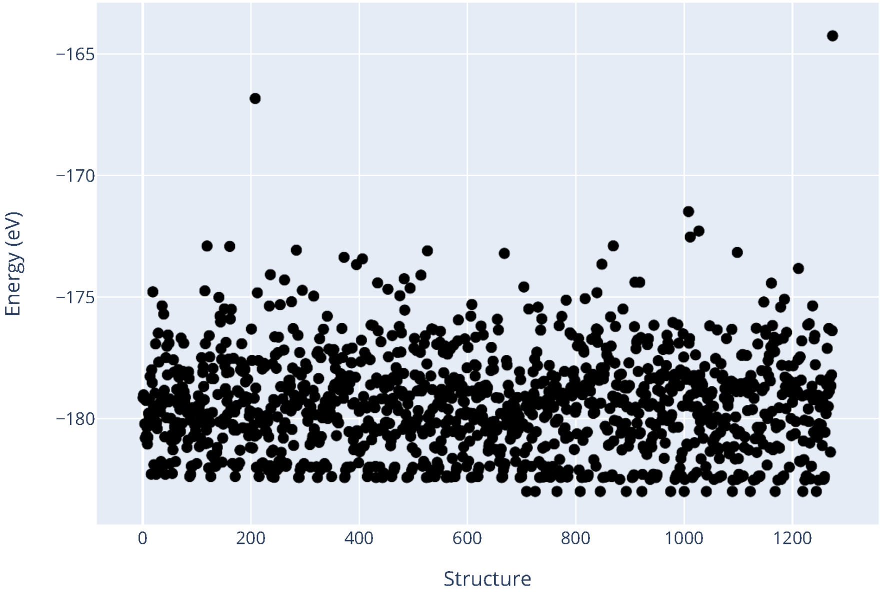

Figure V.2: Total energies of all 1 × 3 structures with oxide composition of InO.

III. USPEX results

Figure V.3 displays the resulting convex hull for all calculations performed for the PdIn(001)/In_xO_y (with $0.42 \leq x \leq 0.60$ and $0.4 \leq y \leq 0.68$) considering three supercell sizes for the PdIn substrate. In the end, 148 484 structures were calculated, ranking 114 as the best structures, using an enthalpy of formation of 0.1 eV/atom as energetic criteria, spanning all compositions whithin the selected range. It is interesting to notice that despite the change in the composition, the range of ΔH_f between structures and supercell sizes stay within the same energy range at around -0.5 eV/atom, which is very close to the calculated value for the enthalpy of formation of the PdIn substrate (-0.49 eV/atom) [50], since its contribution to the total energy is much larger than the ultrathin oxide.

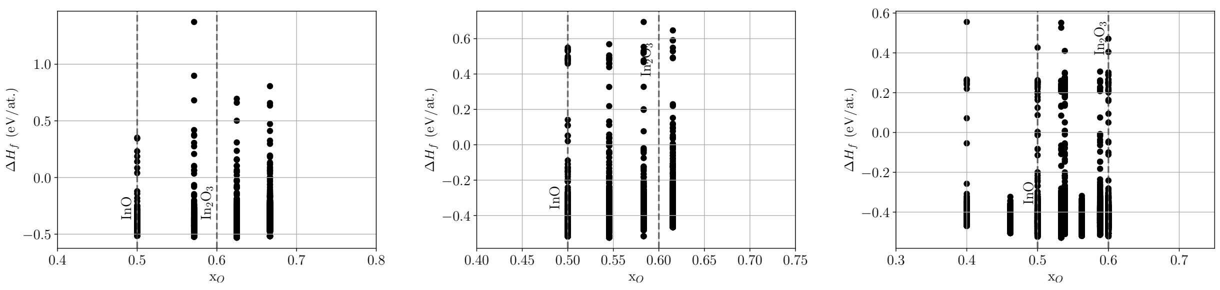

(a) 1 × 3 supercell (b) 1 × 5 supercell (c) 1 × 7 supercell

Figure V.3: Enthalpies of formation of all structures calculated with the USPEX code, using (a) 1 × 3, (b) 1 × 5, and (c) 1 × 7 supercells of PdIn(001).

III.1. Structure analysis

Regarding the structural analysis for all 114 best ranked supported indium oxides, we identified well defined patterns of how these structures are accommodated. We will present here a sample of representative structures, which can be extended to almost all of the other oxides. In addition, we will focus on the tiling configuration of the oxygen atoms that protrude above the average mean surface, for reasons that will become evident in Section V.2., where we present the simulated STM images.

We stored all structural information in a JSON database; it can be found in the Github page `https://github.com/DoriniTT/Thesis_extra_results`. From now on, we will identify each structure by a specific index, which corresponds to an ID number in the JSON database.

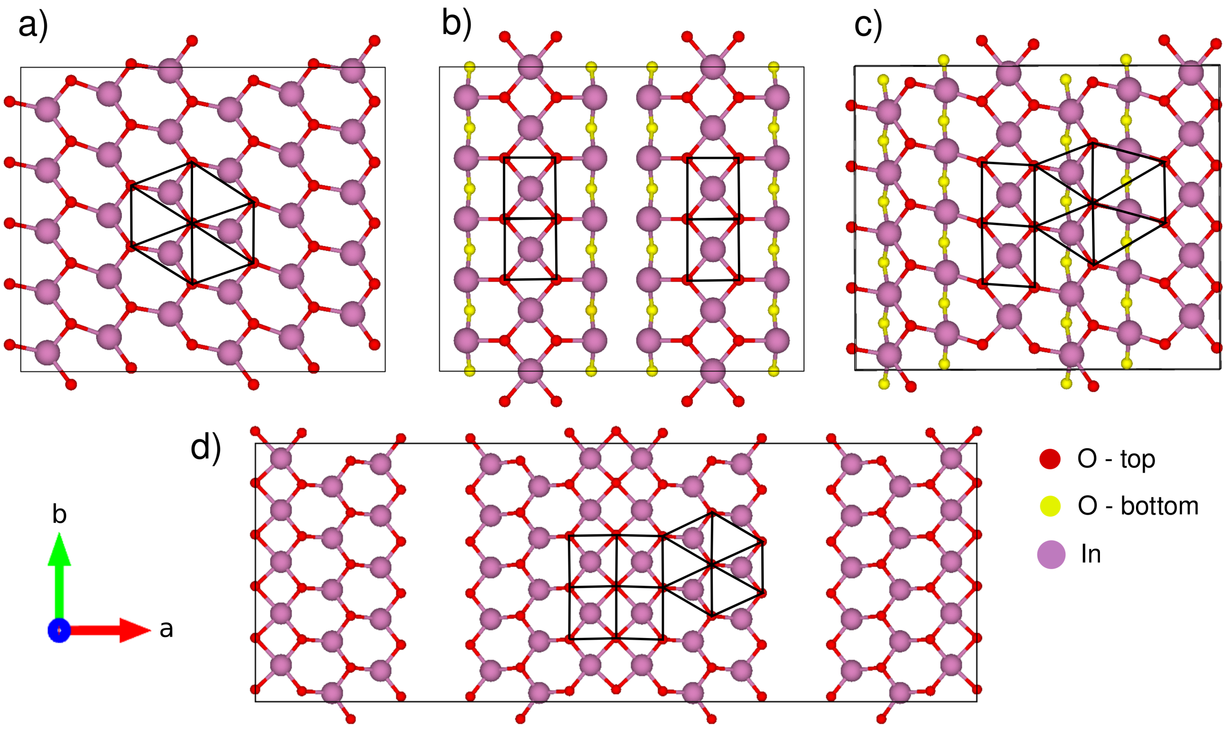

Figure V.4: Top view of representative structures showing the most probable motifs found on the ultrathin indium oxides. (a), (b), (c), and (d) correspond to structures 1, 22, 24, and 89, respectively. The In atoms are represented in purple, while the O atoms are colored according to their height with respect to the average mean plane of the oxide: red balls are O atoms above the mean plane and yellow balls are O atoms below it.

Figure V.4 presents four representative structures along with the most probable tiling configurations found. Figure V.4 (a), with index 1, corresponds to a structure with oxide composition InO, where each In atom bonds to three oxygen atoms, and vice-versa. The resulting structure is a distorted hexagonal configuration for both In and O. By increasing the amount of O atoms in the oxide to $x_O = 0.57$ and $x_O = 0.62$, we can obtain either a rectangular tiling, or a combination of hexagonal and slightly distorted rectangular tiling, with some In atoms bonding to four O atoms, and others to three, whose combination may depend strongly on the composition of the oxide. Interestingly, the oxygen atoms that are not protruded also present the same pattern, as we can, for instance, identify the same rectangular and hexagonal patterns formed by the bottom O atoms (yellow balls), Figure V.4 (b) and (c). Tiling configurations, presented in Figure V.4, are also the basis for other oxides (not shown). Results reveal that tiling configurations depend mainly on the oxide stoichiometry. In total, we found 25 structures that belong to group (a), 6 to group (b), 52 to group (c), and

31 to group (d).

In addition, we noticed that among large 1 × 7 structures, there are a handful of them, such as the one shown in Figure V.4 (d), that, besides showing roughly the same tiling configurations as the smaller oxides, present a hole dividing some parts of the oxide. This probably happened because it is difficult for genetic algorithms to sample such a vast configurational space, usually needing a much larger set of generations to find representative structures. In our case, we believe that we have, nonetheless, a good sampling of the configurational space, since there are only 18 structures with holes out of the 67 final good structures for the 1 × 7 oxides.

III.2. Enthalpies of formation for the best identified structures

After the ranking, we performed a more precise final structural relaxations, by decreasing the forces to 0.01 eV/Å, so that we could obtain a new convex hull with a higher accuracy. The result of these calculations is shown in Figure V.5.

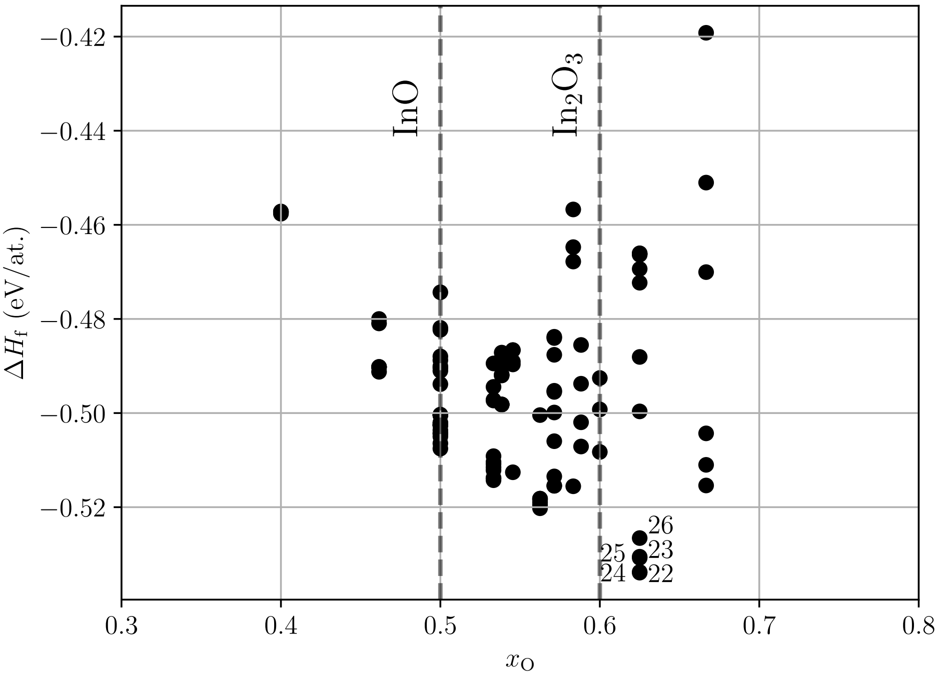

Figure V.5: Relation between the enthalpy of formation and composition of all the 114 best structures.

Within these recalculated 114 compounds, the energy difference between the least and the most stable structures remains about 0.1 eV/atom. Enthalphies of formation (Figure V.5) suggest that structures 22 to 26 are promising candidates for stable ultrathin oxides; these structures are shown in Figure V.6. Interestingly, these structures with the most negative ΔH_f contain a higher amount of oxygen than the stable bulk In_2O_3 oxide. However, one cannot compare directly the stability of compounds of different composition with only ΔH_f, thus requiring us to study in more detail the electronic structure of all these stable compounds, as well as applying more sofisticated surface thermodynamic models to more definitely determine the stability of oxide phases.

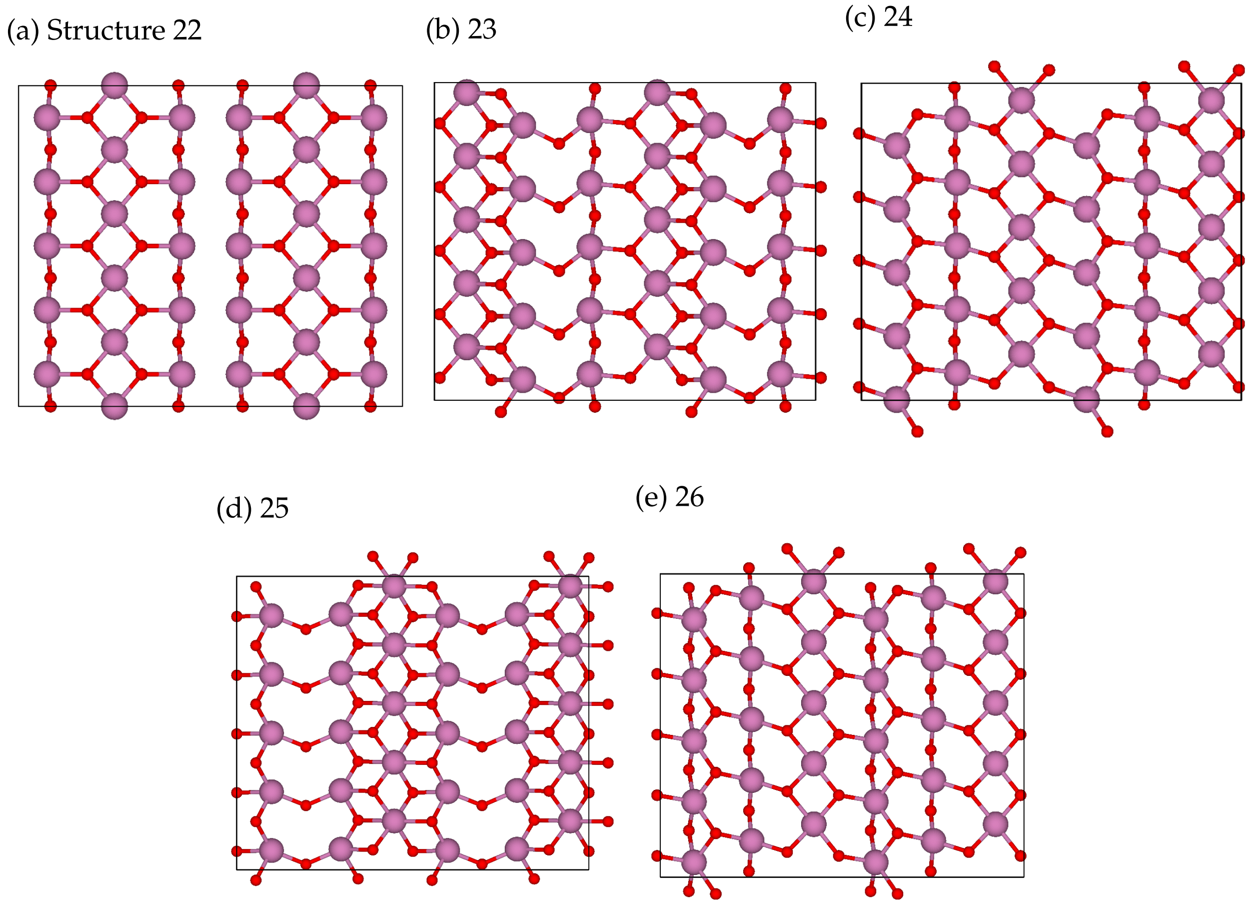

(a) Structure 22

(b) 23

(c) 24

(d) 25

(e) 26

Figure V.6: Top view of structures 22 to 26. O and In are represented by red and purple circles, respectively.

IV. Thermodynamic models

The equation that we want to solve is Equation (II.51) described in Section II.1.2.. For simplicity, we re-write this equation here:

$$\gamma_{\text{surf}}\left(T, P_{O_2}\right) + \gamma_{\text{bottom}} + \gamma_{\text{interface}} = \frac{1}{A}\left[E_{\text{slab}}\left(T, P_{O_2}\right) - N_{\text{Pd}}\left(E^{bulk}_{\text{PdIn}} - \mu_{\text{In}}\right) - N_{\text{In}}\mu_{\text{In}} - N_{\text{O}}\mu_{\text{O}}\right] \quad \text{(V.1)}$$

We will go through each parameter case by case, beginning with γ_{bottom}. Predicting the preferred surface termination for the PdIn(100) substrate is challenging since the specific surface composition is unknown and depends, for example, on the experimental surface preparation conditions. For our case, since the Pd-terminated surface of the PdIn(001) substrate was calculated to have a more stable surface energy according to McGuirk et al. [132] and that it will interact with a oxide rich in In, we assume that the Pd-terminated surface is the most suitable one for our calculations.

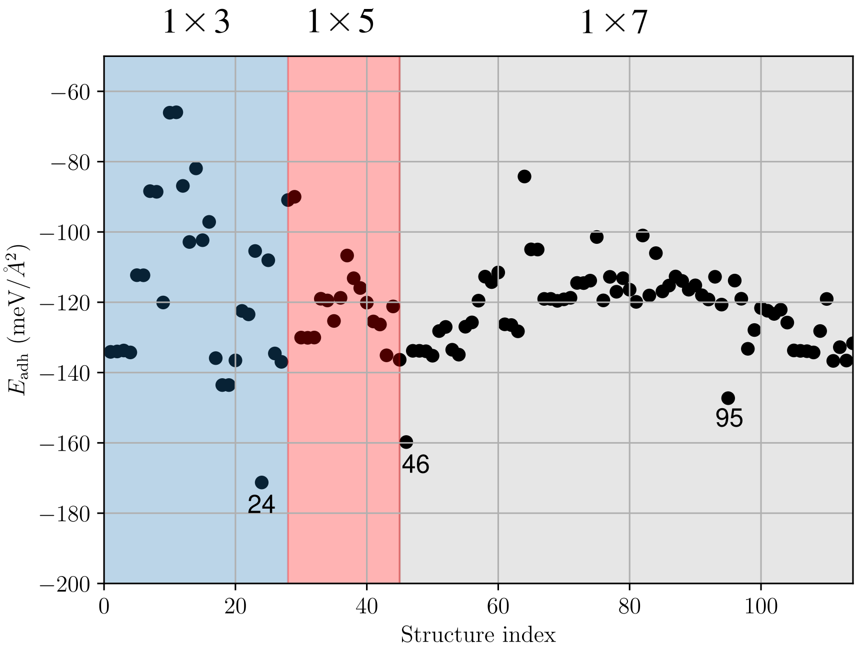

Figure V.7: Adhesion energies (E_{adh}) for all 114 stable phases determined using the USPEX code. All structures were relaxed until forces were below 0.02 eV/Å. The blue, red, and gray regions represent the structures with 1 × 3, 1 × 5, and 1 × 7 supercell substrates, respectively.

We recalculated the surface energy for this termination using a symmetric 13-layer thick slab with the same standard proceedure as described in [132] and in Section II.1.2.2. We obtained 1.40 and 1.77 J/m^2 for the inferior and superior limits of the chemical potential of In when using −0.49 eV/at., 2.43 eV/at., and 3.75 eV/at. for the enthalpy of formation and cohesive energies of In and Pd, respectively. These values are in excellent agreement with the literature values of -0.49 eV/at. [50], 2.52 eV/at., and 3.89 eV/at. [201], but the final values for the surface energy slightly differ from those reported in [132], being 0.93 J/m^2 and 1.40 J/m^2 for the upper and lower limits, probably due to a difference in the final total energy of the slab.

As mentioned in Section II.1.2., the $\gamma_{\text{interface}}$ term in Equation (V.1) is approximated by the adhesion energy (E_{adh}) of each structure, due to the difficulty in calculation an exact value for $\gamma_{\text{interface}}$, following Equation (II.48). The results for all 114 structures are shown in Figure V.7. It is possible to see that most structures display E_{adh} between -140 meV/Å^2 and -100 meV/Å^2, with a few structures being the exception. We noticed that the structures that present the stronger E_{adh} normally have Pd–O bonds at the interface. In addition, we can notice that the overall variation in the adhesion energies for the small 1×3 structures is much greater than those of the 1×5 and 1×7 supercells. Finally, the chemical potential of oxygen is given by Equation (II.43), where we used the approach of [124].

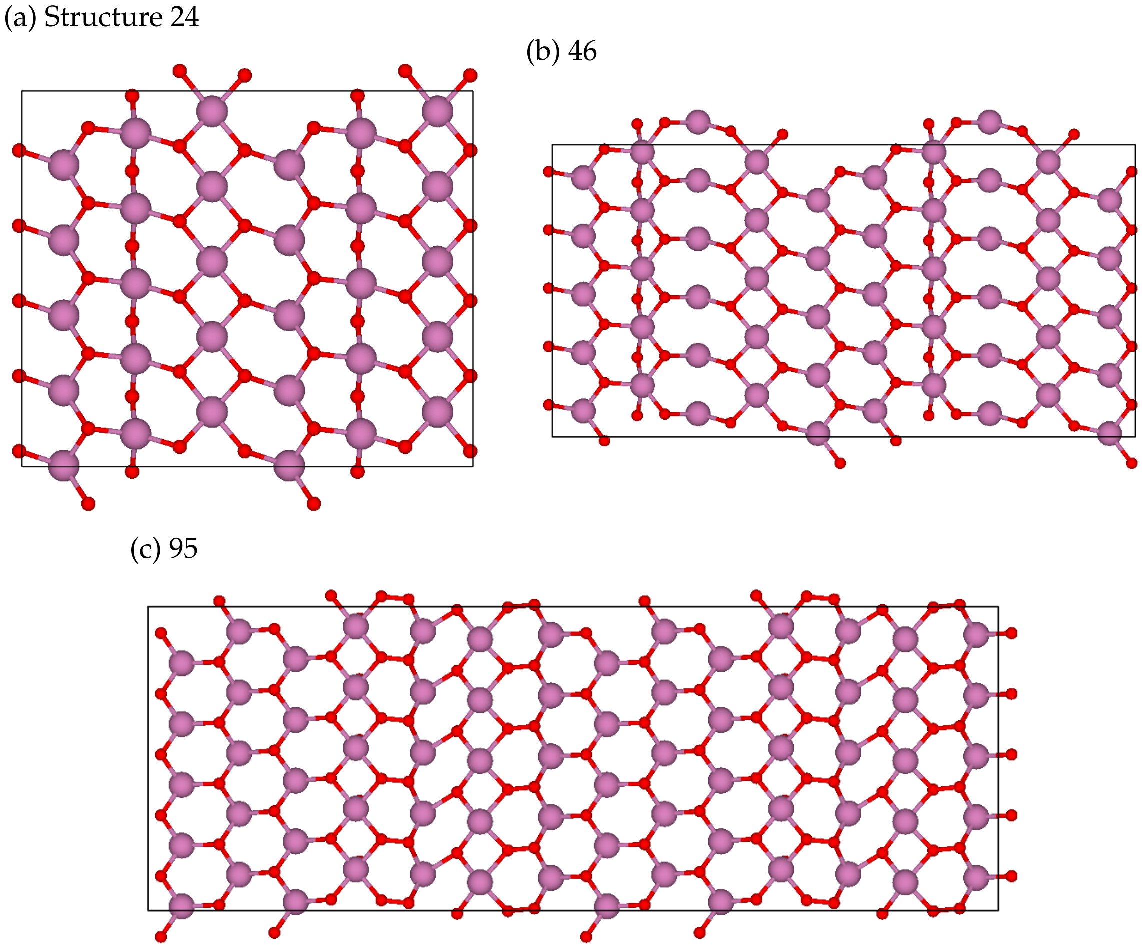

(a) Structure 24

(b) 46

(c) 95

Figure V.8: Top view of structures numbered (a) 24, (b) 46, and (c) 95. O and In are represented as red and purple, respectively.

(a) All structures.

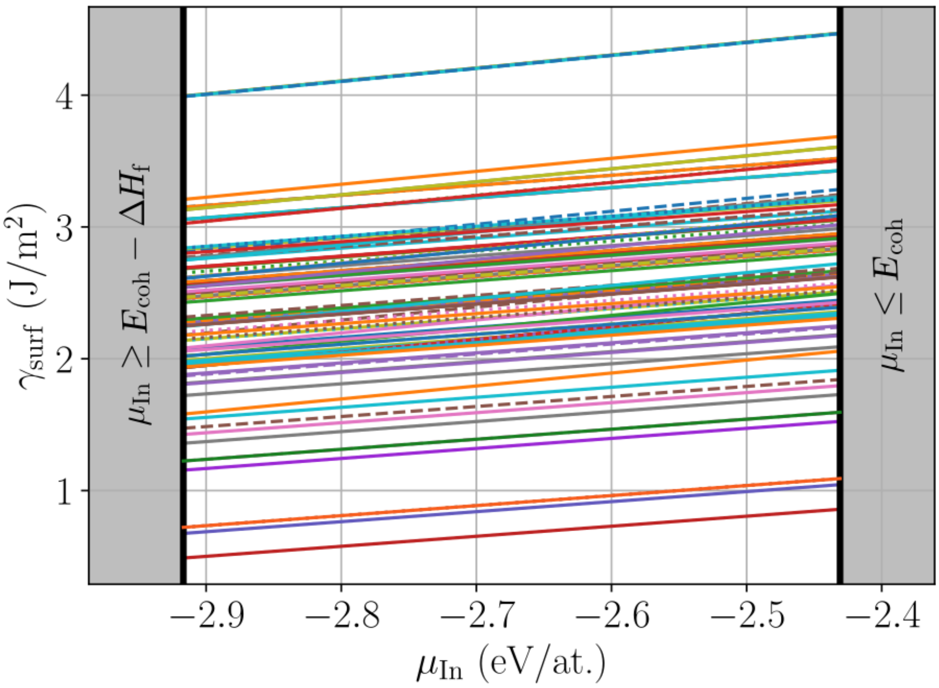

(b) Only structures with the stablest surface free energy.

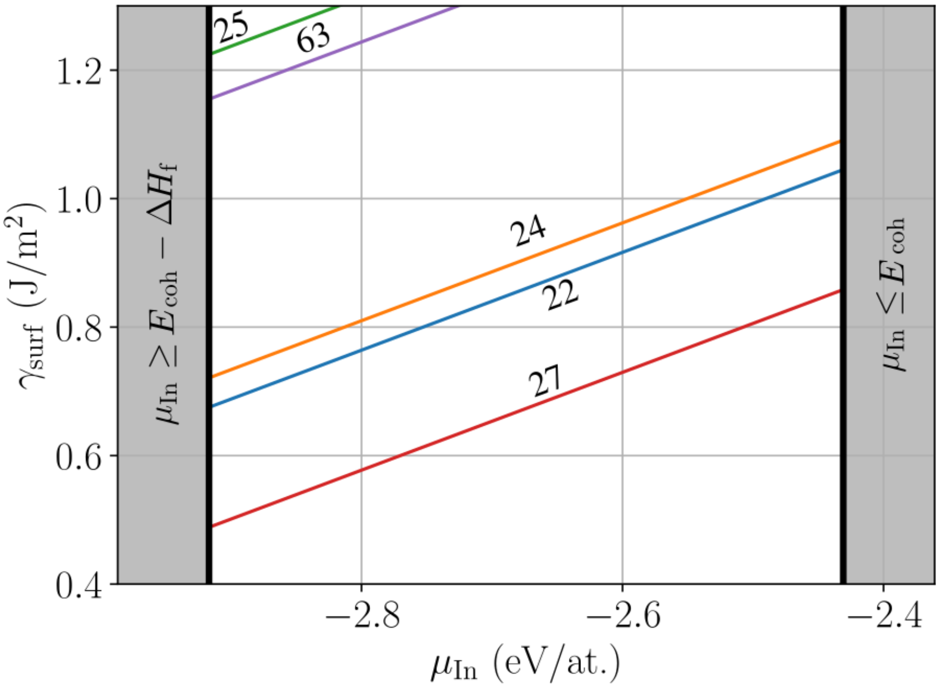

Figure V.9: Thermodynamic analysis calculated with Equation (V.1) at $T = 278$ K and $P = 1$ atm.

(a) Structure 22

(b) 24

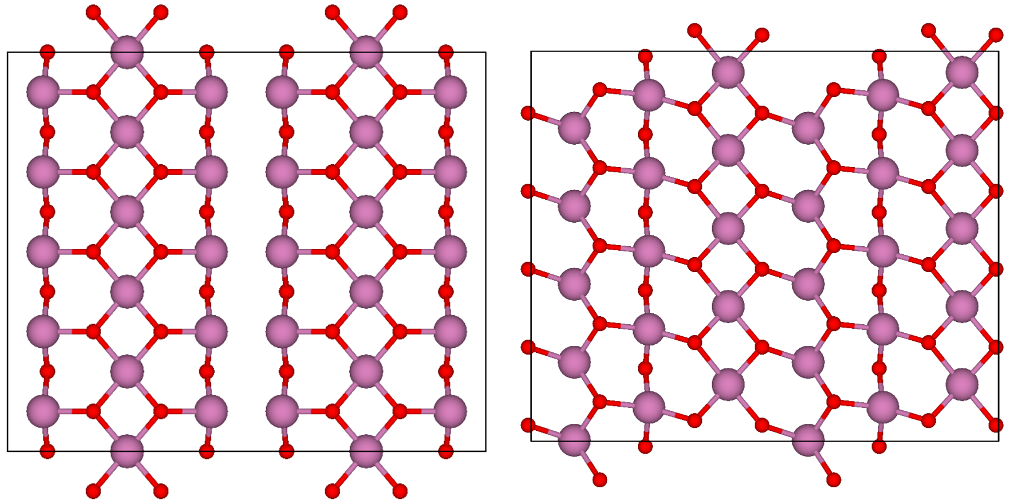

(c) 25

(d) 27

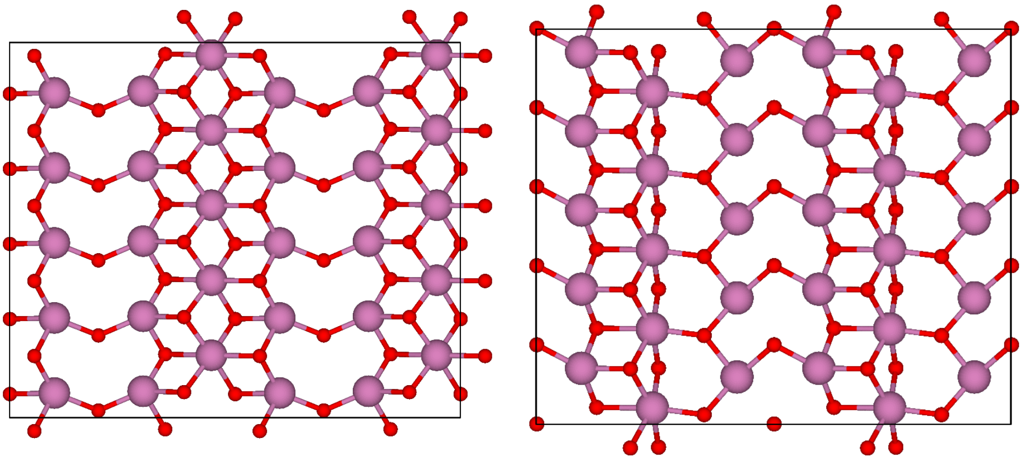

(e) 63

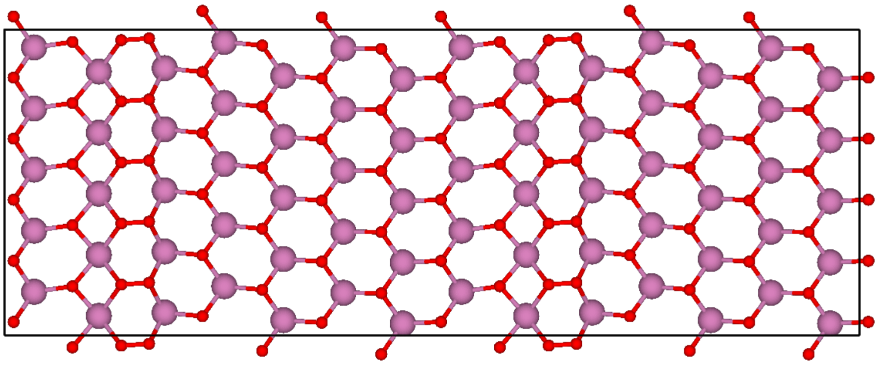

Figure V.10: Top view of structures numbered (a) 22, (b) 24, (c) 25, (d) 27, and (e) 63. O and In are represented as red and purple, respectively.

The results of this thermodynamic treatment can be seen in Figure V.9 (a). To test the stability of these structures at ambient conditions, we've set $T = 278$ K and $P = 1$ atm.

The majority of structures stay within the 1 – 3 J/m^2 range, and we can also notice that the variation between the lower and upper limits of the chemical potential stay at a value around 0.5 J/m^2. Figure V.9 (b) show the same results but zooming in at the structures with the stablest surface energy. From this analysis, it is already possible to identify some promising ultrathin In$_x$O$_y$ candidates that may form on the surface of PdIn(001), which are structures 22, 24, 25, 27, and 63. Interestingly, four of these structures belong to the 1 × 3 supercell, while only structure numbered 63 have a 1 × 7 supercell.

In order to complement the results presented in Figure V.9, we implemented a grand potential model, as described in Section II.1.3., with the surface ultrathin film in contact with a bulk reservoir of In$_2$O$_3$ and in equilibrium with oxygen atmosphere. This model is given by equation Equation (II.56), and the parameters (cohesive energies, enthalpie of formation, and total energies) used were the same as for the previous model.

The results are given in Figure V.11. Interestingly, we can notice that as the size of the ultrathin film grows from 1 × 3 to 1 × 7, the Ω value also decreases, suggesting that, for this model, bigger structures may be more likely to form. Nonetheless, some of the most stable structures correspond to those already identified in Figure V.9, i.e., structures 23 to 27.

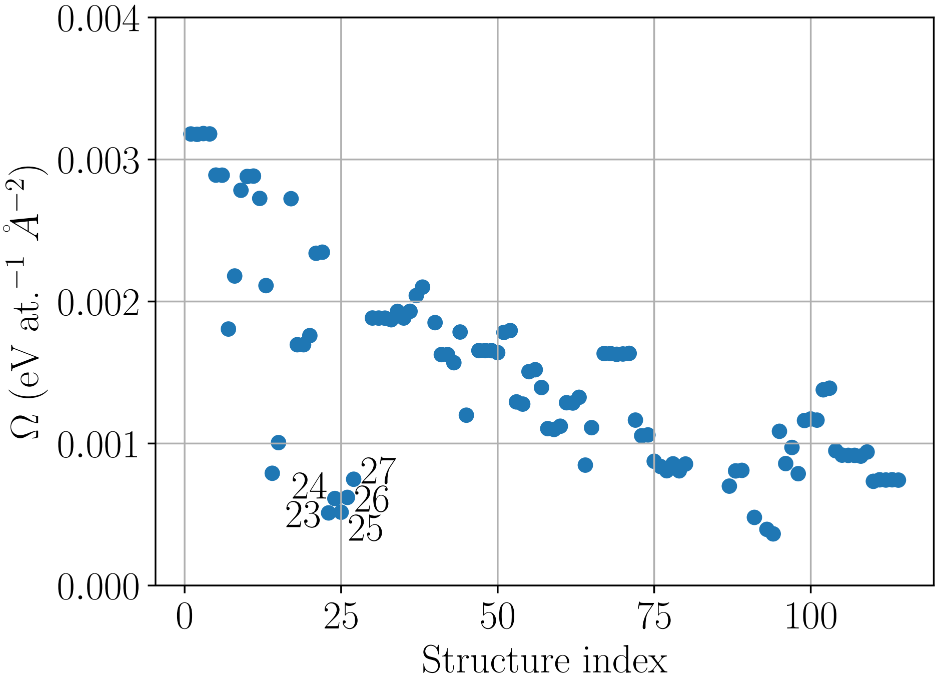

Figure V.11: Grand potential for the 114 structure, showing the indexes with the lowest Ω.

In order to verify the influence of the temperature on the stability of the ultrathin films, we selected two additional temperatures, 800 K and 1200 K, fixing the pressure at $P = 1$ atm. Figure V.12 displays the results of this thermodynamic model, where in (a) and (b) we highlight which are the most stable structures according to Equation (V.1), while in (c) and (d) we show the grand potential (Ω) according to Equation (II.56).

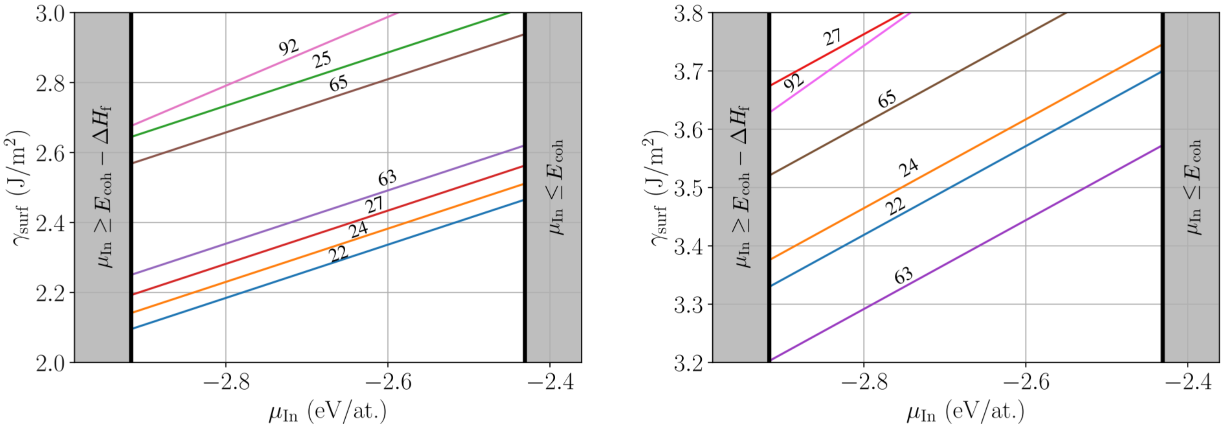
(a) $T = 800$ K; $P = 1$ atm

(b) $T = 1200$ K; $P = 1$ atm

(c) $T = 800$ K; $P = 1$ atm

(d) $T = 1200$ K; $P = 1$ atm

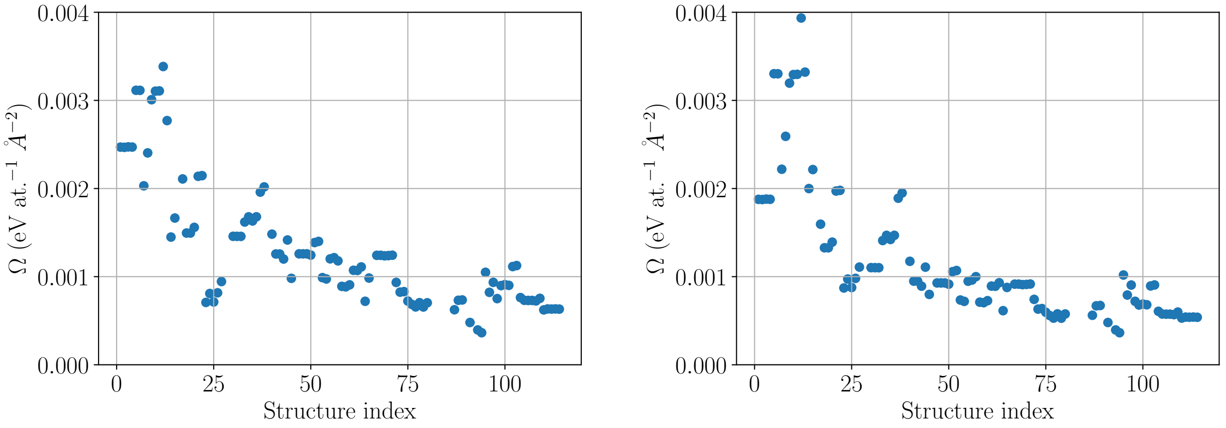

Figure V.12: Thermodynamic model calculated with Equation (V.1) at $P = 1$ atm and (a) $T = 800$ K and (b) $T = 1200$ K. Grand potential (Ω) is calculated using Equation (II.56).

Comparison between Figure V.9 (b), Figure V.12 (a) and Figure V.12 (b), reveals that γ_{surf} increases with increasing temperature, i.e., from about 0.5 J/m^2 at room temperature to around 2.1 J/m^2 at 800 K and about 3.2 J/m^2 at 1200 K.

This increase occurs due to the increase in the oxygen chemical potential. In addition, this energy shift comes also with the stabilization of some large 1×7 structures, for instance, the structures with indexes 63, 65, and 92. By further increasing the temperature to 1200 K the structure 63 becomes the most stable structure.

We can further complement the analysis made by studying the effect of the temperature on the grand potential Ω. As a matter of fact, the temperature seems to have a more significant influence on smaller 1×3 and 1×5 structures than on larger 1×7 structures, where we also identified a shift in the stability because at 1200 K all the most stable structures correspond to 1×7 supercell (Figure V.12 (d)).

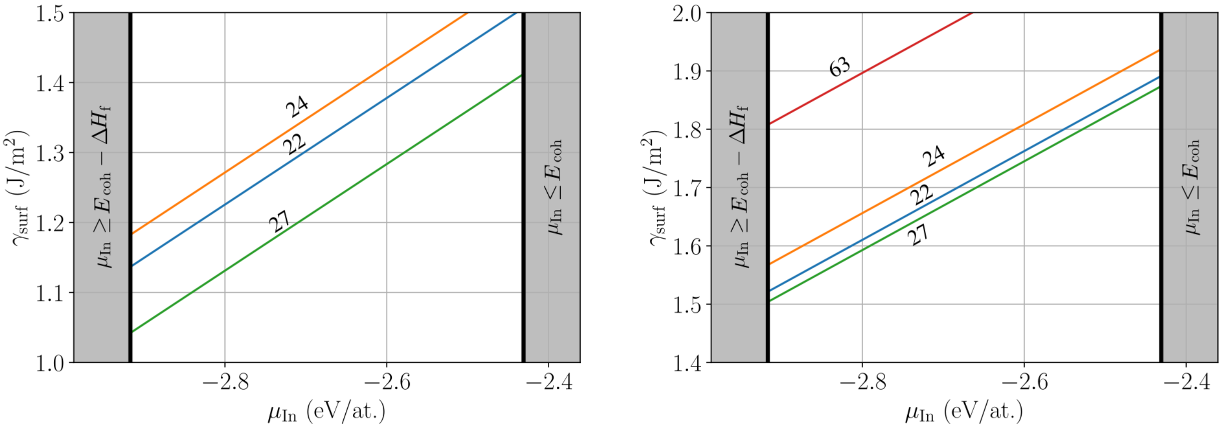

(a) $T = 278$ K; $P = 10^{-06}$ atm (b) $T = 278$ K; $P = 10^{-11}$ atm

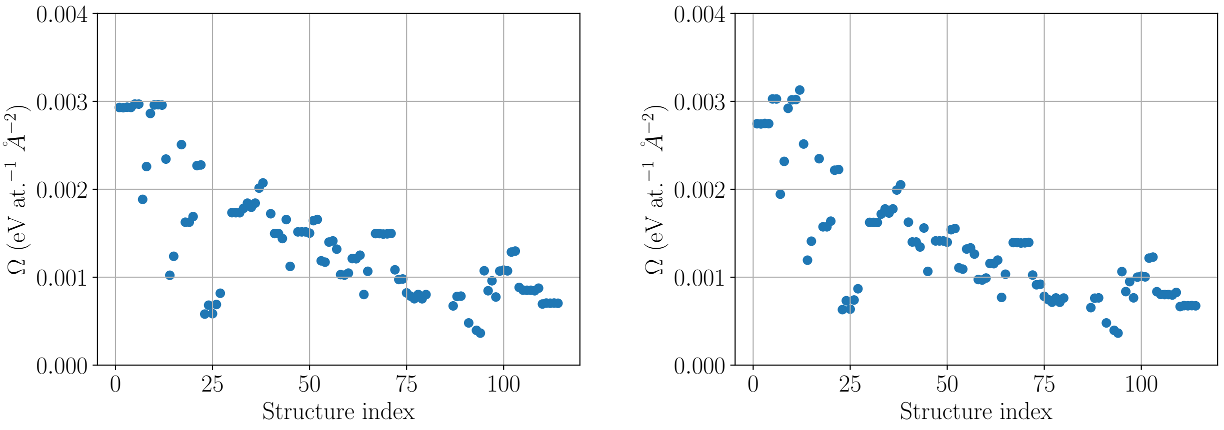

(c) $T = 278$ K; $P = 10^{-06}$ atm (d) $T = 278$ K; $P = 10^{-11}$ atm

Figure V.13: Thermodynamic model obtained by using Equation (V.1) at $T = 278$ K and (a) $P = 10^{-06}$ atm and (b) $P = 10^{-11}$ atm. Grand potential (Ω) was calculated using Equation (II.56).

The same methodology was applied by fixing $T = 278$ K and varying the pressure from 10^{-06} atm to 10^{-11} atm, simulating UHV conditions. The corresponding results are shown in Figure V.13. In this case, the increase of $\gamma_{\rm surf}$ is smaller than for the temperature variation, i.e., $\gamma_{\rm surf}$ increases from 0.5 J/m^2 at ambient pressure to 1.0 J/m^2 and 1.5 J/m^2 at $P = 10^{-06}$

atm and $P = 10^{-11}$ atm, respectively.

Additionally, the shift due to the stabilization of the bigger 1×7 structures is much less pronounced for the case of changing the pressure, indicating that the main parameter for the stabilization of a specific ultrathin indium oxide structure depends more on the temperature than on the pressure.

Thermodynamic models are an excellent tool for screening potential new structures that may form experimentally under specific conditions. However, thermodynamic models do not reveal any particular characteristics that contribute to their stability under given conditions. Therefore, the next section focuses on the intrinsic electronic-structure characteristics of ultrathin films, focusing specially on those most promissing candidates.

V. Electronic structure calculations

V.1. Charge and structural analysis

The Bader method [136] was used to determine the charge on each individual atom for all structures, so that we may determine a relationship between the structure and its electronic properties. In all cases, the oxide layer is in contact and interacts strongly with the topmost Pd layer of the substrate, thus, we may expect that the structural relaxation of the oxide may be correlated with the charge distribution of the Pd layer. To test this hypothesis, we plot the average Bader charge on the first layer of Pd as a function of the oxide rumpling. This structural property is defined the same way as for the approximants in the previous chapter with the following equation:

$$R = z^{\mathrm{In}} - z^{\mathrm{O}} \tag{V.2}$$

where z^{In} and z^{O} are the average heights of the In and O atoms in the oxide, respectively.

The results of this analysis are shown in Figure V.14. According to this graph, the structures can be separated in well defined categories with an almost linear relationship between the average Bader charge and the rumpling. The first category of structures in green represents the oxides in which an O_2 molecule was formed on top of the ultrathin layer. The purple structures are those in which at least one In atom does not bond with the Pd layer of the substrate. The yellow color represents the oxides that could correspond to ultrathin stable compounds, but most of these structures do not present the most stable surface energies, with structures 63 and 18 being the exceptions. Finally, the structures in red are in the region where most of them are the most stable according to the thermodynamic models calculated in Figures V.9 and V.11, with structures 18 and 21 being the exceptions. Representatives of each category are shown in Figures V.15 and V.16.

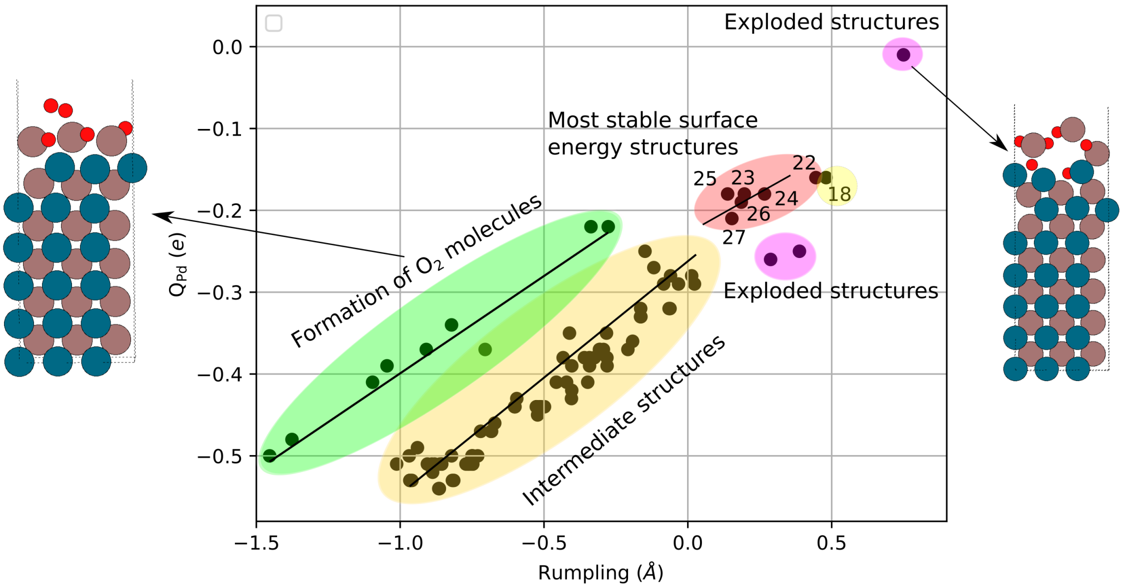

Figure V.14: Average Bader charge on the topmost layer of Pd of the PdIn(001) substrate as a function of the rumpling for all 114 calculated structures.

(a) Structure 27 (b) Structure 12

Top view.

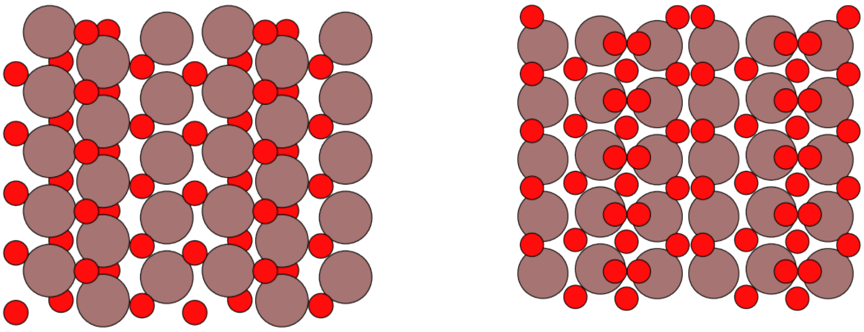

Side view.

Figure V.15: Top and side view of structures numbered (a) 27 (red category) and (b) 12 (green category). O and In are represented as red and grey, respectively.

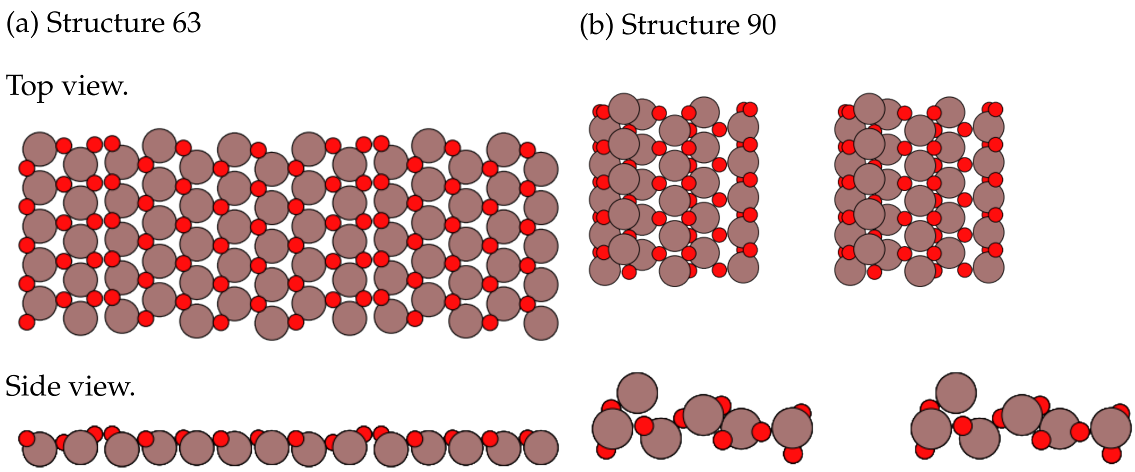

(a) Structure 63

(b) Structure 90

Figure V.16: Top and side view of structures numbered (a) 63 (yellow category) and (b) 90 (purple category). O and In are represented as red and grey, respectively.

From Figure V.14, it becomes clear that the structural stability of the ultrathin In_xO_y oxide supported on a PdIn(001) substrate is correlated to the charge distribution at the interface and the overall relaxation of the oxide. When a specific combination of charge and rumpling is met (red region), it is very likely that the surface energy of the system will be of lower energy, thus more stable. However, without experimental verification, it is hard to be certain which oxide would form because several structures have similar surface energies and charge distributions. Still, these results present a valuable map with several precise characteristics of what a stable oxide might look like. In the end, based on our electronic calculations and thermodynamic models, we identified seven out of 114 structures as the most interesting candidates, which are structures numbered 22, 23, 24, 25, 26, 27, 63.

Lets take a closer look at the stability descriptors discussed so far, with focus on the thermodynamic models, tiling configurations, stoichiometry, and surface atomic density for a few interesting structures. Let us, for the sake of comparison, select structures according to their surface energies at ambient conditions, $T = 278$ K and $P = 1$ atm. The selected structures, in order of increasing stability, are: 70 (it has the highest surface energy), 47 and 1 (structures with intermediate surface energies), and 63 (the most stable structure at higher temperatures, and one of the most stable at ambient conditions). At ambinent conditions, the surface energies of structures 70, 47, 1, and 63 are 3.98 J/m^2, 3.05 J/m^2, 2.68 J/m^2, and 1.15 J/m^2, respectively. A structural comparison of these four structures, alongside a qualitative indication of their surface energies, atomic densities, x_O, and tiling configurations, are shown in Figure V.17. There is an interesting evolution of tiling between these structures. The structure 70 Figure V.17 (a), with the highest surface energy, contains the lowest amount of O ($x_{\text{O}} = 0.4$) and oxide atomic density of 0.14 at./Å^2, and we can clearly see the presence of many holes in the topmost oxide plane. Additionally, it presents an initial formation of a hexagonal configuration, which is not complete due to the lack of oxygen atoms. The next structure is number 47 (Figure V.17 (b)), which has an increased atomic density of 0.18 at./Å^2 and an amount of oxygen of $x_{\text{O}} = 0.46$. The oxygen atoms are now able to organize themselves in a complete 2D hexagonal packing without distortion, but there is still a visible hole in the middle of the structure with a few not-fully coordinated In atoms, still, due to the lack of oxygen in the oxide.

We follow up with structure 1 Figure V.17 (c), which presents an ultrathin oxide without any holes in its structure. It has an atomic density of 0.19 at./Å^2 and oxygen content of $x_{\text{O}} = 0.50$. It is interesting to notice that although all In atoms are fully coordinated each with three oxygen atoms, forming a clear hexagonal structure, there is a distortion in the overall atomic configuration due to the increase in the average In–O bond distance (2.13 Å), compared to 2.10 Å in the undistorded configuration of structures 47 and 70. This distortion may be one of the factors leading to a relatively high value of the surface energy. Finally, one of the most stable surface structures, according to our thermodynamic model, is structure 63 (Figure V.17 (d)). It has an atomic density of 0.21 at./Å and oxygen content of $x_{\text{O}} = 0.53$. The tiling configuration consists of non-distorted hexagonal shapes and the addition of the distorted rectangular shapes. Figure V.17 thus reveals that specific combinations of atomic density, content of oxygen, and the distribution of O atoms into close to non-distorted shapes (by combining specially the hexagonal and rectangular tiles), may be key parameters for the formation of ultrathin indium oxide films.

In summary, we identified that structures 22 to 27 have the lowest surface energies when considering two different thermodynamic models. This stability was correlated to intrinsic electronic properties, such as the oxide structural relaxation and the charge transfer to the substrate, as well as the composition and the oxide atomic density. With an increase in the temperature, larger oxide 1×7 structures seem to stabilize according to both models (structure 63 even has the lowest surface energy at 1200 K for the model given by Equation (V.1)), while an increase in pressure has a minor effect.

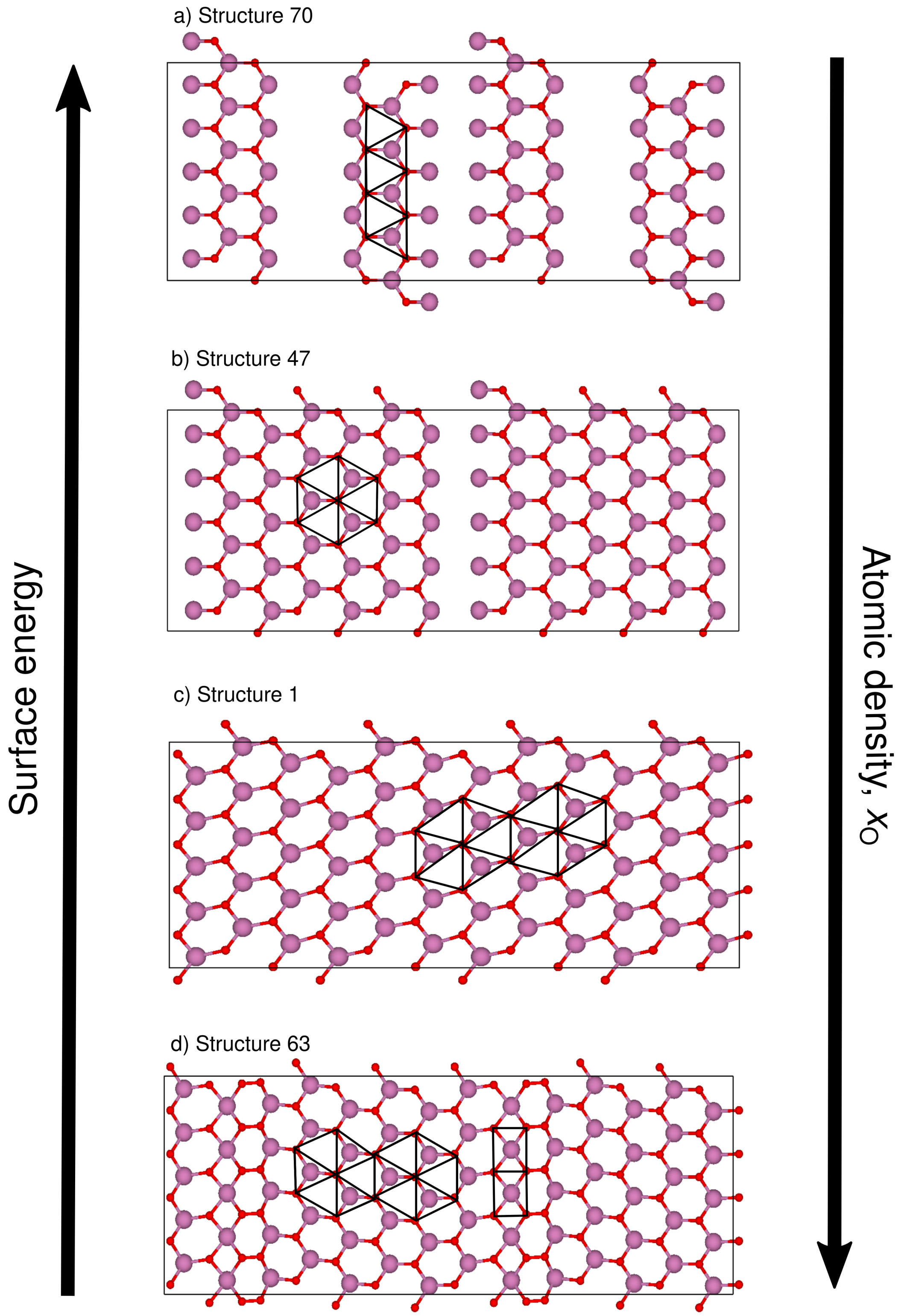

Figure V.17: Comparison of the four representative structures (a) 70, (b) 47, (c) 1, and (d) 63, correlating their tiling configurations, stoichiometry, and surface atomic density with their surface energy. O and In atoms are represented in red and purple, respectively.

In the next section, we present and compare the obtained calculated STM images of these selected structures, showing that the tiling created by the oxygen atoms also corresponds to the bright spots in the STM images, creating the same tiling configurations.

V.2. Simulation of the STM images

The simulated STM images, using the Tersoff-Hamann approximation [141], [142], were calculated for all 114 structures at four different bias voltages (-1.0 V, -0.5 V, 0.5 V, and 1.0 V), so that we created a database of these films that identifies and correlates the structure of supported In$_x$O$_y$ films with the bright spots in an experimental STM. We focus our analysis on a few exemplary structures (based on the thermodynamic models used in the previous section) that have representative properties of the rest of the oxides. A *PDF* file containing all images is available at the github page `https://github.com/DoriniTT/Thesis_extra_results`.

We begin with a comparison between the simulated STM images (Figure V.18) calculated for structures 70, 47, 1, and 63 (Figure V.17). In all STM images, the bright spots are correlated to the electronic structure of the oxygen atoms that are slightly protruded above the average mean height of the In atoms, with a less significant (but also present) electronic tunneling coming from the In atoms. The reason that O and In atoms are seen in the STM images is due to their non-zero LDOS at the Fermi level. The non-zero LDOS results from a substantial charge transfer from the substrate to the oxide, making the ultrathin oxide film a conductor. Because O atoms are higher than the In atoms, they are brighter in the STM image. An exemplary LDOS of structure index 19 is shown in Figure V.19. The LDOS suggests that the configuration of the bright spots in an experimental STM image likely corresponds the protruded oxygen atoms. For most of the 114 structures calculated in the present work, there are two main building blocks in which the protruded oxygen atoms form rectangular and distorted hexagonal shapes, which can be seen specially in structure 63, in Figure V.17 (d).

The correlation between the position of the O atoms and the bright spots in the calculated STM images can be clearly seen in the four STM images shown in Figure V.18, where the same patterns of the protruded oxygen atoms in the oxide are identified. As a result, by simply looking at an experimental (or calculated) STM image, one might have an idea of the overall structure of the oxide, as well as correlate it with the composition and atomic density.

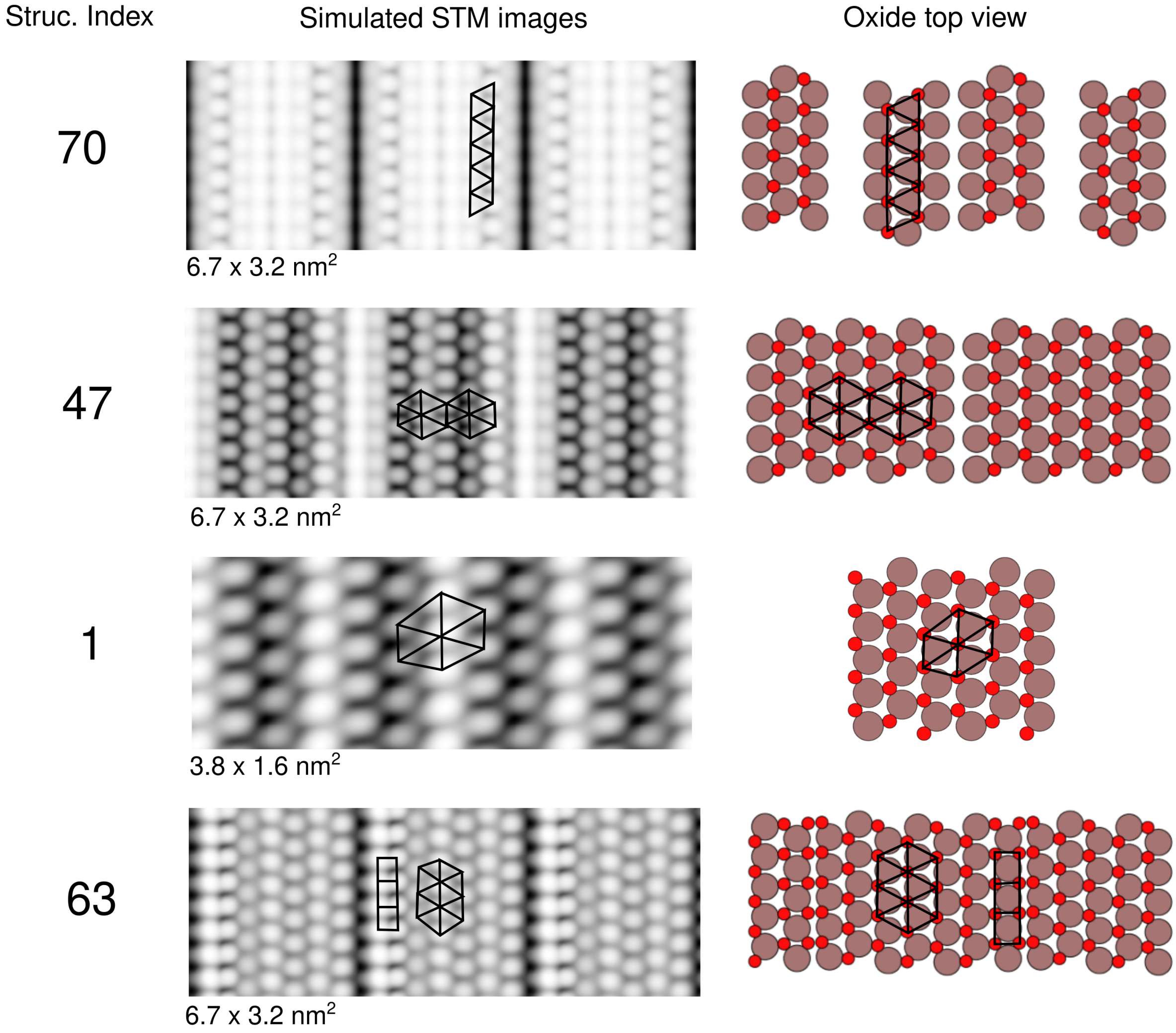

Figure V.18: Calculated STM images, with bias voltage of 1.0 V (left), and the top view of structures 70, 47, 1, and 63 (right). The stability of the shown structures increases from top to bottom. The tiling configurations are represented with black lines. O and In atoms are represented by red and gray, respectively.

Calculated STM images of two additional selected structures (24 and 21) are shown in Figures V.20 and V.21, showing also the difference between two different bias voltages (-1 V and $+1$ V). Structure 24 (red category) has one of the lowest surface energies according to Figures V.11 and V.14 (0.72 J/m^2), while structure 21 has higher surface energy (2.30 J/m^2).

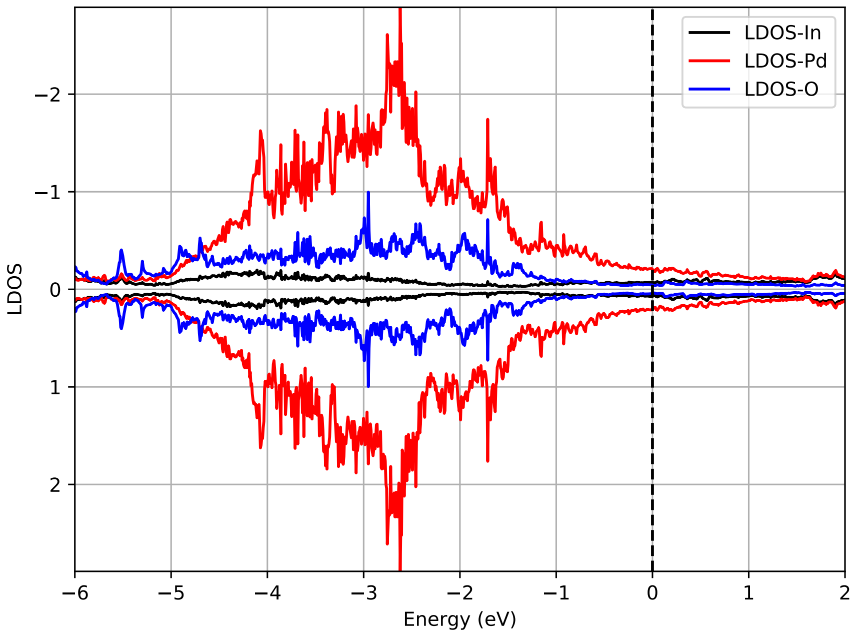

Figure V.19: Local density of states (LDOS) of structure 19, showing projections to In and O from the In$_x$O$_y$ oxide and Pd from the first layer of the PdIn(001) substrate.

STM images of some structures strongly depend on the applied bias. For instance, there is a huge difference between images of Figure V.21 (a) and (b), demonstrating a huge shift in the distribution of the bright spots, while on Figure V.20, this difference is less pronounced, making only the identification of the protrusion's motives harder to identify.

By combining the correlations reported here regarding surface energies, STM images, charge distribution, and structural motifs to all best ranked structures, one can use the information contained in the database (either the *PDF* with all the STM images, or the *JSON* file with the atomic information) for future experimental or computational work. This way, it would be possible to understand the building principles that rules the preferential growth modes of UTOx and make precise predictions on new structures on these ultrathin films, as was applied in the work by Barcaro et al. [44] on ultrathin TiO$_x$ films.

(a) STM image with bias voltage of −1 V.

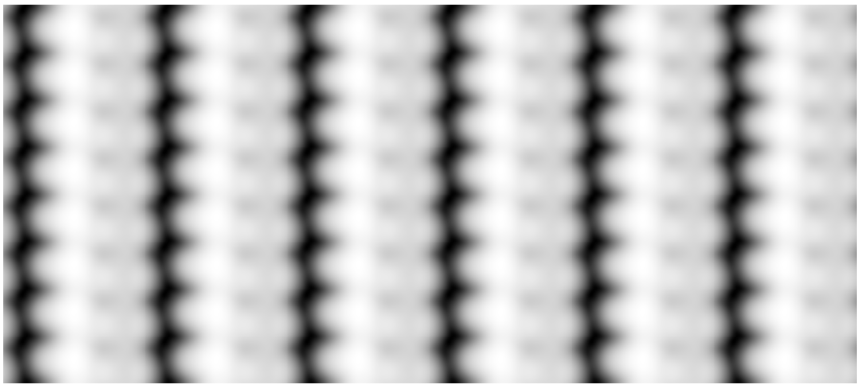

(b) STM image with bias voltage of +1 V.

(c) Top view.

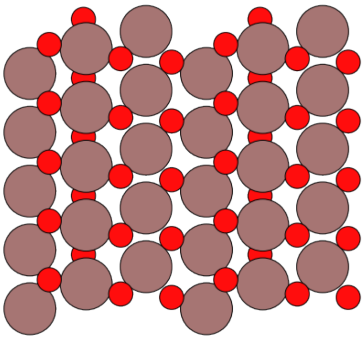

(d) Side view.

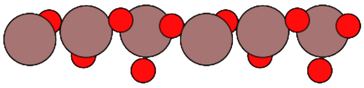

Figure V.20: STM images with bias voltages of (a) −1 V and (b) +1 V. (c) Top and (d) side views of structure 24.

(a) STM image with bias voltage of −1 V.

5.8×3.2 nm^2

(b) STM image with bias voltage of +1 V.

5.8×3.2 nm^2

(c) Top view.

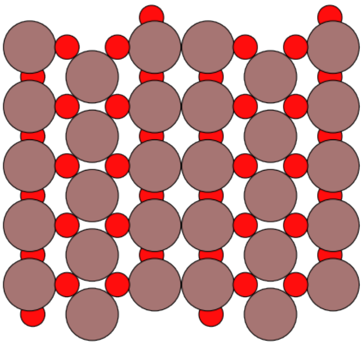

(d) Side view.

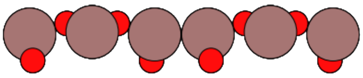

Figure V.21: STM images with bias voltages of (a) −1 V and (b) +1 V. (c) Top and (d) side views of structure 21.

VI. Conclusion

The structures of a plethora of ultrathin oxide films of In$_x$O$_y$ considering several compositions supported on a PdIn(001) substrate with three different supercells (1×3, 1×5, and 1×7) were determined using the USPEX software. Starting with 148 484 initial individuals calculated, we selected 114 best structures according to their enthalpy of formation to determine their electronic and thermodynamic properties. To do so, we have developed a Python code called Vulcan, which automates all calculations, from parallel and sequential running of many different types of calculation for each structure to the post processing of data (LDOS, Bader charge, adhesion energies, total energies, etc.).

With all the results for the total energies gathered, we applied two distinct thermodynamic models to study the stability of the selected 114 structures at ambient conditions, arriving at 12 most stable surface structures. Surface free energies increase with increasing temperature and less so with increasing pressure. A temperature increase stabilizes the larger 1×7 structures relative to the smaller 1×3 ones.

Subsequently, we correlated the surface stability of these surfaces with their electronic and structural parameters. We discovered that there is a specific combination of charge distribution in the first layer of Pd in the substrate and the rumpling in the oxide that is present in the most of the stable structures, making it a possible criterium for selecting ultrathin oxide films that may actually exit and be observed experimentally.

In order to help experimentalists better compare their future results with our calculations, we generated the STM image of all 114 structures at four different bias voltages (-1.0 V, -0.5 V, $+0.5$ V, and $+1.0$ V). The bright spots in the calculated STM images are assigned to the electronic density of the protruded oxygen atoms and can be aggregated in two main tiling configurations: rectangular and distorted hexagonal. In contrast the electronic density of In is less visible. We hope that these results may serve as a helpful roadmap with several exemplary structures and characteristics that future experimentalists can use to compare their results.

General conclusions

We report here the main conclusions from each of the results chapters, highlighting the main achievements and ideas. In Chapter III, more than 80 ABO_3/Me materials (A = alkali earth metal, B = transition metal, Me = metal substrate) have been computationally investigated, which concerns the Förster-σ approximant model [10]. An understanding of how the OQA chemistry affects the atomic structures and attributes of aperiodic oxide ultra-thin films has been gained from comparisons of their relative stability to periodic atomic arrangements with similar compositions.

The substrate's characteristics and the B-metal have an impact on the magnetic properties, whilst the kind of earth alkaline metal A has an effect on the work function, i.e., the change in the metallic substrate's work function brought on by the deposition of the oxide film. Although the size-mismatch is commonly thought to be the key driving force towards the production of ultra-thin oxide layers on metals, including OQAs, no direct association between the surface cell mismatch and the rumpling or the adhesion energies (Figure III.5a-d)) was discovered. On the other hand, electronic effects were shown to be crucial factors affecting the stability of OQAs. Among the investigated properties, adhesion energies and rumplings closely correlate with the charge transfer, which is dictated by the B-type metal. In the second part of Chapter III, we also analyzed the σ-phase with the model of Cockayne et al. The structure with this model appears to be considerably more stable according to the enthalpy of formations, adhesion energies, and ICOHP calculations. However, despite the fact that many of the parameters are very different, such as the rumpling and the surface atomic density, there are some that are intriguingly similar between these two models. One such parameter is the overall charge distribution in the substrate and oxide, which is explained by the charge density difference and the average atomic Bader charge. Using AIMD, the overall stability of this Cockayne-σ approximant phase was examined. AIMD simulation demonstrates that this oxide is in fact reasonably stable on the surface of Pt(111), maintaining its structural motifs throughout the entire simulation. However, AIMD demonstrates that some Ti–O bonds may be more likely to break and form other types of tilings, such as a transition from a triangle to a rhombus, while other Ti–O bonds remain unbroken.

Since the COHP calculation of the unsupported approximant shows a significant amount of anti-bonding type of interaction not only at the interface but also for the intra-oxide bonds, such as Sr–O and Ti–O, we believe that the Pt–Ti bonds stabilize the structure of the oxide approximant as a whole.

In Chapter IV, we have concentrated on the structural and electronic characteristics of approximant phases that were discovered experimentally (Cockayne-σ, giant, hexagonal, small hexagonal, and two monoclinic phases), as well as three simulated phases that were manually created from the ideal dodecagonal NGT tiling. We also compared their stabilities in terms of surface free energies, adhesion energies, and charge analysis. We discovered that the experimental and simulated STM images for the giant and hexagonal approximant phases, where the electronic density of the Sr atoms is evident as the bright protrusions, match perfectly when the approximant structures are created using Cockayne's model. The analysis of simulated STM images reveals that the primary factor determining the bright spots is the height of the protruded atoms on the ultrathin oxide surface. A study of the stability of all approximants reveals that the two most stable phases at 0 K are the fictional approx. 2 and 3. This finding suggests other approximant phases may still be discovered in addition to those already identified. As for the lateral position of the oxide with respect to the substrate, the energy does not significantly change when the Ti atoms, which we find responsible for the adhesion of the oxide, are located in different sites on the Pt(111) substrate. The main factor that affects the adhesion energy (and other properties) is the amount of Ti in the oxide film. We conclude that the model by Cockayne et al. can be used to simulate these and other yet-to-be-discovered phases of ultrathin oxide films. Our calculations may serve as a helpful roadmap for subsequent calculations and tests because they have a good match with STM images measured in our laboratory, and are also coherent with various other characteristics between approximants (such as the adhesion energies).

In Chapter V, the USPEX program was used to predict structures of a variety of ultrathin oxide films of In_xO_y supported on a PdIn(001) substrate with three distinct supercells (1×3, 1×5, and 1×7). We chose 114 of the best structures based on their enthalpy of formation from a total of 148 484 computed individuals in order to analyze their electronic and thermodynamic characteristics. In order to do this, we developed the Python program Vulcan, which automates calculations, from the parallel and sequential execution of several different types of computations for each structure to the post-processing of data (LDOS, Bader charge, adhesion energies, total energies, etc.). We used two different thermodynamic models to analyze the stability of the best 114 structures in ambient conditions. This analysis singled out 12 out of the 114 structures as the most stable. The surface free energy of these oxides increases with increasing temperature and less so for the pressure. The thermodynamic analysis also shows that the larger 1 × 7 structures are stabilized relative to the smaller 1 × 3 ones with increasing temperature. We also correlated the electronical and structural properties of these phases with their stabilities. We found that stable supported ultrathin oxide films have a certain combination of charge distribution in the topmost layer of Pd in the substrate and the rumpling in the oxide. We calculated the STM images of all 114 structures with four distinct bias voltages (1.0 V, 0.5 V, 0.5 V, and 1.0 V), to enable experimentalists to compare their future findings with our computations. While the electronic density of In is less apparent, the bright spots in the simulated STM images are connected to the electronic density of the protruded oxygen atoms and may be arranged in two major tiling configurations: rectangular and hexagonal. We anticipate that by providing future experimenters with a wealth of illustrative structures and their characteristics, these data will serve as a helpful roadmap for future experiments and computations.

Perspectives

From our experience throughout this work, we suggest a plethora of interesting ideas as follow-up work that other modelers or experimentalists might pursue.

For Chapter III and Chapter IV, one could further verify the stability of the approximant phases on the (Ba/Sr)–Ti–O/Pt(111) systems by phonon calculations as to search for imaginary frequencies that indicate structural instability. This could be done mainly for the "smaller" approximants investigated in this study, since phonon calculations are computationally quite demanding. These phonon calculations could also be used to verify the stability of the two models used on this work, the Forster's and Cockayne's models. In addition, AIMD simulations could be performed for longer simulation times for the Cockayne-σ approximant, covering a larger phase space to identify other stable motifs and possibly study the oxide stability by phasons. On the application side for these structures, it would be interesting to calculate the adsorption energies of C_{60} molecules on the surface of these approximants and compare with recent experiments [202]. For Chapter V, in order to use other methods to search for new structures in the phase space, one could use AIMD with several compositions, supercell sizes, and temperatures to determine other "best" structures to add to the database, or to compare them with the structures obtained with USPEX. Aditionally, one could increase the number of supercells used for the PdIn(001) substrate, for instance 2 × 2 and 2 × 3, to obtain a richer set of structures, or even change the substrate orientation to the (110) plane since it is one of the most stable. To verify the similarities of our simulated STM images, one could attempt to produce experimentally such ultrathin oxide films and obtain STM images to compare with our database. Finally, to test whether these ultrathin films are potential candidates to substitute the commonly used catalyst $Cu/ZnO/Al_2O_3$ for methanol formation, we suggest doing Nudge Elastic Band (NEB) calculations on a few selected best structures among the most stable calculated ones, as to calculate the energetic barriers for the formation of methanol starting from CO or CO_2 molecules.

Appendix A

Supplementary images and tables

I. E_{cut} energy and k-mesh

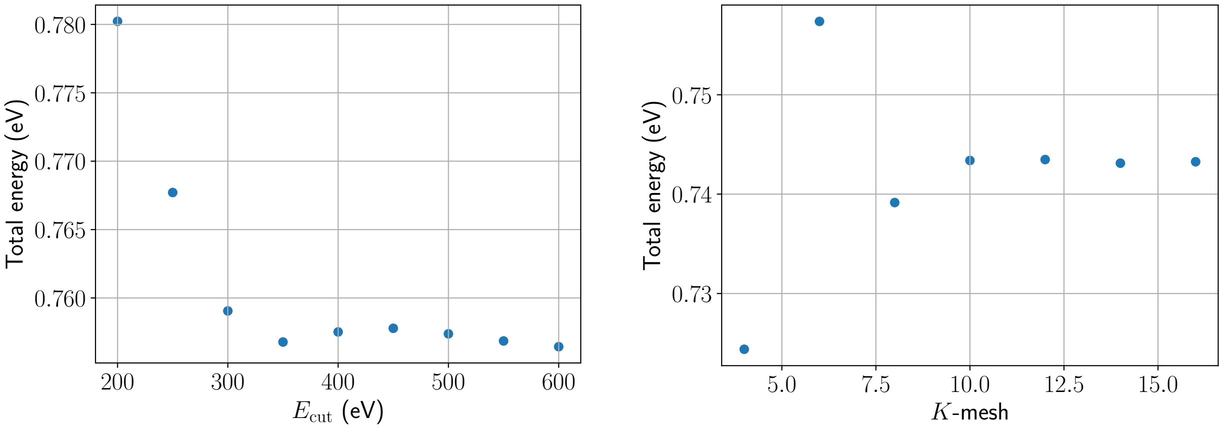

(a) Ba ($Im-3m$) – E_{cut}

(b) Ba ($Im-3m$) – k-mesh

Figure A.1: Influence of the (a) E_{cut} and the (b) k-mesh for Ba ($Im-3m$) using the optPBE-vdW functional. In (b), we consider the same number of points in all three xyz directions (i.e., k-meshes were scanned from $4 \times 4 \times 4$ to $16 \times 16 \times 16$).

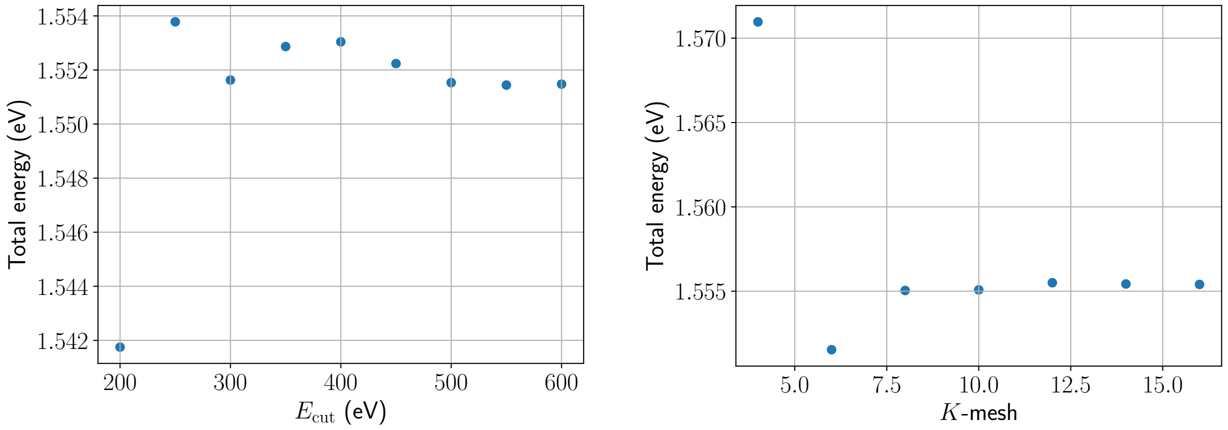

(a) Sr ($Fm-3m$) – E_{cut}

(b) Sr ($Fm-3m$) – k-mesh

Figure A.2: Influence of the (a) E_{cut} and the (b) k-mesh for Sr ($Fm-3m$) using the optPBE-vdW functional.

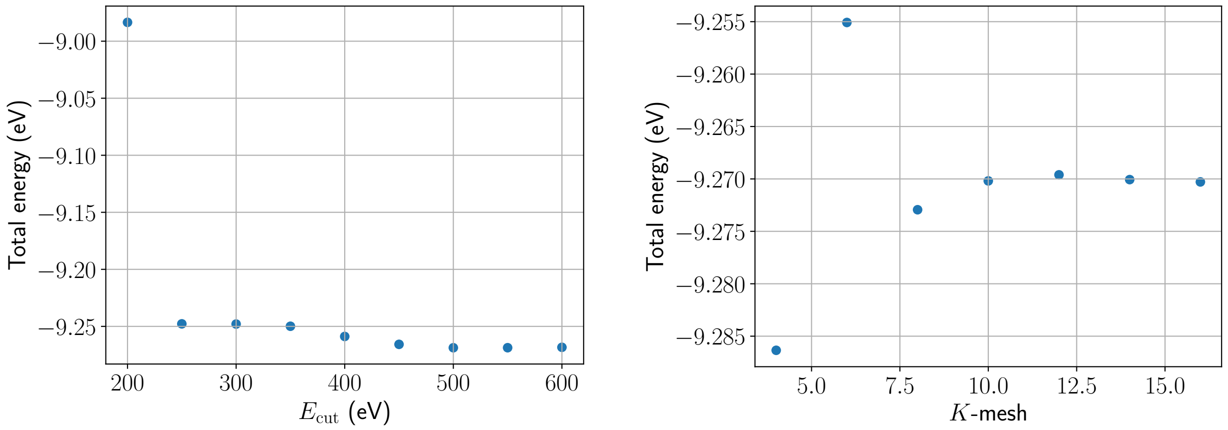

(a) Ti ($P6/mmm$) – E_{cut}

(b) Ti ($P6/mmm$) – k-mesh

Figure A.3: Influence of the (a) E_{cut} and the (b) k-mesh for Ti ($P6/mmm$) using the optPBE-vdW functional.

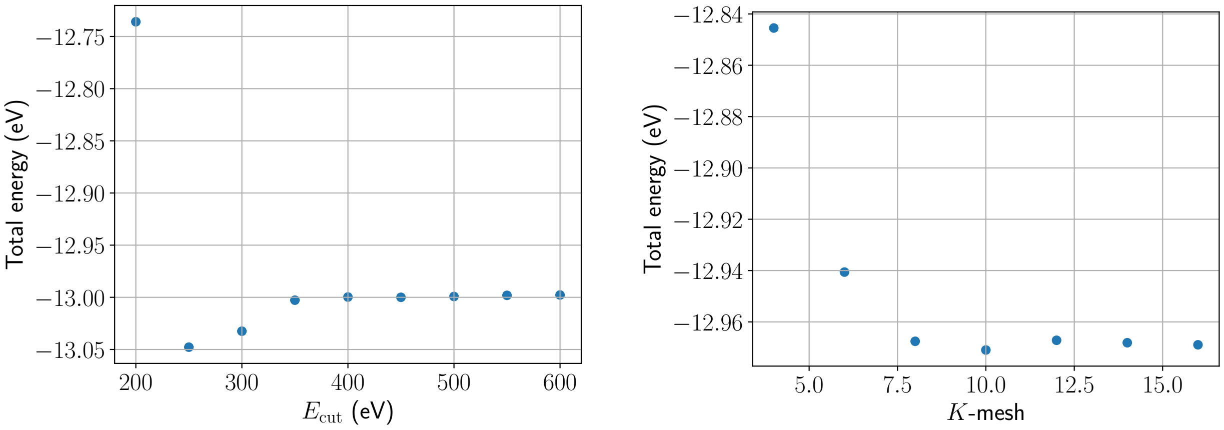
(a) Pt $(Fm-3m)$ – E_{cut}

(b) Pt $(Fm-3m)$ – k-mesh

Figure A.4: Influence of the (a) E_{cut} and the (b) k-mesh for Pt$(Fm-3m)$ using the optPBE-vdW functional.

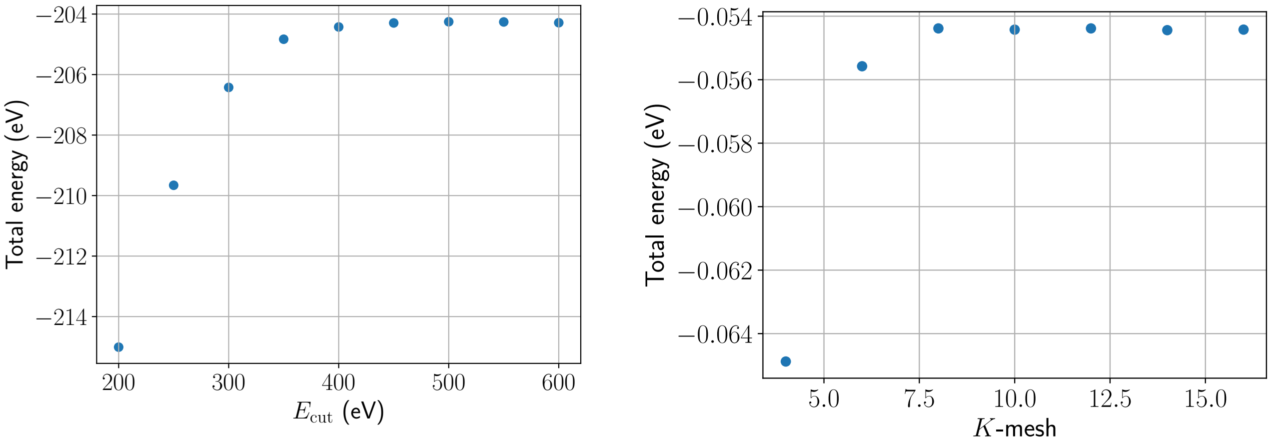
(a) Ti_2O_3 $(Pnma)$ – E_{cut}

(b) Ti_2O_3 $(Pnma)$ – k-mesh

Figure A.5: Influence of the (a) E_{cut} and the (b) k-mesh for $Ti_2O_3(Pnma)$ using the optPBE-vdW functional.

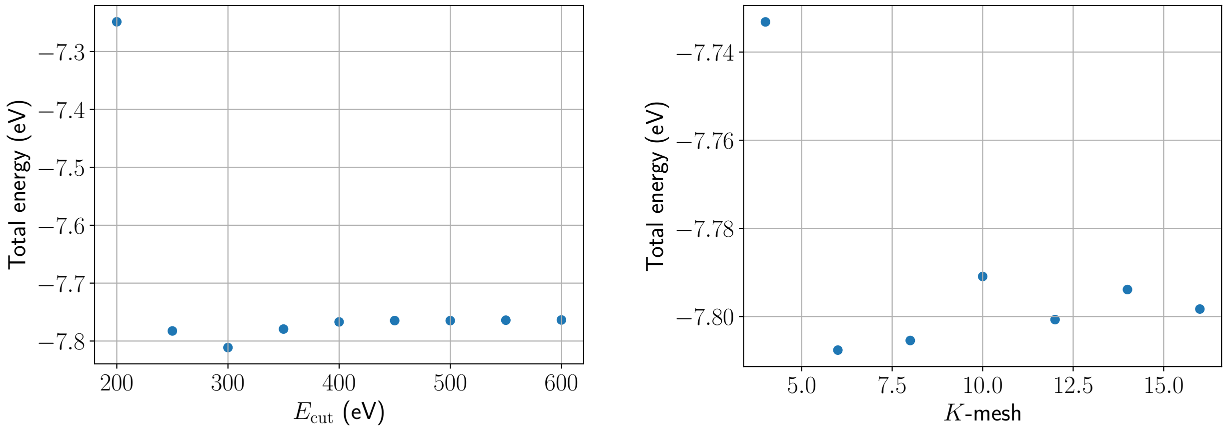

(a) Pd $(Fm-3m)$ – E_{cut}

(b) Pd $(Fm-3m)$ – k-mesh

Figure A.6: Influence of the (a) E_{cut} and the (b) k-mesh for Pd$(Fm-3m)$ using the GGA functional.

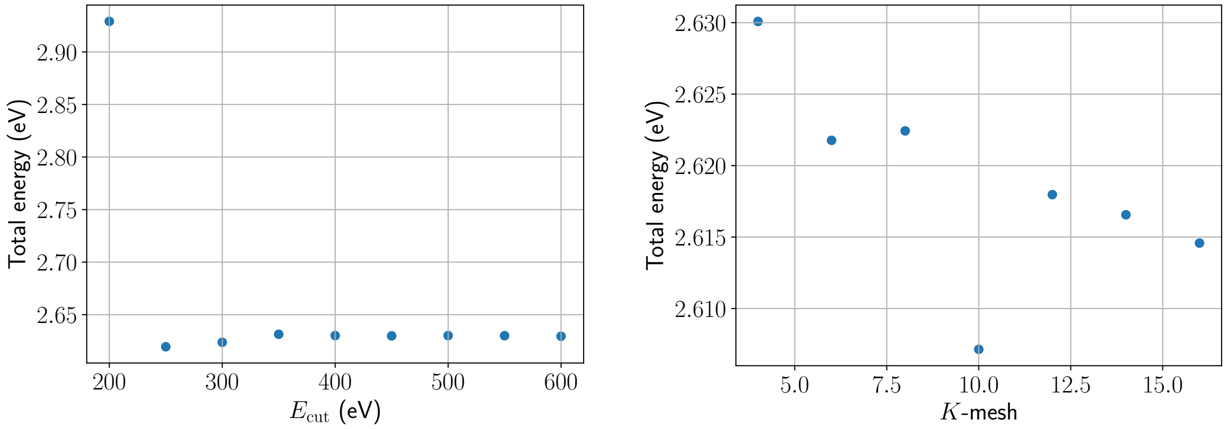

(a) In $(I4/mmm)$ – E_{cut}

(b) In $(I4/mmm)$ – k-mesh

Figure A.7: Influence of the (a) E_{cut} and the (b) k-mesh for In$(I4/mmm)$ using the GGA functional.

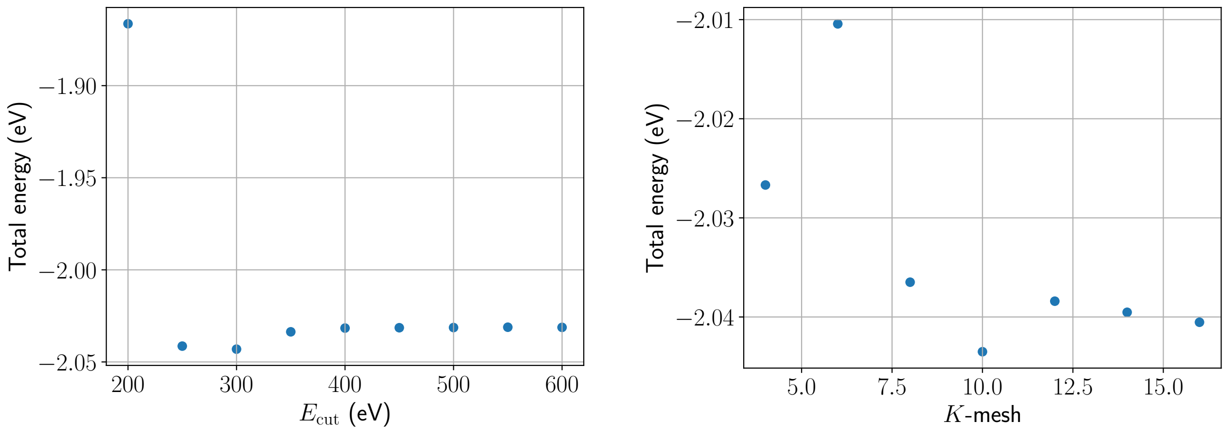

(a) PdIn $(Pm-3m)$ – E_{cut}

(b) PdIn $(Pm-3m)$ – k-mesh

Figure A.8: Influence of the (a) E_{cut} and the (b) k-mesh for PdIn$(Pm-3m)$ using the GGA functional.

II. Influence of the exchange and correlation functionals to ΔH_{f} and E_{coh}

Formation enthalpy (eV/at.)	PBZ	PDA	PBEsol	revPBE	optPBE-vdW	optB88-vdW	exp.
$BaTiO_3$ ($P4mm$)	−3.463	−3.369	−3.490	−3.298	−3.350	−3.461	−3.284 [203]
$SrTiO_3$ ($P4mm$)	−3.533	−3.435	−3.545	−3.363	−3.382	−3.525	−3.351 [204]
Ti_2O_3 ($Pnma$)	−3.245	−3.152	−3.269	−3.06	−3.152	−3.244	−3.153 [205]
PdIn ($Pm-3m$)	−0.458	−0.484	−0.549	−0.454	−0.484	−0.481	−0.507 [206]

Table A.1: Enthalpy of formation for four relevant structures to this work considering six different functionals and comparison with experimental values.

Cohesive energies (eV/at.)	PBE	LDA	PBEsol	revPBE	optPBE-vdW	optB88-vdW	exp.
Ba	−1.87	−1.9	−2.2	−1.68	−1.91	−1.99	−1.91 [180], [181]
Sr	−1.53	−1.56	−1.84	−1.36	−1.57	−1.60	−1.73 [181], [182]
Ti	−6.23	−6.34	−6.9	−5.91	−5.17	−5.85	−4.85 [181], [182]
Pt	−5.74	−5.86	−6.72	−5.22	−5.63	−6.14	−5.84 [181], [182]
Pd	−3.75	−3.79	−4.5	−3.25	−3.79	−4.04	−3.89 [181], [182]
In	−2.3	−2.33	−2.76	−2.01	−2.33	−2.50	−2.52 [181]

Table A.2: Cohesive energies for seven relevant structures to this work considering six different functionals and comparison with experimental values.

III. COHP – Förster-σ

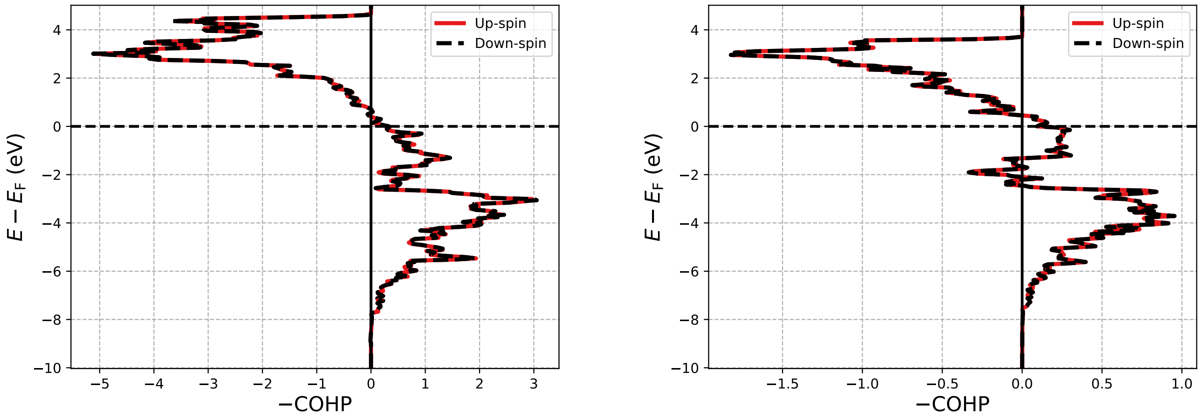
(a) Ti–Pt

(b) Ti–Au

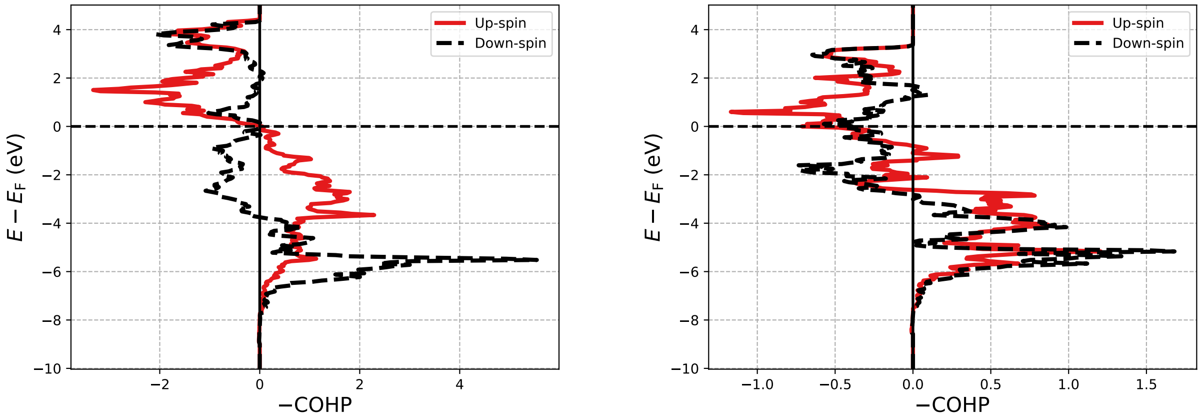
(c) Fe–Pt

(d) Fe–Au

Figure A.9: COHPs for specific bonds up to 3 Å in the BaBO$_3$/Pt(111) systems (with B = Ti, Fe).

(a) Co–Pt (b) Co–Au

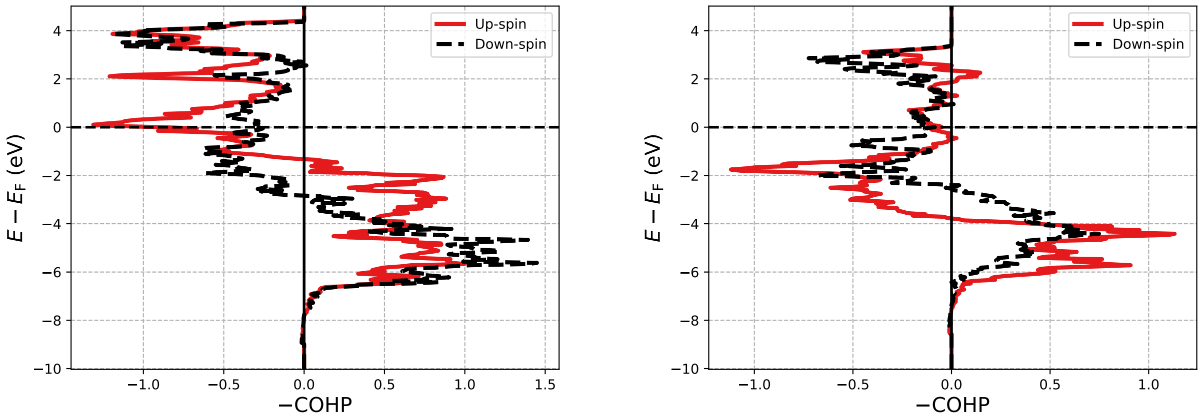

(c) Ni–Pt (d) Ni–Au

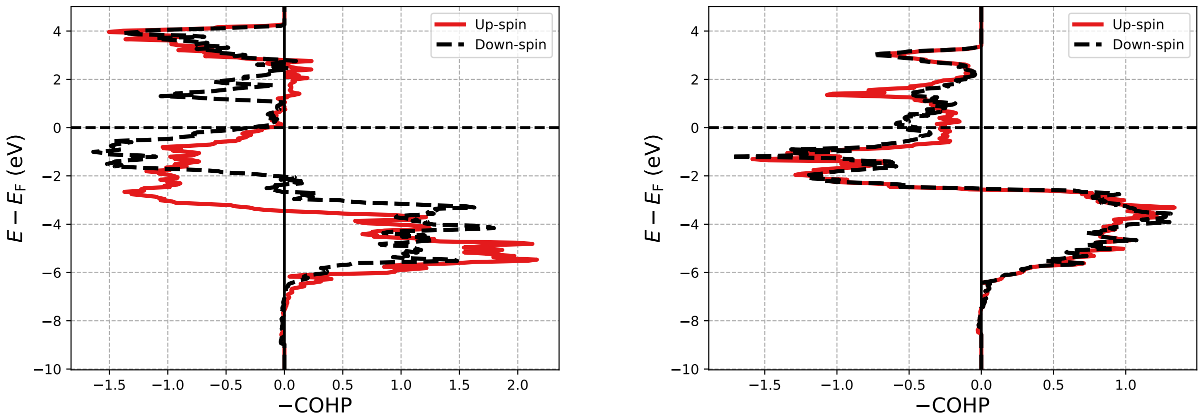

Figure A.10: COHPs for specific bonds up to 3 Å in the BaBO$_3$/Pt(111) systems (with B = Co, Ni).

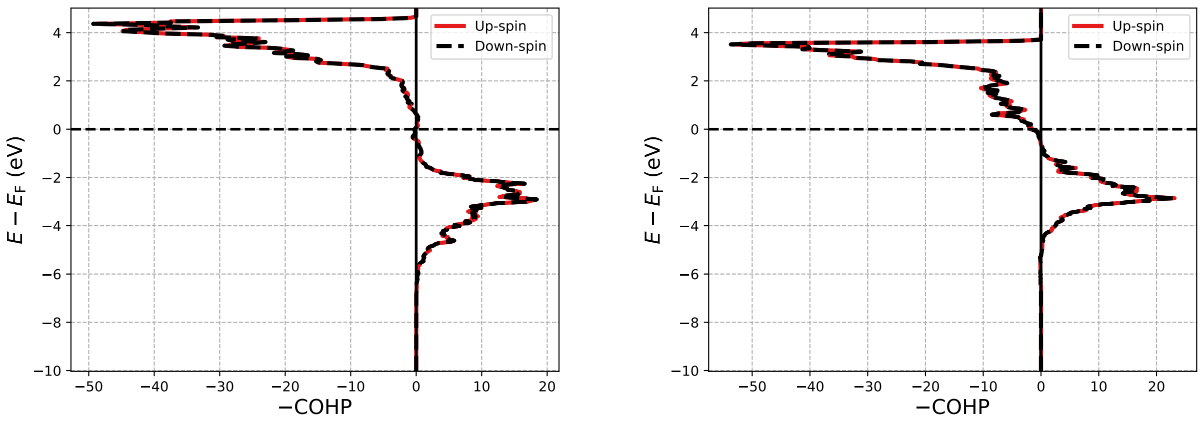
(a) Ti–O (with Pt)

(b) Ti–O (with Au)

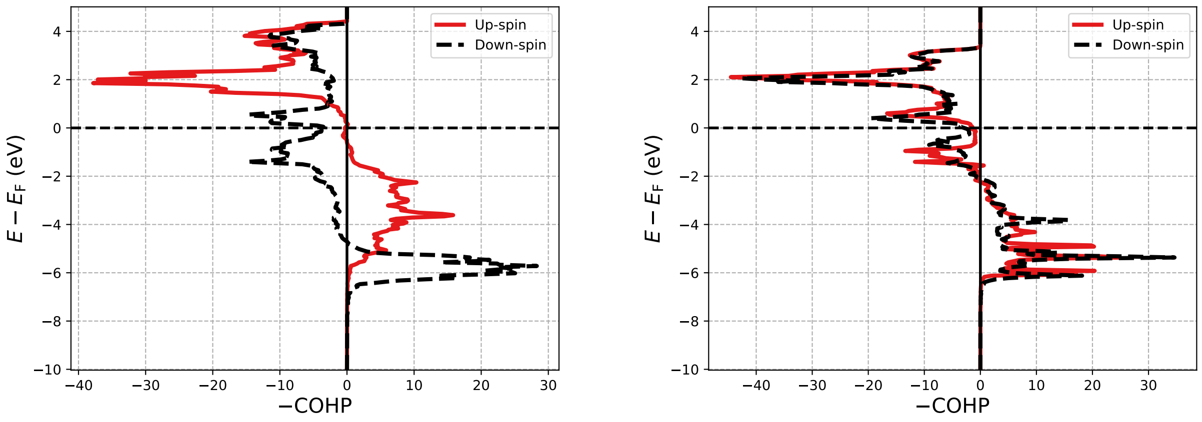
(c) Fe–O (with Pt)

(d) Fe–O (with Au)

Figure A.11: COHPs for specific bonds up to 3 Å in the BaBO$_3$/Me(111) systems (with B = Ti, Fe).

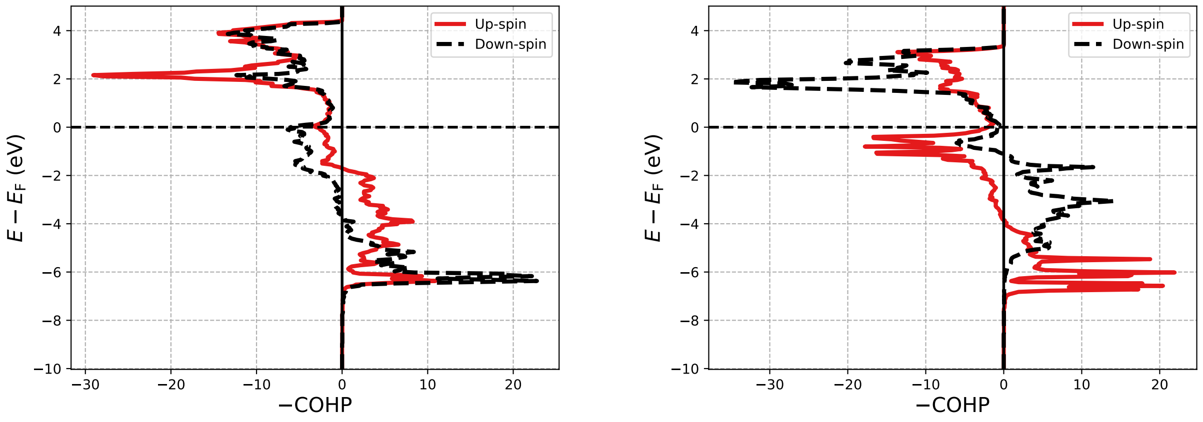
(a) Co–O (with Pt)

(b) Co–O (with Au)

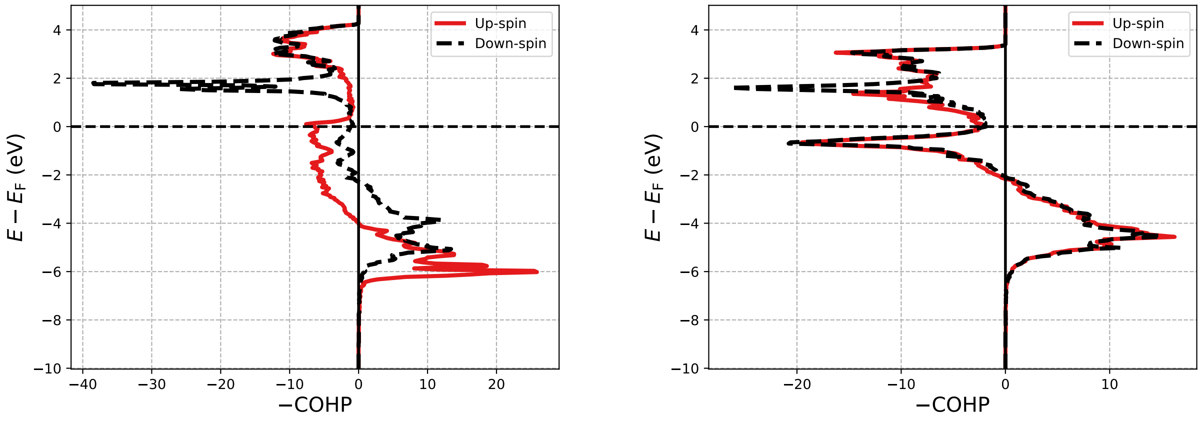
(c) Ni–O (with Pt)

(d) Ni–O (with Au)

Figure A.12: COHPs for specific bonds up to 3 Å in the BaBO$_3$/Pt(111) systems (with B = Co, Ni).

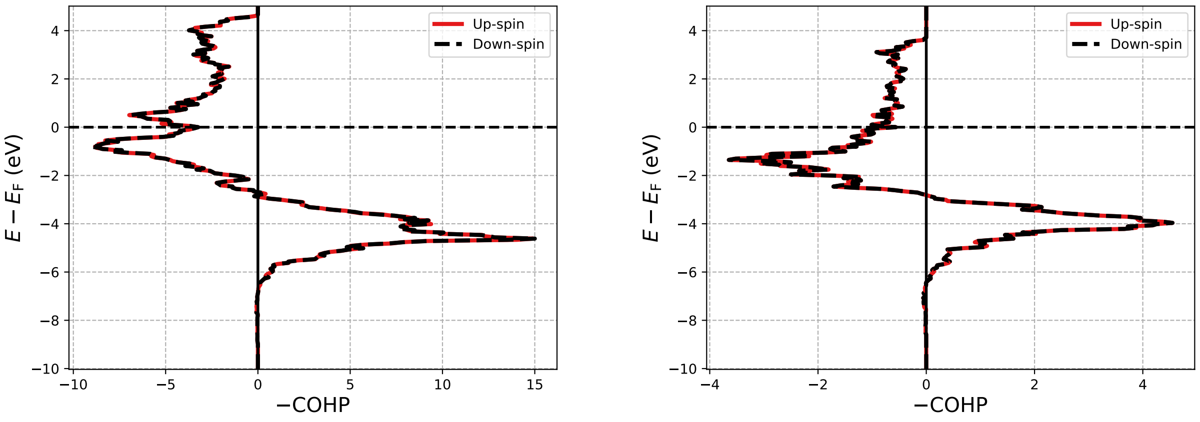
(a) Pt–O (with Ti)

(b) Au–O (with Ti)

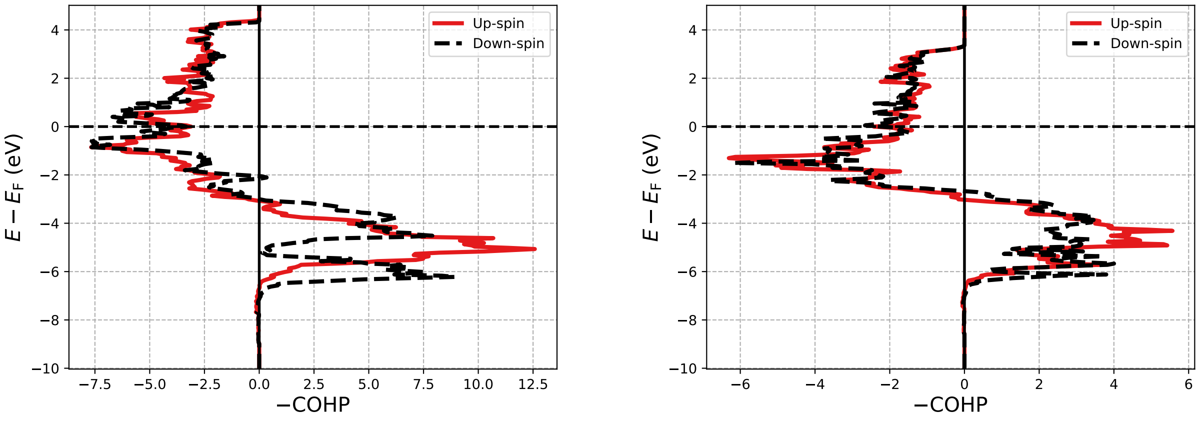
(c) Pt–O (with Fe)

(d) Au–O (with Fe)

Figure A.13: COHPs for specific bonds up to 3 Å in the BaBO$_3$/Me(111) systems (with B = Ti, Fe).

(a) Pt–O (with Co) (b) Au–O (with Co)

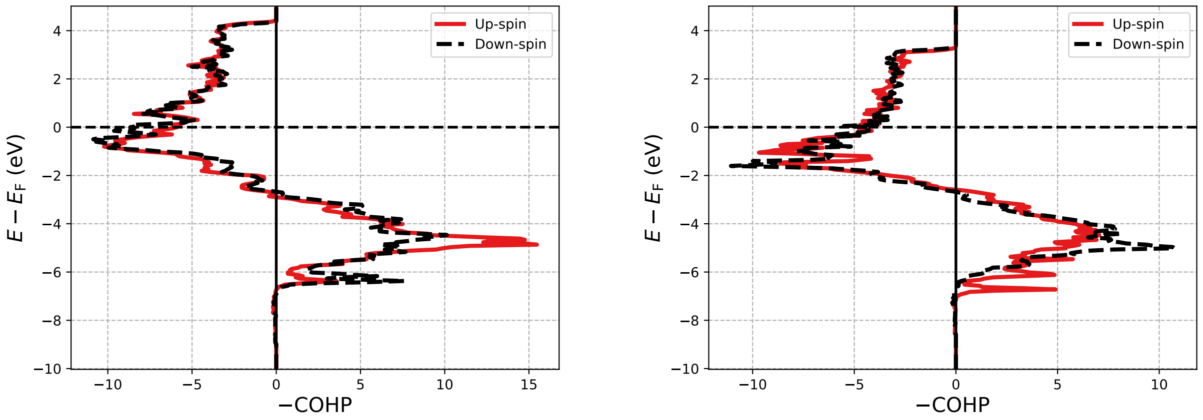

(c) Pt–O (with Ni) (d) Au–O (with Ni)

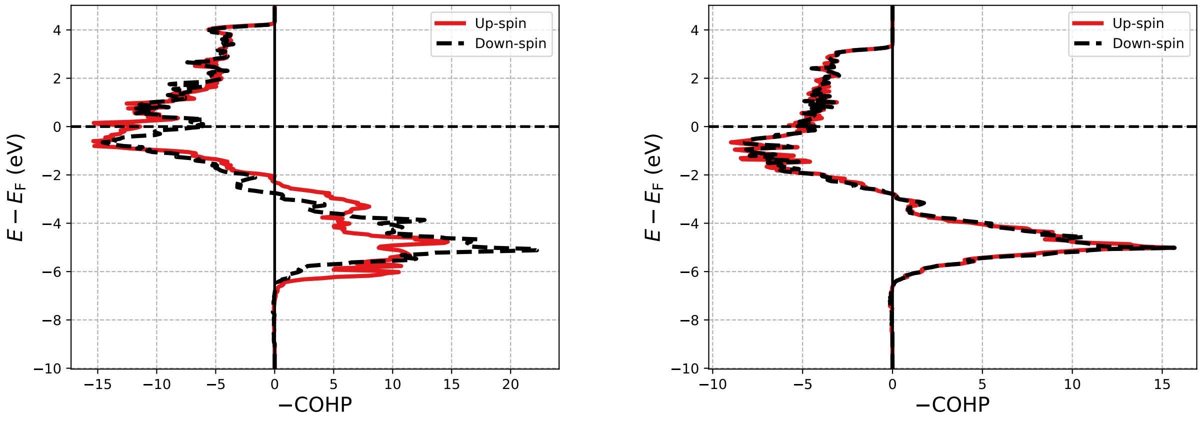

Figure A.14: COHPs for specific bonds up to 3 Å in the BaBO$_3$/Pt(111) systems (with B = Co, Ni).

IV. DOS – Förster-σ

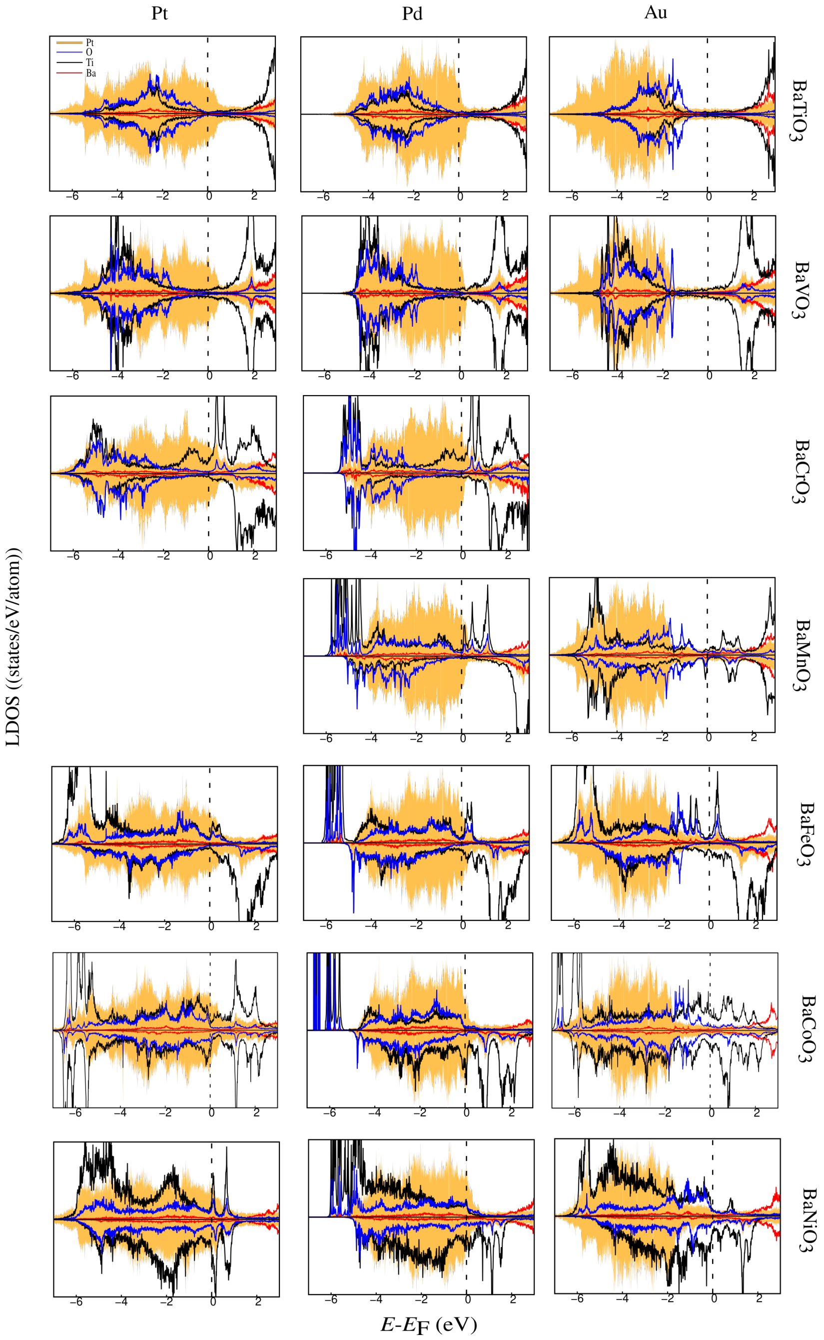

Figure A.15: Atom projected LDOS for BaBO$_3$ (B = Ti, V, Cr, Mn, Fe, Co, Ni) with Pt, Pd, and Au substrates. *Me*, Ba, B, and O are represented by orange, red, black, and blue colors, respectivelly, as indicated in the top-left plot.

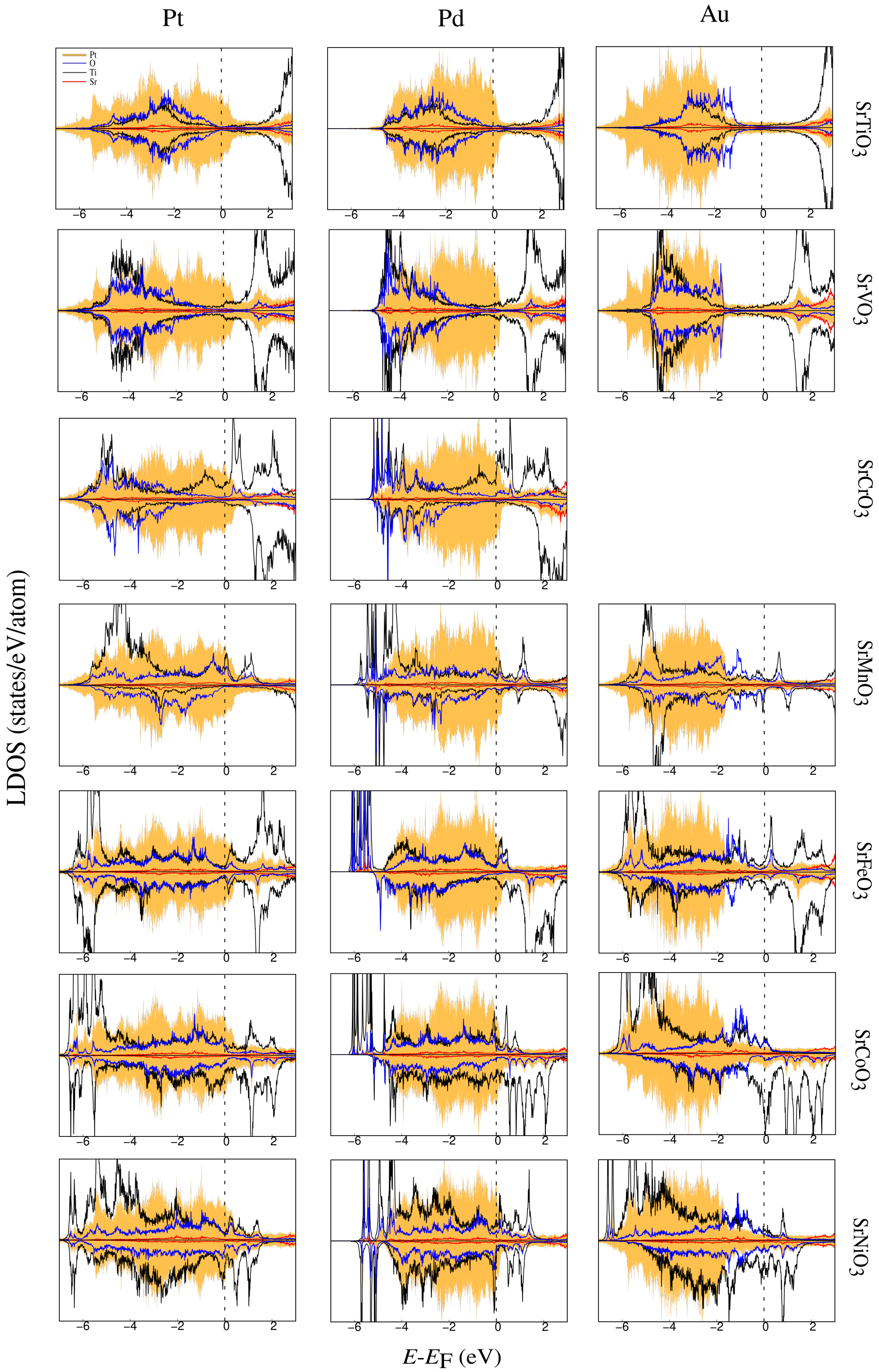

Figure A.16: Atom projected LDOS per atom for SrBO$_3$ (B = Ti, V, Cr, Mn, Fe, Co, Ni) with Pt, Pd, and Au substrates. *Me*, Sr, B, and O are represented by orange, red, black, and blue colors, respectivelly, as indicated in the top-left plot.

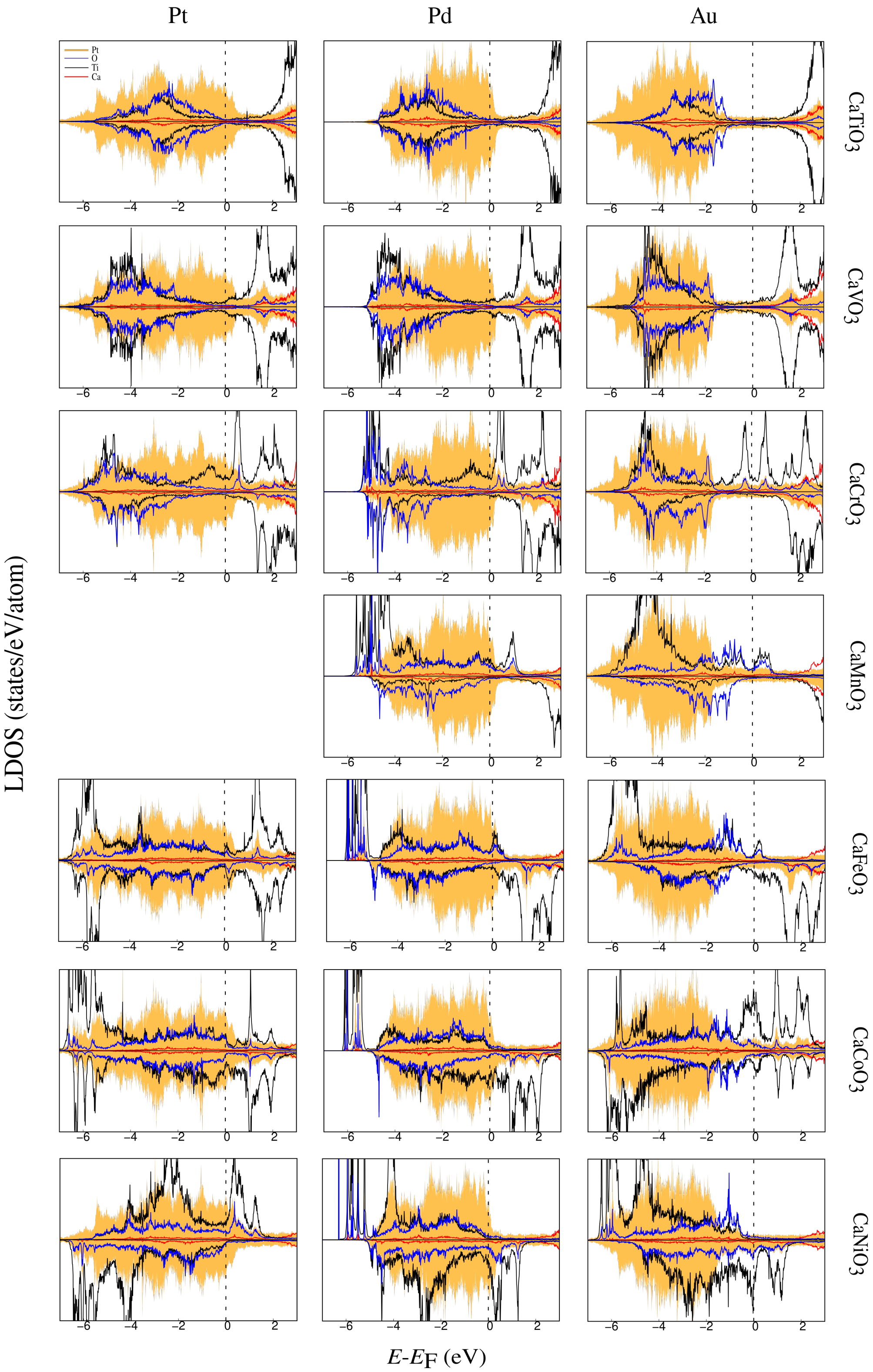

Figure A.17: Atom projected LDOS per atom for CaBO$_3$ (B = Ti, V, Cr, Mn, Fe, Co, Ni) with Pt, Pd, and Au substrates. *Me*, Ca, B, and O are represented by orange, red, black, and blue colors, respectivelly, as indicated in the top-left plot.

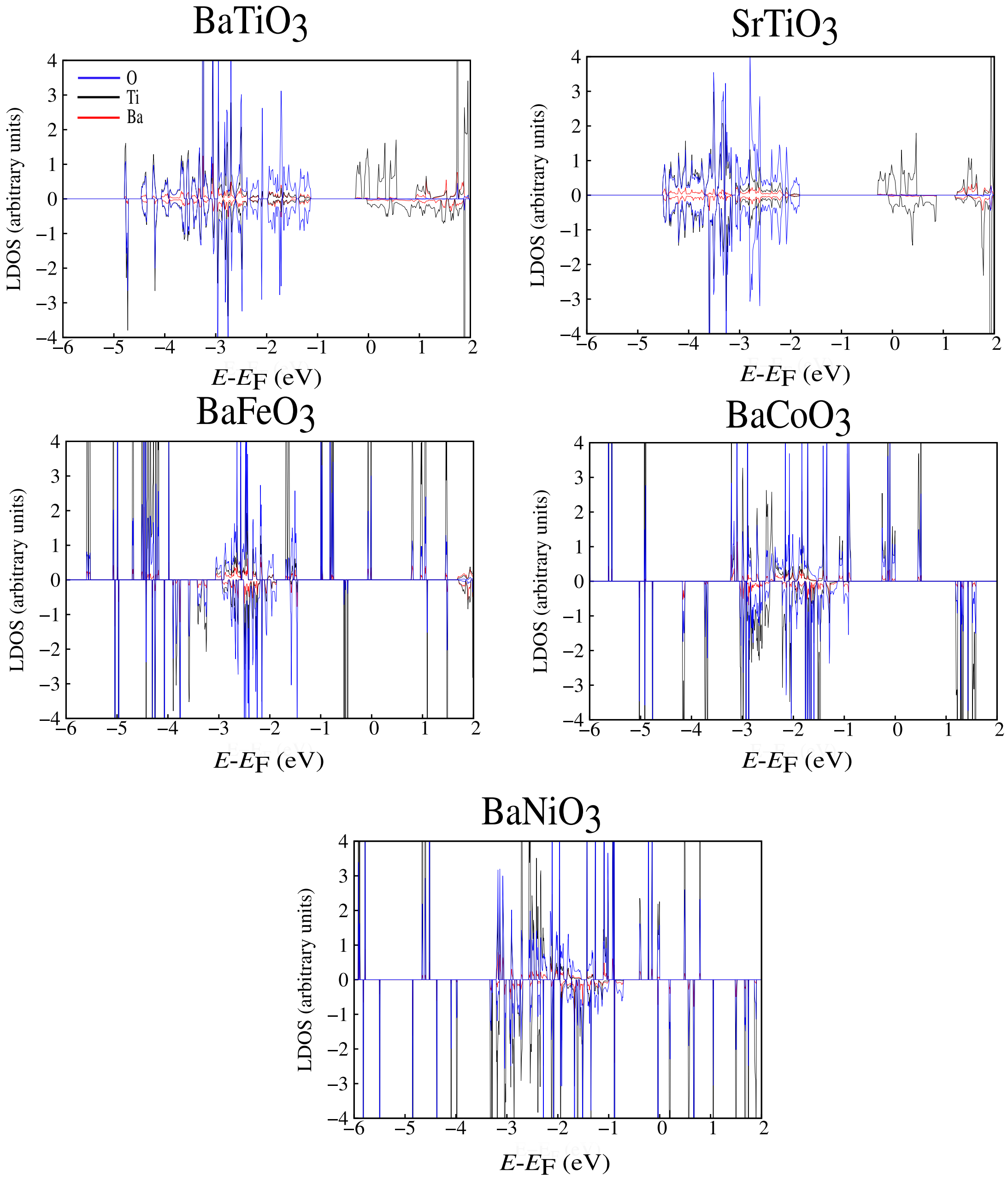

Figure A.18: Atom projected LDOS per atom for the oxide freestanding layers. Ba, *B*, and O are represented by red, black, and blue colors, respectivelly, as indicated in the top-left plot.

V. Thermodynamic model – Förster-σ

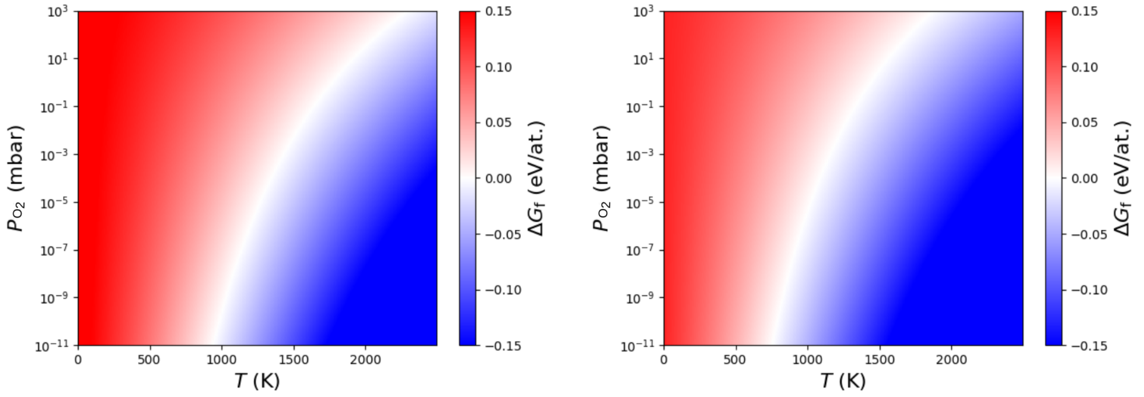
(a) $BaTiO_3$/Pt(111)

(b) $BaTiO_3$/Au(111)

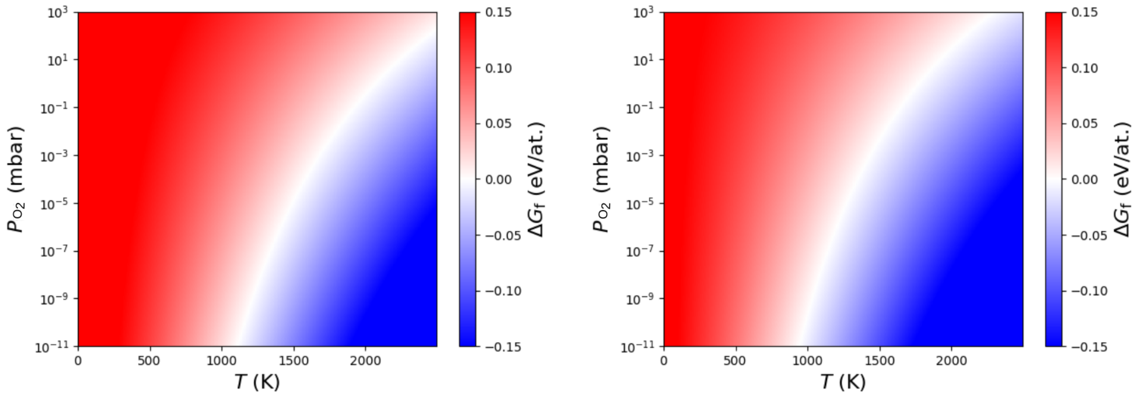
(c) $BaFeO_3$/Pt(111)

(d) $BaFeO_3$/Au(111)

Figure A.19: Gibbs free energy of the reaction 15 $Pt_{32}Ba_8B_6O_{24} \rightarrow$ 4 $Pt_{120}Ba_5B_4O_{12}$ + 74 $BaBO_3$ + 45 O_2 + 26 Ba. The thick ABO_3 film is more stable than the OQA in the red region. The OQA is more stable than the thick ABO_3 film in the blue region.

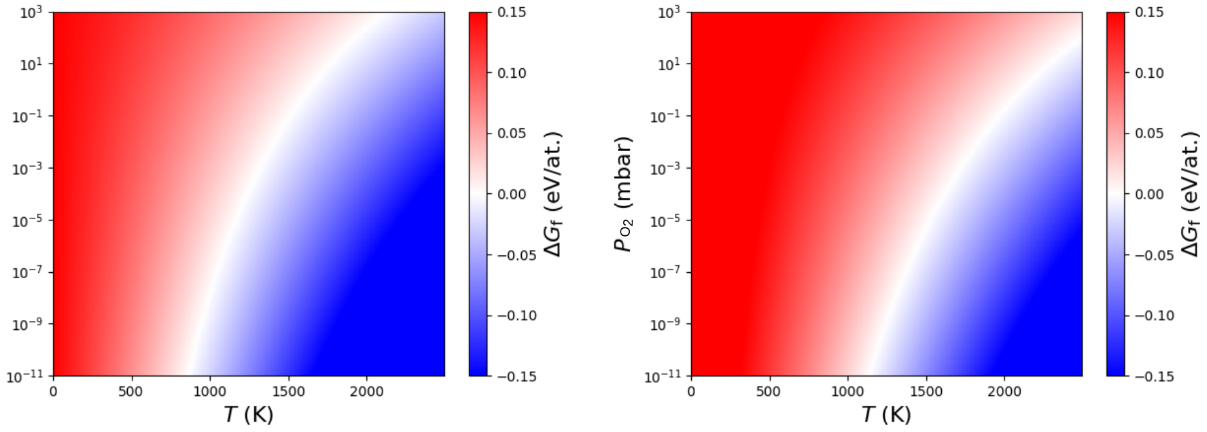

(a) $BaCoO_3$/Pt(111)

(b) $BaCoO_3$/Au(111)

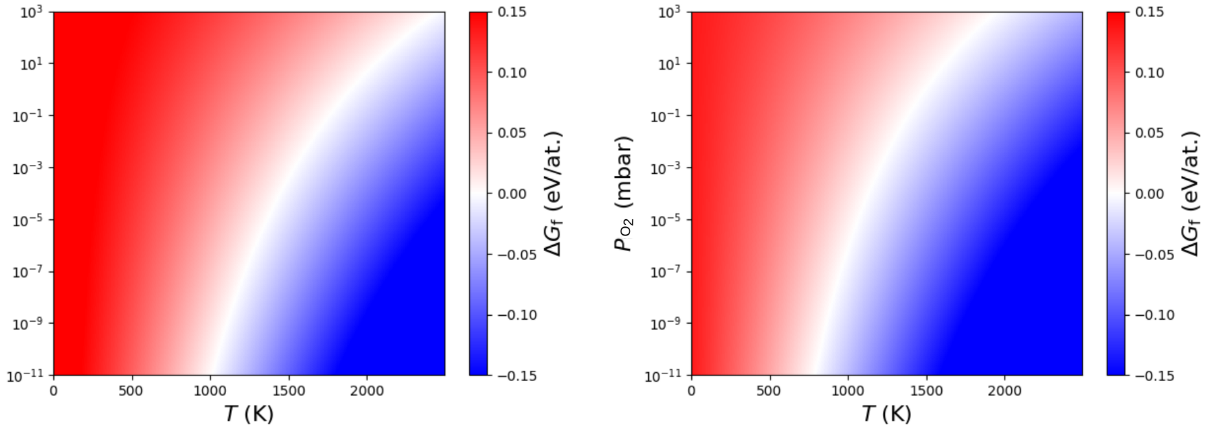

(c) $BaNiO_3$/Pt(111)

(d) $BaNiO_3$/Au(111)

Figure A.20: Gibbs free energy of the reaction 15 $Pt_{32}Ba_8B_6O_{24} \rightarrow$ 4 $Pt_{120}Ba_5B_4O_{12}$ + 74 $BaBO_3$ + 45 O_2 + 26 Ba. The thick ABO_3 film is more stable than the OQA in the red region. The OQA is more stable than the thick ABO_3 film in the blue region.

(a) $BaTiO_3$/Pt(111) (b) $BaTiO_3$/Au(111)

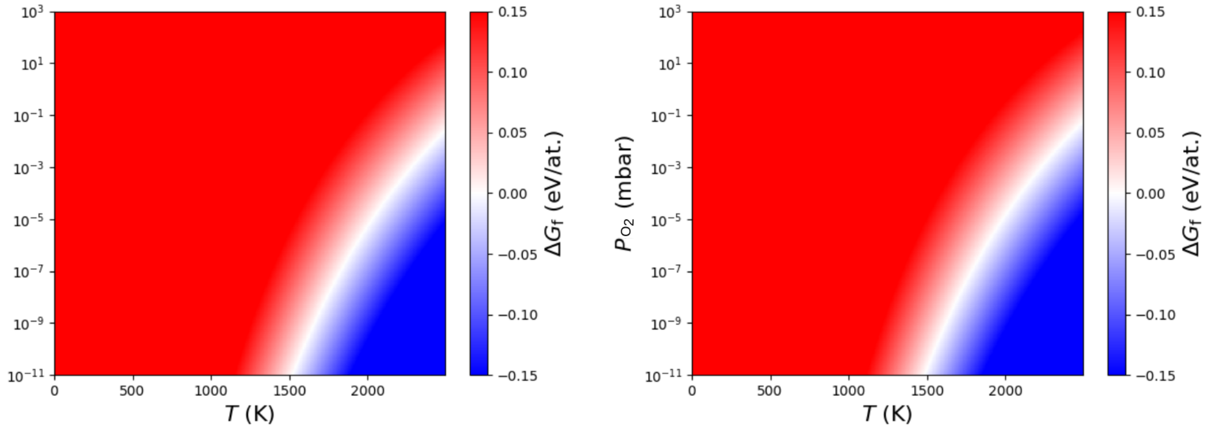

(c) $BaFeO_3$/Pt(111) (d) $BaFeO_3$/Au(111)

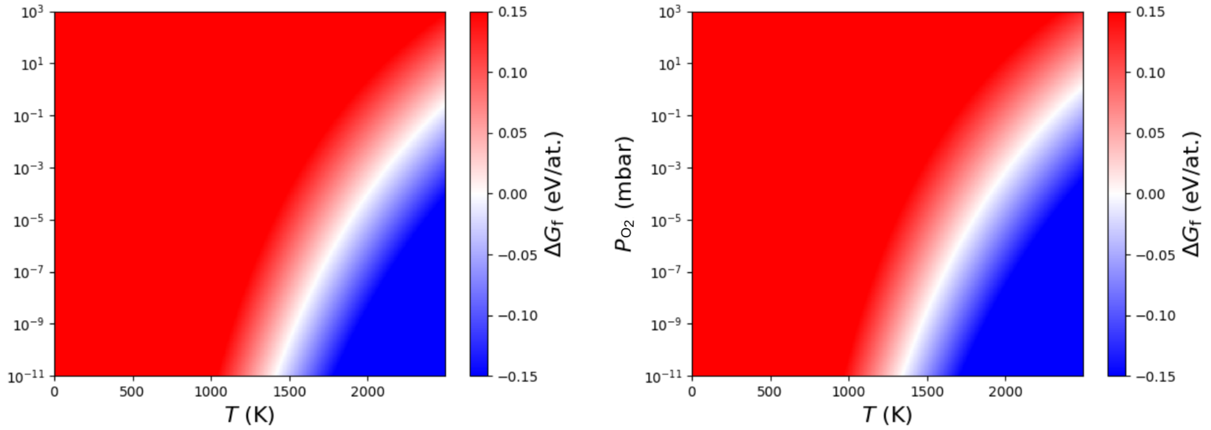

Figure A.21: Gibbs free energy of the reaction $Pt_{32}Ba_8B_6O_{24} \rightarrow Pt_{32}BaB_4O_6 + 2\ BaBO_3 + 6\ O_2 + 5/2\ Ba$. The thick ABO_3 film is more stable than the SHS in the red region. The SHS is more stable than the thick ABO_3 film in the blue region.

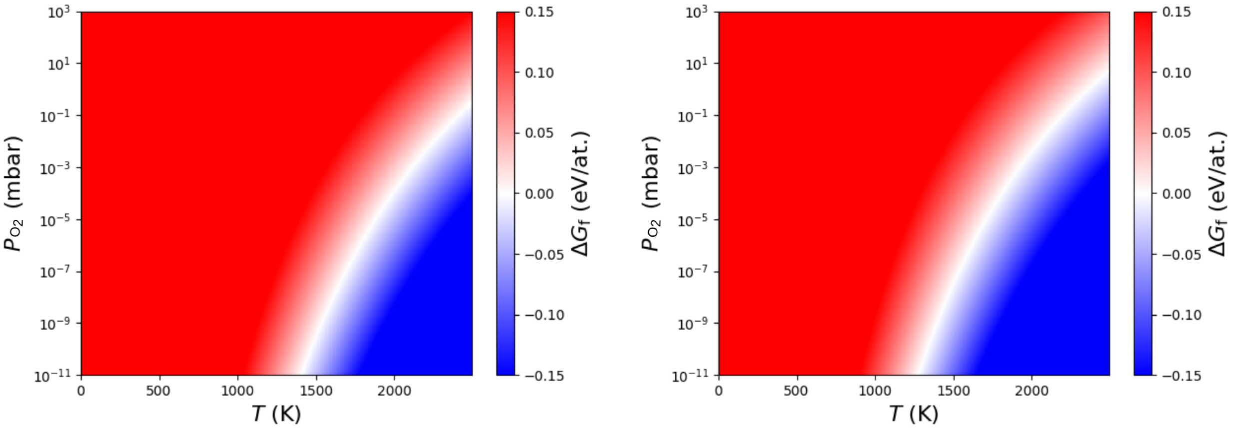

(a) $BaCoO_3$/Pt(111)

(b) $BaCoO_3$/Au(111)

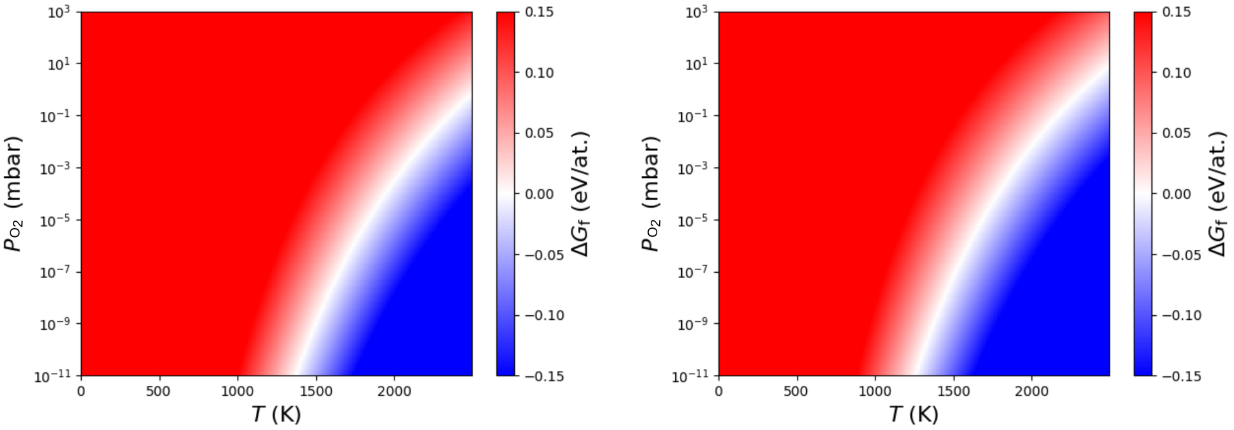

(c) $BaNiO_3$/Pt(111)

(d) $BaNiO_3$/Au(111)

Figure A.22: Gibbs free energy of the reaction $Pt_{32}Ba_8B_6O_{24} \rightarrow Pt_{32}BaB_4O_6$ + 2 $BaBO_3$ + 6 O_2 + 5/2 Ba. The thick ABO_3 film is more stable than the SHS in the red region. The SHS is more stable than the thick ABO_3 film in the blue region.

VI. Magnetic stability – Förster-σ

Formula	Energy FM (eV/at.)	Energy AFM (eV/at.)	RMC (IMC = FM)	RMS (IMC = AFM)	$\overline{m}_B$ (μ_B) (IMS = FM)	$\overline{m}_B$ (μ_B) (IMS = AFM)	SIC
$Pt_{120}Ba_5Cr_4O_{12}$	−3.15717	−3.15781	FM	AFM	1.09	−0.03	AFM
$Pt_{120}Ba_5Fe_4O_{12}$	−3.09922	−3.09826	FM	AFM	3.32	−0.12	FM
$Pt_{120}Ba_5Co_4O_{12}$	−3.02495	−3.02418	AFM	FM	0.04	−2.69	FM
$Pt_{120}Ba_5Ni_4O_{12}$	−2.98047	−2.96809	FM	AFM	0.59	−0.67	FM
$Pt_{120}Sr_5Cr_4O_{12}$	−3.13384	−3.13454	FM	FM	1.16	1.17	AFM
$Pt_{120}Sr_5Fe_4O_{12}$	−3.07669	−3.07763	AFM	AFM	−0.12	−0.14	AFM
$Pt_{120}Sr_5Co_4O_{12}$	−2.99597	−2.99534	AFM	AFM	−0.04	−0.04	FM
$Pt_{120}Sr_5Ni_4O_{12}$	−2.9303	−2.95691	AFM	AFM	0.69	0.32	AFM
$Pt_{120}Ca_5Fe_4O_{12}$	−3.08253	−3.08354	AFM	AFM	−0.26	−0.2	AFM
$Pt_{120}Ca_5Co_4O_{12}$	−3.0078	−3.00612	AFM	AFM	−0.11	−0.11	FM
$Pt_{120}Ca_5Ni_4O_{12}$	−2.95689	−2.9563	AFM	FM	0.03	1.44	FM
$Pd_{120}Ba_5Cr_4O_{12}$	−2.08172	/	AFM	/	0.59	/	FM
$Pd_{120}Ba_5Mn_4O_{12}$	−2.01345	/	AFM	/	0.92	/	FM
$Pd_{120}Ba_5Fe_4O_{12}$	−2.02899	−2.03089	FM	FM	3.58	3.58	AFM
$Pd_{120}Ba_5Co_4O_{12}$	−1.95797	−1.95604	FM	FM	2.57	−2.57	FM
$Pd_{120}Ba_5Ni_4O_{12}$	−1.89289	−1.9067	FM	AFM	1.49	−0.03	AFM
$Pd_{120}Sr_5Cr_4O_{12}$	−2.05863	−2.05942	FM	FM	1.21	1.23	AFM
$Pd_{120}Sr_5Fe_4O_{12}$	−2.01027	−2.01489	FM	FM	3.47	3.76	AFM
$Pd_{120}Sr_5Co_4O_{12}$	−1.94105	/	FM	/	2.59	/	FM
$Pd_{120}Sr_5Ni_4O_{12}$	−1.88425	−1.88285	FM	AFM	−0.48	0.4	FM
$Pd_{120}Ca_5Cr_4O_{12}$	−2.072	/	FM	/	1.14	/	FM
$Pd_{120}Ca_5Fe_4O_{12}$	−2.01331	−2.01448	FM	AFM	3.5	0.26	AFM
$Pd_{120}Ca_5Co_4O_{12}$	−1.93052	−1.93402	AFM	AFM	1.04	0.12	AFM
$Pd_{120}Ca_5Ni_4O_{12}$	−1.89952	−1.89853	AFM	FM	0.7	1.45	FM
$Au_{120}Ba_5Mn_4O_{12}$	−0.72306	/	AFM	/	1.77	/	FM
$Au_{120}Ba_5Fe_4O_{12}$	−0.72789	−0.73004	AFM	FM	−0.0	3.4	AFM
$Au_{120}Ba_5Co_4O_{12}$	−0.6368	−0.6345	FM	FM	−2.77	2.76	FM
$Au_{120}Ba_5Ni_4O_{12}$	−0.56556	−0.57633	FM	AFM	1.17	−0.05	AFM
$Au_{120}Sr_5Fe_4O_{12}$	−0.69417	−0.69365	AFM	AFM	1.5	−0.03	FM
$Au_{120}Sr_5Co_4O_{12}$	−0.61276	−0.61436	FM	AFM	−2.41	−0.11	AFM
$Au_{120}Sr_5Ni_4O_{12}$	−0.56751	−0.56264	FM	AFM	0.44	−0.01	FM
$Au_{120}Ca_5Cr_4O_{12}$	−0.75502	/	AFM	/	0.65	/	FM
$Au_{120}Ca_5Fe_4O_{12}$	−0.70948	−0.70957	FM	AFM	3.65	0.17	AFM
$Au_{120}Ca_5Co_4O_{12}$	−0.61741	−0.61429	AFM	FM	−1.33	2.66	FM
$Au_{120}Ca_5Ni_4O_{12}$	−0.56905	/	FM	/	1.24	/	FM

Table A.3: Magnetic stability considering, as the initial magnetic moment, a ferromagnetic (FM) and an antiferromagnetic (AFM) state of the B (B = Cr, Mn, Fe, Co, Ni) elements in the approximant structure. Since there are four B atoms in the approximant with two equivalent positions, we consider the initial AFM state with the m_B of the non-equivalent positions in opposite directions. RMS = Resulting magnetic moment; IMC = Initial magnetic configuration; SIC = Stable as initial configuration.

VII. Different compositions for the Cockayne-σ model

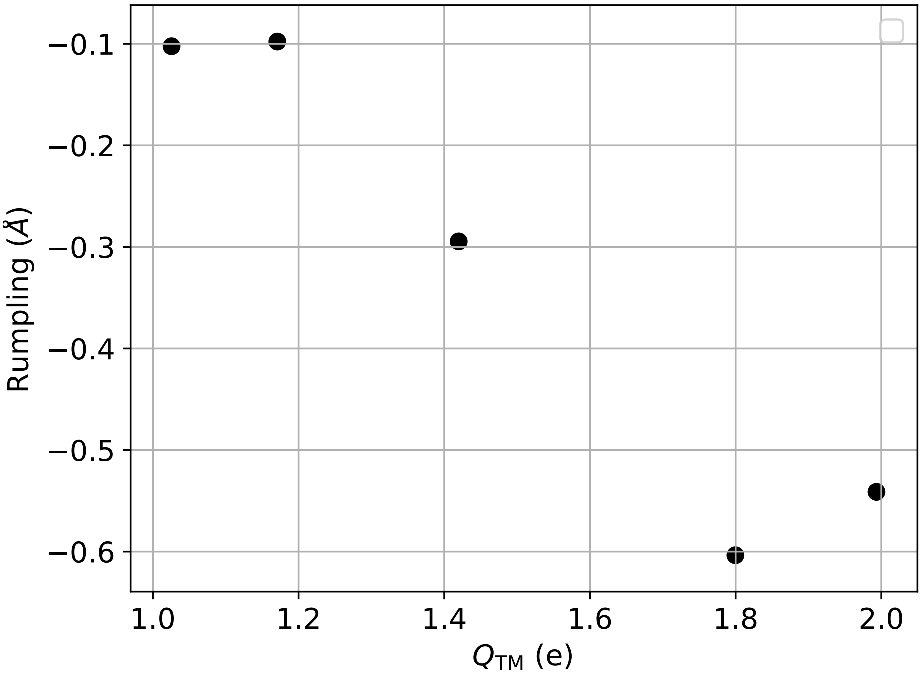

Figure A.23: Rumpling (R) vs. Bader charges for the transition metal (Q_B, with B = Ti, V, Fe, Co, Ni) in the Cockayne-σ approximant.

Bibliography

[1] H. Zhang, “Ultrathin Two-Dimensional Nanomaterials,” *ACS Nano*, vol. 9, pp. 9451–9469, 2015.

[2] A. K. Geim and K. S. Novoselov, “The rise of graphene,” *Nanosci. Technol.*, vol. 6, p. 9, 2009.

[3] G. Barcaro and A. Fortunelli, “2D oxides on metal materials: Concepts, status, and perspectives,” *Phys. Chem. Chem. Phys.*, vol. 21, pp. 11 510–11 536, 2019.

[4] C. Tan *et al.*, “Recent Advances in Ultrathin Two-Dimensional Nanomaterials,” *Chem. Rev.*, p. 107, 2017.

[5] F. Sedona *et al.*, “Ultrathin TiO_x Films on Pt(111): A LEED, XPS, and STM Investigation,” *J. Phys. Chem. B*, vol. 109, pp. 24 411–24 426, 2005.

[6] F. Li *et al.*, “Two-dimensional manganese oxide nanolayers on Pd(100): The surface phase diagram,” *J. Phys.: Condens. Matter*, vol. 21, p. 134 008, 2009.

[7] S. Surnev *et al.*, “Novel Interface-Mediated Metastable Oxide Phases: Vanadium Oxides on Pd(111),” *Phys. Rev. Lett.*, vol. 87, p. 4, 2001.

[8] G. Kresse *et al.*, “First-principles calculations for V_xO_y grown on Pd(111),” *Surface Science*, vol. 492, pp. 329–344, 2001.

[9] S. Förster *et al.*, “Quasicrystalline structure formation in a classical crystalline thin-film system,” *Nature*, vol. 502, pp. 215–218, 2013.

[10] S. Förster *et al.*, “Observation and Structure Determination of an Oxide Quasicrystal Approximant,” *Phys. Rev. Lett.*, vol. 117, p. 095 501, 2016.

[11] S. Förster *et al.*, “Growth and decay of a two-dimensional oxide quasicrystal: High-temperature in situ microscopy,” *Ann. Phys.*, vol. 529, p. 1 600 250, 2017.

[12] S. Schenk *et al.*, “Observation of a dodecagonal oxide quasicrystal and its complex approximant in the $SrTiO_3$-Pt(1 1 1) system,” *J. Phys.: Condens. Matter*, vol. 29, p. 134 002, 2017.

[13] N. Köwitsch *et al.*, “Proving a Paradigm in Methanol Steam Reforming: Catalytically Highly Selective In_x Pd_y/In_2 O_3 Interfaces,” *ACS Catal.*, vol. 11, pp. 304–312, 2021.

[14] G. A. Olah, “Beyond Oil and Gas: The Methanol Economy,” *Angew. Chem. Int. Ed.*, vol. 44, pp. 2636–2639, 2005.

[15] D. Laudenschleger *et al.*, “Identifying the nature of the active sites in methanol synthesis over Cu/ZnO/Al_2O_3 catalysts,” *Nat Commun*, vol. 11, p. 3898, 2020.

[16] K. Kovnir *et al.*, “A new approach to well-defined, stable and site-isolated catalysts,” *Science and Technology of Advanced Materials*, vol. 8, pp. 420–427, 2007.

[17] W. M. H. Sachtler, “Chemisorption Complexes on Alloy Surfaces,” *Catalysis Reviews*, vol. 14, pp. 193–210, 1976.

[18] O. Martin *et al.*, “Indium Oxide as a Superior Catalyst for Methanol Synthesis by CO_2 Hydrogenation,” *Angew. Chem. Int. Ed.*, vol. 55, pp. 6261–6265, 2016.

[19] M. S. Frei *et al.*, “Atomic-scale engineering of indium oxide promotion by palladium for methanol production via CO_2 hydrogenation,” *Nat Commun*, vol. 10, p. 3377, 2019.

[20] J. L. Snider *et al.*, “Revealing the Synergy between Oxide and Alloy Phases on the Performance of Bimetallic In–Pd Catalysts for CO_2 Hydrogenation to Methanol,” *ACS Catal.*, vol. 9, pp. 3399–3412, 2019.

[21] H. Lorenz *et al.*, “Pd–In_2O_3 interaction due to reduction in hydrogen: Consequences for methanol steam reforming,” *Applied Catalysis A: General*, vol. 374, pp. 180–188, 2010.

[22] J. Ye *et al.*, “Methanol synthesis from CO_2 hydrogenation over a Pd_4/In_2O_3 model catalyst: A combined DFT and kinetic study,” *Journal of Catalysis*, vol. 317, pp. 44–53, 2014.

[23] E. Cockayne *et al.*, “Structure of periodic crystals and quasicrystals in ultrathin films of Ba-Ti-O,” *Phys. Rev. B*, vol. 93, p. 020 101, 2016.

[24] R. Dronskowski and P. E. Bloechl, “Crystal orbital Hamilton populations (COHP): Energy-resolved visualization of chemical bonding in solids based on density-functional calculations,” *J. Phys. Chem.*, vol. 97, pp. 8617–8624, 1993.

[25] R. Nelson *et al.*, “LOBSTER: Local orbital projections, atomic charges, and chemical-bonding analysis from projector-augmented-wave-based density-functional theory,” *J Comput Chem*, vol. 41, pp. 1931–1940, 2020.

[26] T. T. Dorini *et al.*, “Two-dimensional oxide quasicrystal approximants with tunable electronic and magnetic properties,” *Nanoscale*, vol. 13, pp. 10 771–10 779, 2021.

[27] J. Goniakowski and C. Noguera, “Intrinsic Properties of Pure and Mixed Monolayer Oxides in the Honeycomb Structure: M_2O_3 and $MM'O_3$ (M, M′ = Ti, V, Cr, Fe),” *J. Phys. Chem. C*, p. 13, 2019.

[28] K. S. Novoselov *et al.*, “Electric Field Effect in Atomically Thin Carbon Films,” *Science*, vol. 306, pp. 666–669, 2004.

[29] Y. Lin *et al.*, “Soluble, Exfoliated Hexagonal Boron Nitride Nanosheets,” *J. Phys. Chem. Lett.*, vol. 1, pp. 277–283, 2010.

[30] M. Chhowalla *et al.*, "The chemistry of two-dimensional layered transition metal dichalcogenide nanosheets," *Nature Chem*, vol. 5, pp. 263–275, 2013.

[31] X. Huang *et al.*, "Metal dichalcogenide nanosheets: Preparation, properties and applications," *Chem. Soc. Rev.*, vol. 42, p. 1934, 2013.

[32] M. Xu *et al.*, "Graphene-Like Two-Dimensional Materials," *Chem. Rev.*, vol. 113, pp. 3766–3798, 2013.

[33] M. Chhowalla *et al.*, "Two-dimensional transition metal dichalcogenide (TMD) nanosheets," *Chem. Soc. Rev.*, vol. 44, pp. 2584–2586, 2015.

[34] A. Bhalla *et al.*, "The perovskite structure – a review of its role in ceramic science and technology," *Materials Research Innovations*, vol. 4, pp. 3–26, 2000.

[35] M. Osada and T. Sasaki, "Exfoliated oxide nanosheets: New solution to nanoelectronics," *J. Mater. Chem.*, vol. 19, p. 2503, 2009.

[36] J. C. Slonczewski and P. R. Weiss, "Band Structure of Graphite," *Phys. Rev.*, vol. 109, pp. 272–279, 1958.

[37] J. W. McClure, "Diamagnetism of Graphite," *Phys. Rev.*, vol. 104, pp. 666–671, 1956.

[38] G. W. Semenoff, "Condensed-Matter Simulation of a Three-Dimensional Anomaly," *Phys. Rev. Lett.*, vol. 53, pp. 2449–2452, 1984.

[39] F. D. M. Haldane, "Model for a Quantum Hall Effect without Landau Levels: Condensed-Matter Realization of the 'Parity Anomaly'," *Phys. Rev. Lett.*, vol. 61, pp. 2015–2018, 1988.

[40] J. Wang *et al.*, "CO_2 Hydrogenation to Methanol over In_2O_3-Based Catalysts: From Mechanism to Catalyst Development," *ACS Catal.*, vol. 11, pp. 1406–1423, 2021.

[41] X. Wang *et al.*, "Heteroatom-doped graphene materials: Syntheses, properties and applications," *Chem. Soc. Rev.*, vol. 43, pp. 7067–7098, 2014.

[42] C. Freysoldt *et al.*, "Ultrathin Oxides: Bulk-Oxide-Like Model Surfaces or Unique Films?" *Phys. Rev. Lett.*, vol. 99, p. 086 101, 2007.

[43] F. P. Netzer and A. Fortunelli, Eds., *Oxide Materials at the Two-Dimensional Limit*, ser. Springer Series in Materials Science. Cham: Springer International Publishing, 2016, vol. 234.

[44] G. Barcaro *et al.*, "Building Principles and Structural Motifs in TiO_x Ultrathin Films on a (111) Substrate," *J. Phys. Chem. C*, vol. 116, pp. 13 302–13 306, 2012.

[45] J. Nowotny and M. Rekas, "Defect chemistry of BaTiO3," *Solid State Ion.*, vol. 49, p. 20, 1991.

[46] M. Mori *et al.*, "Effect of the Atomic Ratio of Ba to Ti on Optical Properties of Gold-Dispersed $BaTiO_3$ Thin Films," *J. Am. Ceram. Soc.*, vol. 78, pp. 2391–2394, 1995.

[47] D. Hennings *et al.*, "Advanced dielectrics: Bulk ceramics and thin films," *Adv. Mater.*, vol. 3, pp. 334–340, 1991.

[48] H. Hayashi *et al.*, "In-situ Raman spectroscopy of $BaTiO_3$ particles for tetragonal–cubic transformation," *Journal of Physics and Chemistry of Solids*, vol. 74, pp. 957–962, 2013.

[49] S. Lee *et al.*, "Modified Phase Diagram for the Barium Oxide–Titanium Dioxide System for the Ferroelectric Barium Titanate," *J. Am. Ceram. Soc.*, vol. 90, pp. 2589–2594, 2007.

[50] A. Jain *et al.*, "Commentary: The Materials Project: A materials genome approach to accelerating materials innovation," p. 12, 2013.

[51] D. A. Tenne *et al.*, "Probing Nanoscale Ferroelectricity by Ultraviolet Raman Spectroscopy," *Science*, vol. 313, pp. 1614–1616, 2006.

[52] D. D. Fong *et al.*, "Ferroelectricity in Ultrathin Perovskite Films," *Science*, vol. 304, pp. 1650–1653, 2004.

[53] R. E. Cohen, "Origin of ferroelectricity in perovskite oxides," *Nature*, vol. 358, pp. 136–138, 1992.

[54] S. Förster and W. Widdra, "Growth, structure, and thermal stability of epitaxial $BaTiO_3$ films on Pt(111)," *Surface Science*, vol. 604, pp. 2163–2169, 2010.

[55] W. Li *et al.*, "Predicting the thermodynamic stability of perovskite oxides using machine learning models," *Computational Materials Science*, vol. 150, pp. 454–463, 2018.

[56] C. J. Heard *et al.*, "2D Oxide Nanomaterials to Address the Energy Transition and Catalysis," *Adv. Mater.*, vol. 31, p. 1 801 712, 2019.

[57] D. Ji *et al.*, "Freestanding crystalline oxide perovskites down to the monolayer limit," *Nature*, vol. 570, pp. 87–90, 2019.

[58] S. Li *et al.*, "2D Perovskite $Sr_2Nb_3O_{10}$ for High-Performance UV Photodetectors," *Adv. Mater.*, vol. 32, p. 1 905 443, 2020.

[59] T. Tybell *et al.*, "Domain Wall Creep in Epitaxial Ferroelectric $Pb(Zr_{0.2}Ti_{0.8})O_3$ Thin Films," *Phys. Rev. Lett.*, vol. 89, p. 097 601, 2002.

[60] D. Shechtman *et al.*, "Metallic Phase with Long-Range Orientational Order and No Translational Symmetry," *Phys. Rev. Lett.*, vol. 53, pp. 1951–1953, 1984.

[61] D. Gratias and M. Quiquandon, "Discovery of quasicrystals: The early days," *Comptes Rendus Physique*, vol. 20, pp. 803–816, 2019.

[62] W. Steurer, "Quasicrystals: What do we know? What do we want to know? What can we know?" *Acta Crystallogr A Found Adv*, vol. 74, pp. 1–11, 2018.

[63] D. Castelvecchi, "First nuclear test created 'impossible' quasicrystals," *Nature*, vol. 593, p. 487, 2021.

[64] S. Förster *et al.*, "Quasicrystals and their Approximants in 2D Ternary Oxides," *Phys. Status Solidi B*, vol. 257, p. 1 900 624, 2020.

[65] P. Guyot *et al.*, *Physics and Chemistry of Finite Systems: From Clusters to Crystals*. Kluwer Academic Publishers, 1992, vol. 1.

[66] A. I. Goldman and R. F. Kelton, "Quasicrystals and crystalline approximants," *Rev. Mod. Phys.*, vol. 65, pp. 213–230, 1993.

[67] M. Gardner, "Mathematical games," *Sci. Am.*, vol. 236, pp. 128–138, 1977.

[68] R. Penrose, "Pentaplexity A Class of Non-Periodic Tilings of the Plane," *The Mathematical Intelligencer*, vol. 2, pp. 32–37, 1979.

[69] L. A. Bursill and P. Ju Lin, "Penrose tiling observed in a quasi-crystal," *Nature*, vol. 316, pp. 50–51, 1985.

[70] F. Gahler, "Crystallography of dodecagonal quasicrystals," *World Sci.*, pp. 272–284, 1988.

[71] N. Niizeki and H. Mitani, "Two-dimensional dodecagonal quasilattices," *J. Phys. A: Math. Gen.*, vol. 20, pp. L405–L410, 1987.

[72] B. Grunbaum and G. C. Shephard, "Tilings by Regular Polygons," *Math. Mag.*, vol. 50, pp. 227–247, 1977.

[73] J. Kepler, "Harmonices mundi," *Cesammelte Werke*, vol. 6, p. 270, 1619.

[74] A. W. Huran *et al.*, "Two-dimensional binary metal-oxide quasicrystal approximants," *2D Mater.*, vol. 8, p. 045 002, 2021.

[75] J. Goniakowski and C. Noguera, "Properties of Metal-Supported Oxide Honeycomb Monolayers: M_2O_3 and $MM'O_3$ on Me(111) (M, M′ = Ti, V, Cr, Fe; Me = Ag, Au, Pt)," *J. Phys. Chem. C*, vol. 124, pp. 8186–8197, 2020.

[76] J. Goniakowski and C. Noguera, "Properties of M_2O_3/Au(111) Honeycomb Monolayers (M=Sc, Ti, V, Cr, Mn, Fe, Co, Ni)," *J. Phys. Chem. C*, vol. 123, pp. 9272–9281, 2019.

[77] C. Wu *et al.*, "Stoichiometry engineering of ternary oxide ultrathin films: $Ba_xTi_2O_3$ on Au(111)," *Phys. Rev. B*, vol. 91, p. 155 424, 2015.

[78] X. Li *et al.*, "Growth of Ba–O ultrathin films on Pt(111) followed by Ti incorporation to prepare oxide crystalline approximants and quasicrystals," *Applied Surface Science*, vol. 561, p. 150 099, 2021.

[79] C. Ruano Merchan *et al.*, "Two-dimensional square and hexagonal oxide quasicrystal approximants in $SrTiO_3$ films grown on Pt(111)/Al_2O_3(0001)," *Phys. Chem. Chem. Phys.*, vol. 24, pp. 7253–7263, 2022.

[80] C. Ruano Merchan *et al.*, "Synthesis and characterization of 2D complex oxide films in the $SrTiO_3$/Pt(111)/Al_2O_3(0001) system," PhD thesis, Université de Lorraine, 2022.

[81] E. Maria Zollner *et al.*, "Two-Dimensional Wetting Layer Structures of Reduced Ternary Oxides on Ru(0001) and Pt(111)," *Phys. Status Solidi B*, vol. 257, p. 1 900 655, 2020.

[82] M. Maniraj *et al.*, “Hexagonal approximant of the dodecagonal oxide quasicrystal on Pt(111),” *Phys. Rev. Materials*, vol. 5, p. 084 006, 2021.

[83] F. E. Wührl *et al.*, “Antiphase Domain Boundary Formation in 2D Ba–Ti–O on Pd(111): An Alternative to Phase Separation,” *Physica Status Solidi (b)*, p. 2 100 389, 2021.

[84] P. Wu and B. Yang, “Intermetallic PdIn catalyst for CO_2 hydrogenation to methanol: Mechanistic studies with a combined DFT and microkinetic modeling method,” *Catal. Sci. Technol.*, vol. 9, pp. 6102–6113, 2019.

[85] A. García-Trenco *et al.*, “PdIn intermetallic nanoparticles for the Hydrogenation of CO_2 to Methanol,” *Applied Catalysis B: Environmental*, vol. 220, pp. 9–18, 2018.

[86] Q. Feng *et al.*, “Isolated Single-Atom Pd Sites in Intermetallic Nanostructures: High Catalytic Selectivity for Semihydrogenation of Alkynes,” *J. Am. Chem. Soc.*, vol. 139, pp. 7294–7301, 2017.

[87] P. Giannozzi *et al.*, “Quantum ESPRESSO: A modular and open-source software project for quantum simulations of materials,” *J. Phys.: Condens. Matter*, vol. 21, p. 395 502, 2009.

[88] X. Gonze *et al.*, “The Abinit project: Impact, environment and recent developments,” *Computer Physics Communications*, vol. 248, p. 107 042, 2020.

[89] G. Kresse and J. Hafner, “*AB INITIO* molecular dynamics for liquid metals,” *Phys. Rev. B*, vol. 47, pp. 558–561, 1993.

[90] G. Kresse and J. Furthmüller, “Efficiency of ab-initio total energy calculations for metals and semiconductors using a plane-wave basis set,” *Computational Materials Science*, vol. 6, pp. 15–50, 1996.

[91] G. Kresse and J. Furthmuller, “Efficient iterative schemes for *ab initio* total-energy calculations using a plane-wave basis set,” *Phys. Rev. B*, vol. 54, pp. 11 169–11 186, 1996.

[92] G. Feliciano, *Materials Modelling Using Density Functional Theory: Properties and Predictions*. Oxford University Press, 2014.

[93] W. Andreoni and S. Yip, Eds., *Handbook of Materials Modeling: Methods: Theory and Modeling*. Cham: Springer International Publishing, 2020.

[94] J. C. Slater, “The self consistent field and the structure of atoms,” *Phys. Rev.*, vol. 32, p. 339, 1928.

[95] P. Hohenberg and W. Kohn, “Inhomogeneous Electron Gas,” *Phys. Rev.*, vol. 136, B864–B871, 1964.

[96] D. M. Ceperley and B. J. Alder, “Ground State of the Electron Gas by a Stochastic Method,” *Phys. Rev. Lett.*, vol. 45, pp. 566–569, 1980.

[97] J. P. Perdew and A. Zunger, “Self-interaction correction to density-functional approximations for many-electron systems,” *Phys. Rev. B*, vol. 23, pp. 5048–5079, 1981.

[98] D. C. Langreth and J. P. Perdew, "Theory of nonuniform electronic systems. I. Analysis of the gradient approximation and a generalization that works," *Phys. Rev. B*, vol. 21, pp. 5469–5493, 1980.

[99] J. P. Perdew *et al.*, "Atoms, molecules, solids, and surfaces: Applications of the generalized gradient approximation for exchange and correlation," *Phys. Rev. B*, vol. 46, p. 6671, 1992.

[100] A. D. Becke, "Density functional calculations of molecular bond energies," vol. 84, p. 7, 1986.

[101] M. Dion *et al.*, "Van der Waals Density Functional for General Geometries," *Phys. Rev. Lett.*, vol. 92, p. 246 401, 2004.

[102] O. A. von Lilienfeld *et al.*, "Optimization of Effective Atom Centered Potentials for London Dispersion Forces in Density Functional Theory," *Phys. Rev. Lett.*, vol. 93, p. 153 004, 2004.

[103] J. Antony and S. Grimme, "Density functional theory including dispersion corrections for intermolecular interactions in a large benchmark set of biologically relevant molecules," *Phys. Chem. Chem. Phys.*, vol. 8, p. 5287, 2006.

[104] A. D. Becke and E. R. Johnson, "Exchange-hole dipole moment and the dispersion interaction revisited," *The Journal of Chemical Physics*, vol. 127, p. 154 108, 2007.

[105] S. Grimme *et al.*, "Density functional theory with dispersion corrections for supramolecular structures, aggregates, and complexes of (bio)organic molecules," *Org. Biomol. Chem.*, vol. 5, pp. 741–758, 2007.

[106] T. Sato *et al.*, "Long-range corrected density functional study on weakly bound systems: Balanced descriptions of various types of molecular interactions," *The Journal of Chemical Physics*, vol. 126, p. 234 114, 2007.

[107] A. Tkatchenko and M. Scheffler, "Accurate Molecular Van Der Waals Interactions from Ground-State Electron Density and Free-Atom Reference Data," *Phys. Rev. Lett.*, p. 4, 2009.

[108] J. P. Perdew *et al.*, "Generalized Gradient Approximation Made Simple," *Phys. Rev. Lett.*, vol. 77, pp. 3865–3868, 1996.

[109] Y. Zhang and W. Yang, "Comment on "Generalized Gradient Approximation Made Simple"," *Phys. Rev. Lett.*, vol. 80, pp. 890–890, 1998.

[110] J. Klimeš *et al.*, "Chemical accuracy for the van der Waals density functional," *J. Phys.: Condens. Matter*, vol. 22, p. 022 201, 2010.

[111] J. S. Zaanen *et al.*, "Band gaps and electronic structure of transition-metal compounds," *Phys. Rev. Lett.*, vol. 55, p. 418, 1985.

[112] S. Hüfner, "Electronic structure of NiO and related 3d-transition-metal compounds," *Advances in Physics*, vol. 43, pp. 183–356, 1994.

[113] N. F. Mott, "Metal-insulator transitions," *Contemporary Physics*, vol. 14, pp. 401–413, 1973.

[114] S. L. Dudarev *et al.*, "Electron-energy-loss spectra and the structural stability of nickel oxide: An LSDA+U study," *Phys. Rev. B*, vol. 57, pp. 1505–1509, 1998.

[115] F. Bloch and J. J. Thomson, "About the Quantum Mechanics of the Electrons in Crystal Lattices," *Proc. R. Soc. Lond. A*, vol. 13à, pp. 449–513, 1931.

[116] P. E. Blöchl, "Projector augmented-wave method," *Phys. Rev. B*, vol. 50, p. 17 953, 1994.

[117] G. Kresse and D. Joubert, "From ultrasoft pseudopotentials to the projector augmented-wave method," *Phys. Rev. B*, vol. 59, pp. 1758–1775, 1999.

[118] K. Reuter *et al.*, "Ab initio atomistic thermodynamics and statistical mechanics of surface properties and functions," in *Handbook of Materials Modeling*, Springer, 2005, pp. 149–194.

[119] E. Kaxiras *et al.*, "*AB INITIO* theory of polar semiconductor surfaces. I. Methodology and the (22) reconstructions of GaAs(111)," *Phys. Rev. B*, vol. 35, pp. 9625–9635, 1987.

[120] M. Scheffler, "Thermodynamic Aspects of Bulk and Surface Defects–First-Principle Calculations -," in *Studies in Surface Science and Catalysis*, vol. 40, Elsevier, 1988, pp. 115–122.

[121] K. Reuter and M. Scheffler, "First-Principles Atomistic Thermodynamics for Oxidation Catalysis: Surface Phase Diagrams and Catalytically Interesting Regions," *Phys. Rev. Lett.*, vol. 90, p. 046 103, 2003.

[122] D. A. McQuarrie, *Statistical Mechanics*. Row Publishers, 1976.

[123] J. Rogal and K. Reuter, "Ab initio atomistic thermodynamics for surfaces: A primer," Max Plank Gesellschaft zur foerderung der wissenschaften ev berlin, Tech. Rep., 2006.

[124] M. W. Chase *et al.*, "JANAF Thermochemical Tables, 1982 Supplement," p. 247,

[125] Q. Sun *et al.*, "Effect of a humid environment on the surface structure of RuO_2(110)," *Phys. Rev. B*, vol. 67, p. 205 424, 2003.

[126] K. Reuter and M. Scheffler, "Composition and structure of the RuO_2(110) surface in an O_2 and CO environment: Implications for the catalytic formation of CO_2," *Phys. Rev. B*, vol. 68, p. 045 407, 2003.

[127] J. R. Kitchin *et al.*, "Alloy surface segregation in reactive environments: First-principles atomistic thermodynamics study of Ag_3Pd(111) in oxygen atmospheres," *Phys. Rev. B*, vol. 77, p. 075 437, 2008.

[128] S. Muller, "Bulk and surface ordering phenomena in binary metal alloys," *J. Phys. Condens. Matter*, vol. 15, R1429, 2003.

[129] M. Asta *et al.*, "A first-principles approach to modeling alloy phase equilibria," *JOM*, vol. 53, pp. 16–19, 2001.

[130] A. Walle and G. Ceder, "Automating first-principles phase diagram calculations," *JPE*, vol. 23, pp. 348–359, 2002.

[131] M. Meier *et al.*, "Semihydrogenation of Acetylene on Al_5Co_2 Surfaces," *J. Phys. Chem. C*, vol. 121, pp. 4958–4969, 2017.

[132] G. M. McGuirk *et al.*, "The atomic structure of low-index surfaces of the intermetallic compound InPd," *The Journal of Chemical Physics*, vol. 143, p. 074 705, 2015.

[133] J. Gao *et al.*, "Structural and Chemical Transformations of Zinc Oxide Ultrathin Films on Pd(111) Surfaces," *ACS Appl. Mater. Interfaces*, p. 11, 2021.

[134] A. Kokalj, "XCrySDen—a new program for displaying crystalline structures and electron densities," *J Mol Graph. Modell*, vol. 17, pp. 176–179, 1999.

[135] D. Koch and S. Manzhos, "On the Charge State of Titanium in Titanium Dioxide," *J. Phys. Chem. Lett.*, vol. 8, pp. 1593–1598, 2017.

[136] R. Bader and T. Nguyen-Dang, "Quantum Theory of Atoms in Molecules–Dalton Revisited," in *Advances in Quantum Chemistry*, vol. 14, Elsevier, 1981, pp. 63–124.

[137] W. Tang *et al.*, "A grid-based Bader analysis algorithm without lattice bias," *J. Phys.: Condens. Matter*, vol. 21, p. 084 204, 2009.

[138] E. Sanville *et al.*, "Improved grid-based algorithm for Bader charge allocation," *J. Comput. Chem.*, vol. 28, pp. 899–908, 2007.

[139] G. Henkelman *et al.*, "A fast and robust algorithm for Bader decomposition of charge density," *Comput. Mater. Sci.*, vol. 36, pp. 354–360, 2006.

[140] M. Yu and D. R. Trinkle, "Accurate and efficient algorithm for Bader charge integration," *J. Chem. Phys.*, vol. 134, p. 064 111, 2011.

[141] J. Tersoff and D. R. Hamann, "Theory and Application for the Scanning Tunneling Microscope," *Phys. Rev. Lett.*, vol. 50, pp. 1998–2001, 1983.

[142] J. Tersoff and D. R. Hamann, "Theory of the scanning tunneling microscope," *Phys. Rev. B*, vol. 31, pp. 805–813, 1985.

[143] R. S. Mulliken, "Electronic Population Analysis on LCAO–MO Molecular Wave Functions. II. Overlap Populations, Bond Orders, and Covalent Bond Energies," *The Journal of Chemical Physics*, vol. 23, pp. 1841–1846, 1955.

[144] E. R. Davidson, "Electronic Population Analysis of Molecular Wavefunctions," *The Journal of Chemical Physics*, vol. 46, pp. 3320–3324, 1967.

[145] K. R. Roby, "Quantum theory of chemical valence concepts: I. Definition of the charge on an atom in a molecule and of occupation numbers for electron density shared between atoms," *Molecular Physics*, vol. 27, pp. 81–104, 1974.

[146] R. Hoffmann, "How Chemistry and Physics Meet in Solid State," *Angew. Chem. Int.*, vol. 26, pp. 846–878, 1987.

[147] R. Hoffmann and W. N. Lipscomb, "Theory of Polyhedral Molecules. I. Physical Factorizations of the Secular Equation," *The Journal of Chemical Physics*, vol. 36, pp. 2179–2189, 1962.

[148] R. Hoffmann, "An Extended Hückel Theory. I. Hydrocarbons," *The Journal of Chemical Physics*, vol. 39, pp. 1397–1412, 1963.

[149] V. L. Deringer *et al.*, "Crystal Orbital Hamilton Population (COHP) Analysis As Projected from Plane-Wave Basis Sets," *J. Phys. Chem. A*, vol. 115, pp. 5461–5466, 2011.

[150] S. Maintz *et al.*, "Analytic projection from plane-wave and PAW wavefunctions and application to chemical-bonding analysis in solids," *J. Comput. Chem.*, vol. 34, pp. 2557–2567, 2013.

[151] D. J. Chadi, "Localized-orbital description of wave functions and energy bands in semiconductors," *Phys. Rev. B*, vol. 16, pp. 3572–3578, 1977.

[152] D. Sánchez-Portal *et al.*, "Analysis of atomic orbital basis sets from the projection of plane-wave results," *J. Phys.: Condens. Matter*, vol. 8, pp. 3859–3880, 1996.

[153] M. D. Segall *et al.*, "Population analysis in plane wave electronic structure calculations," *Molecular Physics*, vol. 89, pp. 571–577, 1996.

[154] M. D. Segall *et al.*, "Population analysis of plane-wave electronic structure calculations of bulk materials," *Phys. Rev. B*, vol. 54, pp. 16 317–16 320, 1996.

[155] N. Börnsen *et al.*, " E_{COV} - a new tool for the analysis of electronic structure data in a chemical language," *J. Phys.: Condens. Matter*, vol. 11, pp. L287–L293, 1999.

[156] B. D. Dunnington and J. R. Schmidt, "Generalization of Natural Bond Orbital Analysis to Periodic Systems: Applications to Solids and Surfaces via Plane-Wave Density Functional Theory," *J. Chem. Theory Comput.*, vol. 8, pp. 1902–1911, 2012.

[157] D. Sanchez-Portal *et al.*, "Projection of plane-wave calculations into atomic orbitals," *Solid State Communications*, vol. 95, pp. 685–690, 1995.

[158] D. P. Kroese and R. Y. Rubinstein, "Monte Carlo methods," *WIREs Comput. Stat.*, vol. 4, pp. 48–58, 2012.

[159] M. P. Allen and D. J. Tildesley, *Computer Simulation of Liquids*, Second edition. Oxford, United Kingdom: Oxford University Press, 2017.

[160] W. C. Swope *et al.*, "A computer simulation method for the calculation of equilibrium constants for the formation of physical clusters of molecules: Application to small water clusters," *The Journal of Chemical Physics*, vol. 76, pp. 637–649, 1982.

[161] D. K. Remler and P. A. Madden, "Molecular dynamics without effective potentials via the Car-Parrinello approach," *Molecular Physics*, vol. 70, pp. 921–966, 1990.

[162] M. C. Payne *et al.*, "Iterative minimization techniques for *ab initio* total-energy calculations: Molecular dynamics and conjugate gradients," *Rev. Mod. Phys.*, vol. 64, pp. 1045–1097, 1992.

[163] R. Iftimie *et al.*, "*AB INITIO* molecular dynamics: Concepts, recent developments, and future trends," *Proc. Natl. Acad. Sci. U.S.A.*, vol. 102, pp. 6654–6659, 2005.

[164] W. D. Callister and W. D. Callister, *Fundamentals of Materials Science and Engineering: An Interactive Etext*. New York: Wiley, 2001.

[165] A. R. Oganov *et al.*, "How Evolutionary Crystal Structure Prediction Works—and Why," *Acc. Chem. Res.*, vol. 44, pp. 227–237, 2011.

[166] Y. Wang *et al.*, "CALYPSO: A method for crystal structure prediction," *Computer Physics Communications*, vol. 183, pp. 2063–2070, 2012.

[167] C. W. Glass *et al.*, "USPEX—Evolutionary crystal structure prediction," *Computer Physics Communications*, vol. 175, pp. 713–720, 2006.

[168] A. O. Lyakhov *et al.*, "New developments in evolutionary structure prediction algorithm USPEX," *Computer Physics Communications*, vol. 184, pp. 1172–1182, 2013.

[169] L. B. Vilhelmsen and B. Hammer, "Systematic Study of Au 6 to Au 12 Gold Clusters on MgO(100) F Centers Using Density-Functional Theory," *Phys. Rev. Lett.*, vol. 108, p. 126 101, 2012.

[170] A. R. Oganov and C. W. Glass, "Crystal structure prediction using *ab initio* evolutionary techniques: Principles and applications," *The Journal of Chemical Physics*, vol. 124, p. 244 704, 2006.

[171] A. R. Oganov *et al.*, "Evolutionary Crystal Structure Prediction as a Method for the Discovery of Minerals and Materials," *Reviews in Mineralogy and Geochemistry*, vol. 71, pp. 271–298, 2010.

[172] A. O. Lyakhov *et al.*, "How to predict very large and complex crystal structures," *Computer Physics Communications*, vol. 181, pp. 1623–1632, 2010.

[173] H. Niu *et al.*, "Simple and accurate model of fracture toughness of solids," *Journal of Applied Physics*, vol. 125, p. 065 105, 2019.

[174] A. Hjorth Larsen *et al.*, "The atomic simulation environment—a Python library for working with atoms," *J. Phys.: Condens. Matter*, vol. 29, p. 273 002, 2017.

[175] K. Momma and F. Izumi, "VESTA: A three-dimensional visualization system forelectronic and structural analysis," *J. Appl. Crystallogr.*, vol. 41, pp. 653–658, 2008.

[176] J. Klimeš *et al.*, "Van der Waals density functionals applied to solids," *Phys. Rev. B*, vol. 83, p. 195 131, 2011.

[177] O. Köksal *et al.*, "Confinement-driven electronic and topological phases in corundum-derived 3d-oxide honeycomb lattices," *Phys. Rev. B*, vol. 97, p. 035 126, 2018.

[178] G. Barcaro *et al.*, "Validation of density-functional versus density-functional+U approaches for oxide ultrathin films," *The Journal of Chemical Physics*, vol. 132, p. 124 703, 2010.

[179] K. Lejaeghere *et al.*, "Error Estimates for Solid-State Density-Functional Theory Predictions: An Overview by Means of the Ground-State Elemental Crystals," *Critical Reviews in Solid State and Materials Sciences*, vol. 39, pp. 1–24, 2014.

[180] C. S. Barrett, "Crystal Structure of Barium and Europium at 293, 78, and 5 K," *The Journal of Chemical Physics*, vol. 25, pp. 1123–1124, 1956.

[181] C. Kittel, *Introduction to Solid State Physics*, Seventh. USA: John Wiley & Sons, 1996.

[182] P. Villars and L. D. Calvert, *Pearson's Handbook of Crystallographic Data for Intermetallic Phases*. USA: ASE International: Metals Park, 1998.

[183] J. Spreadborough and J. W. Christian, "The Measurement of the Lattice Expansions and Debye Temperatures of Titanium and Silver by X-ray Methods," *Proc. Phys. Soc.*, vol. 5, pp. 609–615, 1959.

[184] P. Janthon *et al.*, "Bulk Properties of Transition Metals: A Challenge for the Design of Universal Density Functionals," *J. Chem. Theory Comput.*, vol. 10, pp. 3832–3839, 2014.

[185] X. Shao *et al.*, "Strain-induced formation of ultrathin mixed-oxide films," *Phys. Rev. B*, p. 5, 2011.

[186] W. A. Adeagbo *et al.*, "Electronic and Magnetic Properties of $BaFeO_3$ on the Pt(111) Surface in a Quasicrystalline Approximant Structure," *Phys. Status Solidi B*, vol. 257, p. 1 900 649, 2020.

[187] C. Noguera, *Physics and Chemistry at Oxide Surfaces*. Cambridge University Press, 1996.

[188] J. Goniakowski *et al.*, "Adsorption of metal adatoms on FeO(111) and MgO(111) monolayers: Effects of charge state of adsorbate on rumpling of supported oxide film," *Phys. Rev. B*, vol. 80, p. 125 403, 2009.

[189] C.-T. Chiang *et al.*, "Electronic band structure of a two-dimensional oxide quasicrystal," *Phys. Rev. B*, vol. 100, p. 125 149, 2019.

[190] R. Tran *et al.*, "Anisotropic work function of elemental crystals," *Surf. Sci.*, vol. 687, pp. 48–55, 2019.

[191] R. Jacobs *et al.*, "Counterintuitive Reconstruction of the Polar O-Terminated ZnO Surface with Zinc Vacancies and Hydrogen," *J. Phys. Chem. Lett.*, vol. 7, pp. 4483–4487, 2016.

[192] U. Martinez *et al.*, "Tuning the work function of ultrathin oxide films on metals by adsorption of alkali atoms," *The Journal of chemical physics*, vol. 128, p. 164 707, 2008.

[193] S. Forster, *Accounting for complexity in periodic systems: A classification scheme for quasicrystal approximants*, Proceeding of the IRN-Aperiodic, Carry le Rouet, France, 2021.

[194] V. Wang *et al.*, "VASPKIT: A User-friendly Interface Facilitating High-throughput Computing and Analysis Using VASP Code," *Comput. Phys. Commun.*, vol. 267, p. 108 033, 2021.

[195] S. P. Ong *et al.*, "Python Materials Genomics (pymatgen): A robust, open-source python library for materials analysis," *Computational Materials Science*, vol. 68, pp. 314–319, 2013.

[196] S. Schenk *et al.*, *Dodecagonal oxide quasicrystal approximant with 72 tiling elements*, Presentation at ECMetAC Days, Proceeding of the ECMetAC Days, online conference, 2020.

[197] M. Methfessel and A. T. Paxton, "High-precision sampling for Brillouin-zone integration in metals," *Phys. Rev. B*, vol. 40, pp. 3616–3621, 1989.

[198] X.-F. Zhou *et al.*, "Two-dimensional magnetic boron," *Phys. Rev. B*, vol. 93, p. 085 406, 2016.

[199] F. Brix and É. Gaudry, "Two-dimensional metal structures revealed by evolutionary computations: Pb/$Al_{13}Co_4$(100) as a case study," *Journal of Vacuum Science & Technology A*, vol. 40, p. 012 203, 2022.

[200] A. B. Mazitov and A. R. Oganov, "Evolutionary algorithm for prediction of the atomic structure of two-dimensional materials on substrates," *ArXiv210307677 Cond-Mat*, 2021. arXiv: `2103.07677 [cond-mat]`.

[201] A. M. Halpern, "From Dimer to Crystal: Calculating the Cohesive Energy of Rare Gas Solids," *J. Chem. Educ.*, vol. 89, pp. 592–597, 2012.

[202] E. M. Zollner *et al.*, "C_{60} adsorption on a dodecagonal oxide quasicrystal," *Phys. Rev. B*, vol. 100, p. 205 414, 2019.

[203] H. T. Evans Jnr, "An X-ray diffraction study of tetragonal barium titanate," *Acta Crystallogr.*, vol. 14, pp. 1019–1026, 1961.

[204] W. Jauch and A. Palmer, "Anomalous zero-point motion in $SrTiO_3$: Results from X-ray diffraction," *Phys. Rev. B*, vol. 60, p. 3, 1999.

[205] R. Robinson, "Structural Changes in the Solid Solution $(Ti_{1-x}\text{-}V_x)_2O_3$ as x Varies from Zero to One," p. 10,

[206] E. Hellner and F. Laves, "Kristallchemie des In und Ga in Legierungen mit einigen Übergangselementen (Ni, Pd, Pt, Cu, Ag und Au)," *Z. Für Naturforschung A*, vol. 2, pp. 177–184, 1947.

Abstract: The growth of two dimensional (2D) oxide materials on metals or intermetallics can lead to complex atomic arrangements, whose structural description at the atomic scale is not straightforward. Considerable progress has been made in crystal structure prediction in recent years through the development of efficient computer codes and the availability of powerful computational resources. In this work, several approaches are used that are based on tiling configurations, evolutionary algorithms, and ab initio molecular dynamics, combined with Density Functional Theory. We focus on two distinct ultrathin films systems : oxide quasicrystalline approximants (OQA) and complex oxide films grown on PdIn(001). In the former system, we start from the structural models derived from the works of Förster et al. and Cockayne et al., and systematically investigate the intrinsic properties of these 2D OQA supported on metallic substrates. We reveal structure-property relationships and compare with recently discovered phases. On the latter system, we apply a combination of DFT and evolutionary computations to propose several possible atomic structures of ultrathin indium oxide films on PdIn(001). For both systems, the stability is investigated with formation enthalpies and surface free energies, using thermodynamic models to account for the growth conditions. The scanning tunneling microscopy (STM) images, which are correlated with the tiling configurations for each structure, are simulated as well. Electronic-structure calculations also provide insights about the oxide–substrate interactions. This computational work can be used as a basis for future experiments and is valuable for the theoretical understanding of the structure-properties relationship for these ultrathin films.

Key words: *Ab initio*, Density Functional Theory (DFT), ultrathin films, oxide quasicrystalline approximants (OQA), Sr–Ti–O/Pt(111), Genetic Algorithm (GA), In_xO_y/PdIn(001).

Résumé : La croissance de matériaux oxydes bidimensionnels (2D) sur des métaux ou des intermétalliques peut conduire à des arrangements atomiques complexes, dont la description structurale à l'échelle atomique n'est pas simple. Des progrès considérables ont été réalisés dans la prédiction de structures cristallines ces dernières années, grâce au développement de codes de calcul efficaces et à la disponibilité de ressources de calcul importantes. Dans ce travail, plusieurs approches sont utilisées, basées sur des configurations de pavage, un algorithmes évolutif, ou des calculs de dynamique moléculaire ab initio, combinés à la Théorie de la Fonctionnelle de la Densité. Nous nous concentrons sur deux systèmes de films ultra-minces distincts : les approximants quasi-cristallins d'oxyde (OQA) et les films d'oxyde complexes supportés sur PdIn(001). Dans le premier système, on part des modèles structuraux issus des travaux de Förster et al. et Cockayne et al. et nous étudions systématiquement les propriétés intrinsèques de ces OQA 2D lorsqu'ils sont déposés sur des substrats métalliques. Cela nous permet de révéler les relations structure-propriété et les comparer aux phases récemment découvertes. Sur le deuxième système, nous appliquons une combinaison de DFT et de calculs évolutifs pour proposer plusieurs structures atomiques possibles de films d'oxyde d'indium ultrafins sur PdIn(001). Pour les deux systèmes, la stabilité est évaluée par le calcul des enthalpies de formation et des énergies de surface, en utilisant des modèles thermodynamiques pour rendre compte des conditions de croissance. Les images de microscopie à effet tunnel (STM), qui sont corrélées avec le pavage (arrangements des des tuiles) pour chaque structure, sont simulées. Les calculs de structure électronique fournissent également des informations sur l'interaction oxyde-substrat. Ce travail théorique peut être utilisé comme base solide pour de futures expériences et est précieux pour la compréhension théorique de la relation structure-propriétés de ces films ultra-minces.

Mots-clés : *Ab initio*, Théorie de la fonctionnelle de la densité (DFT), films ultraminces, oxide quasicrystalline approximants (OQA), Sr–Ti–O/Pt(111), algorithme génétique (GA), In_xO_y/PdIn(001).